

DEVELOPMENT OF ATMOSPHERIC CORRECTION ALGORITHMS FOR VERY HIGH SPECTRAL AND SPATIAL RESOLUTION IMAGES:

APPLICATION TO SEOSAT AND THE FLEX/SENTINEL-3 MISSIONS



NEUS SABATER MEDINA

Directores:

José Moreno Méndez

Jochem Verrelst

Doctorado en Teledetección

Marzo 2018



DEVELOPMENT OF ATMOSPHERIC
CORRECTION ALGORITHMS FOR VERY
HIGH SPECTRAL AND SPATIAL
RESOLUTION IMAGES: APPLICATION TO
SEOSAT AND THE FLEX/SENTINEL-3
MISSIONS

By

María de las Neus Sabater Medina



PHD THESIS · TESIS DOCTORAL
Programa de Doctorado en Teledección

THESIS ADVISORS · DIRECTORES DE TESIS
José Moreno Méndez
Jochem Verrelst

Laboratorio de Procesado de Imágenes
Parque Científico
UNIVERSITAT DE VALÈNCIA – ESTUDI GENERAL
València, Marzo 2018

Development of atmospheric correction algorithms for very high spectral and spatial resolution images: Application to SEOSAT and the FLEX/Sentinel-3 missions

María de las Neus Sabater Medina, 2018.



Departamento de Física de la Tierra y Termodinámica
Facultad de Física · Universitat de València

D. JOSÉ F. MORENO, Doctor en Ciencias Físicas, Profesor Titular del Departamento de Física de la Tierra y Termodinámica de la Facultad de Física de la Universitat de València, y

D. JOCHEM VERRELST, Doctor en 'Remote Sensing', investigador post-doc en el Laboratorio de Procesado de Imágenes, Parque Científico de la Universitat de València

HACEN CONSTAR QUE:

Emiten este informe **favorable** para el depósito y la defensa de la Tesis del trabajo realizado bajo nuestra supervisión por la licenciada en Física **María de las Neus Sabater Medina** y titulado "DEVELOPMENT OF ATMOSPHERIC CORRECTION ALGORITHMS FOR VERY HIGH SPECTRAL AND SPATIAL RESOLUTION IMAGES: APPLICATION TO SEOSAT AND THE FLEX/SENTINEL-3 MISSIONS", que se presenta en esta memoria para optar al grado de Doctor (con Mención Internacional) en Teledetección por la Universidad de Valencia.

Y para que así conste a los efectos oportunos, firmamos el presente certificado, en Valencia, a 21 de marzo de 2018.

José F. Moreno

Jochem Verrelst

Tesis Doctoral: DEVELOPMENT OF ATMOSPHERIC CORRECTION ALGORITHMS
FOR VERY HIGH SPECTRAL AND SPATIAL RESOLUTION IMAGES:
APPLICATION TO SEOSAT AND THE FLEX/SENTINEL-3 MISSIONS

Autor: MARÍA DE LAS NEUS SABATER MEDINA

Directores: Dr. JOSE F. MORENO MÉNDEZ
 Dr. JOCHEM VERRELST

El tribunal nombrado para juzgar la citada Tesis Doctoral, compuesto por:

Presidente: _____

Vocales: _____

Secretario: _____

Acuerda otorgarle la calificación de _____

Y para que así conste a los efectos oportunos, firmamos el presente certificado.

Valencia, a

*Mon dessin ne représentait pas un chapeau.
Il représentait un serpent boa qui digérait un éléphant.
J'ai alors dessiné l'intérieur du serpent boa,
afin que les grandes personnes puissent comprendre.*

– Le Petit Prince – Antoine de Saint-Exupéry



Acknowledgments

Son muchas las personas a las que tengo algo que agradecer porque de alguna forma u otra han contribuido en lo personal y/o profesional durante estos primeros años de profesión.

En primer lugar, Pepe, ¡por tantas cosas! Por ser el primero que me abrió las puertas del mundo de la investigación y por el entusiasmo que le pones a la ciencia (aunque no lo sepas, se contagia). Para mí hay una frase que resume muchos aspectos de estos últimos años. Recuerdo que antes de mi primera reunión en la *esa*, puede que por mi cara de circunstancia, me dijo: *'No te preocupes, si algo va mal yo voy a estar ahí'*. Para mí esa frase resume gran parte de la forma de trabajar de estos últimos años, siendo independiente y trabajando en equipo con un fin común, muchas veces con estrés, pero sabiendo que contaba con el apoyo necesario.

El siguiente en la lista es Jochem, junto con Pepe has ayudado a hacer posible que se culmine este trabajo. Jochem, I am so grateful for all the support you have offered me, especially this last months reviewing the manuscript sometimes even faster than I was updating it. Every day you show us those skills that any scientist requires to achieve a successful career... Many thanks for all!

Mi tercer supervisor (extraoficial) ha sido Luis. Buf! Ahora sí que me quedo corta... Contigo he aprendido tanto (y lo que me queda porque no dejas de sorprenderme). Tu pasión por enseñar y dedicarte más a los demás que a ti mismo es un hecho. Gracias por todo lo que me has enseñado y por tantos cafés que muchas veces han sido más provechosos que 2 horas programando enfrente del ordenador (o al menos yo los he disfrutado mucho más). Ha sido una suerte inmensa tenerte en el despacho de al lado (y brevemente en el mismo).

Si sigo por orden de despachos en el grupo LEO (el esquema antiguo que tengo en mente), le tocaría a Jorge, aunque ahora esté a cientos de kilómetros. Contigo empecé mano a mano en este grupo y en FLEX. En tu tesis ponías que había gran parte de mí en ese trabajo, pues ahora, un año más tarde te digo lo mismo. Hay gran parte de ti en este trabajo también. Gracias por los años compartidos de trabajar 100% en equipo.

Y como sigo esa estructura antigua de despachos, la siguiente es mi compañera de mesa, Caro. Has sido un apoyo increíble estos años, tú eres el simulador de FLEX. Es increíble la capacidad de trabajo que tienes y como sacas delante las cosas de una forma extraordinaria. De verdad que espero que la siguiente en ser doctora seas tú, porque para mí lo eres hace tiempo.

Y hablar de Caro, es hablar de Antonio, el 'dream team'. Viniste en el mejor momento para aportar esa chispa especial que te hace único. Sé que el magnífico científico que llevas dentro

lleva tiempo retenido para dejar paso al manager brillante que eres. Como a Luis, lo de ser doctor ya se os queda pequeño. . .

Si aún no he pasado de despacho es porque ahí está Jesús, viniendo con su bici y diciendo: ‘Buenos días, ¡bonica!’ Me despertabas una sonrisa matutina cada día.

Estos últimos meses antes de venirme a Invernia he tenido la suerte de que Shari asomara por la puerta del despacho diciendo: Coffee? I’ve found such a really close friend in you. Thanks for all the talks about science, life in general. . . about all.

Y el grupo LEO sigue creciendo: Marcela, Nieves, Patricia, Mariapi (de regreso), Eati-dal. . . y tod@s los que vendrán. Disfrutad de este gran grupo de científicos, pero sobre todo de personas.

Gracias también por esos momentos de las comidas o viajes de congresos a Emma, Gus, Valero, Luis, Julia, Jordi, Jesús, Ana, Gonzalo, Daniel, . . . sois un grupo fantástico.

Durante el doctorado, he podido hacer estancias que me han abierto las puertas a nuevas experiencias. Thanks Betsy for hosting me last year at NASA and for your always kind words. Ahora en invernia (Helsinki), thanks Gerrit for hosting me at FMI, gracias Edith por recibirme con los brazos abiertos y Pekka, thanks for the coffee moments that make feel like at home!

Y porque no todo en esta vida es trabajo, fuera del IPL, gracias a la gente que me rodea, a Lorena por siempre estar ahí, a Paula por ser fuente de inspiración y superación, a Rosa, Noelia, Vero, Marioleta, Cata, Sandra, Emilio. . . y todos los que no menciono pero formáis parte de Mislata y Picassent.

A mis padres, por todo y porque creo que tenían más ganas que yo de que acabara la tesis.

A Boro, és difícil trobar les paraules, tot es queda curt... gràcies per aquesta vida junts (i per aquesta increíble portada ;)).

Acronyms and Abbreviations

AARDVARC Atmospheric Aerosol Retrieval Dual View Angle Reflectance Channels

AATSR Advanced Along-Track Scanning Radiometer

AC Atmospheric Correction

AERONET AErosol RObotic NETwork

AI Atmospheric Inversion

AOT Aerosol Optical Thickness

APDA Atmospheric Pre-corrected Differential Absorption technique

ARA Absolute Radiometric Accuracy

ATCOR Atmospheric & Topographic CORrection

BQ Band Quotient

BRDF Bidirectional Reflectance Distribution Function

CHRIS Compact High Resolution Imaging Spectrometer

CIRB Continuum Interpolated Band Ratio

CWV Columnar Water Vapour

DB DataBase

DDV Dark Dense Vegetation

DEM Digital Elevation Model

DHG Double Henyey-Greenstein

DOS Dark Object Subtraction

ENSO El Niño–Southern Oscillation

ERS European Remote Sensing

ESA European Space Agency

EVI Enhanced Vegetation Index

FLD Fraunhofer Linear Discriminator

FLEX FLuorescence EXplorer

FLORIS FLORIS

FWHM Full Width High Maximum

GOME Global Ozone Monitoring Experiment

GOSAT Greenhouse Gases Observing Satellite

GPP Gross Primary Productivity

GSD Ground Sampling Distance

GSD Ground Sampling Distance

HG Henyey-Greenstein

HITRAN High-resolution TRANsmision molecular absorption database

ISRF Instrumental Spectral Response Function

LAI Leaf Area Index

LIRR Linear Regression Ratio

LOS Line Of Sight

LST Land Surface Temperature

LTDN Local Time of Descending Node

LUT Look Up Table

MACC Monitoring Atmospheric Composition and Climate

MERIS MEDium Resolution Imaging Spectrometer

MISR Multi-angle Imaging SpectroRadiometer

ML Machine Learning

MODTRAN MODerate resolution atmospheric TRANsmision

MOMO Matrix Operator Model

MSG METEOSAT Second Generation

MSI MultiSpectral Instrument

MTF Modulation Transfer Function

NBS Narrow Band Spectrometer

NDVI Normalized Difference Vegetation Index

NIR Near-Infrared

OCO Orbiting Carbon Observatory

OLCI Ocean and Land Colour Instrument

OPAC Optical Properties of Aerosols and Clouds

PAN Panchromatic

PH Peak Height

PNOTS Spanish Earth Observation National Program for Satellites (acronym in Spanish)

POLDER POLarization and Directionality of the Earth's Reflectances

PSF Point Spread Function

QUAC QUick Atmospheric Correction

RGB Red-Green-Blue

RSRA Relative Spectral Radiometric Accuracy

RXRA Relative Spatial Radiometric Accuracy

RTM Radiative Transfer Model

S3 Sentinel-3

SCOPE Soil–Canopy Observation of Photosynthesis and Energy

SEOSat Scientific Earth Observation Satellite

SEVIRI Spinning Enhanced Visible and Infra-Red Imager

SFM Spectral Fitting Methods

SIF Solar-Induced chlorophyll Fluorescence

SLSTR Sea and Land Surface Temperature Radiometer

SNR Signal to Noise Ratio

SR Spectral Resolution

SSD Spatial Sampling Distance

SSI Spectral Sampling Interval

SST Sea Surface Temperature

SWIR Short-wave Infrared

SZA Solar Zenith Angle

TOA Top Of Atmosphere

TOC Top of Canopy

UAV Unmanned Aerial Vehicles

VZA Visual Zenith Angle

WBS Wide Band Spectrometer

Contents

Acknowledgments	ix
Acronyms and Abbreviations	xi
1 Introduction	1
1.1 Context	1
1.2 Motivation and objectives	2
1.3 Research questions	4
1.4 Thesis outline	6
2 Background	9
2.1 The Earth's atmosphere	9
2.2 Atmospheric major constituents and their radiative effects	15
2.3 Atmospheric correction: an ill-posed problem	20
2.4 Aerosol and water vapour retrieval strategies	26
2.5 Considerations for high spatial and spectral resolution images	35
3 Analysing the atmospheric effects on high spatial resolution satellite images: Application to the Ingenio/SEOsat space mission	39
3.1 Abstract	40
3.2 Introduction	41
3.3 The Ingenio/SEOsat space mission	42
3.4 The Ingenio/SEOsat sensitivity to atmospheric effects	43
3.5 Exploiting the spatial information for aerosol detection	50
3.6 Hybrid atmospheric correction strategy	55

3.7	Discussion	66
3.8	Conclusions	69
4	A proposed atmospheric correction algorithm for the FLEX/Sentinel-3 tandem space mission	71
4.1	Abstract	72
4.2	Introduction	73
4.3	FLORIS spectral sensitivity analysis to detect Solar-Induced chlorophyll Fluorescence (SIF)	75
4.4	The two-steps algorithm	81
4.5	Database simulation	92
4.6	Results	101
4.7	Discussion	107
4.8	Conclusions	111
5	Atmospheric Inversion Effects on Solar-Induced Chlorophyll Fluorescence and apparent reflectance exploitation	113
5.1	Abstract	114
5.2	Introduction	115
5.3	The AI process: from TOA radiance to SIF through the apparent reflectance inversion	116
5.4	Apparent reflectance error analysis and its predictive power	122
5.5	Discussion	130
5.6	Conclusions	133
6	Atmospheric compensation on proximal sensing data for satellite validation	135
6.1	Abstract	136
6.2	Introduction	137
6.3	SIF retrieval methods for proximal sensing	141
6.4	Impact of oxygen transmittance compensation on SIF	146
6.5	Analysis in Temperature and Pressure Environmental Conditions	157
6.6	Discussion	160
6.7	Conclusions	163

7	Summary and conclusions	165
7.1	Summary. Main results	165
7.2	General conclusions	169
8	Relevance	177
8.1	Achievements and relevance	177
8.2	Acknowledgments	184
8.3	Research collaboration in other centres	184
8.4	Future and on-going research projects	185
9	Summary in Spanish	187
9.1	Introducción	187
9.2	Motivación y objetivos	189
9.3	Metodología y estructura	190
9.4	Resultados	191
9.5	Conclusiones	195
A	Appendix: Instruments	203
A.1	Ingenio/SEOsat	204
A.2	FLORIS	206
A.3	OLCI	209
A.4	SLSTR	212
	Bibliography	215

1

Introduction

Contents

1.1	Context	1
1.2	Motivation and objectives	2
1.3	Research questions	4
1.4	Thesis outline	6

1.1 Context

The perfect location where we can learn the most about our planet is found nowhere on the Earth but high up above it, in space [European Space Agency, 2017a]. Satellite remote sensing has opened new ways of seeing the world and its dynamics at a global scale. With every sunrise, the Earth's surface is bathed in solar energy, which is then absorbed or reflected back to space. Making use of the solar reflected light, passive optical remote sensing instruments monitor the coupled Earth–atmosphere system.

While the study of the atmospheric components and dynamic is a subject of Earth observation monitoring itself, even when we are only interested in studying the underlying Earth surface, atmospheric effects must always be accounted for, i.e., through an **atmospheric correction** process.

Atmospheric correction can be defined as the process that transforms radiances acquired at a satellite or air–borne scale to surface reflectance. This process commonly implies the knowledge of the atmospheric state or at least the characterization of the main physical processes that

occur as the solar light passes through the atmosphere, i.e., light scattering and absorption, both from aerosols and molecules.

Atmospheric correction algorithms have been designed and applied to correct optical remote sensing data for over 30 years, from simple approximations [Chavez, 1988] to complex physical model inversion methods [Vermote *et al.*, 1997a]. Under a historical perspective, the development of atmospheric correction algorithms has occurred hand in hand with advances in optical remote sensing sensors. While the first Earth observation satellite missions were only equipped with some bands located in the well-known atmospheric windows, i.e., spectral regions where atmospheric effects can be ignored, current Earth observation satellite sensors are equipped with spectral bands located in the atmospheric windows as well as in some strategically atmospheric component's absorption bands.

Some examples of these strategically located bands to characterize the atmospheric state include: (1) bands located in the blue spectral region to increase aerosol detection sensitivity; (2) bands located in and outside one of the main water vapour absorption regions (940 nm), which allows the estimation of the total columnar water vapour content; (3) bands located in the oxygen (O₂-A) absorption region, which allows estimating the surface pressure and helps in the identification of the cloud top height; (4) bands located in the strong water vapour absorption region around 1300 nm to detect thin *Cirrus* clouds, etc. On top of that, thermal bands also provide an extra source of information, not only to determine surface temperature but also to improve cloud screening algorithms.

Parallel to the increase in sensor bands, the ongoing development of sensor specifications and capabilities, i.e., the increasing high spectral, spatial and radiometric resolution; makes an in-depth study mandatory to adapt the already formulated atmospheric correction strategies or even the definition of new methodologies able to cope with these new sensor specifications.

1.2 Motivation and objectives

Each time more advanced high spectral and spatial resolution imager spectrometers on board a new generation of Earth Observation missions bring new exciting opportunities to the remote sensing scientific community. However, the exploitation of data acquired from these family of advanced instruments requires, without a doubt, new processing algorithms able to deal with these particularities. As part of this evolution, atmospheric correction algorithms, which are applied prior to the Earth surface reflectance data exploitation, must also be adapted or reformulated, thereby paying special attention to how atmospheric effects disturb the acquired signal in the spectral and spatial domains.

For these reasons, this Thesis aims to analyse and define new atmospheric correction strategies to be applied over very high spectral and spatial resolution data. Following this goal, this Thesis considers the FLEX/Sentinel-3 tandem space mission (for high spectral resolution data) and the SEOSat/Ingenio space mission (for high spatial resolution data). In the context of these missions, an additional challenge is introduced when acquiring proximal remote sensing data

for their validation. In particular, atmospheric effects must be compensated in order to guarantee a proper satellite validation strategy for the FLEX mission, even when acquiring the signal at proximal remote sensing scale, i.e., few meters from the target.

Following this motivation, the main objective of this Thesis is threefold: (1) to analyse atmospheric effects on the Ingenio/SEOsat high spatial and low spectral resolution satellite mission and define a new atmospheric correction strategy focused on the exploitation of high spatial resolution data at satellite level; (2) to define a new atmospheric correction strategy that is focused on the exploitation of very high spectral resolution data also at satellite level, and finally; (3) to develop a strategy that deals with the atmospheric correction of very high spectral and spatial resolution data acquired at lower atmospheric scales such as Unmanned Aerial Vehicles (UAVs) or systems mounted on towers.

The Thesis in a nutshell:

How is this Thesis addressed?

This Thesis is addressed under the following theoretical framework. It starts with introducing the most fundamental physical aspects that describes the atmospheric radiative effects, including main atmospheric gaseous components and aerosols. Then, a review of the most popular atmospheric correction algorithms is provided. Taking that as a baseline, the proposed atmospheric correction strategies developed within this Thesis will address the specific particularities for high spectral and spatial resolution data at multiple scales using simulated images that were developed under context of the preparatory activities for the FLEX/Sentinel-3 and Ingenio/SEOsat space missions.

What are the main goals?

To design new atmospheric correction strategies to be successfully applied over: (1) high spatial resolution satellite images (in the context of the Ingenio/SEOsat mission); (2) high spectral resolution satellite images (in the context of the FLEX/Sentinel-3 mission); and (3) high spatial and spectral resolution data at lower atmospheric scale (also in the context of the FLEX/Sentinel-3 mission).

Why is the topic important?

Because of the ongoing progress towards more advanced passive optical spectrometers mounted on satellites, airborne or towers that are able to acquire the radiance signal at a each time higher spectral and spatial resolution. In this respect, in order to ensure an optimal data exploitation, missions with advanced sensors dedicated to the Earth's surface monitoring and exploitation require an evaluation and adaptation of the currently existing atmospheric correction algorithms.

1.3 Research questions

This Thesis contributes to the field of developing new atmospheric correction algorithms that are able to cope with each time more advanced remote sensing spectrometers. An important aspect hereby is that atmospheric effects analysed in this Thesis cannot be understood without considering both, the spectral and the spatial domain. Regarding the spectral domain, atmospheric correction algorithms based on the inversion of a physical radiative transfer model are generally applied to multispectral and hyperspectral (~ 10 nm of spectral sampling interval) imaging spectrometers. However, the application of such atmospheric correction techniques to very high spectral resolution spectrometers (~ 0.1 nm of spectral sampling interval) is not straightforward. Therefore, the main objective of this part is twofold: (1) to analyse under the context of the FLEX mission the validity of the application of an atmospheric correction strategy based on a radiative transfer model inversion scheme, and (2) to determine if the exploitation of the very high spectral resolution data can deal with a technique that improves the atmospheric characterization. Regarding the spatial domain, atmospheric spatial effects are studied to determine if there is a need for compensation in the context of the Ingenio/SEOSat space mission; and if so, what would be the best strategy to be applied. All these objectives are guided by the following research questions:

- ***What are the particularities to be considered when developing an atmospheric correction strategy for high spatial resolution satellite images?*** Atmospheric effects in the spatial domain generate a kind of blurring effect in the image that can be observed even with the naked eye. In other words, aerosol and molecular scattering tend to reduce the image contrast. This effect can be particularly noticed on images acquired by high spatial resolution sensors; which in turn, typically are provided with only few bands in the spectral domain. Due to this reason, when facing the development of a new atmospheric correction strategy addressed for high spatial resolution sensors, two considerations must be kept in mind: (1) the use of auxiliary information to characterize the atmospheric state, and (2) the exploitation of the spatial information in such a way that it can improve the atmospheric characterization process. Finally, since adjacency effects are critical on high spatial resolution sensors, it is mandatory that the developed atmospheric correction strategy deals with the compensation of this effect, especially in areas with high radiometric contrast.
- ***What are the particularities to be considered when developing an atmospheric correction strategy for high spectral resolution satellite images?*** The exploitation of the acquired radiance in the spectral domain with the purpose of characterizing the atmospheric state is common practise in remote sensing data processing. However, when facing the development of an atmospheric correction strategy for very high spectral resolution data, then the suitability of classical atmospheric inversion schemes needs to be analysed in terms of: (1) the formulation used to perform the inversion, and (2) the possibility to optimally exploiting the very high spectral resolution data in order to improve the atmospheric characterization. Moreover, the FLEX mission context imposes an additional

challenge related to the required accuracy of the estimated surface reflectance products. Thus, in this respect, the following research questions are addressed:

- ***What kinds of limitations have to be resolved when a classical atmospheric correction strategy (by means of a radiative transfer model inversion) is applied to the FLEX/Sentinel-3 tandem space mission?*** FLEX is designed as a tandem mission with the Copernicus Sentinel-3 space mission. The main reason for flying in tandem is to expand FLEX capabilities for its atmospheric correction. The very high spectral resolution spectrometer on board FLEX, called FLORIS, is specifically designed to vegetation monitoring only covering wavelengths from 500 nm to 800 nm. Therefore, given this tandem mission configuration using simulated data, this Thesis proposes and evaluates an atmospheric correction algorithm based on a physical radiative transfer model inversion technique.
 - ***Is the current mathematical formulation used for the atmospheric inversion process suitable for working with high spectral resolution data?*** Atmospheric correction algorithms based on the inversion of an atmospheric radiative transfer model are considered as the most accurate and recommended strategy to atmospherically correct passive optical remote sensing images. However, common assumptions related to the mathematical inversion might not be valid when working with very high spectral resolution data or for certain specific scientific goals. To this end, this Thesis explores the suitability of the mathematical formulation used as part the atmospheric inversion process in the context of the FLEX mission.
 - ***In the particular case of the FLEX mission: How can the exploitation of the very high spectral resolution help in the characterization of the aerosol optical properties?*** Retrieving the surface apparent reflectance at high spectral resolution opens opportunities not only to measure the contribution of the solar-induced vegetation chlorophyll fluorescence, but also to detect inaccuracies in aerosol optical properties and in the instrument characterization. Following this aim, this Thesis explores the possibility to detect inaccuracies in the aerosol characterization by exploiting the surface apparent reflectance spectrum, and therefore the improvement of the overall atmospheric correction process.
- ***At proximal sensing scale: Is it necessary to compensate for atmospheric effects?*** While for certain scientific purposes atmospheric effects at proximal sensing scale (few meters from the surface), can be reasonably neglected, that may be not the case when monitoring SIF at canopy level. SIF is generally estimated by exploiting information at the oxygen features, implying that its estimation is therefore sensitive to atmospheric effects. This topic is of importance in the context of FLEX's future validation activities where field campaigns will be developed at a proximal sensing scale.

1.4 Thesis outline

This Thesis addresses how atmospheric effects disturb the signal acquired by remote sensing instruments at multiple scales and for diverse instrument configurations. It is organized as follows. It starts with a general background description, including the explanation of the physical radiative transfer processes occurring in the atmosphere, and a brief overview of the most relevant atmospheric correction algorithms used by the passive optic remote sensing community (*Chapter 2*). Although the presented overview of the atmospheric correction algorithms focusses mainly on satellite scale, it lays the foundation to understand the proposed atmospheric correction strategies for each of the different scenarios tackled in this Thesis, as outlined in Figure 1.4.1.

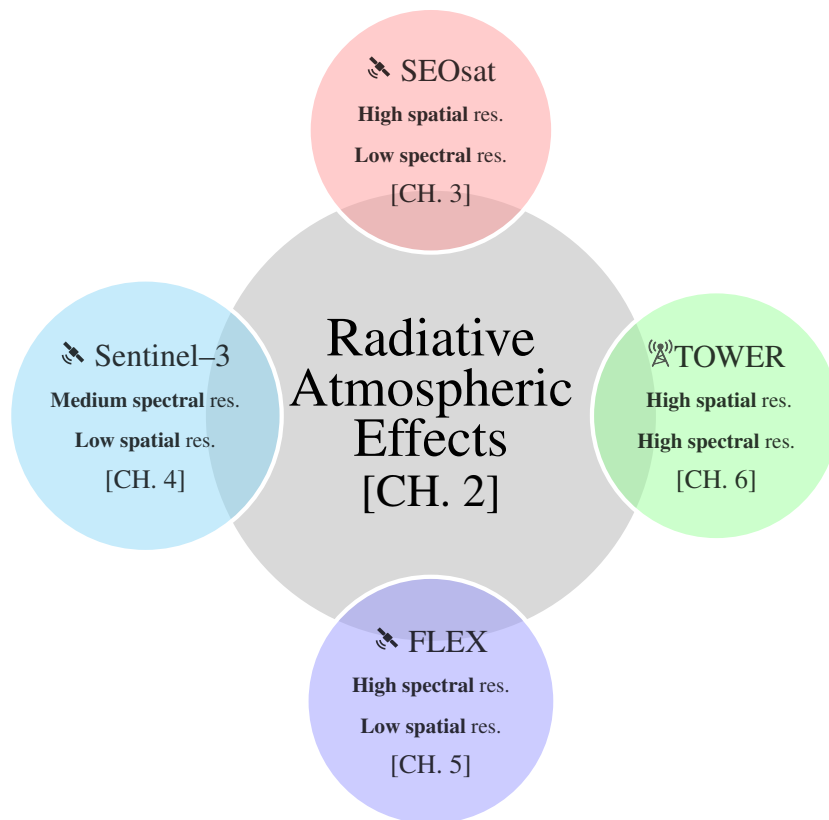


FIGURE 1.4.1: Bubble diagram linking the four thematic chapters [CH.] 3–6 with the Thesis scientific background chapter [CH.] 2.

Accordingly, four thematic chapters focus on high spatial (*Chapter 3*) and spectral (*Chapters 4 and 5*) resolution at satellite scale, and then continuing at a lower scale, i.e., at proximal remote sensing (*Chapter 6*), where ultimately both the high spectral and spatial resolution are met. To close this Thesis, the main conclusions are synthesized in *Chapter 7*.

The outline is summarized as follows:

- **CHAPTER 2** [CH. 2] describes the interaction between the atmosphere, surface and solar radiation, which is considered as a baseline to understand the atmospheric correction process of optical remote sensing data. This overview covers the description of the absorption and scattering processes produced as the solar light passes through the atmosphere, as well as the description of the main atmospheric components. Also, an overview of the most relevant atmospheric correction strategies is given.
- **CHAPTER 3** [CH. 3] analyses the aerosol effects in the spectral and spatial domain given the Ingenio/SEOsat space mission specifications. In this chapter, a new methodology is developed to exploit the high spatial resolution data to infer information about the atmospheric state under a theoretical framework. Subsequently, a new atmospheric correction strategy to correct the future Ingenio/SEOsat space mission data is proposed and tested using Sentinel-2 images for its validation.
- **CHAPTER 4** [CH. 4] proposes a new atmospheric correction algorithm for the tandem space mission FLEX/Sentinel-3, based on the exploitation of the Sentinel-3 data for the atmospheric characterization. This strategy is evaluated in view of the FLEX mission requirements to estimate SIF. In this chapter, scenarios that accomplish and do not accomplish the mission requirements are analysed. Consequently, the possible exploitation of the high spectral resolution data to improve the atmospheric characterization, and therefore the SIF estimation, is afterwards studied in the next chapter.
- **CHAPTER 5** [CH. 5] is dedicated to the assessment of the mathematical formulation used as part of the mathematical inversion procedure applied during the atmospheric correction of the FLORIS instrument on board FLEX. The assessment focusses on the suitability of this formulation when working with high spectral resolution data and coupling two methodologies: (1) for the atmospheric inversion, and (2) for the fluorescence estimation. In this chapter, the capability of the apparent reflectance to correct inaccuracies in the aerosol characterization as part of the atmospheric correction process is presented.
- **CHAPTER 6** [CH. 6] focusses on the particularities to be addressed when the atmospheric correction algorithms are applied on proximal sensing scale. This chapter analyses the importance of correcting aerosol and oxygen absorption effects to detect SIF with high spectral resolution spectrometers.
- **CHAPTER 7** [CH. 7] synthesizes the accomplished scientific objectives of this Thesis and presents main conclusions.
- **CHAPTER 8** [CH. 8] highlights the Thesis' achievements in a broader scientific context. International and national publications related with the activities developed under the framework of this Thesis, as well as the international collaborations with other research centres are detailed.
- **CHAPTER 9** [CH. 9] presents an overview of the Thesis in Spanish. This chapter includes a section dedicated to the Thesis introduction, motivation and outline. Finally, achieved results are presented and main conclusions are summarized.

The here mentioned thematic chapters [**CH. 3-6**] address the atmospheric correction problem from multiple points of views. To facilitate the understanding and the readability of this Thesis, all these chapters are self-consistent, meaning that a brief introduction as well as main conclusions are presented at the beginning and at the end of each chapter, respectively.

2

Background

Contents

2.1	The Earth's atmosphere	9
2.2	Atmospheric major constituents and their radiative effects	15
2.3	Atmospheric correction: an ill-posed problem	20
2.4	Aerosol and water vapour retrieval strategies	26
2.5	Considerations for high spatial and spectral resolution images	35

This chapter introduces the fundamentals of Earth's atmospheric composition and atmospheric radiation, which are the essential concepts needed to understand most remote sensing atmospheric correction algorithms. Following, the most relevant atmospheric correction algorithms are reviewed to establish the state of the art. Finally, this chapter closes with some remarks about the design and development of new atmospheric correction algorithms devoted to high spectral and spatial resolution sensors.

2.1 The Earth's atmosphere

Earth's atmosphere can be understood as a homogeneous gaseous blend composed by a mixture of molecules and particles, all of them attracted by the Earth's gravity field, which conforms a protective layer for the development of biological life. Typically, the Earth's atmosphere is divided in different strata – let us consider an strata as an horizontal or plane-parallel layer for simplicity – according to the regions where the temperature gradient changes abruptly. In the atmosphere, while air pressure and density generally decrease with altitude, temperature

has a more complicated profile (See figure 2.1.1). According to this, the atmosphere is commonly divided into 5 distinct layers: *troposphere*, *stratosphere*, *mesosphere*, *thermosphere*, and *exosphere*.

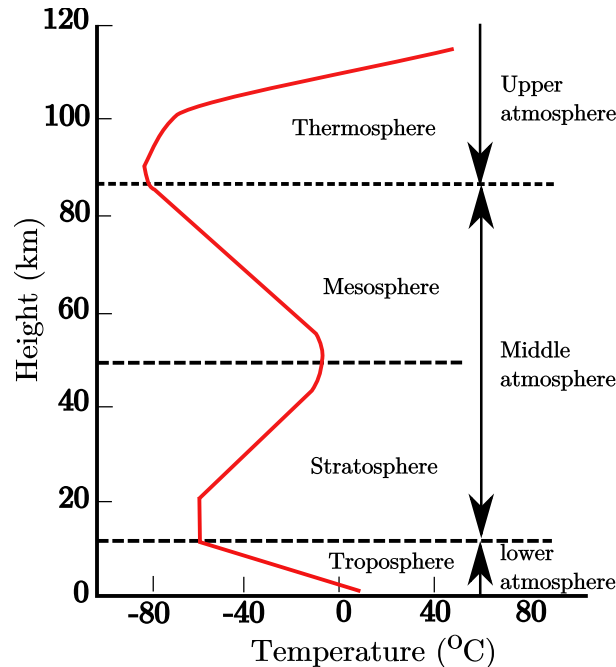


FIGURE 2.1.1: Typical temperature vertical profile used to illustrate the atmospheric layers division.

Although the actual thermal structure of the atmosphere is more complicated than the profile shown in Figure 2.1.1, essentially, the thermal structure is a consequence of the atmospheric gaseous composition vertical structure and its interaction with the solar radiation. The lower and middle atmosphere can be considered as an homogeneous gaseous blend, where the three major constituents are nitrogen (N_2), oxygen (O_2), and argon (Ar). See Figure 2.1.2 for more atmospheric constituents details.

Thus, the atmosphere can be studied from diverse scientific point of views. From a thermodynamical point of view, the presence of water content in the troposphere at different physical phases: gaseous, liquid and solid (ice particles), determines cloud and liquid drop formation as part of the water cycle. From a dynamical perspective, atmospheric circulation, coupled with ocean circulation, results into global phenomenons such as the El Niño–Southern Oscillation (ENSO), known as 'El Niño' and 'La Niña' effects. From a chemical orientation, industry development is currently altering on gaseous concentration, especially greenhouse gases, which impacts our climate. However, for remote sensing applications, and particularly in view of developing atmospheric correction algorithms, Earth's atmosphere must be studied as an absorbing and scattering medium.

The general radiative transfer theory analyses the interaction of the radiation field with a scattering–absorbing–emitting medium, where photons are submitted to multiple scatterings [Lenoble *et al.*, 2013]. For the Earth's atmosphere, the natural sources of radiation are the short

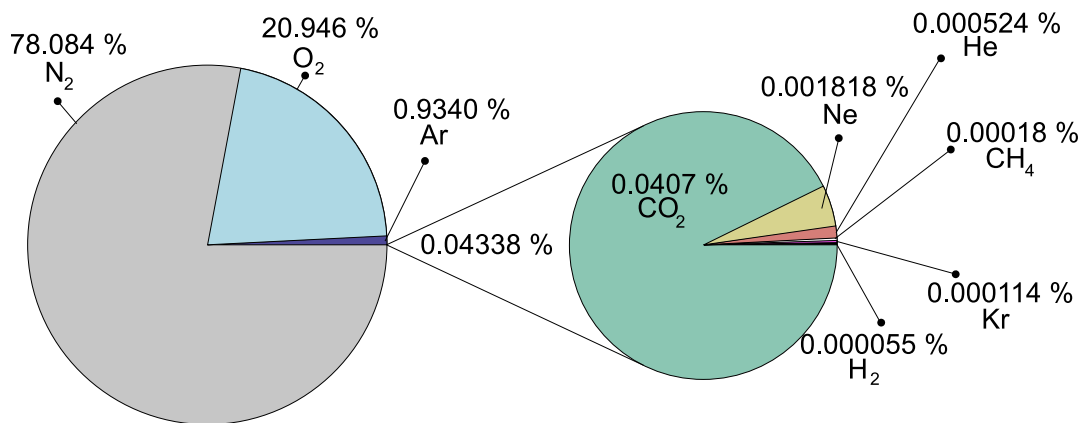


FIGURE 2.1.2: Composition of Earth Atmosphere by volume percentage. (The proportion of water vapour (H_2O) is variable so it is not represented in this chart, however it averages about 1% in the troposphere.)

wave solar radiation received at the Top Of Atmosphere (TOA), and the long wave radiation emitted by the Earth. Interactions between electromagnetic radiation and the target (absorption and scattering inside the target, and reflection by its surface) modulate the characteristics of the emerging radiation. The modulation may result in changes in brightness, polarization and direction of radiation [Asrar *et al.*, 1989].

In the following sections a brief description of the atmospheric radiative transfer formulation is provided to set the physical fundamentals of this Thesis.

2.1.1 Principles of atmospheric radiative transfer

Atmospheric transmittance

To start with, let us consider an infinitesimal thickness ds layer inside the atmosphere composed by separately distributed scatters (Figure 2.1.3).

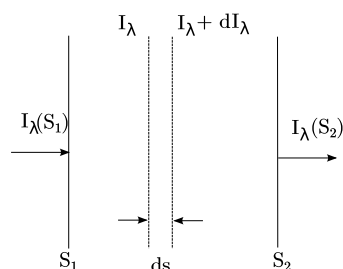


FIGURE 2.1.3: Depletion of a radiant intensity in traversing an absorbing and scattering medium.

If a parallel beam, which intensity is defined as I_λ at the entrance of the layer (let us avoiding

the wavelength dependency for now) incidents perpendicularly to the surface, its intensity at the exit will be $I + dI$, where the term dI is proportional to the product of I and ds .

$$dI = -\sigma_e I ds \quad (2.1.1)$$

where σ_e (m^{-1}) is the local extinction coefficient. In the formulation of Equation 2.1.1, it is assumed that the layer is composed by spherically symmetric randomly orientated scatters. The extinction accounts for the absorption (determined by the absorption coefficient σ_a) and the scattering (determined by the absorption coefficient σ_s) phenomena, and both molecules and aerosols absorb and scatter radiation. Therefore, the extinction coefficient can be described as:

$$\sigma_e = \sigma_a + \sigma_s \quad (2.1.2)$$

For a finite-thickness layer located between S_1 and S_2 , the integration of Equation 2.1.1 yields:

$$I(S_2) = I(S_1)e^{-\tau_e} \quad (2.1.3)$$

where:

$$\tau_e = \int_{S_1}^{S_2} \sigma_e(s) ds \quad (2.1.4)$$

Thus, τ_e is the optical thickness of the layer and, $e^{-\tau_e}$, is its optimal transmissivity. Usually, Equation 2.1.3 is also known as *Bouguer-Beer's* exponential extinction law. This formulation applies only to monochromatic radiation. However, it can also be applied to narrow wavelength intervals over which the intensity and the extinction vary slowly [Lenoble *et al.*, 2011]. For wider spectral ranges, the spectral variation of τ_e can be explained by the exponential Ångström law. See Equation 2.1.5:

$$\frac{\tau_\lambda}{\tau_{\lambda_0}} = \left(\frac{\lambda}{\lambda_0} \right)^\alpha \quad (2.1.5)$$

where τ_λ and τ_{λ_0} are the Aerosol Optical Thickness (AOT) at λ and λ_0 , respectively; and α is the so-called Ångström exponent. Although the α dependency on wavelength is not explicitly mentioned in Equation 2.1.5, α depends on the selected wavelength interval [Ångström, 1929]. Thus, the Ångström exponent is related to the wavelength variation of the AOT, but also it is physically related to the average size of the particles; being the smaller particles, the larger exponent and vice versa.

Atmospheric scattering

Scattering can be explained by the classic electromagnetic theory. Depending on the relation between the incident wavelength and the size of the particle, defined by means of the size parameter¹, $\alpha = \frac{2\pi r}{\lambda}$; two different theories were formulated to describe the scattering processes: The molecular **Rayleigh** scattering and the **Mie** scattering theory.

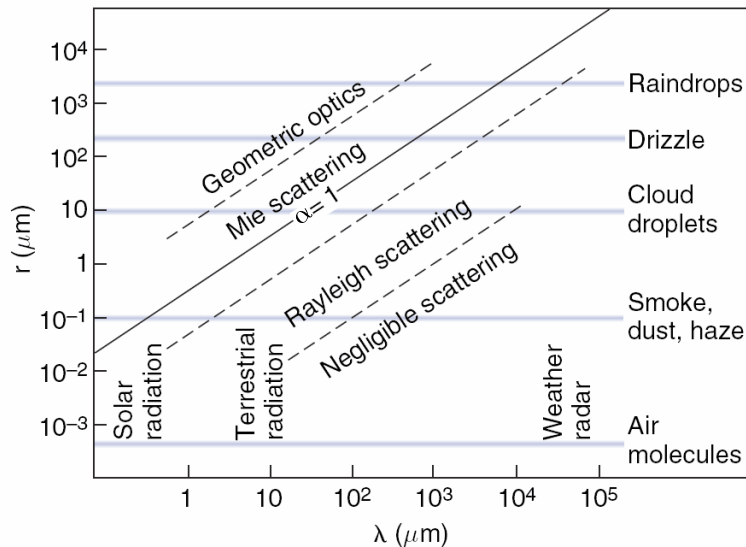


FIGURE 2.1.4: Distribution of Rayleigh and Mie scattering areas according to the wavelength and the particle size (radius).

Figure 2.1.4 shows the size parameter α as function of the incident radiation wavelength and the particle's radius. When solar radiation is scattered by air molecules then scattering falls within the so-called **Rayleigh scattering regime**. For longer wavelengths such as microwave radiation, scattering also falls in the Rayleigh regime. However, for intermediate values of the size parameter between about 0.1 and 50 in the optical spectral domain, the scattering phenomenon must be described in terms of a more general theory developed by Gustav Mie. In the following paragraphs, main aspects of both scattering regimes are outlined:

- The theory of molecular scattering was first developed by John William Strutt, later known as lord Rayleigh [Strutt, 1871] and [Rayleigh, 1871]. Rayleigh theory assumes that an incident electromagnetic wave induces an electric dipole moment of the same frequency in the molecule. This dipole emits, according to the classical electromagnetic theory at the same wavelength. This occurs when scatter particles are smaller than the incident wavelength radiation (as shown in Figure 2.1.4). The molecular Rayleigh scattering coefficient results into a dependency on the wavelength as λ^{-4} . Thus, Rayleigh scattering increases as the wavelength decreases. This is the reason why blue light is scattered in the sky, since blue light is scattered around four times more than red light.

¹Not to be confused with the Ångström exponent although the same term is generally used in the literature

- The complete theory of electromagnetic scattering by an individual spherical particle was first presented by Gustav Mie [Mie, 1908]. Mie scattering occurs in the atmosphere when particles causing the scattering are larger than wavelengths of radiation in contact with them. Scattering produced by cloud particles is described by the Mie scattering regime.

Figure 2.1.5 shows the ideal scattering pattern described by the Rayleigh and Mie scattering regimes due to the light interaction with an spherical particle. It can be noted how Rayleigh regime produces a more isotropic scattering pattern than the Mie scattering regime.

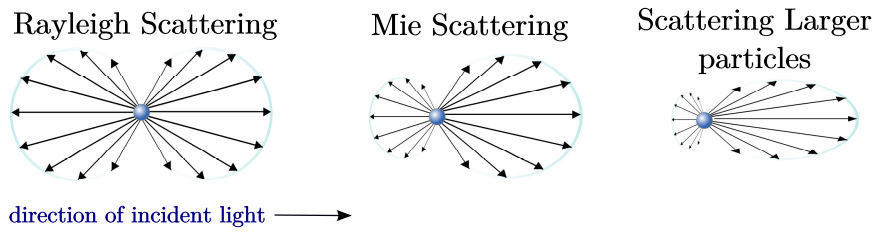


FIGURE 2.1.5: Rayleigh, Mie and large particles scattering patterns produced.

Regardless of the Rayleigh or Mie scattering regime, if we consider an elementary volume dV of the scattering medium, radiance scattered into a solid angle $d\Omega$ around a direction θ is given by :

$$d\bar{I} = \sigma_s p(\theta) I dV d\Omega / (4\pi) \quad (2.1.6)$$

Where $p(\theta)$ is the phase function, which expresses the probability of light to be scattered into a certain direction or scattering angle $\theta \in [0, \pi]$; i.e., the angle between the incident and scattering directions. The conservation of energy implies that $p(\theta)$ is normalized to 4π when this expression is integrated over all possible scattering directions.

In the case of non-spherical particles randomly oriented, it is more convenient to expand Equation 2.1.6 in a series of Legendre's polynomials P_l , becoming the formulation more complex [Lenoble *et al.*, 2011]. To simplify this mathematical formulation, a more convenient analytical approximation formulated in 1941 can be used [Henyey and Greenstein, 1941]. This approximation is known as the Henyey-Greenstein (HG) scattering phase function (see Equation 2.1.7)

$$p(\theta) = \frac{1 - g^2}{(1 + g^2 - 2g\cos(\theta))^{(3/2)}} \quad (2.1.7)$$

The HG expression is basically driven by the asymmetry parameter g . This phase function has been widely used because of its simplicity in many remote sensing applications for years. However, this approximation usually poorly reproduces backscattering. To overcome this shortcoming while keeping a simplistic analytical formulation, a Double Henyey-Greenstein (DHG)

phase function was formulated [Kattawar, 1975]. In this case, two different terms describe the forward and the backward scattering process individually. See Equation 2.1.8.

$$p(\theta) = \gamma \frac{1 - g_1^2}{(1 + g_1^2 - 2g_1 \cos(\theta))^{(3/2)}} + (1 - \gamma) \frac{1 - g_2^2}{(1 + g_2^2 - 2g_2 \cos(\theta))^{(3/2)}} \quad (2.1.8)$$

where γ indicates the proportion of forward and backward scattering.

Finally, to close this topic, it should be mentioned that scattering process can also be classified according to the conservation or non-conservation of the kinetic energy in the centre-of mass frame, therefore distinguishing between an elastic or an inelastic scattering process. In this last case, the outgoing scattered photon's frequency is increased or decreased. For instance, if part of the photon's energy is transferred to the scattered matter, then the shift direction goes to increase the wavelength, i.e., to decrease the frequency and hence, the outgoing energy. This process is also called *Stokes–Raman scattering*. Conversely, if the shifted frequency has increased, it means that part of the internal energy of the matter is transferred to the scattered photon, which is typically known as *anti–Stokes Raman scattering*.

2.2 Atmospheric major constituents and their radiative effects

Earth's atmosphere is mostly composed by diverse molecular gaseous species and a number of suspended particles, e.g., aerosols, raindrops, ice crystal particles, etc. Under the perspective of most atmospheric correction algorithms, and assuming no cloud contamination, the atmosphere can be described by characterizing its two major constituents, i.e., the molecular gaseous species and aerosols.

Atmospheric molecular gases are generally detected and quantified by analysing the absorption bands produced in the sun–surface–sensor path. Conversely, aerosols characterization commonly exploits a wider spectral range and typically requires the use of previously–defined aerosols models, which historically were developed to reproduce the most frequent mixtures of aerosol components. Therefore, in order to better understand the work developed in the framework of this Thesis, the following paragraphs provide the reader a brief description of those two major atmospheric constituents.

2.2.1 Atmospheric molecular absorption

Absorption can be defined as the way in which the energy of a photon is taken up by matter, typically by atoms or molecules. Thus, the electromagnetic energy is transformed into internal energy of the absorber. The energy required to generate a transition from a lower to a higher

state is inversely proportional to the wavelength, i.e., $\Delta E = h \cdot \Delta\nu = h \cdot \frac{c}{\Delta\lambda}$ being h the *Planck* constant and c the speed of the light. Thus, the types of mechanisms that induce absorption also depend on the wavelength of the absorbed photon. Mechanisms responding fastest occur at the shortest wavelengths, which are more energetic; whereas the more sluggish mechanisms produce absorption at longer wavelengths. In the visible and ultraviolet region excitation of valance electrons results in moving electric charges in the molecule. Changes in the electric dipole give rise to a spectrum by its interaction with the incident oscillating electric radiation field. In the mid- and near-infrared region, absorption by molecules occur by vibration or a by a mixture of vibration and rotation. Thus, atmospheric gaseous species present in the atmosphere can be identified and quantified by analysing their absorption spectra. A review of the absorption spectra from the most important gases in the atmosphere is presented below.

Molecular oxygen

Molecular oxygen, O₂, is one of the main constituents of the atmosphere (See Figure 2.1.2). Due to the molecule symmetry, O₂ has no permanent electric dipole but it has a permanent magnetic dipole, which ensures that it is active through magnetic dipole transitions. Although magnetic dipole transitions are less intense than electric dipole transitions, the O₂ abundance in the atmosphere compensates this fact by producing a large atmospheric absorption spectra.

The electronic transition from the ground state to any of the two other excited states of the O₂ molecule, accompanied with vibrational and rotational transitions, produced the so-called O₂-A and O₂-B bands centred at 760 nm and 686 nm respectively (see Figure 2.2.1).

Water vapour

This gas dominates the absorption spectrum from the near infrared beyond the far infrared into the microwave region. Main reasons for that are: (1) the complex vibrational-rotational absorption spectrum of the water vapour, and (2) the abundance of this gas in the lower atmosphere. Water vapour is considered the strongest greenhouse gas, and its concentration is largely dominated by temperature in the atmosphere. Water vapour absorption spectrum can be understood as two contributions: (1) the line absorption, and (2) the continuum absorption (see Figure 2.2.1).

Ozone

Atmospheric ozone, O₃, is a relatively minor greenhouse gas because it is found in relatively low concentrations in the troposphere. O₃ absorption is produced, on the one hand, by electronic bands in the visible and in the ultraviolet spectral regions and, on the other hand, by vibrational-rotational transitions in the infrared regions (see Figure 2.2.1).

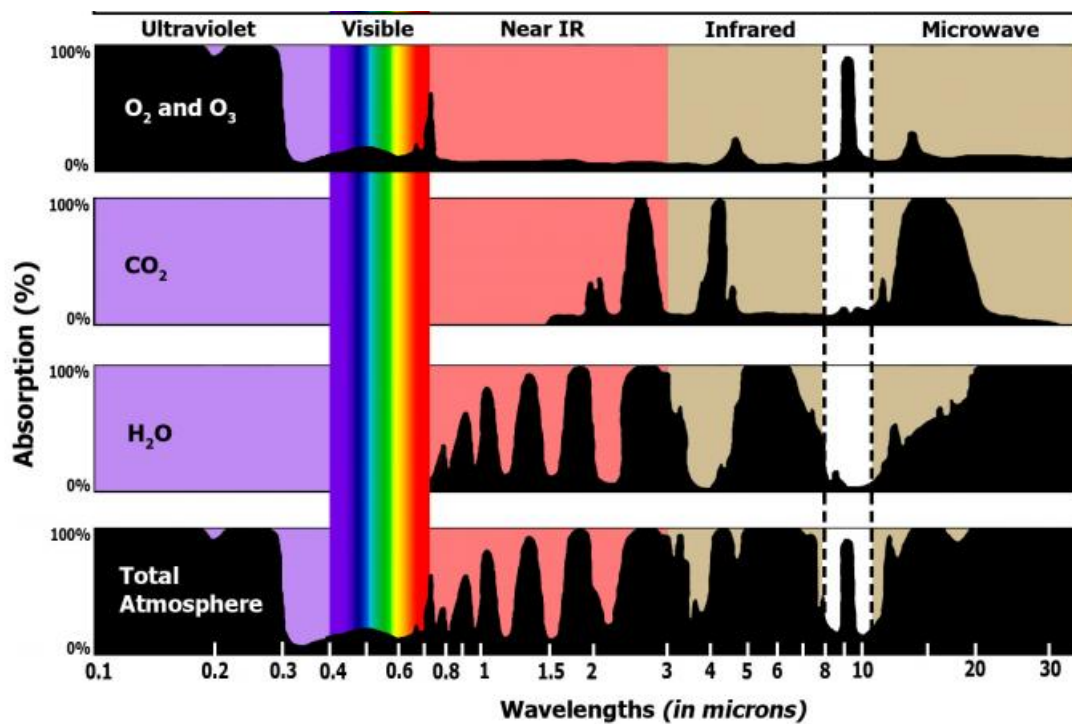


FIGURE 2.2.1: Greenhouse gas absorption spectrum. Source from NASA Science Climate Investigation (SCI) [SCI NASA, 2016]

Carbon dioxide

Carbon dioxide, CO_2 , absorbs in a number of spectral regions (See Figure 2.2.1). This is an important greenhouse gas that has a long time–life in the atmosphere. CO_2 constantly moves into and out of the atmosphere by different mechanisms: photosynthesis, respiration, organic decomposition or decay, combustion, etc. The absorption produced in the near infrared occurs through vibrational–rotational mechanisms. The absorption spectrum of the CO_2 is dominated in the infrared by the very strong absorption bands produced at $4.3 \mu\text{m}$ and $15 \mu\text{m}$. The latter is particularly important in temperature sounding techniques.

2.2.2 Aerosols

Particles suspended in gas are called *Aerosols*. In principle, atmospheric aerosol is a term that properly could describe dust, haze particles, cloud water droplets, and ice crystals [Stephens, 1994]. Aerosols affect the climate in multiple ways. For instance, they directly influence the radiation budget of the atmosphere by scattering and absorbing solar radiation, in both short-wave and longwave regions. In addition, they also act as condensation nuclei that modify the cloudiness of the sky as well as cloud optical properties.

Conversely to molecular gaseous mixtures, aerosols are so variable in concentration and – in the case of haze and dust particles – in chemical composition that it is difficult to generalize their

properties. Their strong temporal and spatial variability makes the correct parametrization of aerosol properties a challenging task in atmospheric modelling, and hence in those atmospheric correction algorithms based on a physical model inversion.

Aerosols are typically concentrated in the inner atmospheric layer surrounding the Earth's surface, known as the boundary layer, which ranges up to 2-2.5 km above the surface. Therefore, the planetary boundary layer, differs from the remainder of the troposphere due to the strong interaction with the underlying surface and the aerosol presence.

Aerosols can be classified according to their origin, size, shape, chemical composition, and some other features. In this section, aerosols will be first classified according to the source of formation. Secondly, the most important aerosol models defined and used in many atmospheric radiative transfer models, and hence in many atmospheric correction algorithms, are also reviewed.

Aerosols production mechanisms, sizes and lifetimes

A basic aerosol classification is defined by distinguishing between *primary* and *secondary* sources, i.e., between primary and secondary production mechanisms.

- *Primary* or direct sources are mostly of natural origin including extraterrestrial dust, sea-salt particles, soil dust, volcanic debris and biological material.
- *Secondary* or indirect sources are found in the atmospheric layers², where chemical reactions take place and convert the available natural and man-made atmospheric trace gases into solid and liquid particles. This process is also known as Gas-to-Particle Conversion (GPC), which produces small particles of radii lower than $0.1\ \mu\text{m}$.

Thus, aerosol size is strongly related with the formation mechanism. In 1955, [Junge, 1955] introduced the following aerosol categories based on the aerosol size:

- *Aitken* particles with dry radii $< 0.1\ \mu\text{m}$
- *Large particles* with dry radii $0.1 \leq r \leq 1.0\ \mu\text{m}$
- *Giant particles* with dry radii in excess of $1.0\ \mu\text{m}$

Aerosol size, production mechanisms, lifetime, and radiative effects are very closely interlinked [Stephens, 1994; Wetterdienst, 2016]. Besides aerosol's distinction into *Primary* or *Secondary* production mechanisms, and besides the classification according to their size; D' Almeida *et al.*, 1991 classified aerosols mainly by their location and sources:

²Here *layers* refers to strata defined in Section 2.1

- **Extraterrestrial sources** or also called interplanetary dust yield solid particles. These particles can range from tenths of a micrometer to some millimetres in diameter. Extraterrestrial particles can reach the troposphere mostly by dry deposition or sedimentation.
- **Sea–salt particles** are generated in maritime environments via bubbles building and subsequent jet drop by bursting bubbles. The following characteristic particles are commonly found in sea–salt particles: $NaCl$, KCl , $CaSO_4$, $(NH_4)_2SO_4$, etc. These particles are formed when sea–spray drops are evaporated and after they are dried and fractioned.
- **Crustal–derived aerosol** includes also mineral aerosol and desert dust. These are originated from wind–blown sand abrasion of bedrock in arid regions. The following elements are characteristic of this kind of particles: Al , Fe , Ti , Si , and Ca .
- **Sulphate particles** are generated both naturally and anthropogenically. On the one hand, the natural production of sulfur–bearing gases occurs within the marine flora, the terrestrial biota, and through volcanic eruptions. On the other hand, counterpart stems mostly from combustion processes such as oil burning, petroleum refinement and traffic.
- **Nitrate particles** are formed both naturally and anthropogenically, being and final product of many reactions in the atmosphere involving trace gases.
- **Organic particles** are originated both naturally and anthropogenically. Among the natural sources of organic particles, forest are maybe the most significant source of volatile organic material called *isoprene* and *terpene*.
- **Carbonaceous substances** are generated either (a) directly through aggregation of a set of molecules formed in combustion processes, or (b) indirectly by condensation from a supersaturated gas from chemical reactions. The direct process generated the so–called primary carbon which consists on two components: (1) the graphitic carbon, highly absorbing, and (2) primary organics, with a weak absorbing property.
- **Volcanic aerosol** are generally confined to the stratosphere. However, this can also be transported to the high tropospheric layers, particularly in the polar region. Since the volcanic aerosol source are volcanic eruptions, its spatial and temporal distribution will highly depend on these events occurrence.

Based on the above classification, different global aerosol models have been defined and updated in the last 40 years, e.g., [Shettle and Fenn, 1979](#), [D' Almeida *et al.*, 1991](#). Assuming the vertical aerosol distribution as known, typically a log–normal or an exponential distribution; each of the defined aerosol models generally consists of a combination of many aerosol components. In this sense, most atmospheric Radiative Transfer Model (RTM) include some aerosol models by default. For instance, the MODerate resolution atmospheric TRANsmission (MODTRAN) [[Berk *et al.*, 2005](#)] has 4 pre–defined aerosol models for the atmospheric boundary layer region based on the [Shettle and Fenn, 1979](#) classification: rural, desert, maritime, and urban.

Aerosol Model	Fenn & Shettle	[Shettle and Fenn, 1979; Shettle, 1990]	Rural, Urban, Maritime, Tropospheric, Fog
	d'Almeida	[D'Almeida <i>et al.</i> , 1991]	Continental (clean and average), Forest, Desert (background and dust), Urban, Maritime (clean, mineral and polluted), Polar (clean and polluted), Antarctic
SW	OPAC	[Hess <i>et al.</i> , 1998]	Continental (clean, average and polluted), Urban, Desert, Maritime (clean, polluted and tropical), Artic, Antarctic
RTM	MODTRAN	[Berk <i>et al.</i> , 2005]	Rural, Urban, Maritime, Desert
	6S	[Vermote <i>et al.</i> , 2006]	Continental, Maritime, Urban, Biomass burning smoke, background desert stratospheric
	LibRadtran	[Mayer and Kylling, 2005; Emde <i>et al.</i> , 2016]	Rural, Urban, Maritime, Tropospheric, Fog

TABLE 2.2.1: Aerosol models defined in D'Almeida *et al.*, 1991 and Shettle and Fenn, 1979; and included in OPAC, and MODTRAN, 6S RTM, and LibRadtran.

A summary of the aerosol models names available in three popular atmospheric RTMs: MODTRAN³, 6S⁴, and LibRadtran are detailed in Table 2.2.1. Notice that, these mentioned aerosol mixtures names not necessarily indicate the same proportion of components; however, it gives a general idea about the most common aerosol models used. In addition, default aerosol models defined in the OPAC software [Hess *et al.*, 1998], which is dedicated to the aerosol optical properties generation based on mixing different aerosol components, is also included for completion.

2.3 Atmospheric correction: an ill-posed problem

In optical remote sensing, information about biophysical processes and properties is extracted by the analysis of the reflected and(or) emitted light over(from) the natural surfaces. This reflected and emitted light generally acquired by airborne and space-borne instruments is strongly affected by the scattering and absorption induced by the atmospheric components in the sun-target-sensor optical path. For satellite remote sensing applications, atmospheric correction can be understood as the process by which surface reflectance is obtained from TOA radiance or TOA reflectance. Basically, atmospheric correction algorithms, mostly used by land and ocean-color remote sensing community, tries to *remove* or *disentangle* that fraction of the signal that comes from the atmosphere to isolate the information related to the surface. However, since part of the atmospheric correction process is dedicated to the atmospheric state characterization, atmospheric correction algorithms are also of interest for the atmospheric community, which aims to isolate the fraction of the signal that merely comes from the atmosphere.

Thus, whatever the scope of study, the atmospheric correction problem is, per se, an ill-posed problem since light interaction with the Earth's atmosphere and surface is completely

³MODTRAN also allows the user to introduce the optical aerosol properties instead of using the default aerosol models stored.

⁴6S code allows the user to create its own aerosol mixture combining dust-like, oceanic, water-soluble and soot components in different proportions

coupled. In this section, a review of the most basic formulation needed to understand and follow the atmospheric correction algorithms developed in this Thesis is detailed. Additionally, and overview of the most used atmospheric correction strategies is presented.

2.3.1 TOA radiance modelling

Neglecting the thermal fluxes, TOA radiance can be described as the sum of three terms (see Equation 2.3.1):

$$L_{TOA} = L_0 + L_{TOC}T_{dir}^{\uparrow} + L_{adj}T_{dif}^{\uparrow} \quad (2.3.1)$$

where L_0 is the atmospheric scattered radiance, $L_{TOC}T_{dir}^{\uparrow}$ is the radiance at Top of Canopy (TOC) level (L_{TOC}) directly transmitted to the observer (T_{dir}^{\uparrow}), and finally $L_{adj}T_{dif}^{\uparrow}$, is the radiance from surroundings (L_{adj}), which is diffusely transmitted to the observer (T_{dif}^{\uparrow}).

On the one hand, radiance at TOC level can be expressed as equation 2.3.2:

$$L_{TOC} = \frac{\rho_{so}E_{sun} + \rho_{do}E_{sky}}{\pi} \quad (2.3.2)$$

being the E_{sun} and E_{sky} the solar irradiance directly and diffusely transmitted to the surface level (see Equations 2.3.3 and 2.3.4):

$$E_{sun} = E_s^0 \cos \theta T_{dir}^{\downarrow} \quad (2.3.3)$$

and,

$$\begin{aligned} E_{sky} &= (T_{dif}^{\downarrow} + T_{dir}^{\downarrow}\bar{\rho}_{sd}S)I_o[1 + S\bar{\rho}_{dd} + S^2\bar{\rho}_{dd}^2 + \dots] = \\ &= (T_{dif}^{\downarrow} + T_{dir}^{\downarrow}\bar{\rho}_{dif}S)I_o \left[\sum_{n=0}^{\infty} (\bar{\rho}_{dd}S)^n \right] \end{aligned} \quad (2.3.4)$$

where:

$$I_o = \frac{E_s^0 \cos \theta}{\pi} \quad (2.3.5)$$

and:

- E_s^0 : solar irradiance arriving at TOA
- θ : solar zenith angle
- $T_{dir}^{\downarrow}, T_{dif}^{\downarrow}$: direct and diffuse atmospheric downward transmittance from sun to target

- $T_{dir}^\uparrow, T_{dif}^\uparrow$: direct and diffuse atmospheric upward transmittance from target to sensor
- S : atmospheric spherical albedo
- $\rho_{so}, \rho_{do}, \bar{\rho}_{sd}, \bar{\rho}_{dd}$: are the four reflectance components that reproduce the non-Lambertian surface behaviour as function of down/upward direct and diffuse atmospheric transmittance (see Figure 2.3.1).

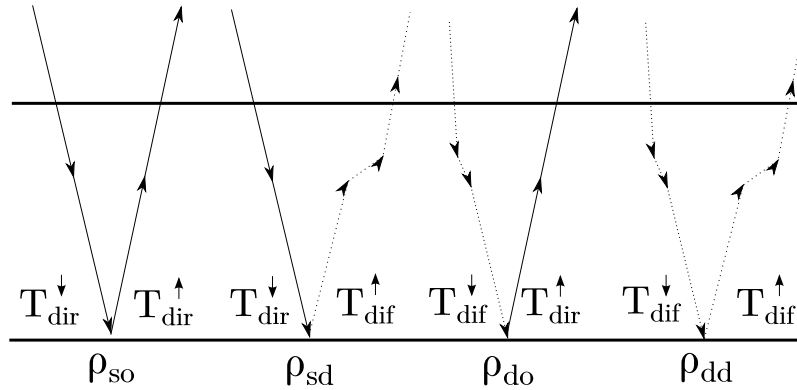


FIGURE 2.3.1: Surface reflectance non-lambertian behaviour represented by 4-components: (a) ρ_{so} , (b) $\bar{\rho}_{sd}$, (c) ρ_{do} and (d) $\bar{\rho}_{dd}$ description.

Therefore, summation from Equation 2.3.4 corresponds to the geometric series case which converges to Equation 2.3.6 when $|\bar{\rho}_{dd}S| < 1$. Thus:

$$E_{sky} = \left[\frac{(T_{dif}^\downarrow + T_{dir}^\downarrow \bar{\rho}_{sd} S) I_o}{(1 - \bar{\rho}_{dd} S)} \right] \quad (2.3.6)$$

On the other hand, adjacency effects are included by means of the term L_{adj} described as Equation 2.3.7:

$$\begin{aligned} L_{adj} &= I_o (T_{dif}^\downarrow \bar{\rho}_{dd} + T_{dir}^\downarrow \bar{\rho}_{sd}) [1 + S \bar{\rho}_{dd} + S^2 \bar{\rho}_{dd}^2 + \dots] = \\ &= I_o (T_{dif}^\downarrow \bar{\rho}_{dd} + T_{dir}^\downarrow \bar{\rho}_{sd}) \left[\sum_{n=0}^{\infty} (\bar{\rho}_{dd} S)^n \right] \end{aligned} \quad (2.3.7)$$

which can also be expressed, considering the geometric series convergence, as Equation 2.3.8:

$$L_{adj} = I_o \frac{(T_{dif}^\downarrow \bar{\rho}_{dd} + T_{dir}^\downarrow \bar{\rho}_{sd})}{(1 - S \bar{\rho}_{dd})} \quad (2.3.8)$$

This formulation here briefly described is presented with more detail in [Verhoef and Bach, 2012](#).

Assuming a Lambertian surface reflectance

Characterizing the actual Bidirectional Reflectance Distribution Function (BRDF) of the surface is only possible when radiance is acquired by multiple viewing angles. Although there are satellite missions dedicated to acquire images with multiple viewing geometry, such as the Multi-angle Imaging SpectroRadiometer (MISR) instrument (5 viewing angles) [Diner *et al.*, 1998] or the PROBA-CHRIS mission (5 viewing angles) [Barnsley *et al.*, 2004]; in most satellite missions each pixel is only acquired with a particular geometry, e.g., MEDIUM Resolution Imaging Spectrometer (MERIS) [Rast *et al.*, 1999], Landsat-8 [Roy *et al.*, 2014], etc. Thus, in this last case, it is not possible to infer the surface reflectance BRDF due to the lack of geometrical information. Therefore, when applying the atmospheric correction process to a single viewing instrument, surface reflectance is typically assumed as Lambertian. Consequently, the above formulation is simplified under the Lambertian assumption $\bar{\rho}_{dd} = \bar{\rho}_{sd} = \rho_{do} = \rho_{so}$, resulting the TOA radiance expression as Equation 2.3.9:

$$L_{TOA} = L_0 + \frac{E_{TOC}\rho(T_{oo}^\uparrow + T_{do}^\uparrow)}{\pi(1 - S\rho)} \quad (2.3.9)$$

where E_{TOC} is defined as:

$$E_{TOC} = E_s^0 \cos(\theta) T_{dir}^\downarrow + E_s^0 T_{dif}^\downarrow \quad (2.3.10)$$

Including fluorescence emission

Since part of this Thesis is focused on the definition of an atmospheric correction algorithm for the FLEX mission, it is also essential to describe how the TOA radiance formulation is modified when SIF emission is included. Given that SIF is at least two-orders of magnitude lower than the radiance reaching the sensor, it can be included in the TOA radiance formulation as an extra contribution composed by two different sources: one totally directional F_d and the other hemispherical \bar{F}_d [Verhoef *et al.*, 2014].

Furthermore, just as ground solar reflected radiance, SIF emission is also scattered by aerosols and molecules as it passes through the atmosphere, resulting a small fraction of it re-absorbed and re-emitted by surface. Thus, taking into account the expressions detailed before (Equations 2.3.1- 2.3.8) and the SIF emission terms, F_d and \bar{F}_d , the final TOA radiance expression used in this work becomes Equation 2.3.11:

$$\begin{aligned}
L_{TOA} = L_0 + & \left[\rho_{so} T_{dir}^{\downarrow} \left(\frac{E_s^0 \cos\theta}{\pi} \right) + F_d + \rho_{do} \frac{(T_{dif}^{\downarrow} + T_{dir}^{\downarrow} \bar{\rho}_{sd} S) E_s^0 \cos\theta + \pi \bar{F}_d S}{\pi(1 - \bar{\rho}_{dd} S)} \right] T_{dir}^{\uparrow} \\
& + \left[\frac{(T_{dif}^{\downarrow} \rho_{dd} + T_{dir}^{\downarrow} \bar{\rho}_{sd}) E_s^0 \cos\theta + \pi \bar{F}_d}{\pi(1 - \bar{\rho}_{dd} S)} \right] T_{dif}^{\uparrow}
\end{aligned} \tag{2.3.11}$$

2.3.2 Overview of state-of-the-art atmospheric correction algorithms

A variety of atmospheric correction schemes have been developed during the last 30 years, ranging from simple empirical and approximated corrections like the classic Dark Object Subtraction (DOS) approach [Chavez, 1988] or the statistical QUick Atmospheric Correction (QUAC) method [Bernstein *et al.*, 2005], to more developed model-inversion strategies using information that exploit the instrument design like the spectral range, multi-angularity of polarimetry. While empirical methods are generally fast but less reliable, model-inversion techniques are generally time consuming but offer more reliable solutions based on a physical approach to the problem of scattering and absorption. In general, atmospheric correction algorithms can be classified into three main categories [Gao *et al.*, 2009]:

- **Empirical atmospheric correction approaches.** Historically they represent the initial steps of atmospheric correction algorithms, e.g., DOS. Under this class, some **statistical approaches** such as the QUAC algorithm can also be included.
- **Physical RTM inversion approaches.** This family of algorithms can be considered as the most complex, time-consuming but also the most accurate group. This technique corrects the signal from atmospheric scattering and absorption by inverting the radiative transfer equation by using an atmospheric radiative transfer model, e.g., Gao *et al.*, 1993; Adler-Golden *et al.*, 1999.
- **Hybrid approaches.** As its name indicates, these strategies combine some of the assumptions from the empirical strategies and some RTM inversion techniques. Some examples can be found in Boardman, 1998 and Goetz *et al.*, 1997.

Given this classification, worth mentioning is another small group of atmospheric correction algorithms that are completely separated from the strategies mentioned above. These refer to strategies based on exploiting the spatial information. Only a few atmospheric correction algorithms based on contrast maximization are found in the literature, e.g., Hadjimitsis, 2009; Thomas *et al.*, 2011. The main reason why only few of these type of algorithms were developed is because while the other strategies exploit somehow the spectral information, this family of algorithms require high spatial resolution images. In this respect, the here called contrast-methods, are addressed to satellite or air-borne images with few meters of spatial resolution, and hence, few spectral bands too.

Among the four groups presented above (3 items plus the contrast–method), this section will only focus on reviewing the physical RTM inversion approaches, since it lays the foundation to understand most of the approaches developed under this Thesis. Atmospheric correction algorithms based on physical RTM inversion approaches involve characterizing atmospheric scattering and absorption processes by quantifying aerosols and molecular gaseous mixing ratios. To do so, this family of algorithms performs the inversion of the radiative transfer equation that, on the approximation of Lambertian surfaces, takes the form given in Equation 2.3.9.

In general, physical RTM inversion strategies follow a common processing chain varying only certain particularities regarding the RTM used, the aerosol models inverted, the assumptions considered to model surface reflectance as part of the inversion process, or certain mathematical details such as the weighting in the minimization cost function, etc. However, the common structure of the processing chain always involves a minimum number of steps dedicated to: (1) cloud screening, (2) aerosol retrieval, (3) water vapour retrieval and (4) surface reflectance inversion (see Figure 2.3.2). More advanced algorithms also include adjacency effects correction, or even retrieve the light polarization state or the surface BRDF. However, these retrievals depend always on the sensors characteristics.

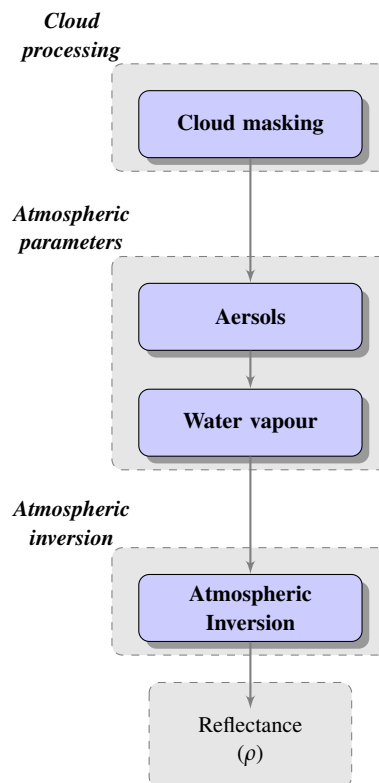


FIGURE 2.3.2: Processing chain commonly followed by physical inversion RTM atmospheric correction algorithms composed by: (1) cloud screening, (2) atmospheric parameters characterization, and (3) atmospheric inversion.

Thus, an essential step prior to the application of any atmospheric correction algorithm is the

cloud screening or cloud masking process. Cloud screening algorithms can range from approximations mainly based on a threshold classification [Ackerman *et al.*, 1998; Frey *et al.*, 2008] to complex statistical methods that are not only dedicated to detect clouds but also to characterise cloud properties such as cloud height, thickness, brightness, etc., such as Gómez-Chova *et al.*, 2009. Essentially, the choice of the most suitable cloud screening algorithm depends on the available spectral, spatial and geometrical information, as well as the posterior remote sensing application. In general terms, cloud screening algorithms can be separated into two main groups as clear sky conservative and cloud conservative algorithms, respectively depending on if they minimize the clear sky detection error or try to minimize the cloud detection error. In this respect, when applying an atmospheric correction algorithm, depending on the step performed, a more or less restrictive cloud mask will be needed. For instance, a very conservative cloud mask is needed in the aerosol characterization step. The main reason to do so is because clouds (especially thin cirrus clouds) can be assimilated by the aerosol retrieval algorithms as aerosols, leading to errors in the aerosol quantification. However, for water vapour retrieval a less restrictive cloud mask is required since this kind of algorithms are limited to the spectral region where water vapour absorption plays a role [Guanter, 2006].

In general, cloud detection methods are based on the assumption that clouds always present several common features such as the fact that they are brighter and colder than the underlying surface. The simplest approach to mask clouds is based on statistical thresholds (e.g., over features such as albedo or temperature), and is applied to every pixel of the scene. As a result, a binary matrix is provided indicating if a pixel is cloud-free or not. However, depending on the posterior application, it can be considered that these methods can fail for several reasons, such as sub-pixel clouds, high reflectance surfaces, illumination and observation geometry, sensor calibration, variation of the spectral response of clouds, transparency of clouds, etc. Other more sophisticated methods are based on the previous feature extraction of the image using meaningful physical facts and a posterior unsupervised classification or a neuronal network training to label if pixels are cloud-free or not [Gómez-Chova *et al.*, 2007].

Although cloud screening is considered as an essential step of any atmospheric correction algorithm, this Thesis is not explicitly dedicated to this topic. Conversely, atmospheric parameters retrieval, i.e., aerosols and water vapour retrieval are more extensively reviewed in Section 2.4. Since the spectral behaviour of light scattered/absorbed by aerosols and water vapour is completely different, it was chosen to distinguish between techniques to derive or characterize, on the one hand, aerosol optical properties, and; on the other hand, columnar water vapour content.

2.4 Aerosol and water vapour retrieval strategies

2.4.1 Aerosols retrieval algorithms

As it was earlier mentioned, aerosol retrieval strategies can be distinguished according to: (1) the aerosol models assumed in the inversion, i.e., the number of aerosol models considered and

the different aerosol mixtures generated, (2) the mathematical expression to perform the TOA radiance inversion, (3) the strategy to model surface reflectance, etc. However, sensor specifications play an essential role in determining the available information; and hence, the kind of aerosol retrieval algorithm to be applied. Because of that, in this section aerosol retrieval algorithms have been divided into three distinct groups according the sensor geometry acquisition mode: (1) single viewing, (2) double or dual viewing, and (3) synergy viewing.

Single view

Single view instruments are commonly used in Earth Observation and the strategy for the retrieval of aerosol properties can only depend on the spectral range covered by the instrument. Due to the coupling between surface reflected light and aerosol scattering, a priori knowledge or assumptions about the surface reflectance is needed in order to disentangle these two effects. Several methods are found in the literature and can be classified into two families:

- **(Semi) Empirical methods** are based on very rough assumptions on the radiative transfer and the inversion of surface reflectance like the classical Dark Object Subtraction (DOS), [Chavez, 1988], or Empirical Line Method (EML) [Smith and Milton, 1999]. These atmospheric correction methods are easily implemented and fast to execute but provide poor results in terms of retrieved surface reflectance and aerosol properties.

More developed methods based on image statistics are also included in these semiempirical methods. These statistical methods are based on the assumption that the atmospheric state is invariant over a limited area of around 30x30 km [Guanter *et al.*, 2007b], and that the image statistics is only due to the variability of surface reflectance. In particular the statistical QUAC method is based on the following assumptions:

1. The term $(1 - S\rho) \approx 1$, which is reasonable for low reflectance values and with atmospheres with low aerosol loads.
2. For each cell of invariant atmosphere there are a large number of diverse pixel spectra (≥ 10) in a scene. This premise is reasonable for most of the remote sensing scenes except for those scenes acquired over large and homogeneous areas.
3. The standard deviation of the reflectance spectra for a collection of diverse materials is nearly wavelength independent. This assumption tends to fail for large spectral range covered, e.g., from the visible to the SWIR, in the majority of scenes.

When these assumptions are met, Equation 2.3.9 can be linearised becoming the TOA reflectance proportional to the surface reflectance, $\rho_{TOA} = \rho_0 + T^\uparrow \rho T^\downarrow$. Note that ρ_{TOA} and ρ_0 are respectively L_{TOA} and L_0 normalized by solar irradiance. First, the contribution of the ρ_0 is computed by determining a dark pixel as a baseline. Second, spectral end-members are selected from the image and used to compute $\sigma(\rho_{TOA})$. Therefore, by using a precomputed reference value of $\sigma(\rho)$ from an external database and taking assumption (3) into account, atmospheric transmittance can be estimated by: $\sigma(\rho_{TOA}) = T(\lambda)\sigma(\rho)$.

- **Physical-based approaches** require the use of an atmospheric radiative transfer code for the simulation of the acquired at-sensor radiance. To model the at-sensor TOA radiance (see Equation 2.3.9), these methods need to consider certain assumptions about the ground reflectance and the aerosol properties. Typically, to characterize the atmosphere these methods minimize a cost-function that computes the difference between real and simulated at-sensor TOA radiance.

The most successfully applied algorithms are:

- Algorithms based on the retrieval of aerosols over dark targets where the spectral reflectance is assumed to be known. Among these algorithms, we can find those based on Dark Dense Vegetation (DDV) surfaces as those applied for MODIS [Kaufman and Gao, 1992] and MERIS [Santer *et al.*, 1999], or deep water bodies such as the Tafkaa [Bruegge *et al.*, 1990] and ATREM [Gao and Davis, 1997] family algorithms.
- In order to overcome the limitations and constraints imposed on the aerosol retrieval methods based on dark targets, the **Spectral unmixing methods** offer the flexibility to model the unknown surface reflectance as a linear combination of two spectra selected as end-members. Spectral unmixing methods to model surface reflectance spectra such as Von Hoyningen-Huene *et al.*, 2003; Van der Meer and De Jong, 2000; North *et al.*, 2009a; typically assume that the atmosphere is invariant for a set of pixels (close to each other) and that the surface reflectance is a linear combination of two predefined vegetation and soil spectra like in Equation 2.4.1.

$$\rho_i = C_{v,i}\rho_v + C_{s,i}\rho_s \quad (2.4.1)$$

where ρ_i is the surface reflectance modelled at each pixel i , ρ_v and ρ_s are the surface vegetation and soil spectra end-members; and $C_{v,i}$ and $C_{s,i}$ the vegetation and soil contribution, respectively.

- Another alternative to retrieve aerosol optical properties would be based on the prior knowledge of the surface reflectance obtained after the atmospheric correction of another sensor. These approaches are limited by the error propagation of data quality prior to the atmospheric correction, as well as errors associated with different observation angles, time of acquisition or spectral sampling. Nevertheless these methods allow constraining reflectance values and can be used in combination with dark target or spectral mixing methods.

Dual view

The use of dual-viewing imager for the retrieval of aerosol optical properties takes advantage of observing the scene under two (or more) different angles, which implies observing the surface under different optical paths. The following paragraphs summarize some of the most popular algorithms for the retrieval of aerosol optical properties making use of multi-angular

observations from space-borne instruments.

The AATSR dual-view algorithm (ATSR-DV)

The ATSR-DV algorithm, described in [Veefkind and de Leeuw, 1998](#); [Sogacheva et al., 2015](#); [Kolmonen et al., 2016](#), estimates AOT from TOA radiance measurements by inverting an atmospheric RTM and exploiting the dual viewing geometry. It was first applied to the ATSR-2 on board the European Remote Sensing (ERS) satellite, and following to the AATSR instrument on board ENVISAT. The ATSR-DV algorithm assumes a Lambertian surface reflectance behaviour. Thus, it makes use of the well-known TOA radiance expression shown in Equation 2.3.9, but normalized by the solar irradiance at TOA:

$$\rho_{atm} = \rho_0 + \frac{T^\downarrow \rho T^\uparrow}{1 - S\rho} \quad (2.4.2)$$

where ρ_{atm} and ρ_0 are respectively the TOA radiance (L_{TOA}) and path radiance (L_0) normalized by the solar irradiance, ρ is the surface reflectance, S is the spherical albedo, and $T^\downarrow T^\uparrow$ are the downward and upward total atmospheric transmittance.

Then, by assuming two approximations regarding the surface reflectance behaviour, the ATSR-DV algorithm estimates aerosol AOT without using any prior knowledge of surface reflectance:

- The relationship between surface reflectance observed at nadir and forward geometry, ($f = forward, n = nadir$), is spectrally independent:

$$k = \frac{\rho_f(\lambda)}{\rho_n(\lambda)} \approx cte \quad (2.4.3)$$

- The surface reflectance term (ρ) coupled with the spherical albedo (S) in Equation 2.4.2 is assumed as surface albedo for both nadir and forward viewing observations.

The k ratio is estimated at $1.6 \mu m$ where aerosol and gases effects can be neglected. For non-large particles where this assumption is valid [[Sogacheva et al., 2015](#)], the k value is used to obtain information about the atmospheric aerosol and gases by eliminating the surface reflectance contribution of Equation 2.4.2 when applying for the nadir and forward viewing. To disentangle aerosol and gaseous contributions, gaseous effects are estimated by using the atmospheric pressure and temperature as input in the RTM. Then, AOT is estimated by comparing measured aerosol reflectance and modelled reflectance. Modelled aerosol reflectance is determined for a number of aerosol models, each consisting of a mixture of aerosol components [[de Leeuw et al., 2015](#)]. Finally, by means of a least-square fitting process the AOT and the optimal aerosol mixture (proportion of different components) is determined.

Several validation processes show that the ATSR-DV algorithm obtains good results when compared to AEROSOL ROBOTIC NETWORK (AERONET) [Holben *et al.*, 1998]. Comparison between results derived by applying the ATSR–DV algorithm with respect of other single– and dual view algorithms [Kokhanovsky *et al.*, 2009], shows also good agreement.

The AARDVARC algorithm

The Atmospheric Aerosol Retrieval Dual View Angle Reflectance Channels (AARDVARC) algorithm [Grey *et al.*, 2006], likewise proposes a method for retrieving aerosol optical properties using multi–angular observations. The main difference with the previous method is that, instead of considering a Lambertian surface, the AARDVARC method models the BRDF surface scattering and includes it in the inversion through an optimized atmospheric Look Up Table (LUT). The AARDVARC algorithm is able to obtain the AOT and aerosol type from at–sensor measured radiances without prior knowledge of surface reflectance.

Surface reflectance BRDF effects are dominated by the 3–D structure of the surface. In turn, surface scattering is dominated by these geometric effects becoming more wavelength independent as the scattering elements are much larger than the optical wavelengths. The scattering due to aerosols and molecules increases the fraction of diffuse irradiance, and as the **Rayleigh** and **Mie** scattering theory points out, scattering dependency on the wavelength is associated to the relationship between the scatter size and the incident wavelength. Therefore, the model for the surface BRDF, R_{mod} , can be decomposed into two components: one wavelength independent, $P(\Omega)$, and another independent from the viewing direction, $\omega(\lambda)$. Then, ρ_{mod} can be modelled as:

$$\rho_{mod} = [1 - D(\lambda)]P(\Omega)\omega(\lambda) + \frac{\gamma\omega(\lambda)}{1 - g} \{D(\lambda) + g[1 - D(\lambda)]\} \quad (2.4.4)$$

where Ω is the viewing direction, γ is the fraction of the multiple scattering, $D(\lambda)$ is the fraction of diffuse irradiance, and g is defined as $g = (1 - \gamma)\omega(\lambda)$. The objective of the AARDVARC algorithm is to estimate the AOT value, the aerosol type, and the ground surface reflectance spectrum by means of a RTM inversion approach. To do so, the inversion is achieved by two iterations. The first iteration retrieves the ground reflectance and the diffuse irradiance by making a first estimation of the aerosols model and AOT. Then, optimal values of $P(\Omega)$ and $\omega(\lambda)$ are derived by minimizing the difference between the inverted and the modelled surface reflectance. Finally, a second iteration determines the AOT, the aerosol type and the atmospheric profile (temperature) that retrieves the best surface reflectance, obtained by minimizing the following error function 2.4.5:

$$E_{mod} = \sum_{\omega} \sum_{\lambda} \left[\rho_{surf}(\lambda, \Omega) - \rho_{mod}(\lambda, \Omega) \right]^2 \quad (2.4.5)$$

where ρ_{surf} is the inverted surface reflectance, and ρ_{mod} is obtained from the model in Equation 2.4.4 based on estimates of $P(\Omega)$ and $\omega(\lambda)$.

The AARDVARC algorithm includes a preprocessing step that averages Advanced Along-Track Scanning Radiometer (AATSR) pixels to an area of 15 km x 15 km in order to minimize the effects of coregistration between the images acquired at two different observation angles. In addition, a cloud screening algorithm based on Near-Infrared (NIR) and thermal channels is applied to perform the retrieval over cloud-free pixels.

Synergy algorithms

The MERIS/AATSR Synergy Algorithm for Aerosol Retrieval

In the two previous sections an overview of strategies for aerosol retrieval from single and dual-viewing instruments has been described. In this section, a description of synergy algorithms for aerosol retrieval using several instruments is given. In particular, the MERIS/AATSR synergy algorithm for land aerosol and reflectance retrieval [North *et al.*, 2009a] is introduced since it is the technique used as a baseline in the proposed atmospheric correction algorithm developed in this Thesis for the FLEX/Sentinel-3 tandem space mission (See Chapter 4).

The algorithm exploits the synergy between the multi-angular measurements provided by AATSR and the multispectral information acquired by the nadir pointing push-broom sensor MERIS. This algorithm is based on the jointly implementation of the AARDVARC and spectral mixing algorithms described in the sections above. In particular, the algorithm provides with an estimate of the AOT at a reference wavelength, the Ångström coefficient and atmospherically corrected surface reflectance. A two-stage optimization process is used in an iterative procedure: (1) to retrieve surface reflectance based on an initial estimate of the atmospheric state (i.e., atmosphere type, aerosol optical properties, water vapour content, etc.); and (2) to evaluate the goodness of the retrieved surface reflectance based on a comparison with certain constraints imposed by a predefined error metric. The process is summarized in Figure 2.4.1.

The inversion procedure makes use of a precomputed LUT that stores atmospheric TOA reflectance spectra depending on 6 dimensions covering illumination/observation geometry (visual/solar zenith angle and relative azimuth angle), atmospheric parameters (aerosol type and AOT), Lambertian surface albedo, and surface pressure. The TOA radiance is computed using the Matrix Operator Model (MOMO) radiative transfer code with a set of pre-defined aerosol optical properties derived from 40 aerosol types given by the Optical Properties of Aerosols and Clouds (OPAC). The constraints on the retrieved reflectance for a given aerosol type and AOT are based on the mixing spectra for the single view instrument (Equation 2.4.6) and the AARDVARC algorithm for the dual view instrument (Equation 2.4.7)⁵:

$$\rho_{spec-mod}(\lambda) = C_{veg}\rho_{veg}(\lambda) + C_{soil}\rho_{soil}(\lambda) \quad (2.4.6)$$

⁵Terms appearing on Equations 2.4.6 and 2.4.7 are not described since they were already introduced in Equations 2.4.1 and 2.4.4

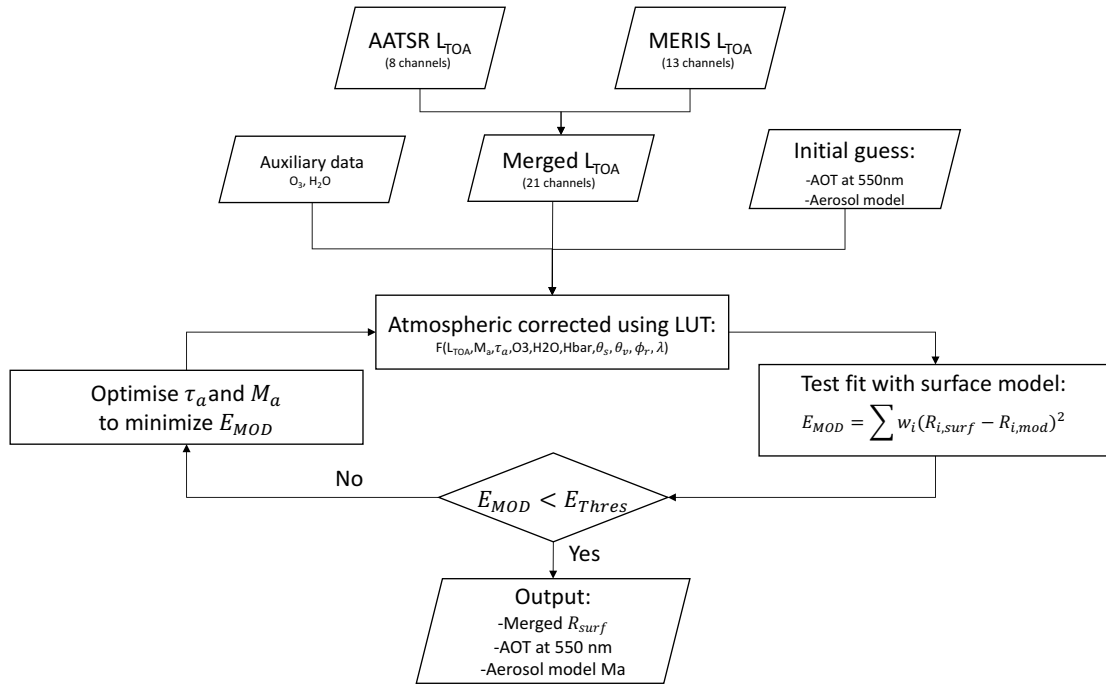


FIGURE 2.4.1: Outline of processing algorithm for synergistic retrieval of surface reflectance and aerosol properties from merged AATSR and MERIS data. Figure originally from [North et al., 2009b](#).

$$\rho_{ang-md}(\lambda, \Omega) = [1 - D(\lambda)]P(\Omega)\omega(\lambda) + \frac{\gamma\omega(\lambda)}{1 - g} \{D(\lambda) + g[1 - D(\lambda)]\} \quad (2.4.7)$$

These constraints allow proposing an error metric, E_{mod} , on the retrieved surface reflectance that it is obtained after inversion of the LUT by given atmospheric properties:

$$E_{mod} = \frac{1}{(M+2)} \sum_{\Omega=1}^2 \sum_{\lambda=1}^M \omega_{\lambda,\omega} [\rho_{surf}(\lambda, \Omega) - \rho_{ang-md}(\lambda, \omega)]^2 + \frac{1}{N} \sum_{\lambda=1}^N \omega_{\lambda} [\rho_{surf}(\lambda) - \rho_{spe-mod}(\lambda)]^2 \quad (2.4.8)$$

where M and N are the number of channels or bands in the dual-viewing and single viewing respectively, and ω_{λ} is a wavelength dependent weighting function used in the minimization process.

2.4.2 Columnar water vapour algorithms

Columnar water vapour (CWV) algorithms can be classified into three big families according to their strategy: (1) curve fitting algorithms; (2) differential absorption techniques; and (3) model inversion techniques.

On the one hand, the curve fitting algorithms offer a detailed parametrization of the problem based on the surface reflectance and atmospheric transfer functions to simulate the at-sensor TOA radiance within the absorption band. These algorithms are computationally expensive but typically provide better results for hyperspectral instruments with several channels inside of the absorption bands. On the other hand, differential absorption techniques are commonly used for the retrieval of gases concentration and are mainly used for multispectral instruments with few channels within the absorption bands. Differential absorption techniques perform the ratio between a channel within an absorption band (measurement channel) with respect to a nearby reference channel not influenced by the gas absorption. This ratio is assumed to be directly related with the depth of the transmittance within the absorption band and so, providing information about the gas concentration. Finally, model inversion techniques make use of atmospheric radiative transfer codes to invert the columnar water vapour by simulation of the at-sensor TOA radiance. These methods are computational intensive but rigorously describe the physics behind the atmospheric absorption and radiative transfer.

Due to their simplicity, fast computation and relatively good results, differential absorption techniques are taken as baseline for most of water vapour retrieval of multispectral instruments (and also in the context of this Thesis, see Chapter 4). Most important differential absorption techniques are summarized in the following paragraphs (see more details in [Schläpfer, 1998](#)).

Band Quotient (BQ)

This is a classic differential absorption method described in [Kaufman and Gao, 1992](#), where the ratio, $R_{BQ} = \frac{L_m}{L_r}$, is defined between a measurement channel (L_m) and a reference channel (L_r). The BQ method assumes that the background reflectance is invariant in both channels, which is an assumption that is not generally met. Systematic errors can be reduced when the ratio is performed by summing all the bands or channels available in and out of the absorption region as the measurement and reference channels, respectively:

$$R_{total} = \frac{\sum_i L_{m,i}}{\sum_j L_{r,j}} \quad (2.4.9)$$

where i and j are the number of bands available in and out the absorption region to compute the BQ.

Narrow/Wide Method (N-W)

The N-W method described in detail in [Frouin and Middleton, 1990](#) performs the ratio between a narrow and wide window both centred in the measurement channel:

$$R_{N-W} = \frac{\sum_i L_{m,i}}{\sum_i L_{m,i} + \sum_j L_{r,i}} \quad (2.4.10)$$

As both reference and measurements channels are within the same absorption band, the ratio is

rather small and the spectral shape of the background reflectance has low influence on the result since no significant variations are expected.

Continuum Interpolated Band Ratio (CIRB)

This method [Bruegge *et al.*, 1990], is an improvement of the Band Quotient method and assumes linearity on the background surface reflectance. The ratio is performed between the measurement channel, L_m , and the linear interpolation between two reference channels at the wavelength of the measurement channel (L_{r1} and L_{r2}):

$$R_{CIRB} = \frac{L_m}{\omega_{r1}L_{r1} + \omega_{r2}L_{r2}} \quad (2.4.11)$$

where $w_{ri} = \frac{\lambda_{ri} - \lambda_m}{\lambda_{r2} - \lambda_{r1}}$ being λ_{r1} and λ_{r2} the wavelength of the two reference channels around the absorption band at λ_m .

Linear Regression Ratio (LIRR)

The LIRR ratio expands the CIRB ratio when several reference and also measurement channels are available [Schläpfer *et al.*, 1996; Schläpfer, 1998]. The radiance inside the absorption band is taken as an average of the selected measurements channels, $\overline{L_m}$, and the reference value is obtained after a linear regression through the reference channels evaluated at the mean wavelength of the measured channels:

$$R_{LIRR} = \frac{\overline{L_m}}{LIR(\lambda_r, L_r)|_{\lambda_m}} \quad (2.4.12)$$

The approach of averaging several channels and then performing a linear regression reduces the impact of instrument noise and spectral calibration error. The term LIR in Equation 2.4.12 means Linear Regression.

Atmospheric Pre-corrected Differential Absorption technique (APDA)

This method developed by Dr. Schläpfer in 1996 [Schläpfer *et al.*, 1998], is an improvement of the CIRB technique (or LIRR when more bands are available) and aims to give a direct measurement of the depth of the transmittance that is directly correlated by the value of the columnar water vapour. Considering $(1 - S\rho) \approx 1$ in Equation 2.3.9, the at-sensor radiance is approximated by $L_s = L_0 + \frac{1}{\pi}E_oT_oT_{cww}\rho$ where the water vapour transmittance, T_{cww} , has been explicitly extracted from the total transmittance. The APDA technique subtracts the atmospheric path radiance from the measured and reflected channels so the ratio is directly related to the transmittance due to water vapour. Following the nomenclature for the CIRB ratio, the

APDA ratio takes the following expression:

$$R_{APDA} = \frac{L_m - L_{0,m}}{\omega_{r1}(L_{r1} - L_{0,r1}) + \omega_{r2}(L_{r2} - L_{0,r2})} \quad (2.4.13)$$

The path radiance term is also function of the columnar water vapour and for its computation in the APDA ratio; an atmospheric radiative transfer code is needed.

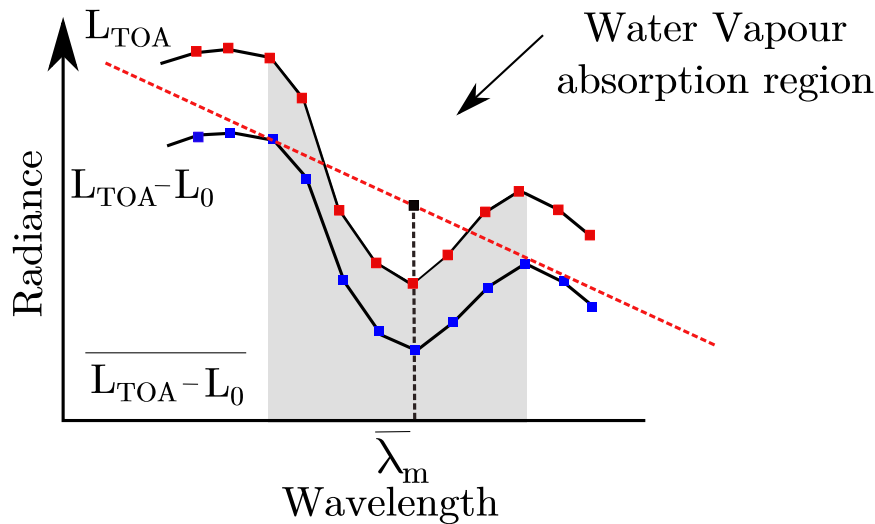


FIGURE 2.4.2: Schematic view of APDA technique in an absorption band. Image adapted from a Figure in [Schläpfer et al., 1998](#)

2.5 Considerations for high spectral and spatial resolution atmospheric correction strategies

As reviewed in this chapter, a wide range of atmospheric correction algorithms – from simplistic approaches to more complex and sophisticated methods – has been developed in the last 30 years. However, *the election of an appropriate atmospheric correction algorithm will be determined by the sensor's specifications*, which depends on the mission's objective.

In essence, the spectral, spatial, temporal or even the radiometric sensor resolution determine the type of information available, and therefore, the type of atmospheric correction strategy to be applied. Generally, the balance between the sensor spectral, spatial and temporal resolutions is bounded by the satellite mission objective. For instance, the meteorological satellite mission of METEOSAT Second Generation (MSG), equipped with the Spinning Enhanced Visible and Infra-Red Imager (SEVIRI), provides an image from Europe and Africa each 15 min, but at a medium spectral resolution (12 channels) and a very low spatial resolution (1 – 3 km). In this case, the low spatial resolution does not involve any limitation to monitor atmospheric dynamics over Europe in the scale of kilometres. Conversely, a high spatial resolution mission like WorldView-4, which are mainly dedicated to 2D and 3D mapping, presents only

4 channels covering the Red-Green-Blue (RGB) and the NIR region with a revisit time of 4.5 days and an incredible spatial resolution of 1.24 m. Regarding the radiometric resolution, although this aspect was a limitation for the early sensors on board spacecraft, in the last years radiometric resolution provided by most sensors covers around 12 – 16 bytes, which can be considered as sufficient to not constrain or limit the atmospheric algorithm design.

2.5.1 High spatial resolution atmospheric correction strategies

High spatial resolution sensors typically offer a quite limited number of spectral channels or bands (from 3–8), covering from the visible to NIR spectral range. Therefore, it complicates to derive information about atmospheric constituents using the same philosophy as for high spectral resolution data, i.e., exploiting the spectral information. Due to that, this family of sensors generally: (1) do not apply any atmospheric correction algorithm, or (2) make use of auxiliary information to characterize the atmospheric state, or (3) try to exploit the spatial information in a way that helps into de atmospheric characterization. Regarding the instrument characterization, since bands are around 20–30 nm width, these sensors are not so sensitive to central wavelengths bands shifts or to slight changes in the instrument spectral response function. On the contrary, images acquired at high spatial resolution must be carefully corrected from adjacency effects. In addition, most of these sensors are also equipped with a panchromatic PAN band, which acquires data in a higher spatial resolution, but with a wider bandwidth compared to other multispectral bands. In these cases, when a pan-sharpening algorithm or a superresolution algorithm aims to be applied to exploit the combination of the multispectral and the PAN bands, atmospheric correction becomes even more relevant since atmospheric spatial effects behave differently at different spatial resolution scales.

2.5.2 High spectral resolution atmospheric correction strategies

Without a doubt, the more spectral information the better atmospheric characterization. For instance, the presence of certain channels located at water vapour absorption bands, e.g., 820 nm or 940 nm, or even at the deep water vapour band of 1300 nm used to detect *Cirrus* clouds, provides the user with valuable information to characterize the atmospheric state. Similarly, bands located on the O₂-A absorption band, with enough spectral resolution, can also be used to estimate surface pressure, to detect fluorescence emission or to derive aerosols scattering effects.

However, the high spectral resolution is normally associated with a medium or low spatial resolution. This determines the impact of some spatial effects, such as adjacency effects or the impact of the surface reflectance BRDF. In case of pixels in the order of hundred of meters or even kilometres, these kinds of spatial effects could become less significant. Conversely, potential sources of errors on high spectral resolution sensors are related to the instrument characterization and calibration. For instance, in very high spectral resolution sensors, central wavelengths spectral shifts or bandwidth broadening effects can extremely impact the acquired data,

especially when monitoring absorption features with high radiometric transitions.

In summary, high spectral resolution sensors offer a huge amount of information providing the most accurate retrievals. Nevertheless, not only a precise atmospheric characterization but also an instrument spectral calibration and characterization is essential to guarantee accurate surface reflectance (or Level-2 products, in general) estimations.

3

Analysing the atmospheric effects on high spatial resolution satellite images: Application to the Ingenio/SEOsat space mission

Contents

3.1	Abstract	40
3.2	Introduction	41
3.3	The Ingenio/SEOsat space mission	42
3.4	The Ingenio/SEOsat sensitivity to atmospheric effects	43
3.5	Exploiting the spatial information for aerosol detection	50
3.6	Hybrid atmospheric correction strategy	55
3.7	Discussion	66
3.8	Conclusions	69

*This chapter is based on the work developed by **Neus Sabater** under the :*

Generation of Level 2 Products for the Ingenio/SEOsat mission



*i+D+i Project funded by the Spanish Ministry of Economy,
Industry and Competitiveness.*

3.1 Abstract

Spatially–explicit atmospheric effects have been typically addressed by remote sensing applications like inland water and ocean color where adjacency effects have a significant impact. However, with the upcoming high spatial and radiometric resolution satellites, such as the Ingenio/SEOsat mission, atmospheric correction strategies that equally compensate for strong adjacency effects are of interest for multiple remote sensing applications. In this chapter, atmospheric effects in the spectral and especially dominant in the spatial domain are analysed for the Ingenio/SEOsat mission specifications. First, with simulated data it was proved that, when the instrument Modulated Transfer Function (MTF) is known, aerosol optical thickness can be estimated by analysing the radiance of pixels around edges between high contrast areas. Second, a complete atmospheric correction strategy called ‘Hybrid’ was formulated and evaluated using Sentinel–2 data. The Hybrid method combines the classical per–pixel physical inversion atmospheric correction strategy together with a spatial deconvolution step to compensate for adjacency effects. Finally, satisfactory validation statistics are achieved when comparing surface reflectance as obtained by the Hybrid method against surface reflectance as provided by the Sen2Cor ESA's Toolbox.

3.2 Introduction

The increasing development of satellite sensors with each time higher spatial resolution expands the possibilities for new optical remote sensing applications. Traditionally, high spatial resolution sensors such as FORMOSAT-2, FORMOSAT-5, SPOT-5, SPOT-6-7 [Kramer, 2017a,b,d,e] have been designed to map rural and urban areas, mining, engineering and change detection purposes. Additionally, in the last decade many commercial satellites with high spatial resolution have been launched, e.g., WorldView 1-4 series [Kramer, 2017f,g,h,i]¹; providing a more detailed description of the surface in the spatial domain (Ground Sampling Distance (GSD) lower than 1 m. in World View-4). Typically, these missions only offer Level-1(b) or Level-1(c) data, i.e., TOA radiance or georeferenced TOA reflectance, as official products. However the increasing number of scientific communities interested in developing agriculture, forestry, and surface analysis with high spatial resolution images underscores the need to offer new higher-level products relying on atmospherically corrected images. Due to that, some algorithms such as the Acomp [Pacifi, 2016] developed by DigitalGlobe, or the multitemporal algorithm developed by Olivier Hagolle et al. for the FORMOSAT, Sentinel-2, Landsat among other missions [Hagolle *et al.*, 2010], provide new strategies to correct high spatial resolution data.

In those cases where the spectral domain is limited, atmospheric correction strategies are re-addressed in the following directions:

- Exploitation of the spatial information by making use of illuminated and non-illuminated homogeneous areas (especially in cities by using shadows generated by building's structures) to derive information regarding the atmospheric state, particularly related to the aerosol content, e.g., Thomas *et al.*, 2011; Schläpfer and Richter, 2017. Generally, this strategy implies the computation of Look-Up-Tables (LUT) containing main aerosol types and contents as well as the use of very high spatial resolution images in order to be able to distinguish buildings and other fine spatial structures.
- Exploitation of the temporal domain by making use of the contrast between atmospheric and surface reflectance temporal resolution. In other words, since changes in the atmosphere are in the order of minutes (water vapour), hours (aerosol); while changes in the surface can be in the order of days [Hagolle *et al.*, 2010], it is possible to assume that the surface reflectance between images is invariant. In this case, high temporal resolution images are required to assume invariant surface reflectance. A similar strategy is also used for multi-temporal clouds masking algorithms where it is assumed that abrupt changes in consecutive images are caused by clouds [Gómez-Chova *et al.*, 2014].
- Exploitation of auxiliary information, either:
 - From meteorological models used for the forecasting, e.g., the aerosol forecasting

¹ Information provided in the ESA's Earth Observation portal <https://directory.eoportal.org> here referenced is originally compiled from the published book [Kramer, 2002]

product from European Commission Monitoring Atmospheric Composition and Climate (MACC) project <http://www.gmes-atmosphere.eu/>, or even from observations AERONET [Holben *et al.*, 1998].

- Even in some cases, for a specific sensor, some atmospheric correction strategies were developed by ESA as an alternative, using a previously trained a Machine Learning (ML) algorithm [European Space Agency, 2017b].

Here an atmospheric correction strategy is proposed for the particular case of the Ingenio/SEOsat space mission. To do so, Section 3.3 summarizes the mission and the instrument main specifications. Then, Section 3.4 presents the Ingenio/SEOsat spectral and spatial sensitivity to detect atmospheric effects. Following, Section 3.5 analyses the possibility to detect aerosol content by exploiting the spatial information when the instrument Modulated Transfer Function (MTF) is known. In case the instrument MTF is unknown but auxiliary information to characterize the atmospheric state is available, an alternative robust atmospheric correction strategy, called **Hybrid**, is presented in Section 3.6. The **Hybrid** strategy performs a per-pixel atmospheric correction inversion method followed by a processing technique to compensate for spatial adjacency effects. The **Hybrid** strategy was validated with Sentinel-2 images that are configured with bands at a 10 m spatial resolution. Validation was conducted by comparing atmospherically corrected Sentinel-2 images from the **Hybrid** strategy and the ESA's Sen2Cor toolbox. Finally, a discussion is presented in Section 3.7 as well as main conclusions are highlighted in Section 3.8.

3.3 The Ingenio/SEOsat space mission

The Spanish Earth Observation Satellite (Ingenio/SEOsat) [Kramer, 2017c] is a passive optical remote sensing high spatial resolution mission developed under the Spanish Earth Observation National Program for Satellites (acronym in Spanish) (PNOTS). The overall mission objective is to provide images for applications in cartography, land use and mapping, urban management, coastal management, agriculture monitoring, precision agriculture, water management, environmental monitoring, risk management and security. The Ingenio/SEOsat satellite will fly on a polar-heliosynchronous orbit at 670 km of altitude, with Local Time of Descending Node (LTDN) 10:30 and 4 days of repeated cycle.

Ingenio/SEOsat main payload is a pushbroom imager providing a PAN channel ² and four multispectral channels (**Blue**, **Green**, **Red**, **NIR**) (See Figure 3.3.1). Main details about spectral, spatial and radiometric resolutions are summarized in Table 3.3.1. More information about the Ingenio/SEOsat instrument and the mission's specifications is given in Appendix A.1.

²The term **channel** is sometimes also referred as **band** during this Thesis

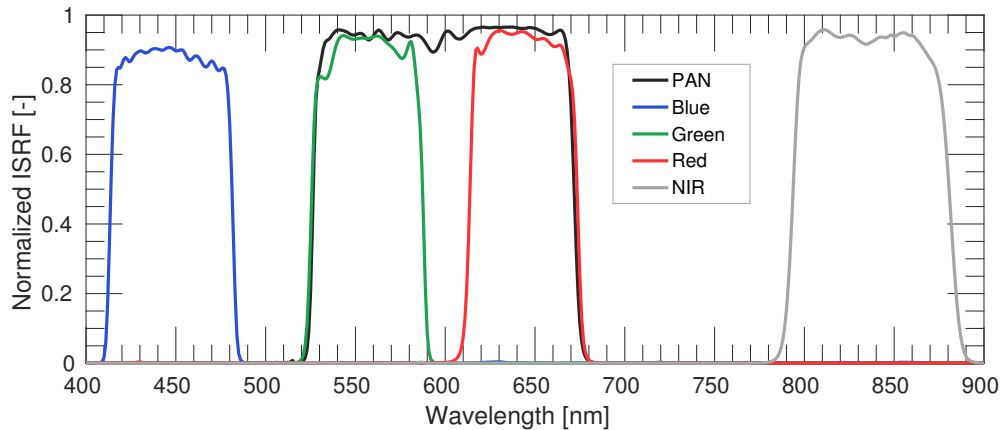


FIGURE 3.3.1: SEOSat normalized instrumental spectral response function.

#	FWHM [nm]	SNR [-]	Spatial res. [m]
PAN	~150	110	2.5
Red	~60	200	10
Green	~60	200	10
Blue	~70	125	10
NIR	~85	200	10

TABLE 3.3.1: Summary of the primary payload Ingenio/SEOSat technical instrument specifications. SNR is calculated using a reference radiance of 80 [mW/m²/sr/nm].

3.4 The Ingenio/SEOSat sensitivity to atmospheric effects

In order to define an appropriate strategy able to correct future Ingenio/SEOSat images for atmospheric effects, it is mandatory to understand how atmospheric effects – especially aerosol, cloud scattering and water vapour absorption – disturbs the expected radiance acquired at satellite level, both in the spectral and in the spatial domain. This way, it is possible to determine whether the capabilities of the sensor are adequate enough to detect or characterize the atmospheric state without using external auxiliary information, or if the proposed strategy should involve the use of external information.

3.4.1 Spectral sensitivity to atmospheric effects

In order to determine how the multispectral channels from the Ingenio/SEOSat optical instrument are affected by different atmospheric conditions, a range of TOA radiance spectra have been simulated using the MODTRAN [Berk *et al.*, 1987] atmospheric RTM covering a series of aerosol optical properties and water vapour values. Aerosol optical properties covered were: (1) The Aerosol Optical Thickness (AOT), related to the aerosol load; (2) the Ångström exponent (α) [Ångström, 1929], related to the spectral dependency of the AOT and the aerosol size; and

(3) the asymmetry parameter of the Henyey–Greenstein scattering phase function (g) [Henyey and Greenstein, 1941], regulating the degree of asymmetry of the aerosol scattering pattern. Because this section only focusses on evaluating the impact of atmospheric effects on the Ingenio/SEOSat channels, a default constant value of 0.5 [-] was used as a surface reflectance spectrum (ρ) in all computed simulations. TOA radiance was therefore simulated following Equation 3.4.1 and assuming a Lambertian surface reflectance behaviour³:

$$L_{TOA} = L_0 + \frac{E_{TOC}\rho T_{TOT}}{\pi(1 - S\rho)} \quad (3.4.1)$$

where L_0 , E_{TOC} , T_{TOT} and S are respectively the path radiance, the solar irradiance at surface level, the total upward transmittance, and the spherical albedo. This set of atmospheric transfer functions were indirectly derived from MODTRAN following the formulation detailed in [Guanter *et al.*, 2009]. Thus, Figure 3.4.1 shows TOA radiance relative difference estimated for all the possible combinations of the aforementioned aerosol optical properties, covering the ranges indicated in the figure's legend. Similarly, the TOA radiance relative difference derived due to changes in the Columnar Water Vapour (CWV) content is presented in Figure 3.4.2.

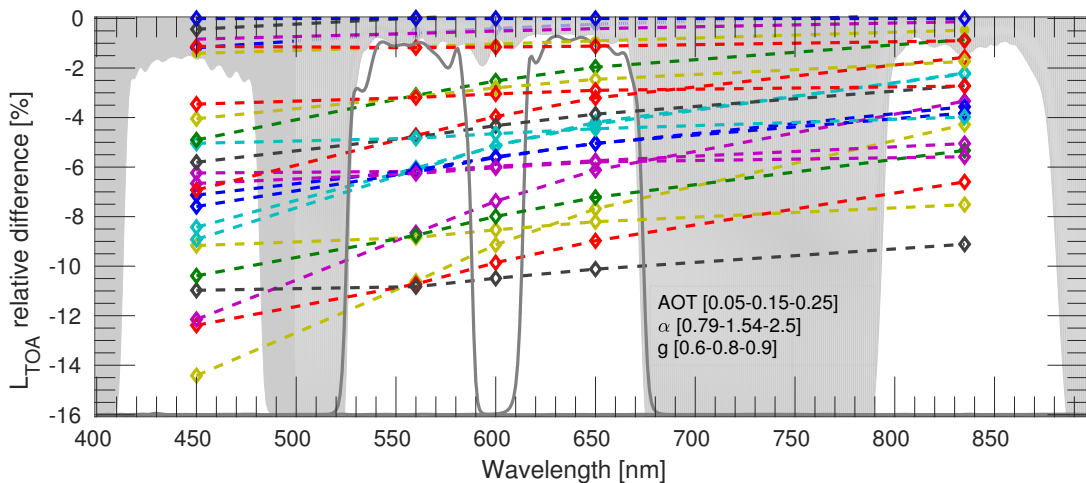


FIGURE 3.4.1: Ingenio/SEOSat TOA radiance spectral sensitivity (computed as Relative Difference [%]) to different aerosol optical properties (all the possible combinations between AOT, α and g values indicated in the legend). Colours represent the possible combinations of the aerosol optical properties values shown in the legend. In this respect, no color legend has been added since the main purpose of this Figure is to evidence that aerosols affect the Ingenio/SEOSat channels, but not to evaluate the independent impact of each of the aerosol optical properties here mentioned.

Regarding the aerosol effects on TOA radiance, Figure 3.4.1 shows how those bands located closer to the blue region are more affected by the aerosol presence. This behaviour is consistent with the aerosol transmittance wavelength–dependency, which effect is stronger at shorter

³This expression was already presented in Chapter 2 (See Equation 2.3.9), but is also here described to ease the understanding of this Section.

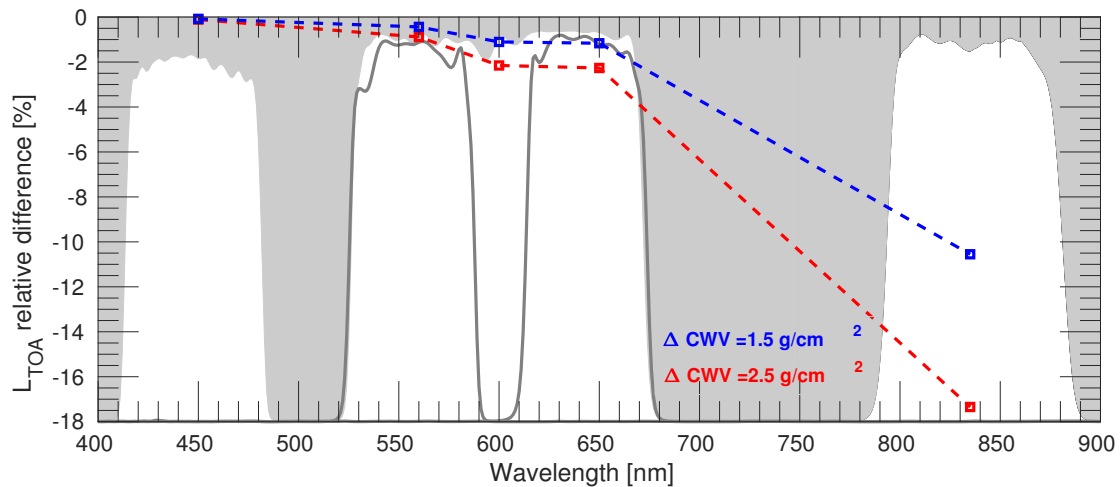


FIGURE 3.4.2: SEOSat/Ingenio TOA radiance spectral sensitivity (computed as Relative Difference [%]) between two different CWV values of 1.5 and 2.5 [g/cm^2] and an atmospheric column free of water vapour content, i.e., $\text{CWV} = 0$ [g/cm^2].

wavelengths. Regarding the CWV content, Figure 3.4.2 evidences how although the red and the green bands are hardly affected, the band centred at the NIR region presents a stronger effect since it is closer to the weak water vapour absorption band centred around 820 nm. However, the quantification of the total CWV content becomes challenging when using only the spectral information available in the Ingenio/SEOSat instrument. Most of the techniques applied to derive the CWV content from the spectrum are typically based on a differential absorption technique (see the background Section 2.4.2 of this Thesis), which means that they make use of two bands in/outside of the water vapour absorption region to compute its ratio assuming a constant or a linear surface reflectance wavelength dependency [Kaufman and Gao, 1992; Bruegge *et al.*, 1990; Schläpfer *et al.*, 1998]. Consequently, given the Ingenio/SEOSat spectral configuration, the impossibility to apply any differential absorption technique requires the use of auxiliary information to characterize the CWV content.

In addition, similarly to the analysis performed for the aerosol and water vapour content, in this section the spectral TOA radiance sensitivity to cloud presence is also analysed. To do so, TOA radiance was computed assuming two contrasting underlying surface types: (1) a desert spectrum (Figure 3.4.3), and (2) a grass surface spectrum (Figure 3.4.4). Then TOA radiance was simulated by including the effects of various types of clouds: *Cirrus*, *Altostratus*, *Nimbostratus*, *Cumulus*, and also the absence of clouds⁴.

In terms of detection and masking, clouds in the spectral domain are typically characterized by being:

⁴ Cloud optical and physical properties such as: cloud base altitude, cloud thickness, ice content, etc.; were all selected as MODTRAN default values. Similarly, used sand and grass surface reflectance spectra were also MODTRAN default spectra contained in an internal database.

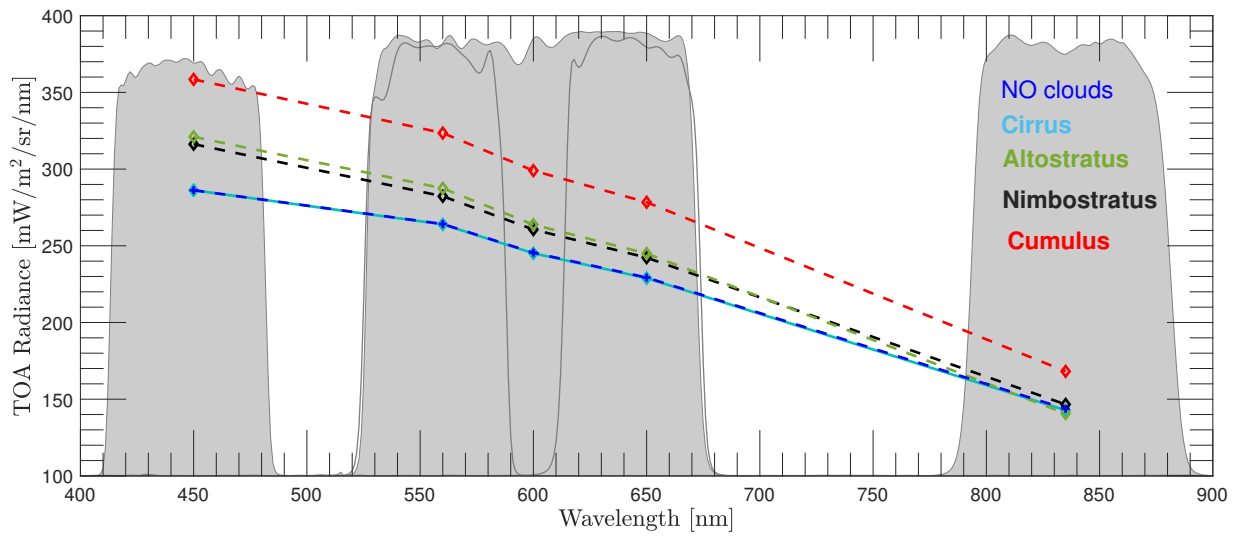


FIGURE 3.4.3: Ingenio/SEOsat TOA radiance signal simulated using a sand surface reflectance spectrum affected by a range of different cloud types: *Cirrus*, *Altostratus*, *Nimbostratus* and *Cumulus*.

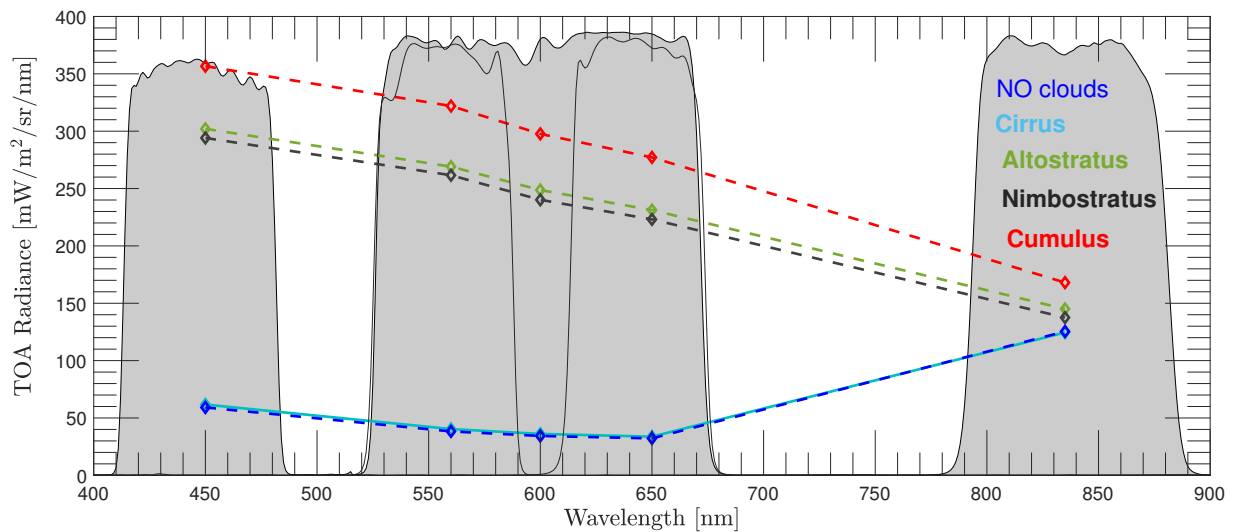


FIGURE 3.4.4: Ingenio/SEOsat TOA radiance signal simulated using a grass surface reflectance spectrum affected by a range of cloud types: *Cirrus*, *Altostratus*, *Nimbostratus* and *Cumulus*.

- Bright \Rightarrow This can be observed in the RGB bands.
- White (flat spectrum) \Rightarrow This can be observed in the RGB bands.
- Cold \Rightarrow This can be appreciated in the thermal bands (not available in Ingenio/SEOsat mission)

- Elevated from the surface \Rightarrow This can be detected using the O_2 -A band, which is sensitive to the surface pressure.

According to the Ingenio/SEOSat spectral information, the only cloud spectral features potentially useful for cloud detection are the brightness and the whiteness. Apart from those methods that rely on the temporal frequency to detect clouds by identifying abrupt changes between images [Hagolle *et al.*, 2010; Gómez-Chova *et al.*, 2014], most traditional cloud screening methods are based on a threshold definition [Guanter, 2006], or training some classifiers using some extracted features [Gómez-Chova *et al.*, 2007].

3.4.2 Spatial sensitivity to atmospheric effects

As the spectral information provided by the Ingenio/SEOSat satellite is quite limited, the role of the spatial information becomes more important. Regarding the aerosol presence, visibility decreases with increasing aerosol content or AOT, appearing a kind of blurring effect even visible in the RGB image to the naked eye. Figure 3.4.5 provides a nice example (from the DigitalGlobe's GBDX platform <https://gbdxdocs.digitalglobe.com>), where the difference in RGB between an image before and after applying the atmospheric correction process is evident. In this particular example, the algorithm applied was the **Acomp** algorithm [Pacifi, 2016] to a Landsat 8⁵ imagery of Naples, Italy.



FIGURE 3.4.5: RGB from Landsat 8 over Naples, Italy, before (a) and after (b) the application of the **Acomp** atmospheric correction algorithm. Source DigitalGlobe's GBDX platform.

Thus, as observed in Figure 3.4.5, atmosphere blurs RGB images decreasing the full scene contrast. Following this idea, atmospheric blurring effect was described in the 80's by defining the atmospheric MTF [Kaufman, 1984] or the atmospheric Point Spread Function (PSF) [Mekler and Kaufman, 1982; Chervet *et al.*, 2002] and [Liew, 1997] in the Fourier and the spatial domain, respectively. In particular, while one of the works developed by Yoram Kaufman in the 80's derived the atmospheric MTF expression as an analytical expression by solving the atmospheric radiative transfer equation for a non-Lambertian surface reflectance [Kaufman, 1982];

⁵Landsat 8 RGB bands are provided with 30 m of spatial resolution, which is three times higher than the expected RGB SEOSat spatial resolution.

another work from this author [Kaufman, 1984] also derived a simplistic empirical expression of the atmospheric MTF (Equations 3.4.2 and 3.4.3):

$$M(k) = M(k = 0)M_n(k) \quad (3.4.2)$$

being $M(k)$ the total atmospheric MTF, k is the spatial frequency here in number of cycles/km, $M(k = 0)$ is the atmospheric MTF for $k = 0$, and $M_n(k)$ the so-called normalized MTF which accounts for the aerosol and molecular variability (see Equation 3.4.3):

$$M_n(k) = 1 - 0.5\tau_r[1 - \exp(-2.5kH_r)] - 0.7\lambda^{(-0.2)}\tau_a[1 - \exp(-1.3kH_a)] \quad (3.4.3)$$

where τ_r , and τ_a are the molecular ⁶ and the aerosol optical thickness respectively for a spectral range between 0.47-1.65 μm ; λ is the selected wavelength and H_r and H_a are the height at which the molecular and the aerosol layer is concentrated. Equation 3.4.3 was also validated against Monte Carlo simulations and physical approximations in Kaufman, 1984 covering the spectral range of 0.47-1.65 μm and the AOT interval value from 0 to 0.64 [-].

Figure 3.4.6 shows an example of the atmospheric empirical MTF described in Equation 3.4.3, covering a range of molecular, τ_r , and aerosols, τ_a , optical thickness while keeping the aerosols, H_r , and molecular, H_m heights invariant.

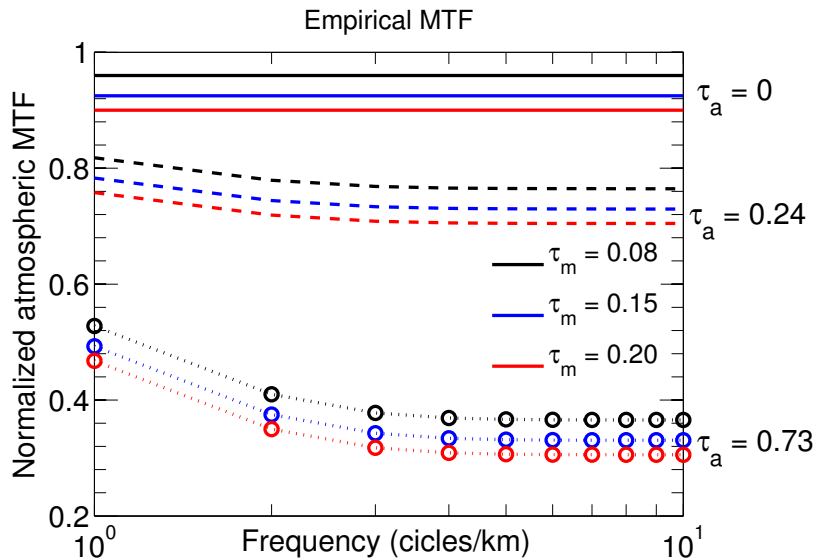


FIGURE 3.4.6: Atmospheric MTF functions, $M_n(k)$, for a range of aerosol optical thickness, (τ_a of 0, 0.24 and 0.73), and molecular optical thickness, (τ_r of 0.08, 0.15 and 0.20). H_r and H_a values were set as 8 km and 1 km, respectively.

⁶the r subscript refers to the Rayleigh scattering.

Therefore, assuming the atmospheric MTF as known, and following the work of [Kaufman, 1982](#), TOA radiance can be expressed as Equation 3.4.4:

$$L_{TOA} = \mathcal{F}^{-1}\{M^*(k)\mathcal{F}\{\rho(x,y)\}\}F_0\mu_0 + L_0 \quad (3.4.4)$$

where L_{TOA} is the TOA radiance, $F_0\mu_0$ is the extraterrestrial solar irradiance, L_0 is the path radiance, i.e., the radiance scattered by the atmosphere, \mathcal{F} and \mathcal{F}^{-1} refers to the Fourier and inverse Fourier transform, and now $M^*(k)$ takes also into account the instrument MTF (M_{sen}):

$$M^*(k) = M_{sen}M(k) = M_{sen}M(0)M_n(k) \quad (3.4.5)$$

Note that Equation 3.4.4, can be also expressed in terms of TOA reflectance as:

$$\frac{L_{TOA}}{F_0\mu_0/\pi} = \rho_{TOA} = \frac{L_0}{F_0\mu_0\pi} + \mathcal{F}^{-1}\{M^*(k)\mathcal{F}\{\rho(x,y)\}\} \quad (3.4.6)$$

Regarding $M(0)$, i.e., the MTF at $k = 0$ following the formulation detailed [[Kaufman, 1984](#)], this term can be computed from the expressions of the radiance above uniform surfaces. Note that the physical meaning of the $M(0)$ term is to describe the contrast between very large fields ($k \ll$ implies large distance between objects, while $k \gg$ implies having objects close to each other). According to the definition provided by [[Pearce, 1977](#)], in which the MTF is defined as the contrast between maximum and minimum radiance above a sinusoidal surface reflectance, L_{max} and L_{min} , respectively; the MTF can be written as Equation 3.4.7:

$$M(k) = \frac{L_{max}(k) - L_{min}(k)}{2\Delta\rho F_0\mu_0} \quad (3.4.7)$$

where $2\Delta\rho$ is the difference in surface reflectance between maxima and minima. F_0 is the incident solar radiance flux at TOA and μ_0 is the cosine of the solar zenith angle. When $k \rightarrow 0$, there are no mutual effects between radiance measured at maximum and minimum since objects are supposed to be largely separated. Therefore, L_{max} and L_{min} can be separately expressed as Equations 3.4.8 and 3.4.9:

$$L_{max} = L_0 + \frac{E_{TOC}[\exp(-\tau_0) + t_d](\rho + \Delta\rho)}{\pi} \quad (3.4.8)$$

$$L_{min} = L_0 + \frac{E_{TOC}[\exp(-\tau_0) + t_d](\rho - \Delta\rho)}{\pi} \quad (3.4.9)$$

where E_{TOC} is the total solar irradiance at surface level, $(\exp(-\tau) + t_d)$ is the total upward transmittance from target to the sensor, and $\rho \pm \Delta\rho$ are maximum and minimum surface

reflectance values. By combining Equations 3.4.7, 3.4.8 and 3.4.9, the expression for the MTF at $k = 0$ results as Equation 3.4.10:

$$M(k = 0) = \frac{E_{TOC}[\exp(-\tau_0) + t_d]}{\pi F_0 \mu_0} \quad (3.4.10)$$

3.5 Exploiting the spatial information for aerosol detection

Based on the formulation detailed in previous Section 3.4.2, here the exploitation of the spatial information for aerosol detection purposes is explored. To do so, the effect of the normalized MTF (M_n) is evaluated over a transition 1-D step function as shown in Figure 3.5.1. In this particular example, two contrasting radiance levels were simulated corresponding to 80 and 20 [$\text{mW}/\text{m}^2/\text{sr}/\text{nm}$] and covering a range of AOT values from a totally clear atmosphere ($\tau_a = 0$) to an extremely hazy atmosphere ($\tau_a = 0.7$). As can be observed, a kind of sigmoid function appears by smoothing the transition areas with increasing AOT. Artefacts observed in the borders of the function, i.e., pixels #0 and #2000, are also a consequence of the MTF application.

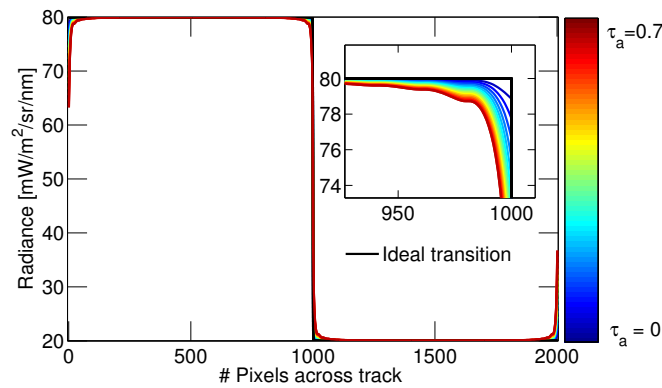


FIGURE 3.5.1: Atmospheric MTF effect applied over a transition between two ideal up-welling radiances from surface corresponding to 80 and 20 [$\text{mW}/\text{m}^2/\text{sr}/\text{nm}$].

In the view of the effects of the atmospheric normalized MTF in transition pixels (around pixel 1000 in Figure 3.5.1), the proposed strategy to exploit the spatial resolution to determine the aerosol content should be based on three main steps:

1. Since the contrast reduction will take place in the borders between contrasting radiance levels, as shown in Figure 3.5.1, then the first step will be detecting image borders.
2. Then, according to Figure 3.5.1, in absence of atmospheric effects transitions between different radiance levels (1-D) will follow the shape of a step function. Therefore, if a deconvolution technique is applied over the image (assuming the shape of the atmospheric

MTF as Equation 3.4.3), the atmospheric corrected image should present an ideal step transition, i.e., a flatness condition in the pixels around the edge or border.

3. Finally, it is mandatory to determine how many pixels around the border will be required to robustly determine the condition of null slope (or flatness) in a realistic situation (10 m of spatial sampling interval).

The first step can be easily performed by applying any of the well-known morphological filters to enhance the image edges, such as the Sobel–Feldman operator or Sobel filter, which computes an approximation of the image intensity gradient [Sobel, 1968]. Regarding the second step, assuming a 1–D image, for any transition between two radiance levels, if the blurring effect produced by the atmosphere is corrected by deconvolving the image using the appropriate atmospheric MTF, then pixels around the edge should accomplish the following mathematical condition regarding the pixels flatness:

$$\min \left(\sum_{n_0-n}^{n_0+n} \frac{dL_{TOC}}{dx} \right) \quad (3.5.1)$$

where, n_0 is the transition, n is the number of pixels around the transition, and x indicates the dimension (See Figure 3.5.3). Thus, Equation 3.5.1 guarantees that if atmospheric effects are properly corrected by applying the corresponding atmospheric MTF, then the sum of the slope before and after the transition n_0 will be minimum. Under ideal conditions, i.e., two infinitive uniform targets, the minimum reached by Equation 3.5.1 should be 0.

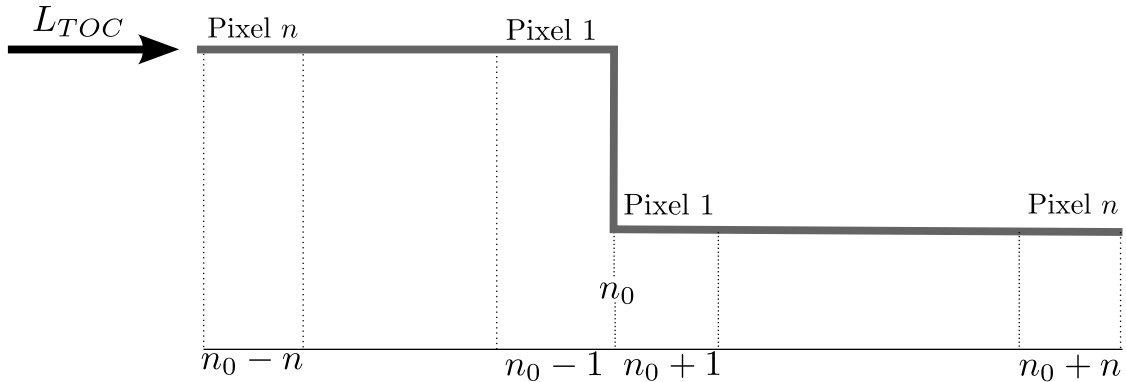


FIGURE 3.5.2: Schematic view of a transition function and the pixels around the edge used to accomplish Equation 3.5.1.

Finally, regarding the identification of the number of pixels required around the transition n_0 , a simulated experiment was performed to determine whether the minimum slope condition formulated in Equation 3.5.1 was reached for a range of AOT values and for a varying number of pixels, from 1 to 20 around the edge (See Figure 3.5.3).

As indicated in Figure 3.5.3, a set of TOA radiance 1–D images were simulated covering a range of AOT values from $\tau = 0$ to $\tau = 0.7$. Then, the set of TOA radiance images were

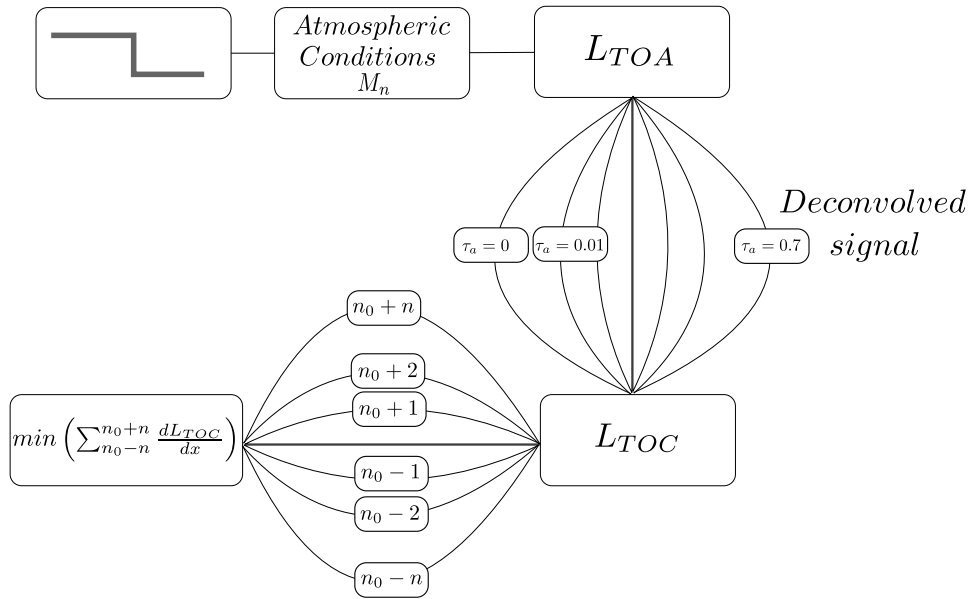


FIGURE 3.5.3: Scheme of the strategy followed to determine the sensitivity of the minimum slope condition to the number of pixels used around the edge n_0 .

deconvolved using the normalized MTF expression covering all the possible AOT values. The resulting cost function for each case (different AOT scenarios (sub-plots) and different number of pixels (coloured lines) around the edge) was plotted in Figure 3.5.4.

From Figure 3.5.4 it can be concluded that regardless the number of pixels selected around the edge n_0 , the minimum slope condition finds the reference AOT, τ_a , defined in the simulation. However, when more pixels are selected around the transition, then the minimum condition to detect AOT becomes more sensitive. This is observed because the higher decay to the minimum occurs when a higher number of pixels around the edge are selected. Alternatively, to better quantifying the sensitivity to find the cost function minimum (Equation 3.5.1) according to the number of pixels selected around the edge and the AOT values a new index H is defined as Equation 3.5.2:

$$H = \left| \frac{f_{n_{min}} - f_{n_{min}-1}}{\Delta\tau_a} \right| + \left| \frac{f_{n_{min}+1} - f_{n_{min}}}{\Delta\tau_a} \right| \quad (3.5.2)$$

where f is the minimization cost function (Equation 3.5.1) evaluated around the minimum, and $\Delta\tau_a$ is the step used for the AOT in the minimization process. Figure 3.5.5 presents the H index values according to the AOT and the number of selected pixels around the edge.

Thus, from Figure 3.5.5 it can be observed that the higher AOT value, the more sensitive the minimum cost function is to detect the minimum. Likewise, for all the AOT values covered, when more than 10 pixels around the edge are evaluated, the H index tends to saturate.

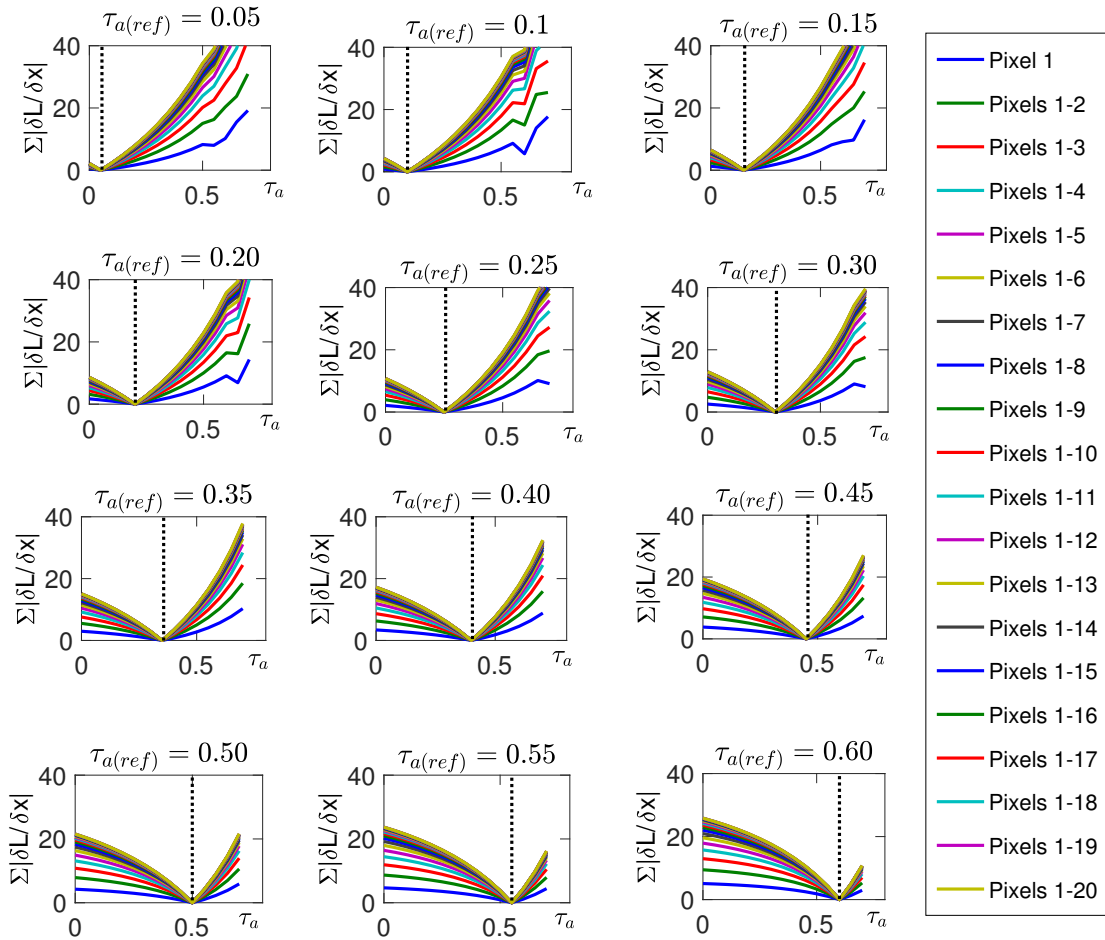


FIGURE 3.5.4: Evaluation of the minimum condition evolution for a range of reference AOT values (labelled as $\tau_{a(ref)}$ at each panel) and number of pixels around the border (coloured lines). The vertical black dotted line indicates also the reference $\tau_{a(ref)}$ in each panel plot.

3.5.1 Application to 2-D simulated images

In this section the minimum flatness condition presented in Section above is now evaluated over a 2-Dimension (2-D) simulated images with three different spatial patterns as shown in Figure 3.5.6.

These three images have been convolved by the atmospheric MTF, thereby ignoring the instrument MTF effect. When the atmospheric MTF deconvolution is applied over these images, covering a wide range of AOT values (0–0.7), some artefacts appear in the pixels around edges for all those AOT values that are not the one used as a reference. Figure 3.5.7 shows the resulting deconvolved image profile from Figure 3.5.6 (b). The behaviour of cases (a) and (c) was identical.

Finally, a Gaussian noise (Equation 3.5.3) was added to Figure 3.5.6 (c) in order to check if

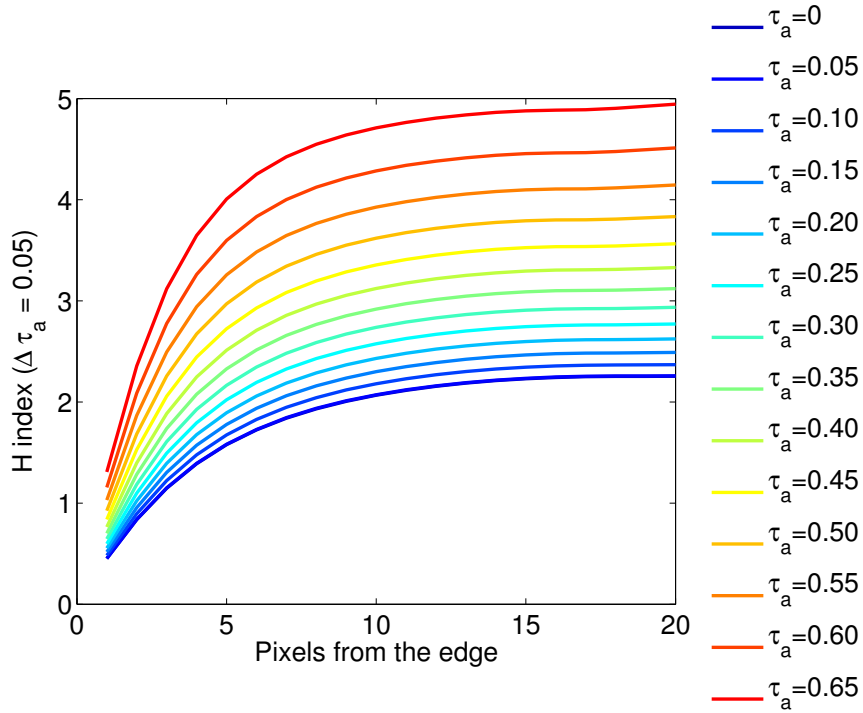


FIGURE 3.5.5: H sensitivity index evaluation for a range of AOT values (from 0 to 0.65 [-]) covering from 1 to 20 pixels around the edge.

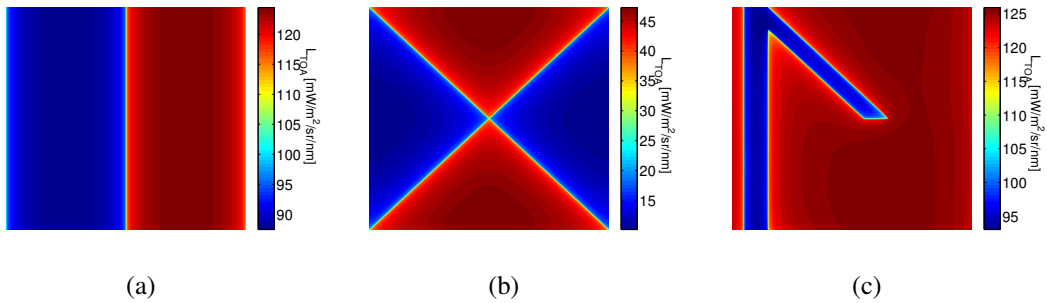


FIGURE 3.5.6: Geometrical patterns simulated to apply the MTF deconvolution **(a)** two squares, **(b)** four triangles, and **(c)** two lines creating an angle between them. Note that radiance levels used in **(a)** and **(c)** are significantly higher than values covered in **(b)**.

it would be feasible to use the flatness condition of the deconvolved signal for AOT estimations even on those cases affected by noise; or in those images where pixels around the edge are not homogeneous (realistic scenarios):

$$L_{i,noise} = L_i + \gamma \sqrt{\frac{(L_i - \bar{L})^2}{10^{SNR/10}}} \quad (3.5.3)$$

where $L_{i,noise}$ and L_i are the radiance signal with and without noise per pixel i , \bar{L} is the mean

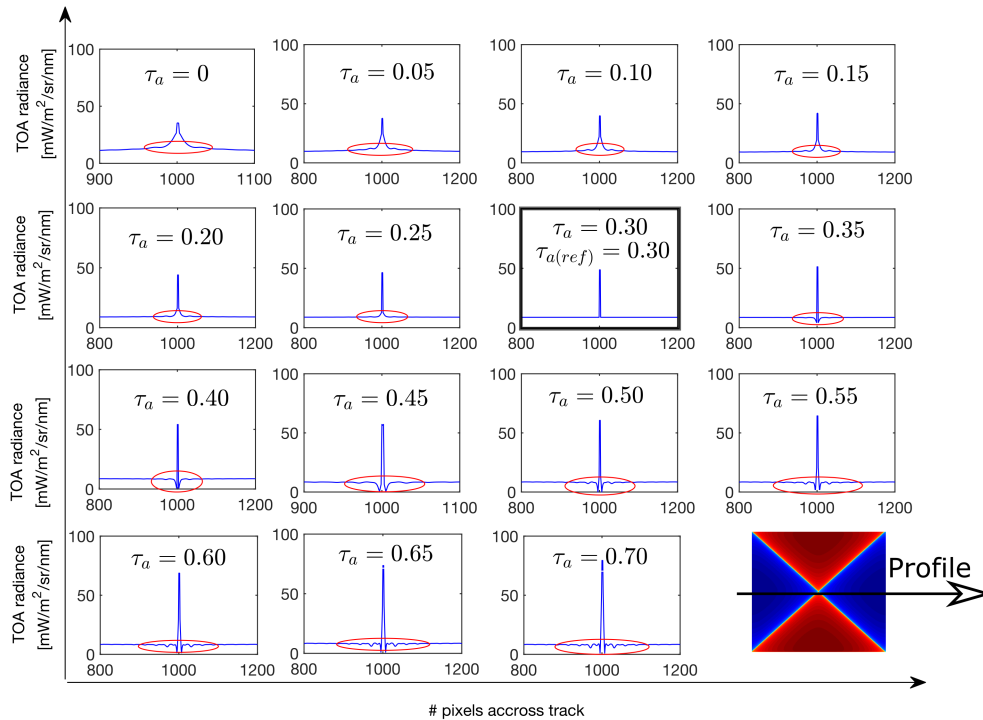


FIGURE 3.5.7: Section profile of the deconvolved 2-D simulated image (Figure 3.5.6 (b)) for a range of AOT values. The panel squared in bold corresponds to the deconvolved profile were the reference AOT ($\tau_{a(ref)}$) used for the simulation and the AOT (τ_a) used for the deconvolution are the same.

of the image radiance, the SNR refers to the signal to noise ratio set as 5 dB, and γ is a random component between [0,1].

The resulting deconvolved profiles were analysed in Figure 3.5.8. As can be observed, now the flatness condition around the edge is affected by the noise; however the cost function still estimates the AOT properly. In this example, the applied flatness condition retrieved successfully the reference AOT only in case 1 or 2 pixels around the edge were selected. It is obvious that the noise affecting the flatness of the deconvolved profile will therefore affect estimated cost function values.

3.6 Hybrid atmospheric correction strategy: validation with the Sen2Cor Sentinel-2 processor.

The above-described Sections showed how aerosols play a role in the spectral and the spatial domain. In particular, a strategy to invert aerosol load was proposed and tested on simulated images in case the instrument MTF is known. Alternatively, in this Section, a full atmospheric correction strategy, called Hybrid, is presented for those cases in which the instrument MTF is not accurately known or the spatial resolution is not high enough to find more than two

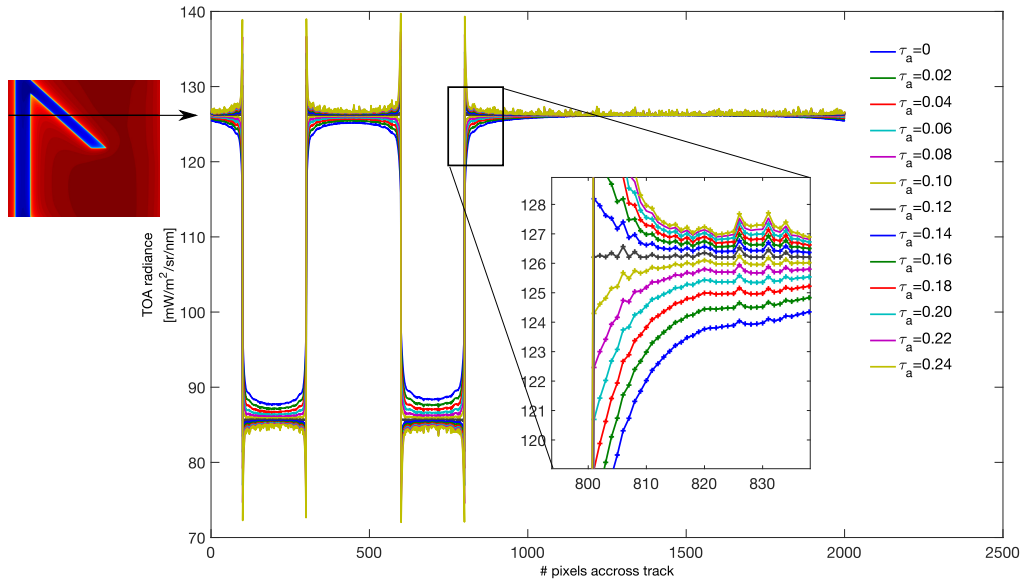


FIGURE 3.5.8: Profile of the deconvolved image for a range of AOT (τ_a) values evaluated in the section shown in 2–D figure at the corner (Upper left panel). In this case, the reference AOT value used was $\tau_{a(ref)} = 0.12$.

homogeneous pixels around the transition edge. The **Hybrid** atmospheric correction strategy combines: (1) a per pixel atmospheric correction by inverting an atmospheric RTM, and (2) a compensation of the spatial aerosol blurring effects by applying the deconvolution of an approximated atmospheric MTF. The **Hybrid** method has been applied to the four bands from the MultiSpectral Instrument (MSI) instrument, on board Sentinel–2, that are closest in terms of spectral and spatial resolution to the multispectral bands from Ingenio/SEOSat (See Table 3.6 and Figure3.6.1 for comparison).

	SEOSat		Sentinel–2A	
	λ_0 (nm)	σ (nm)	λ_0 (nm)	σ (nm)
Blue	450	70	490	98
Green	550	80	560	45
Red	650	60	665	38
NIR	850	140	842	145

TABLE 3.6.1: Comparison between Sentinel–2A and SEOSat, RGB and NIR bands, central wavelength (λ_0) and bandwidth (σ).

Since Sentinel–2 images were used in this Section, derived surface reflectance images from the Hybrid strategy were validated against surface reflectance provided by the Sentinel–2 ESA's Sen2Cor toolbox <http://step.esa.int/main/download/>.

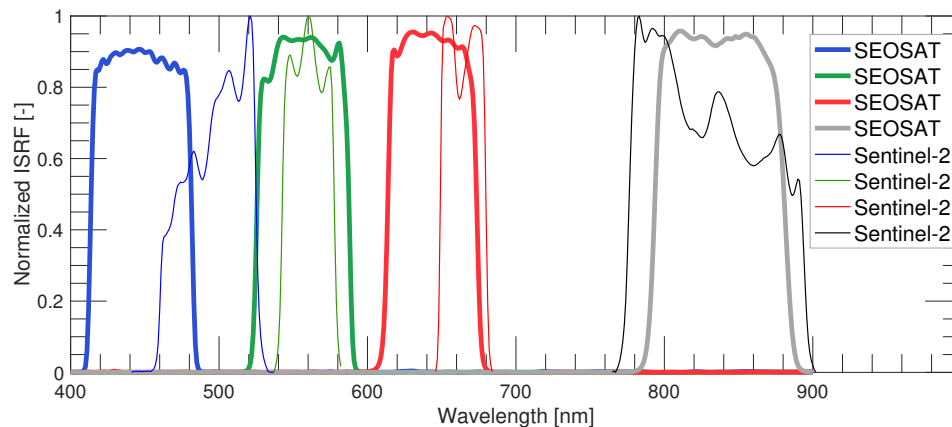


FIGURE 3.6.1: Comparison of the Ingenio/SEOSat and Sentinel-2 filters for the 10 m resolutions bands.

3.6.1 Sen2Cor processor

Sen2Cor is an official toolbox provided by ESA to atmospherically correct the Sentinel-2 images. In essence, the atmospheric correction strategy implemented in the Sen2Cor processor is based on the ATCOR atmospheric correction method [Richter and Schläpfer, 2007a]. Sen2Cor performs a per-pixel atmospheric correction by inverting TOA radiance using the atmospheric transfer functions stored in precomputed LUTs. The stored LUTs are built by running the LiRadtran atmospheric RTM [Mayer and Kylling, 2005; Emde *et al.*, 2016].

Main steps performed by the Sen2Cor processor consist on:

1. A first pixel classification between 11 distinct classes: No data, saturated, dark area pixels, cloud shadows, vegetation, bare soils, water, cloud low probability, cloud medium probability, cloud high probability, thin Cirrus, and snow. Main goal of this classification is dedicated to: (1) cloud detection, and (2) determine if the Dark Dense Vegetation (DDV) method can be applied to characterize the aerosol presence. The application of the DDV requires that at least 5% of the image pixels have a surface reflectance value (computed using a default visibility value of 23 km) between $0.01 < \rho(2.2\mu m) < 0.12$.
2. Characterizing the aerosol presence, mainly AOT and aerosol type, by (1) applying the DDV method if the image have enough dark pixels or, (2) applying an alternative strategy. The alternative strategy starts with setting a default AOT to 0.32 and then decreases this value until the inverted reflectance at $0.865\mu m$ is greater or equal to zero on those pixels classified as water bodies.
3. Characterizing the water vapour content in a pixel basis by means of applying the APDA algorithm [Schläpfer *et al.*, 1998].
4. Inverting TOA radiance assuming a Lambertian surface behaviour (see Equation 2.3.9).

5. Correcting for adjacency effects in a 1 km x 1 km area (optional).
6. Correcting for BRDF effects (optional).

Regarding the aerosol characterization, on the one hand, the DDV strategy is based on a spectral correlation between bands in the SWIR and visible region⁷. In the SWIR region, aerosol effects can be neglected and reflectance can be directly estimated by inverting TOA radiance. Then, the following spectral correlation between surface reflectance bands is assumed:

- $\rho(0.665\mu m) = 0.5\rho(2.2\mu m)$
- $\rho(0.490\mu m) = 0.5\rho(0.665\mu m) + 0.005$
- $\rho(0.443\mu m) = 0.8\rho(0.490\mu m)$

Once having the aerosol and water vapour characterized, the resulting per-pixel surface reflectance is corrected for adjacency effects. To do so, surface reflectance is first averaged in a 1km x 1km area ($\bar{\rho}$):

$$\bar{\rho} = \frac{1}{N^2} \sum_{i,j} \rho(i,j) \quad (3.6.1)$$

where $\rho(i,j)$ corresponds to the surface reflectance value at a pixel with (i,j) coordinates, and N is the number of total pixels selected in the 1 km x 1 km box. Instead of a pixel distance independent weighting, an alternative more accurate pixel distance dependent computation can be performed to compute the averaged reflectance ($\bar{\rho}$) by introducing a exponential decrease of the weighting coefficients (see Equation 3.6.2):

$$\bar{\rho} = \int_0^R \rho(r) A(r) \exp(-r/r_s) dr \quad (3.6.2)$$

where r_s is a scale range, which typically ranges values between 0.2- 0.4 km; R is the radio of influence of adjacency effects defined as $R = 2.3r_s$, ranging from 0.5 to 1 km up to 2 km (depending on the atmospheric conditions); and $A(r)$ is the circular area at radio r .

When approximating circular regions by squared regions, Equation 3.6.2 becomes:

$$\bar{\rho} = \sum_i^{n_R} \bar{\rho}_i w_i \quad (3.6.3)$$

⁷Note the impossibility to apply the technique to characterize the aerosol presence in Ingenio/SEOSat due to the non existing bands in the SWIR region.

where:

$$w_i = \frac{W_i}{\sum_{i=1}^{n_R} W_i} \quad (3.6.4)$$

and:

$$W_i = \int_{r_{i-1}}^{r_i} A(r) \exp(-r) dr \approx \int_{r_{i-1}}^{r_i} (2r)^2 \exp(-r) dr \quad (3.6.5)$$

where $(2r)^2$ is the area A_r considered. Therefore, the derived per-pixel surface reflectance corrected using the estimated averaged $\bar{\rho}$ becomes:

$$\rho^{(adj)}(x, y) = \rho(x, y) + q\{\rho(x, y) - \bar{\rho}(x, y)\} \quad (3.6.6)$$

In Equation 3.6.6, $\rho^{(adj)}$ is the surface reflectance corrected for adjacency effects, and q is a function that accounts for the strength of the adjacency effects by computing the ratio between estimated diffuse and direct transmittance.

3.6.2 The Hybrid atmospheric correction scheme

This strategy is called **Hybrid** since it combines a per-pixel classical physical inversion technique with a per band spatial deconvolution to also compensate atmospheric adjacency effects in the spatial/spectral domain. The processing scheme of the Hybrid strategy is detailed in Figure 3.6.2.

In a **first step**, atmospheric auxiliary data – mainly aerosol content, aerosol type and water vapour– are collected together with other required auxiliary information such as the DEM. Note that, the more information collected, e.g., vertical temperature profile, aerosol scattering phase function, etc.; the more accurate modelling of the atmospheric transfer functions. Once the required auxiliary parameters are collected, they are used to interpolate the precomputed atmospheric LUT. Outputs from the interpolated LUT are the atmospheric transfer functions L_0 , E_{TOT} , T_{TOT} and S ; corresponding respectively to the path radiance, the solar irradiance at surface level, the total upward transmittance, and the spherical albedo.

To compute a first surface reflectance estimation, the contribution of S is neglected and a simple linear relationship between surface reflectance (ρ) and TOA reflectance (ρ_{TOA}) is assumed:

$$\rho_{TOA} = \frac{L_{TOA}}{F_0\mu_0} \approx \frac{L_0}{F_0\mu_0} + \frac{E_{TOC}}{\pi F_0\mu_0} \rho T_{TOT} \quad (3.6.7)$$

Therefore, a first surface reflectance estimation is derived from Equation 3.6.8:

$$\rho(x, y) = \frac{\rho_{TOA} - \rho_0}{M(k=0)} \quad (3.6.8)$$

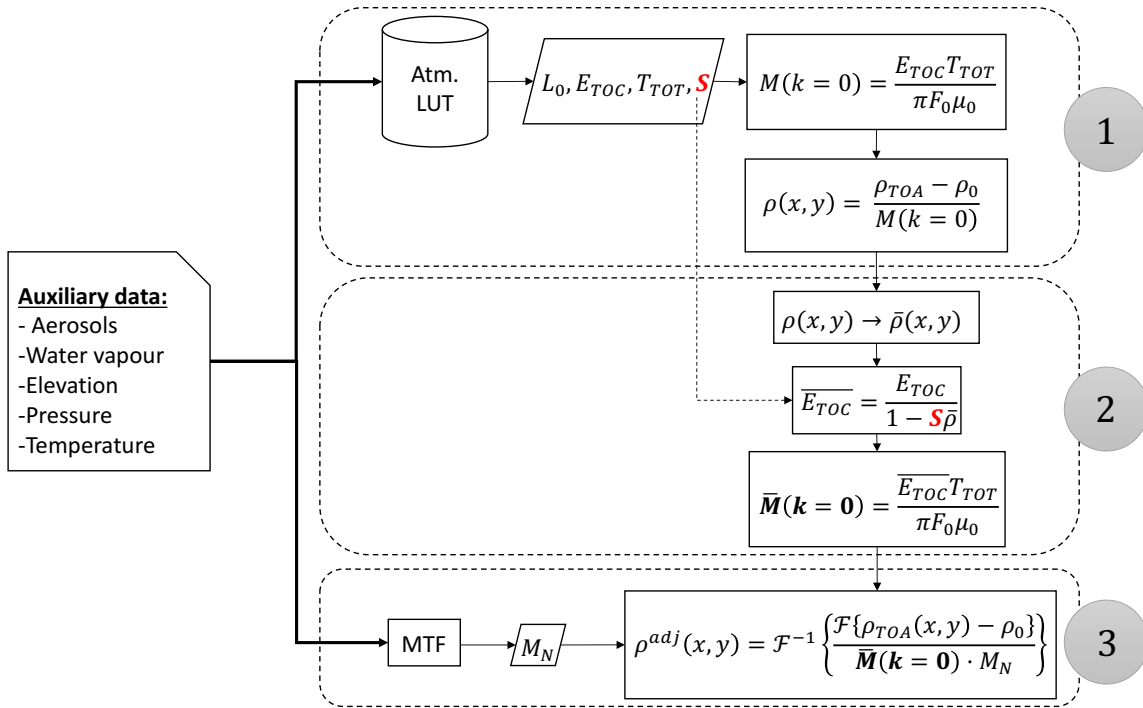


FIGURE 3.6.2: Proposed hybrid atmospheric correction scheme to atmospherically correct the Ingeo/SEOSat images by relying on atmospheric auxiliary data and compensating for atmospheric spatial effects.

where $\rho_0 = L_0/F_0\mu_0$ and $M(k=0)$ is defined as:

$$M(k=0) = \frac{E_{TOC} T_{TOT}}{\pi F_0 \mu_0} \quad (3.6.9)$$

and $F_0\mu_0$ is the extraterrestrial solar irradiance at TOA level corrected by the cosine of the solar zenith angle $\mu_0 = \cos(SZA)$. Since the total transmittance is defined as $T_{TOT} = \exp(-\tau_0) + t_d$, Equation 3.6.9 and Equation 3.4.10 are equivalent. However, for practical reasons, it is more convenient to group the total upward transmittance functions (direct and diffuse) as a single term T_{TOT} corresponding to a unique LUT output.

Then, in a **second step** the estimated per pixel surface reflectance is used to compute an averaged surface reflectance map ($\bar{\rho}$), similarly to the process performed by the Sen2Cor processor (Section 3.6.1). In this step, the $\bar{\rho}$ is computed in a 300 m x 300 m size box without any weighting dependency on the distance to the central pixel of the box. The reason for not introducing any weighting dependency is because the derived $\bar{\rho}$ is only used to improve the estimation of the solar irradiance at surface level $\overline{E_{TOC}}$, but not to totally account for the adjacency effects (see Equation 3.6.11).

$$\overline{E_{TOC}} = \frac{E_{TOC}}{1 - S\bar{\rho}} \quad (3.6.10)$$

In essence, by means of this new term $\overline{E_{TOC}}$ the contribution coming from the multiple scattering is accounted as part of the total solar irradiance reaching the surface. Consequently, an improved atmospheric MTF at $K = 0$ can be now computed as:

$$\overline{M}(K = 0) = \frac{\overline{E_{TOC}}T_{TOT}}{\pi F_0 \mu_0} \quad (3.6.11)$$

Finally, in a **third step**, adjacency effects are corrected following Equation 3.6.12 by deconvolving the image accounting for the normalized atmospheric MTF (M_N) and the $\overline{M}(k = 0)$:

$$\rho^{adj}(x, y) = \mathcal{F}^{-1} \left\{ \frac{\mathcal{F} \{ \rho_{TOA}(x, y) - \rho_0 \}}{\overline{M}(k = 0) M_N} \right\} \quad (3.6.12)$$

This way, spatial blurring effects produced by molecular and aerosol scattering are more accurately approximated than simply weighting a kernel function according to the distance to the central pixel of the kernel. To illustrate the aerosol effect in the spatial domain, Figure 3.6.3 presents the aerosol PSF, i.e. the Fourier inverse transform of the aerosol MTF, for a range of different AOT values ⁸.

3.6.3 Hybrid & Sen2Cor

The proposed **Hybrid** strategy was applied to an acquired image of Sentinel–2 at Level-1C, i.e., TOA reflectance⁹. The required auxiliary data, AOT and water vapour were derived from the Aeronet closest station at the satellite overpass <https://aeronet.gsfc.nasa.gov/Burjassot> (Burjassot, 39.507 N, 0.420 W). More details about the parameters used by the Hybrid strategy to interpolate the atmospheric transfer functions are described in Table 3.6.2. In this Table, also atmospheric parameters estimated as part of the Sen2Cor atmospheric correction has been included.

Parameter	Input (Hybrid)	Input (Sen2Cor)
τ_{550} [-]	0.05	~ 0.25
Aerosol Type [-]	Rural (MODTRAN)[Shettle and Fenn, 1979]	Rural (Libradtran) [Shettle, 1990]
CWV[g/cm ²]	2.14(Burjassot station)	~ 1.9
Elevation[m]	100	100
Atmosphere	Mid Latitude Summer	Mid Latitude Summer

TABLE 3.6.2: Summary of input parameters used to atmospherically correct the selected Sentinel–2 image in the RGB and NIR bands using the Hybrid strategy and the Sen2Cor processor.

⁸Other examples of disentangled aerosol and molecular PSFs can be found in [Reinersman and Carder, 1995](#).

⁹S2A_OPER_PRD_MSIL1C_PDMC_20160620T201630_R051_V20160620T105336_20160620T105336.SAFE, tile 9 which corresponds to the S2A_OPER_PVI_L1C_TL_SGS__20160620T161042_A005196_T30SYJ

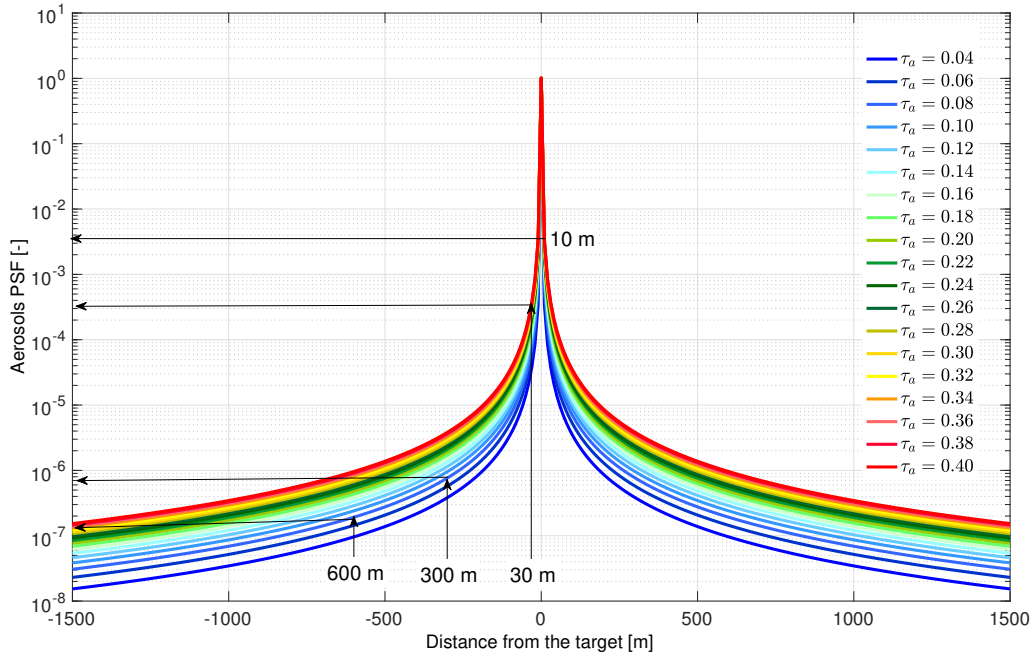


FIGURE 3.6.3: Atmospheric PSF normalized to 1 for a range of AOT values computed against the distance to the central pixel. Aerosol PSF is presented in logarithmic scale while the distance from the target (or central pixel) is shown in m.

In order to compare the estimated surface reflectance derived from the Hybrid atmospheric correction process and the Sen2Cor ESA's Toolbox; density scatter plots from the region of Valencia has been computed for the RGB and NIR bands. Surface reflectance scatter plots (Figure 3.6.4) show a good agreement between estimated surface reflectance by both methods in the green and red bands. However, major differences are found in the blue and the NIR bands. Some explanations regarding differences found between both methodologies are given below:

- AOT input values selected to perform the atmospheric inversion in each case were different. On the one hand, Sen2Cor retrieved an AOT value around 0.25, while the Hybrid method set the AOT as 0.05 (using Aeronet as reference). Thus, due to the AOT overestimation in Sen2Cor compared to Aeronet, estimated surface reflectance by Sen2Corr is lower than the value derived by the Hybrid strategy, especially at the blue band. To better understand this fact, Figure 3.6.5 shows changes in each atmospheric transfer functions due to a small variation in AOT. In general, when increasing AOT, those atmospheric transfer functions that accounts for the direct transmittance of light, such as E_{dir} and t_{dir} , are more attenuated and their value decrease. Conversely, those atmospheric transfer functions that accounts for the scattered light, such as L_0 , E_{dif} and t_{dif} , increase their value. As a result from inverting Equation 3.6.8 the higher AOT value the lower surface reflectance retrieved in the blue band. In addition, differences can also be attributed to the

different procedure followed by each strategy to correct for adjacency effects (analysed in next paragraphs).

- While main differences in the blue band are derived because of the aerosol influence; differences in the NIR band are a combination of discrepancies in aerosol estimation and the water vapour content. The Sen2Cor algorithm computes the water vapour content in a pixel-basis by applying the APDA technique at the band located at 940 nm, which provides a more detailed information about the spatial distribution of the water vapour content. Particularly for the Valencia city region where the scatter plots from Figure 3.6.4 are computed, the averaged CWV is $1.61 \pm 0.12 \text{ g/cm}^2$. Conversely, Aeronet only provides a punctual source of information for the entire image (see Table 3.6.2); which partly explains discrepancies found between the Hybrid and the Sen2Cor correction.

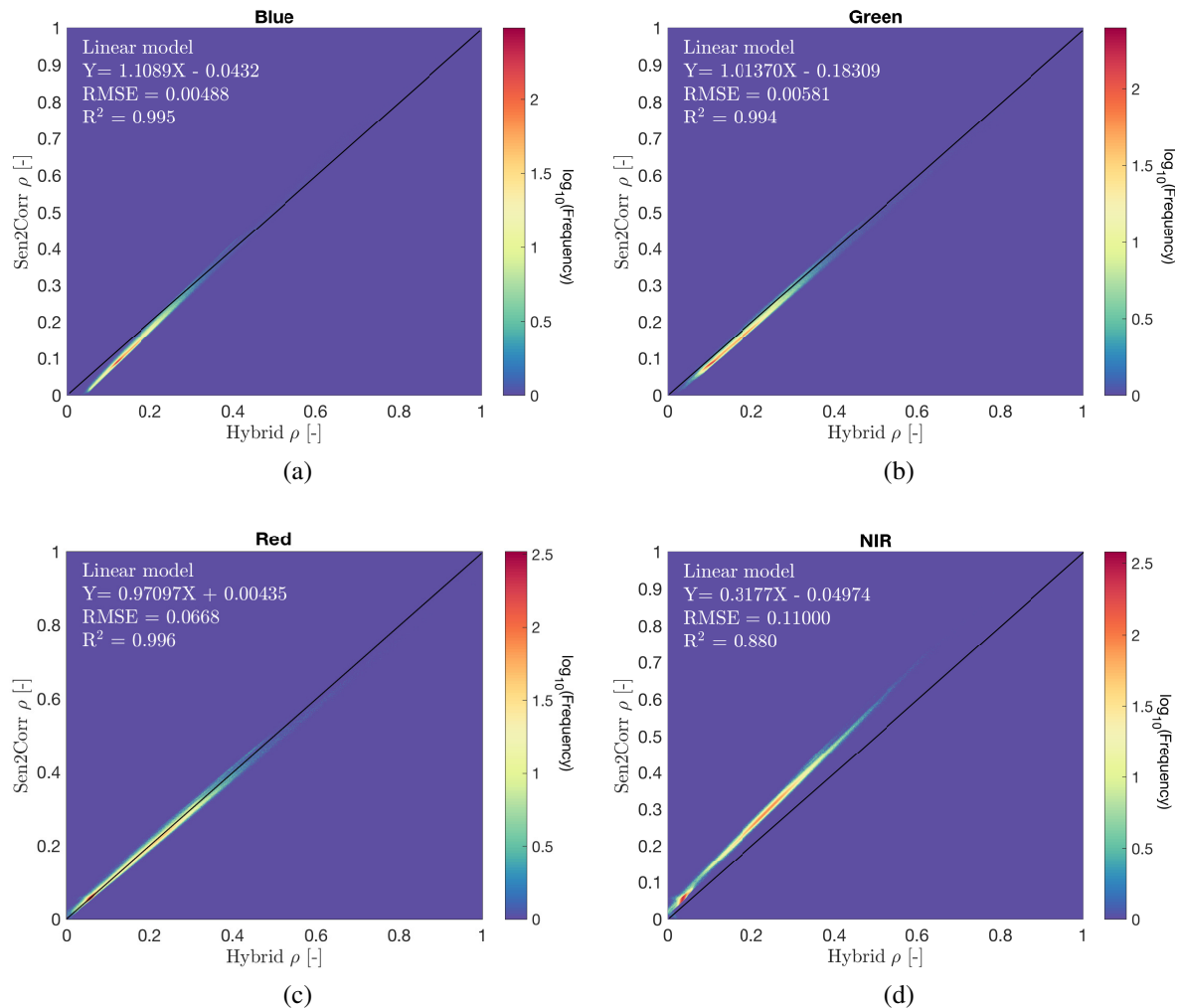


FIGURE 3.6.4: Density scatter plots in logarithmic scale comparing surface reflectance corrected using the Hybrid method and the ESA's Sen2Cor toolbox for the **Blue (a)**, **Green (b)**; **Red (c)**; and **NIR (d)**.

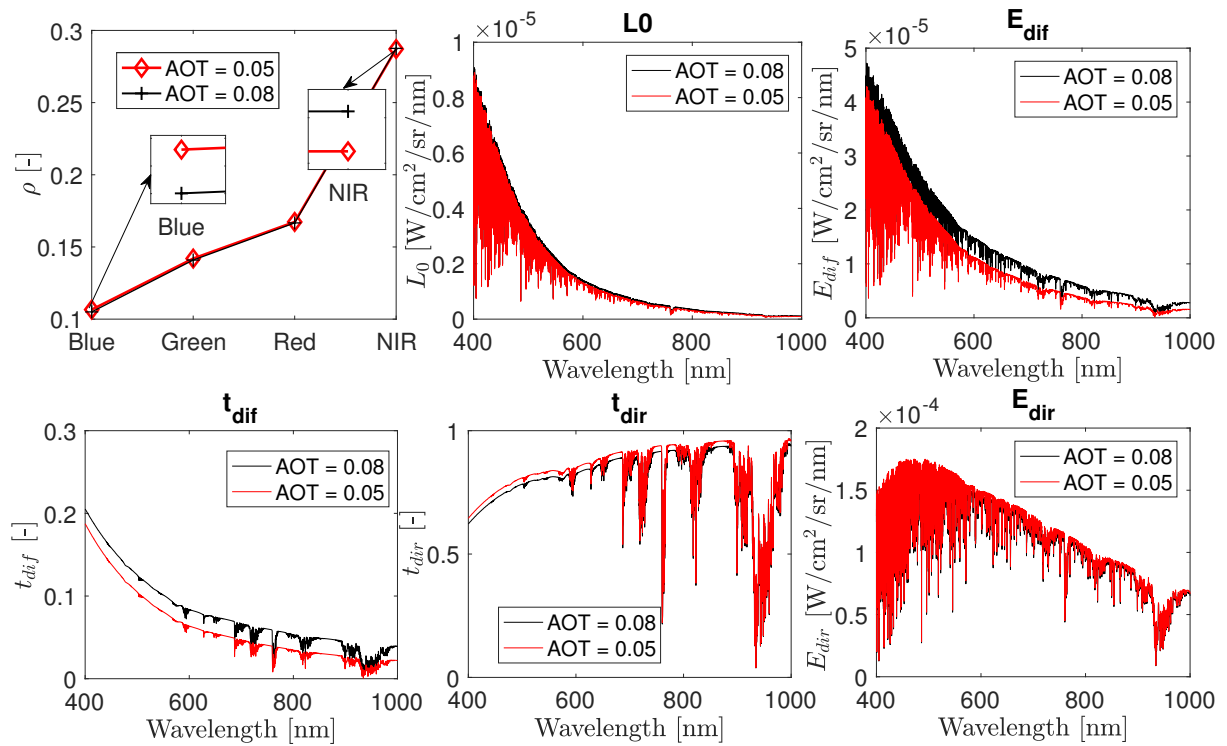


FIGURE 3.6.5: Example of inverted surface reflectance spectra (first panel) considering the atmospheric transfer functions L_0 , t_{dir} , t_{dif} , E_{dir} and E_{dif} computed for the AOT values of 0.05 and 0.08.

Since the comparison between both methods becomes challenging due to contrasting input parameters, and especially due to the distinct AOT value estimated, the Sen2Cor adjacency correction process has been implemented outside the Sen2Cor toolbox. This way, the adjacency correction can be assessed under the same initial conditions as used in the Hybrid strategy, i.e., using the same atmospheric input parameters and taking the same first surface reflectance estimation. On the one hand, the improvement achieved between surface reflectance derived on a pixel-wise basis (step 1 of the Hybrid method); and after applying the deconvolution technique using the atmospheric MTF (step 3) is quantified in Figure 3.6.6 by computing the relative difference in surface reflectance, i.e., $RE(\%) = [\rho_{step1} - \rho_{step3}] / \rho_{step3}$. The Valencia city area was selected due to its urbanism. As an urban region, main streets and the city green belt (old Turia river bed); which is a dense vegetated area, can be easily identified. Thus, in Figure 3.6.6 (Right) it can be observed that reflectance at step 1 was around 10% higher than in step 3, especially in those areas with low reflectance values at the blue band, i.e., vegetated areas, water bodies and sea water (yellowish areas in the relative error (RE) map). Similarly, the difference can also be appreciated in areas close to the harbour. In these regions, there is a remarkable contrast between concrete and water reflectance spectra. Conversely, although being the contrast between the sand and water also significant in the sea shore, transition seems more gradual according to the RE map. On the other hand, the adjacency correction implemented in

the Sen2Cor toolbox (described in Section 3.6.1) was applied over the surface reflectance image derived from step 1; i.e., after the per-pixel inversion. Figure 3.6.7 shows the q function used to weight the adjacency correction kernel in Sen2Cor. Similarly to Figure 3.6.6, Figure 3.6.8 shows the relative difference between the estimated ρ^{adj} (using Equation 3.6.6) and ρ (step 1).

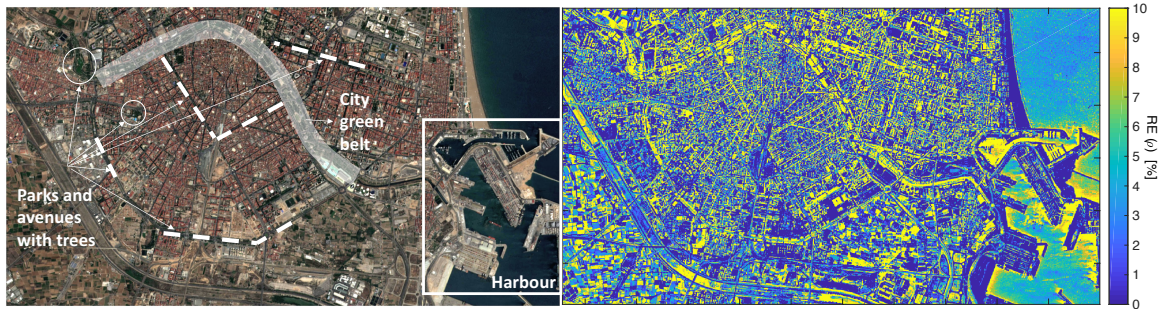


FIGURE 3.6.6: RGB of surface reflectance corrected using the Hybrid method with indications of potential areas where adjacency effects are expected, such as parks, avenues with trees or the harbour (Left). Relative difference in (%) between surface reflectance in the blue band derived from step 1 and step 3 (i.e., after deconvolution); as part of the Hybrid method proposed (Right).

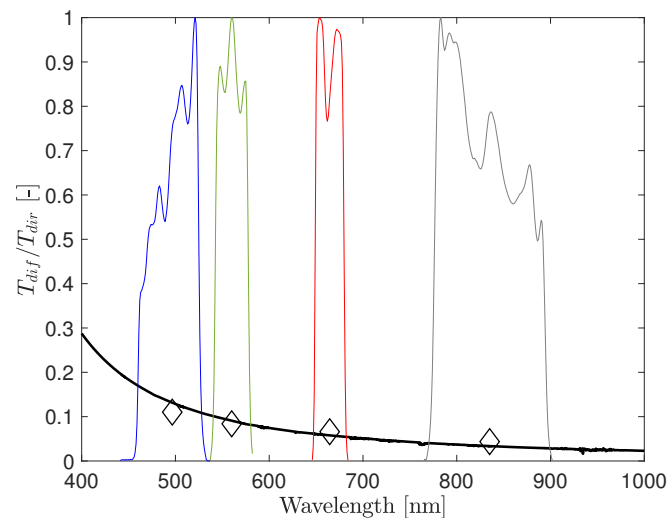


FIGURE 3.6.7: Weighting function q defined in Equation 3.6.6 and applied to the simulated Sen2Cor adjacency correction process.

When comparing Figures 3.6.6 and 3.6.8, many similarities can be found between the performance of the Hybrid and the Sen2Cor adjacency correction strategies. For instance, in the city green belt area or in the harbour, both methods have corrected the excess of light. However, values reported by the Hybrid strategy are higher than values reported by the Sen2Cor strategy. This is especially noticeable in avenues and streets with trees (dashed lines in the Valencia RGB image). In these cases, the Sen2Cor strategy barely corrects for adjacency effects while the level of correction of the Hybrid strategy on these streets is similar to the level achieved in

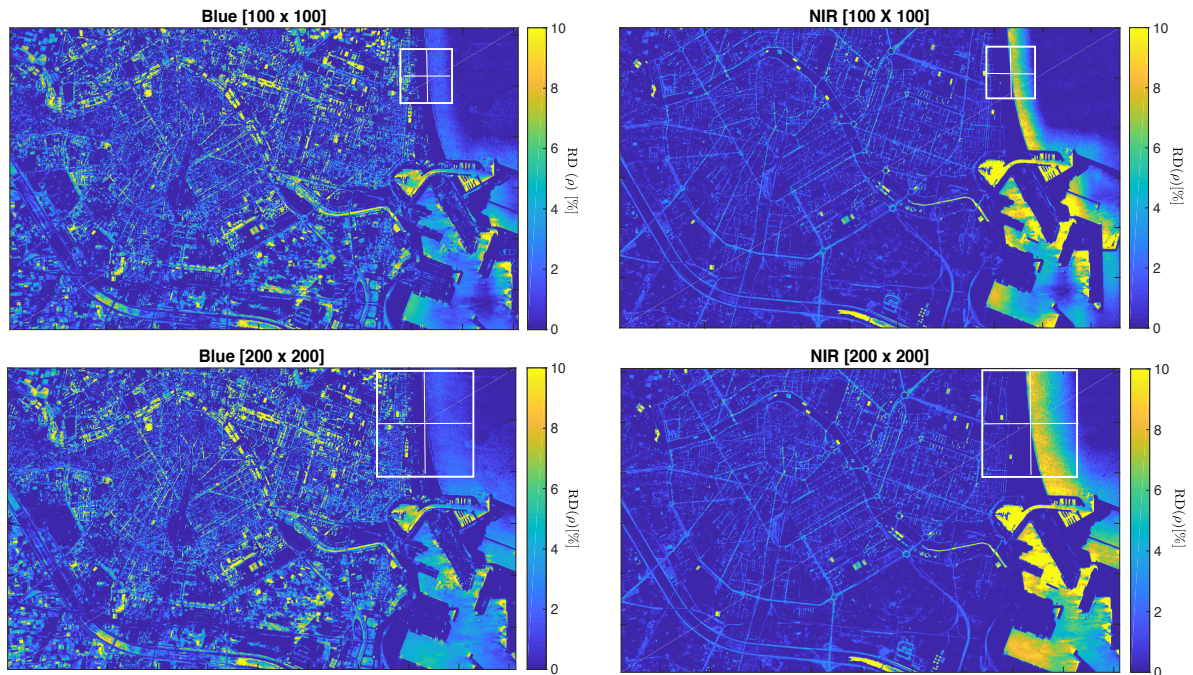


FIGURE 3.6.8: Relative difference in (%) between surface reflectance in the blue and NIR band derived from step 1 and after the Sen2Cor processor using two kernel sizes: 100 x 100 pixels (upper panel), and 200 x 200 pixels (bottom panel).

the vegetated city green belt. Because of the lack of in-situ data, it was not possible to validate the performance achieved by both strategies. Nevertheless, analysing the spatial patterns from Figure 3.6.8 it is possible to infer the Sen2Cor strong dependency on the kernel size used to compute $\bar{\rho}$. In Figure 3.6.8, adjacency effects are strongly corrected in the coast line. This fact was expected due to the existing contrast between sand and sea water reflectance spectra. However, the dependency on the applied kernel size is evidenced between the upper and bottom panels, which corresponds to the kernel's sizes of 100 x 100 pixels and 200 x 200 pixels, respectively.

3.7 Discussion

Atmospheric effects, and especially adjacency contributions, produce an apparent contrast reduction of the image that can be understood as an apparent reduction of the sensor spatial resolution [Kaufman, 1984]. Thus, due to the availability of each time higher spatial and radiometric resolution sensors in the recent years; the urgency to correct these effects becomes critical, not only for water applications but also for land remote sensing. In this context, although this work was framed towards the Ingenio/SEOSat mission; the undertaken study and the proposed methodology are general enough to be applied to any sensor with similar characteristics.

Firstly, atmospheric effects in the spectral domain were evaluated using simulated data for the Ingenio/SEOSat specifications. As expected, this analysis shows the importance of compensating for aerosols effects especially on the blue band, and the influence of the water vapour content in the band situated at NIR. Because of the limited spectral information typically available on high spatial resolution sensors, the use of auxiliary data to estimate the atmospheric state (aerosols, water vapour, temperature profile, etc.) is mandatory. However, although the use of some auxiliary data is required due to the limited spectral information provided by the Ingenio/SEOSat mission, a first attempt to determine the aerosol AOT by exploiting the high spatial resolution available was studied. This strategy was proposed and evaluated using simulated data. The use of simulated data was ideal since both the input or reference AOT to be estimated as well as the instrument characteristics, e.g., instrument MTF, were perfectly known. In essence, the proposed strategy was based on the use of an empirical expression derived from [Kaufman, 1984](#) to model or parametrize the atmospheric blurring effect as a MTF expression. This expression is parametrized by means of four parameters which correspond to the aerosol and molecular optical thickness, τ_a and τ_m respectively; and the height at which the maximum aerosol and molecular concentration was found, H_a and H_r . Nevertheless, in the proposed strategy only one parameter was inverted fixing the others to default typical values. In this case, AOT was the parameter to be estimated due to its driving effect on modelling the atmospheric MTF (See Section 3.4.2 and [Kaufman, 1984](#)). In this study, thanks to the use of simulated data the proposed strategy was focused merely on the inversion of the atmospheric MTF expression. However, when applying this expression to real data where atmospheric and instrument MTFs are completely coupled (Section 3.4.2), then the instrument MTF must be accurately known in order to achieve the performance reported in this Chapter.

The proposed strategy to determine the image AOT was based on quantifying the blurring effect that the atmosphere provokes on the acquired image; in other words, the spatial effects that the application of the atmospheric MTF causes especially on edges between areas with a significant radiometric contrast. Given a particular band, when analysing the transition between pixels with a significant contrast in radiance levels (or in surface reflectance after a per-pixel atmospheric inversion), this can be approximated to a sigmoid function [[Mekler and Kaufman, 1982](#)]. However, this effect could be reverted by deconvolving the image using the appropriate AOT value in the MTF expression. In that case, when the appropriate AOT value is found, the transition between different levels is transformed into a step function. Due to that, the minimization cost function proposed evaluated the flatness on the pixels surrounding the edges or transition zones. As presented in this Chapter, the flatness criteria selected was successful even for noisy data. In this respect, the required number of pixels around the edge to accomplish the flatness criteria with and without noise was also analysed since if a large number of pixels would be required it could become a bottleneck for its application on real data. However, it was verified that even with only 2 pixels, the flatness condition still works for data with and without noise. Consequently, for the Ingenio/SEOSat mission this requirement implies the need to find homogeneous areas of 20 m x 20 m size, which seems a realistic condition.

It is worth noting that the application of the above-mentioned deconvolution strategy focussed mainly on the AOT characterization assuming the instrument MTF is perfectly known.

However, this strategy does not represent a full atmospheric correction methodology itself. In order to fully atmospherically correct the future Ingenio/SEOSat images, not only the aerosol presence requires to be characterized but also the water vapour content, the Digital Elevation Model (DEM), the illumination and acquisition geometry, the vertical temperature profile, etc. In addition, as evaluated in this Chapter, due to the high spatial resolution that the Ingenio/SEOSat mission will provide, it is specially relevant to correct for atmospheric effects in the spectral domain, but also in the spatial domain. All these reasons motivated the formulation of an atmospheric correction strategy, here called as **Hybrid**. The hybrid strategy combines: (1) a per-pixel atmospheric RTM inversion technique using auxiliary data to characterize the atmospheric state, with (2) an image deconvolution process to correct for adjacency effects. Regarding the required atmospheric auxiliary data for (1), given the Ingenio/SEOSat coverage, mainly Europe and Ibero-America (See Table in Appendix A.1), these areas are simultaneously covered by the global measurement aerosol network Aeronet [Holben *et al.*, 1998]. In particular, Aeronet covers the Spanish territory with around 30 stations that can provide essential aerosol parameters such as the AOT, the Ångström exponent, or even the water vapour content. In addition, maps of water vapour and aerosol content are also provided by the ECWMF <https://www.ecmwf.int/> and can also be used as a valuable auxiliary data providing information about the spatial distribution. Note that the use of auxiliary information, specially regarding those parameters related to the aerosol content, makes the application of any prior cloud masking process less demanding. Although not studied in this Chapter, aerosol characterization can be significantly affected if some cloudy pixels are not properly masked out. Once a per-pixel inversion is performed, the first derived surface reflectance estimation is used to recompute the solar irradiance at surface level (\bar{E}). This correction applied to the solar irradiance at surface level is performed to improve the initial approximation assumed in which the acquired radiance at sensor level is linearly related to the surface reflectance, i.e., ignoring the contribution of the spherical albedo term.

Then, in a second step, a new surface reflectance corrected for adjacency effects is derived by using the recomputed \bar{E} and by simultaneously deconvolving the image according to the appropriate atmospheric MTF. While most of the existing atmospheric correction algorithms also account for the correction of the adjacency effects as a second step [Richter, 1996; Richter and Schlöpfer, 2007b; Guanter, 2006], the main difference with the Hybrid strategy is that the resulting surface reflectance is not derived by adding or subtracting any averaged surface reflectance contribution, but by applying the atmospheric MTF deconvolution as part of the atmospheric inversion process. Efforts to find an empirical or analytical expression to model atmospheric spatial effects over uniform and non-uniform surfaces were developed for first time in the 80's [Kaufman, 1982; Mekler and Kaufman, 1982; Kaufman, 1984, 1989]. One of the advantages of deconvolving the image using the atmospheric MTF expression against strategies that average the surface reflectance in a certain box or kernel is that the resulting adjacency corrected surface reflectance does not become so dependent on the size of the kernel applied, which can become critical on seashores [Sterckx *et al.*, 2011], as observed in Section 4.6. In addition, strategies based on averaging surface reflectance in a certain kernel are typically weighted by a factor, which accounts for the ratio between the diffuse and direct transmittance [Richter, 1996]. This

factor merely gives an idea about the role of the scattering process given a certain atmospheric state. However, while the impact of adjacency effects is mainly related to the aerosol concentration and their vertical distribution, molecular concentration and vertical distribution in the atmosphere also play a key role [Kaufman, 1984; Minomura *et al.*, 2001]. In general, the more AOT the stronger aerosol scattering effects and therefore the stronger contribution of adjacency effects. However, while for high AOTs or hazy atmospheres, aerosol atmospheric MTF tend to be dominant compared to molecular MTF, for clear atmospheres the molecular MTF effect is dominant and adjacency effects from distant pixels becomes more significant [Reinersman and Carder, 1995]. The Hybrid strategy was evaluated using the 10 m spatial resolution bands of the Sentinel-2 mission and validated against the atmospheric correction performed by the Sen2Cor processor. Particularly, one sample of an image covering the urban area of the Valencia city (39.45° N, 0.35° W, Spain) was used as example. First, estimated surface reflectance from both methods were compared. Although derived surface reflectance spectra were consistent in the green and red bands; major differences were found in the blue and NIR bands. These discrepancies occurred because the contrasting AOT values derived: (1) from Sen2Cor processor, and (2) from Aeronet (used as input in the Hybrid strategy). Since having contrasting input values makes the assessment of the different adjacency correction strategies challenging, the method used by Sen2Cor to correct for adjacency effects was externally implemented. This way, the adjacency correction process from both methods were compared under the same conditions, i.e., taking the same initial surface reflectance data. When analysing changes in surface reflectance before and after the application of the adjacency correction, as expected, both strategies show similar spatial patterns. Basically dark surfaces become darker as well as bright surface become slightly brighter. However, while both strategies reach at the blue band relatives differences in reflectance around 10 % on main vegetated areas of the city, the Hybrid method also reaches these values on narrow streets from the old city center that are also dark according to the RGB image shown. Conversely, adjacency correction in narrow streets from the city center by using the strategy implemented in Sen2Cor, hardly reaches a correction of around 3 % in reflectance. While simply applying a strategy that averages the estimated surface reflectance in a certain kernel can partly compensate for adjacency effects, it seems that the application of the atmospheric MTF deconvolution better takes into account these effects on narrow dark streets that are closely surrounded by brighter buildings. In addition, a strong dependency on the size of defined kernel was clearly observed in the seashore of the resulting surface reflectance images after applying the Sen2Cor adjacency correction, but not in the Hybrid strategy.

3.8 Conclusions

In this chapter atmospheric effects in the spectral and spatial domain have been analysed for the Ingenio/SEOSat space mission. Due to the limited spectral information available (4 multispectral and 1 panchromatic bands), and the high spatial sampling interval (10 m and 2.5 m for the multispectral and the PAN, respectively), emphasis was on the spatial domain. On the one hand, the possibility to exploit the spatial information to determine the aerosol load

was analysed. In case the instrument Modulated Transfer Function (MTF) is known, it is possible to determine the Aerosol Optical Thickness (AOT) by deconvolving the image applying different atmospheric MTFs and analysing pixels around edges between areas with a high radiometric contrast. On the other hand, when the instrument MTF is not accurately known and auxiliary information regarding the atmospheric state is available, in this Chapter a fully atmospheric correction strategy was proposed and evaluated with Sentinel-2 data. This technique, called Hybrid, combines: (1) a classical per-pixel atmospheric correction by inverting a radiative transfer model using auxiliary information as input, and (2) a compensation of the adjacency effects by deconvolving the image using the atmospheric MTF. Surface reflectance derived with the Hybrid method has been validated against surface reflectance provided by the Sen2Cor ESA's Toolbox, showing in general good agreement. In addition, when comparing the Sen2Cor and the Hybrid adjacency correction methods, the results of the Hybrid method show less dependency to the size of the used kernel.

4

A proposed atmospheric correction algorithm for the FLEX/Sentinel-3 tandem space mission

Contents

4.1	Abstract	72
4.2	Introduction	73
4.3	FLORIS spectral sensitivity analysis to detect SIF	75
4.4	The two-steps algorithm	81
4.5	Database simulation	92
4.6	Results	101
4.7	Discussion	107
4.8	Conclusions	111

*This chapter is based on the work developed by **Neus Sabater** under the :*

 **FLEX- PERFORMANCE ANALYSIS AND REQUIREMENTS CONSOLIDATION STUDY**
(PARCS) ESTEC contract RFQ 3-133397/11/NL/CBi
 **FLEX- FLEX-BRIDGE STUDY** ESTEC contract RFP IPL-PEO/FF/If/14.687

4.1 Abstract

ESA's 8th Earth Explorer, the FLuorescence Explorer (FLEX) space mission, is dedicated to deliver among other biophysical parameters, estimates of Solar-Induced chlorophyll Fluorescence (SIF) of terrestrial vegetation to quantify the photosynthetic activity at a global scale. A challenge hereby is that the SIF signal emitted between 650–750 nm represents only a 5% of the signal reaching the sensor. To capture this subtle signal, FLEX will be equipped with a very fine spectral resolution imaging spectrometer, named FLORIS, which operates in the 500–780 nm spectral window. The FLEX mission concept proposes to disentangle the SIF signal from solar irradiance reflected at Top Of Canopy (TOC) level by mainly exploiting the telluric O₂ absorption bands but also using the spectral information provided in the entire spectral range in which SIF is emitted. To do so, all the atmospheric effects that can disturb the SIF retrieval process at TOC level must be previously characterized and corrected. Following this aim, FLEX was designed as a tandem mission concept with the ESA's Sentinel-3 satellite. The tandem concept allows increasing the spectral information and the number of acquisition geometries to be used for atmospheric characterization purposes. In this chapter, the FLEX/Sentinel-3 mission concept is introduced together with a spectral analyses dedicated to evaluate the potential spectral sensitivity to detect SIF on the different spectral regions covered by FLORIS and according to the mission specifications. Then, an atmospheric strategy based on the exploitation of the Sentinel-3 is proposed and evaluated under a theoretical framework. Results and limitations about the proposed strategy are discussed with emphasis to the hypothetical exploitation of FLORIS data to improve the atmospheric characterization process and consequently SIF estimations.

4.2 Introduction

The ESA's 8th Earth Explorer space mission, the FLuorescence EXplorer (FLEX), is the first satellite specifically designed to quantify the photosynthetic activity and plant stress by mapping, among other biophysical parameters, vegetation Sun-Induced Chlorophyll Fluorescence (SIF) [European Space Agency, 2015a]. SIF are photons of red and far-red light that are emitted by chlorophyll-a pigments in parallel to the photosynthetic processes [Porcar-Castell *et al.*, 2014]. In essence, by absorbing photons through photosynthetic pigments, mainly chlorophyll and carotenoids; these pigments reaches an unstable excited energetic state that returns into its base energetic level by means of four competitive de-excitation mechanisms: (1) regulated heat dissipation, (2) photosynthesis, (3) SIF emission, and (4) constitutive heat dissipation. Figure 4.2 (a) illustrates the percentage of absorbed light which is typically dissipated into one of the early mentioned dissipation mechanisms.

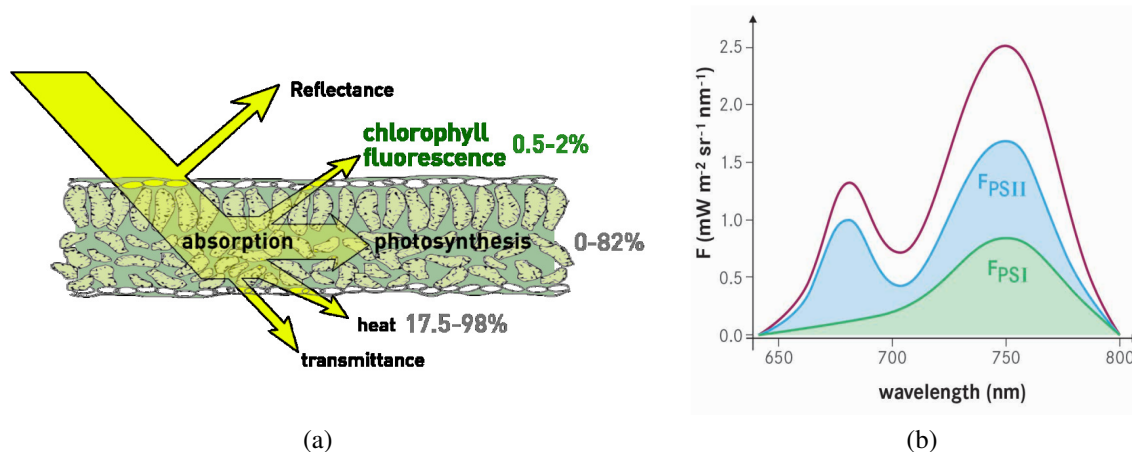


FIGURE 4.2.1: (a) Scheme of light-leaf interaction and energy dissipation mechanisms. (b) Illustration showing the general SIF spectral shape and the contribution of the different photosystems (Original image from European Space Agency, 2015a).

The measurement of SIF can thus result into a sensitive indicator of the efficiency of photosynthetic electron transport – among other processes – and thus serves as a proxy for actual photosynthetic light conversion [Porcar-Castell *et al.*, 2014]. SIF has been also demonstrated to be a useful early indicator for stress detection, even before damage is shown through changes in the reflected light, e.g., [Corp *et al.*, 2003; Rascher *et al.*, 2009; Van Wittenberghe, 2014]. In the last decade, SIF has been measured at a global scale starting from measurements acquired at high-spectral resolution by the Japanese Greenhouse Gases Observing Satellite (GOSAT) mission [Joiner *et al.*, 2011; Frankenberg *et al.*, 2011b; Guanter *et al.*, 2012], or from instruments such as the Global Ozone Monitoring Experiment-2 (GOME-2), instruments on board the Meteorological Operational Satellites MetOp-A, and MetOp-B, SCIAMACHY on ENVISAT, and the Orbiting Carbon Observatory-2 (OCO-2) [Frankenberg *et al.*, 2011a,b, 2012, 2014; Joiner *et al.*, 2012, 2013, 2016b; Guanter *et al.*, 2010; Köhler *et al.*, 2015a; Wolanin *et al.*, 2015].

Therefore, all these global SIF maps evidence the proof that the weak SIF signal can be measured and detected from space. However, the challenge thereby is how this measured SIF signal can be used as a real proxy to photosynthesis.

Although the photosynthetic apparatus is a highly complex structure, the emitted SIF spectrum is well known. It is characterized by two broad band peaks with maxima located (1) on the red (near 685–690 nm), and (2) on the far-red (near 730–740 nm) (see Figure 4.2 (b)). As illustrated in this figure, the total emitted SIF results from the contribution of SIF emitted by the Photosystem I (or PSI) and Photosystem II (PSII) [Taiz and Zeiger, 2002].

The FLEX mission is proposed as a tandem mission concept with the ESA's Sentinel-3 (S3) satellite [Moreno *et al.*, 2014; Kraft *et al.*, 2012; Drusch *et al.*, 2017]. The tandem concept, illustrated in Figure 4.2.2, responds to the need to simultaneously monitoring the atmospheric state through the S3 data, while covering the spectral range in which SIF is emitted at high spectral resolution. To do so, the Fluorescence Imaging Spectrometer FLORIS on board FLEX, will measure TOA radiance between 500 and 800 nm at very high spectral resolution (with a bandwidth between 0.1 nm and 2 nm), providing images with a 150 km swath and 300 m pixel size.

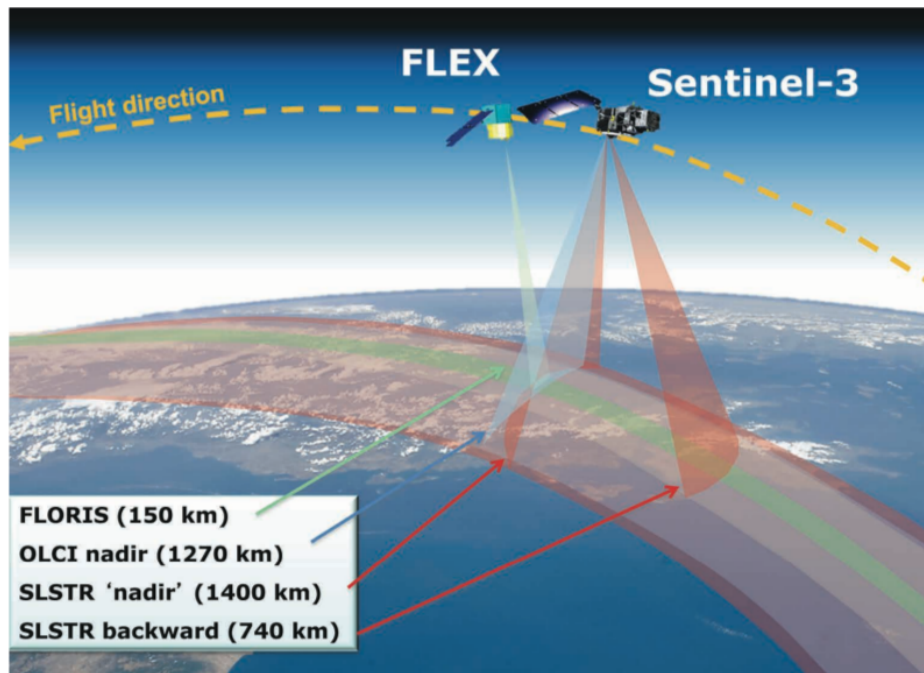


FIGURE 4.2.2: FLEX Sentinel-3 tandem mission concept. Figure originally from ESA.

TOA radiances acquired by imaging spectrometers on board satellites are always subject to absorption and scattering effects by atmospheric gases and aerosols [Deschamps *et al.*, 1980]. To enable using imaging spectrometer data for quantitative remote sensing of land surfaces and ocean color, these atmospheric effects must be carefully addressed. The atmospheric correction problem on passive optical spectrometers has been known for years [Tanre *et al.*, 1981, 1983]. However, this process requires special attention in the particular case of FLEX. To disentangle

SIF from the solar radiation reflected by the surface and the atmosphere, FLEX will measure the infilling caused by the fluorescence signal mainly exploiting the O₂-A and O₂-B regions. According to FLEX retrieval strategy, two main reasons drive the atmospheric correction process. First, the SIF signal represents only a small fraction (1 – 5% in the near-infrared) of the total TOA signal [Meroni *et al.*, 2010]. Secondly, in the last years some studies [Frankenberg *et al.*, 2011a; Guanter *et al.*, 2010] have revealed the impact of atmospheric effects, especially of aerosols, on fluorescence retrievals focused in the O₂-A region. To perform a complete characterization of atmospheric effects, FLEX will make use of the spectral range covered by the Ocean and Land Colour Instrument (OLCI) and the dual viewing geometry provided by the Sea and Land Surface Temperature Radiometer (SLSTR), both on board S3 satellite. In Figure 4.2.3 different spectral ranges covered by each of the instruments involved in the FLEX mission activities are highlighted.

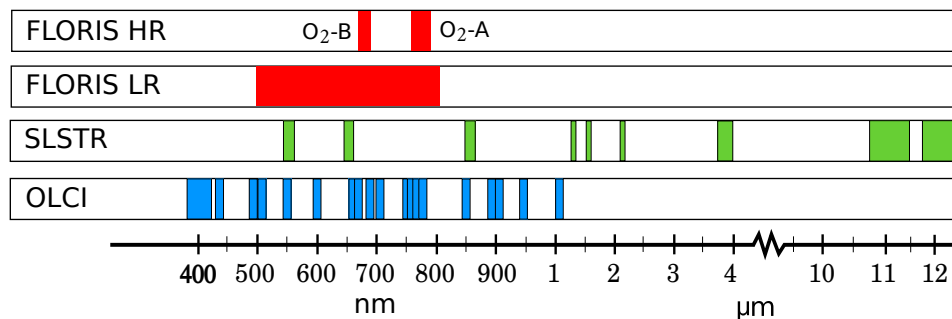


FIGURE 4.2.3: Comparison of FLORIS and Sentinel-3 spectral ranges.

This chapter is first dedicated to analyse the spectral sensitivity of the FLORIS spectrometer to SIF detection, highlighting pros and cons of different spectral ranges. Then, the remainder of the chapter will be dedicated to assess the performance of the proposed so-called **two-steps method** to estimate SIF from FLORIS Level-1b data. As its name indicates, the **two-steps method** involves: (1) to atmospherically correct Level-1b data to obtain radiance at surface level, and (2) to apply a SIF retrieval strategy to disentangle emitted SIF from reflected solar irradiance. The performance assessment of the proposed methodology was developed through the generation of a FLEX-like database (FLEX-DB) by coupling simulated spectra from two radiative transfer models (for surface and atmosphere). Finally, strengths and weaknesses of the proposed strategy are discussed at the end of this chapter, providing a guideline for improvements addressed in Chapter 5.

4.3 FLORIS spectral sensitivity analysis to detect SIF

When retrieving SIF from space, the challenge lies in disentangling such a subtle signal from the total radiance reaching the sensor. Due to that, current satellite missions that retrieve SIF at a global scale, such as GOSAT, Global Ozone Monitoring Experiment (GOME) or Orbiting Carbon Observatory (OCO) [Joiner *et al.*, 2011, 2012; Guanter *et al.*, 2012; Khosravi, 2012;

Köhler *et al.*, 2015a,b; Guanter *et al.*, 2013; Joiner *et al.*, 2013, 2016a], exploit by means of different techniques information embedded in solar and/or telluric absorption bands. In these regions the contrast between the total radiance at TOA and the emitted SIF, is reduced making its detection easier. Figure 4.3.1 shows typical regions used to detect SIF.

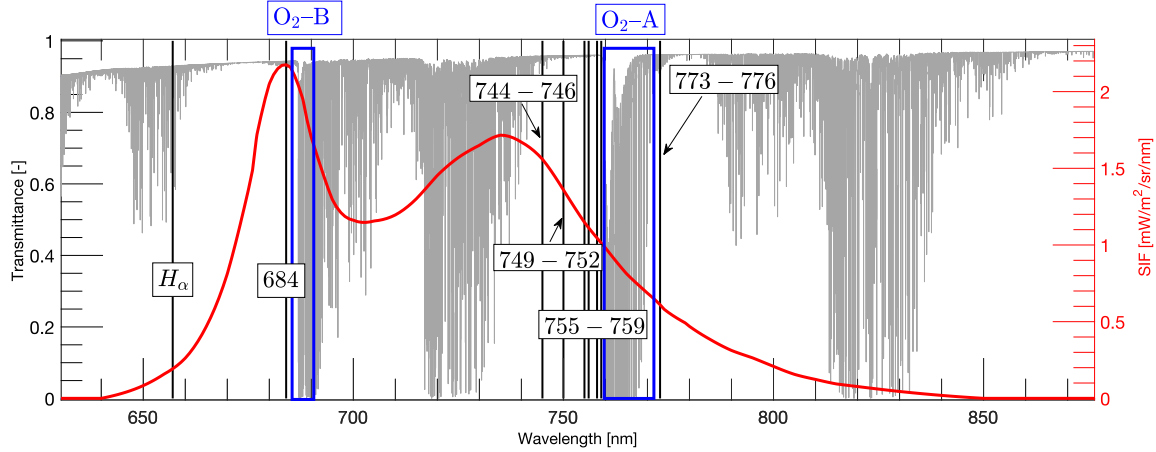


FIGURE 4.3.1: Typical SIF spectral shape emitted at TOC (red). Upward atmospheric transmittance spectrum at high spectral resolution (0.1 cm^{-1}) (gray). Solar and telluric typical absorption regions used to detect SIF are labelled in the Figure. Water vapour absorption regions are excluded due to the high temporal and spatial variability of this gas.

This section focusses on analysing the spectral sensitivity to detect SIF on the range covered by the FLORIS instrument overlapped with the range where SIF is emitted; and according to FLORIS instrument specifications, i.e., Spectral Sampling Interval (SSI) and Spectral Resolution (SR). As highlighted in Figure 4.3.1, evaluated regions can be classified into: solar absorption regions (H_{α} , 684, 744–746, 749–752, 755–759, 773–776, 776–779), and telluric oxygen features (O_2 -B and O_2 -A). Note that other terrestrial absorption bands, such as the water vapour continuum region, have been excluded due to the high spatial and temporal variability of this gas.

The sensitivity to detect SIF on TOA radiance was analysed based on simulated data using the surface reflectance and SIF spectra assumed as a mean reference value in the FLEX mission studies [Drusch, 2016]. To simulate TOA radiance, the atmospheric RTM MODTRAN was used considering a Mid-latitude summer model of atmosphere, with a rural aerosol mixture, and aerosol optical thickness (AOT) of 0.2, Mie aerosol phase function, total column water vapour of 1.5 g/cm^2 , and following Equation 4.3.1:

$$L_{TOA} = L_0 + \frac{(E_{TOC}\rho + \pi F)T^{\uparrow}}{\pi(1 - S\rho)} \quad (4.3.1)$$

where, L_0 is the atmospheric path radiance, E_{TOC} is the total solar irradiance at surface level, T^{\uparrow} is the total atmospheric upward transmittance, S is the spherical albedo, and ρ and F are the surface reflectance and the emitted SIF, respectively. The interrogation technique published in Guanter *et al.*, 2009 was followed to derive all the atmospheric transfer functions.

FLORIS spectral sensitivity to detect SIF is shown in Figure 4.3.2 as the ratio between SIF and the total radiance both at TOA level, i.e., SIF/L_{TOA} .

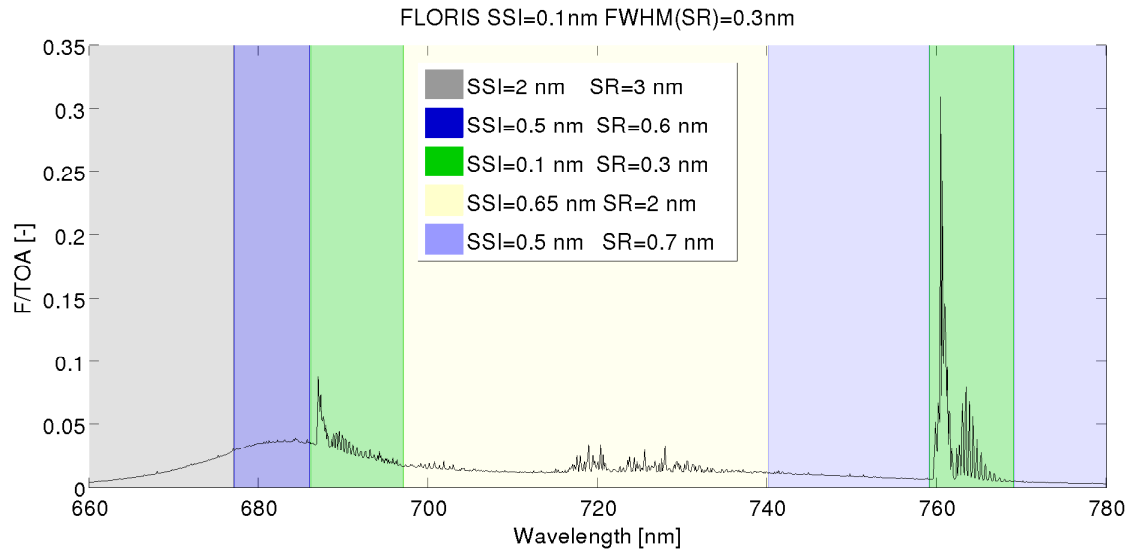


FIGURE 4.3.2: Ratio between emitted SIF and TOA radiance L_{TOA} reaching the sensor.

To better analyse the spectral sensitivity of each of the absorption lines and regions, Figures 4.3.3, 4.3.4, and 4.3.5 zoom the regions considered here, evaluating the SIF/L_{TOA} ratio at different spectral resolutions: (1) the highest spectral resolution provided by the atmospheric radiative transfer model used, (2) the nominal spectral resolution of the spectrometer used at each spectral region (without binning the signal), (3) the spectral resolution provided by the instrument (including binning). Note the different y-axis scale used at each figure.

On the one hand, Figure 4.3.3 is centred on the solar absorption lines located at H_{α} , 684, 744-746, 749-752, 773-776, 776-779, from (a-f) respectively. While for the solar absorption line located at 684 nm the fraction of emitted SIF against TOA radiance represent between 3% to 3.6% (for the FLORIS SR), the remaining absorption regions hardly reach 1% for the 744-746 nm, 749-752 nm; or even 0.4%, in case of H_{α} , 773-776 nm, and 776-779 nm. In addition, as can be observed in this Figure, most of the presented spectral regions or absorption lines of interest are extremely narrow, making its detection significantly dependent on the accuracy achieved on the central wavelength location. Most of these spectral regions are also covered by the FLORIS Wide Band Spectrometer (WBS), making SIF detection even more challenging. However, despite the narrow bands, the high Signal to Noise Ratio (SNR) of FLORIS spectrometer at the region covered by the solar absorptions 744-746, 749-752, (linear from 510 to 1050) can facilitate SIF detection.

On the other hand, Fraunhofer solar bands located in the interval from 754-759 are analysed in Figure 4.3.4. Similarly to the spectral regions studied in Figure 4.3.3, these absorption lines are narrow, making SIF detection significantly dependent on the central wavelength location. Conversely, these spectral region are all covered by the FLORIS Narrow Band Spectrometer (NBS) accounting with a high SNR (linear to 1050).

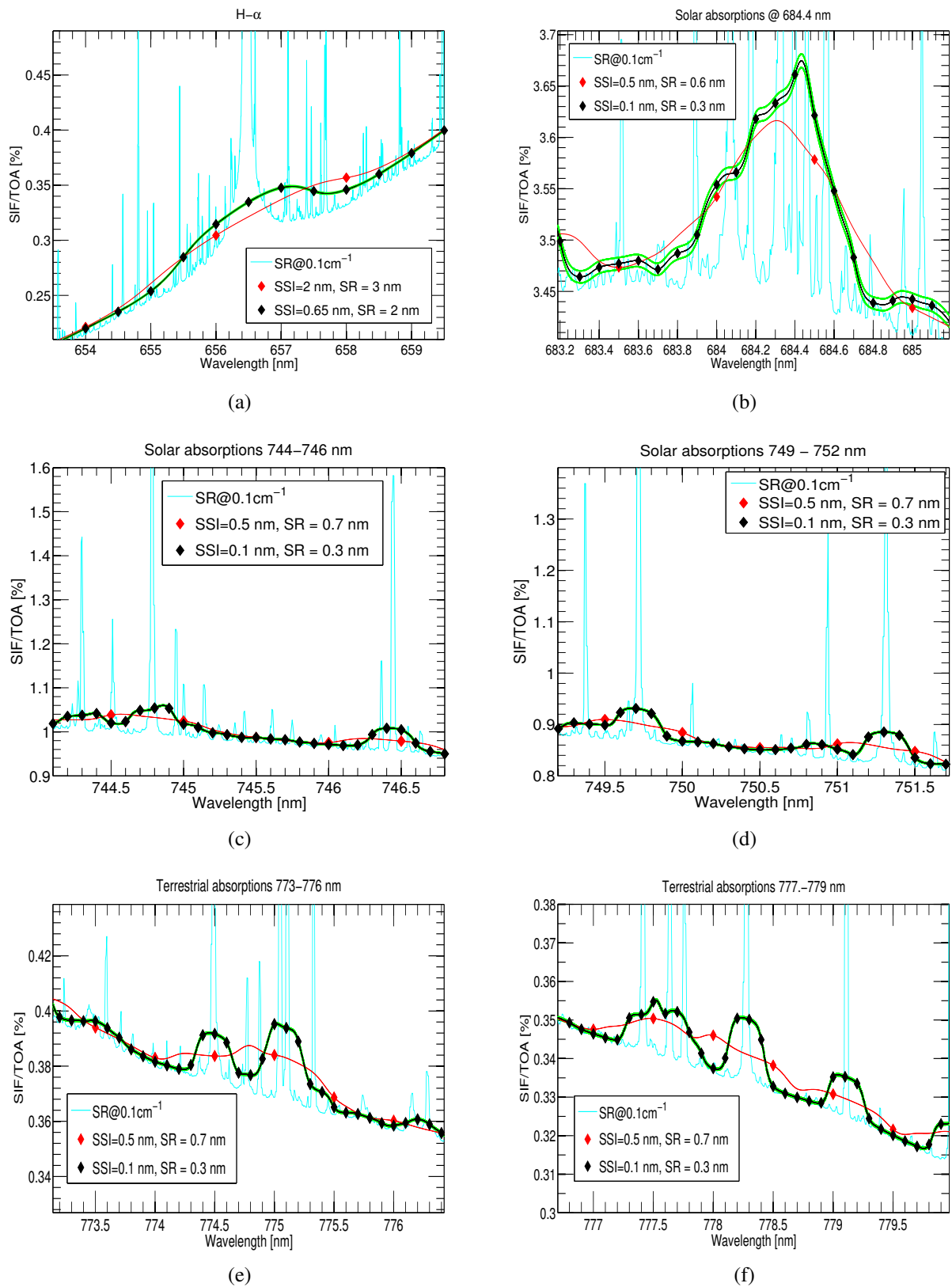


FIGURE 4.3.3: SIF/L_{TOA} ratio analysed for the following spectral regions of interest: (a) H α , (b) 684 nm, (c) 744-746 nm, (d) 749-752 nm, (e) 773-776 nm, (f) 777-779 nm.

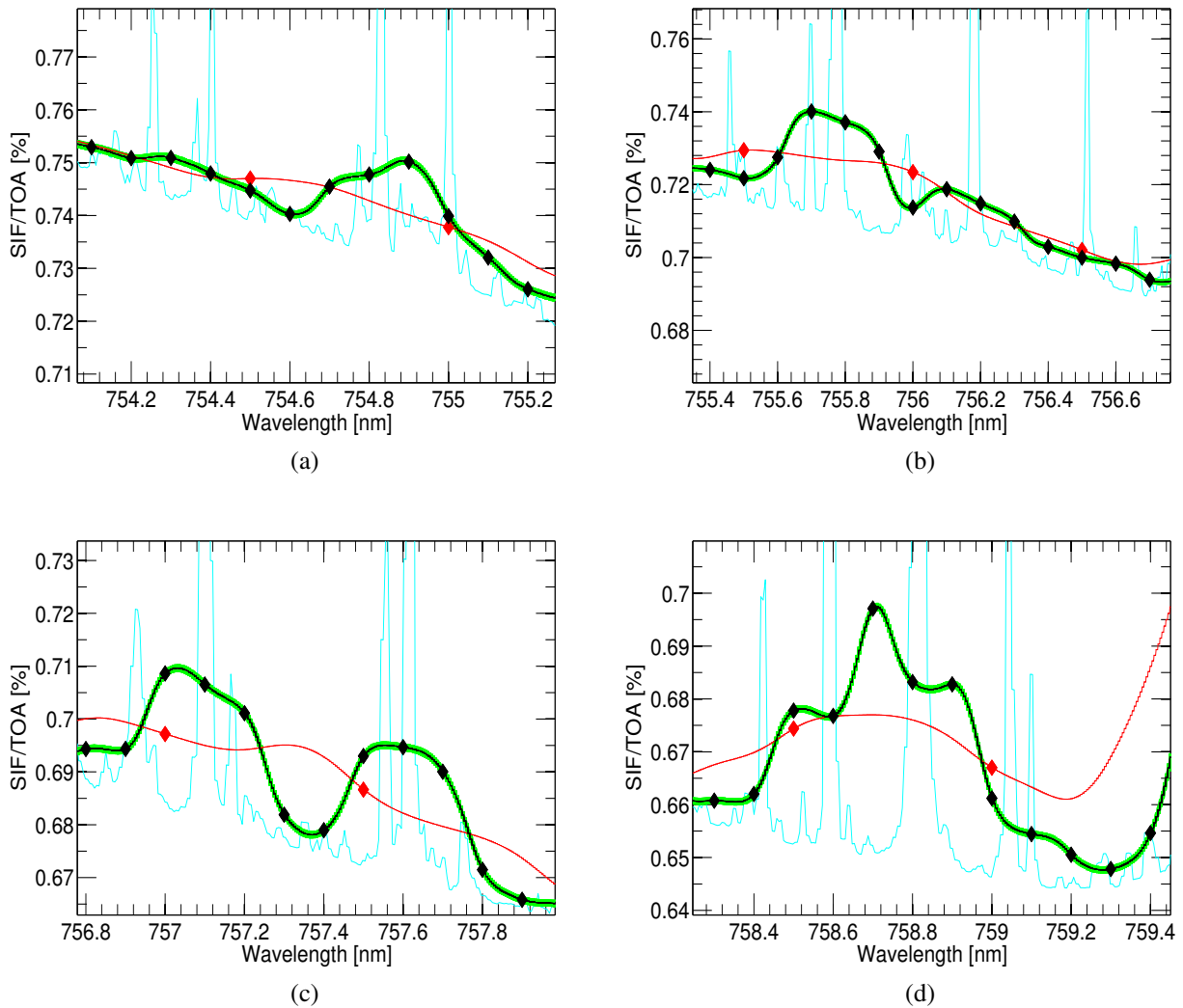


FIGURE 4.3.4: SIF/L_{TOA} ratio analysed for the following spectral regions of interest: (a) 754-755, (b) 755-756 nm, (c) 756-757.9 nm, (d) 758.3-759.4 nm.

Finally, FLORIS sensitivity to detect SIF at the terrestrial O_2 -B and O_2 -A regions is shown in Figure 4.3.5. As can be observed, SIF ratio reaches values of 4% and 2.5% for the O_2 -B and O_2 -A, respectively. Without a doubt, these regions presents the major sensitivity to detect SIF (also presented in Verrelst *et al.*, 2016b). In addition, especially at the O_2 -A absorption region, this oxygen feature is composed by a primary (until ~ 762 nm) and a secondary (from 762 to 770 nm) oxygen absorption spectral region, covering around 9 nm width. These secondary absorption region, despite being less sensitive to SIF detection can play a key role for the instrument characterization (essential to guarantee a proper SIF estimation). However, when using the oxygen absorption regions to detect SIF, atmospheric effects and particularly aerosol scattering, has to be accurately characterized, as pointed out by Frankenberg *et al.*, 2011a. In addition, oxygen absorption regions also depend on temperature and pressure conditions, which should also be taken into account when retrieving SIF by resolving these regions [Pierluisi and

Chang Mind, 1986].

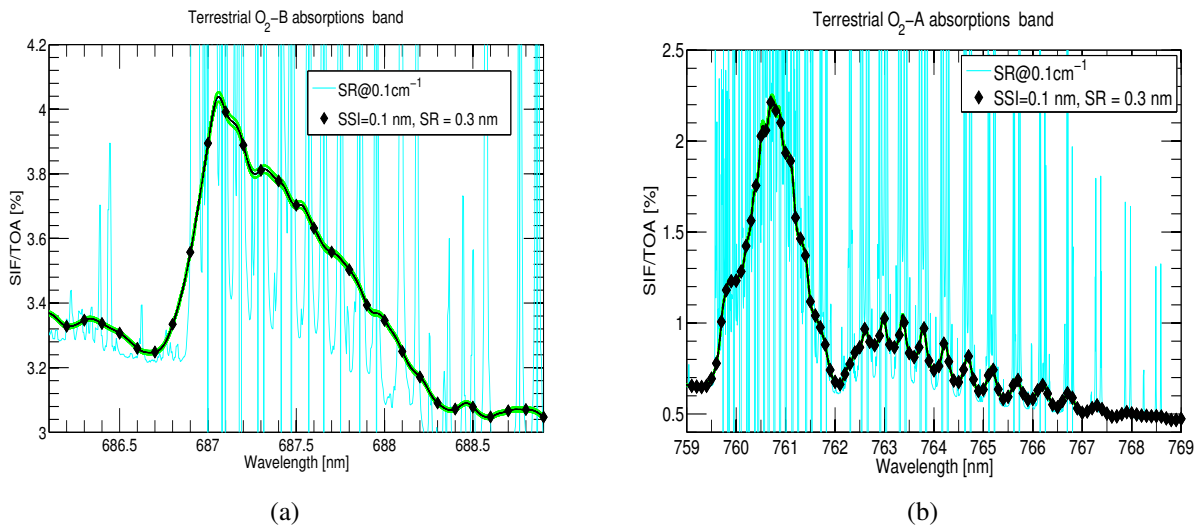


FIGURE 4.3.5: SIF/L_{TOA} ratio analysed for the following spectral regions of interest: (a) O₂-B region, (b) O₂-A region

It is worth noting that aerosol transmittance affects the complete spectral interval in which SIF is emitted, and not only oxygen absorption regions. As observed on Figure 4.3.6, changes in TOA radiance generated by changes on the Ångström exponent value, i.e., related to the spectral AOT dependency and aerosol size; impacts the complete SIF spectral interval. However, in strong absorption features, such as the water vapour and oxygen absorption regions, spectral distortions caused by changes in the Ångström exponent are significantly higher than in the solar absorption lines.

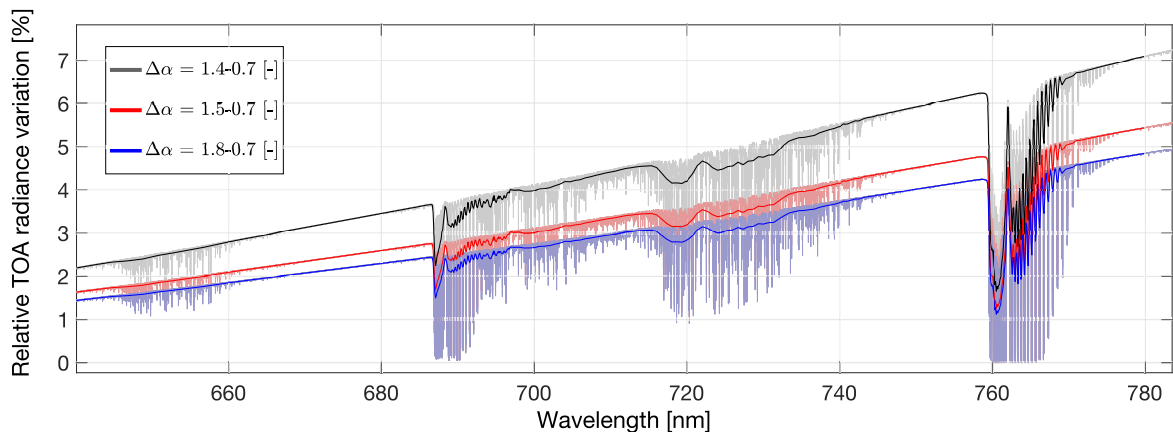


FIGURE 4.3.6: Relative difference [%] in TOA radiance caused by changes in the Ångström exponent (α). TOA radiance simulated by means of Equation 4.3.1 without SIF emission. TOA radiance percentage related to changes in α of 1.4-0.7, 1.5-0.7 and 1.8-0.7 corresponding to black, red and blue colors, respectively.

Therefore, from the above FLORIS spectral sensitivity analysis to detect SIF some highlights are here summarized:

- FLORIS fully covers the SIF emission spectral range. However, FLORIS has been specifically designed to monitor spectral regions of interest, such as the oxygen absorption regions; with high SR, SSI, and SNR. Main reason to do so is justified by the analyses here presented showing that telluric O₂ absorption features present a maximum sensitivity to detect SIF.
- SIF can be detected at any wavelength inside the spectral interval of 650–800 nm. However, the narrower and weaker the absorption lines are, the more challenging its detection.
- When using the oxygen absorption bands to estimate SIF, atmospheric effects must be carefully identified and corrected, especially aerosols scattering effects.

In line with these highlights, the proposed algorithm to estimate SIF from the FLEX/S3 tandem space mission Level-1b data will be based on the exploitation of the spectral range of 650–800 nm, but paying special attention to oxygen absorption regions. Consequently, atmospheric effects and especially aerosol scattering must be treated carefully. In the next section the proposed **two-steps method** is presented.

4.4 The two-steps algorithm

The so-called **two-steps method** is here described and applied to a simulated FLEX-DB. It is called **two-steps method** due to it is composed by two main modules: (1) The atmospheric correction (**AC**), and (2) the SIF retrieval strategy. Both modules are highlighted in gray in the high level scheme of Figure 4.4.1.

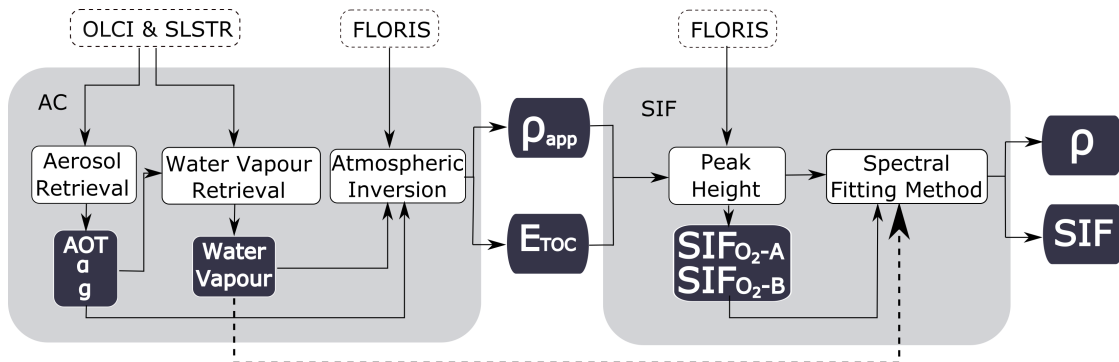


FIGURE 4.4.1: Scheme of the **two-steps method** proposed to estimate SIF from TOA radiance.

This way, previous experience in both modules can be combined into a single algorithm. On the one hand, since FLEX is designed as a tandem mission with S3, the proposed atmospheric correction algorithm is based on previous experience with similar data from the MERIS and the AATSR instruments (detailed in Section 4.4.1). On the other hand, SIF retrieval strategies to disentangle SIF from reflected light at surface level have been developed for years. Thus, in this case the combination of two techniques to estimate SIF, first at the oxygen absorptions and secondly to the entire spectra is here presented (Section 4.4.2).

4.4.1 Atmospheric algorithm description

The atmospheric correction scheme is based on the synergy atmospheric correction algorithms developed for MERIS and the AATSR [North *et al.*, 2009b; Guanter, 2006], predecessors of S3's, OLCI and SLSTR, instruments. The proposed method relies on the inversion of the parameters that characterize the atmospheric status by relying on predefined MODTRAN-based atmospheric Look-Up-Tables (LUTs) without making use of prior information about the atmosphere.

The radiance reaching the sensor at satellite level can be simplified as the contribution of three different fluxes (Figure 4.4.2) [Vermote *et al.*, 2006]:

1. The scattered light from the atmosphere or path radiance (thick dashed-dotted line).
2. The reflected light from the observed target which is transmitted to the sensor (solid line).
3. The light coming from multiple reflections between the surface and the atmosphere, not necessarily produced at the observed target, but finally reaching the sensor (thin dashed line).

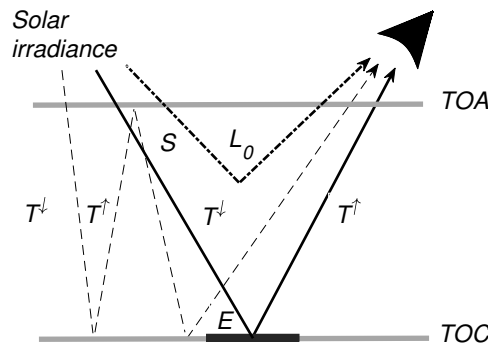


FIGURE 4.4.2: Contribution of distinct fluxes acquired at satellite level assuming a Lambertian surface reflectance behaviour. The thick black area at TOC level represents the observed target.

Assuming a Lambertian surface reflectance (ρ) the radiance reaching the sensor (L_{sen}) can consequently be formulated as Equation 4.4.1:

$$L_{sen} = L_0 + \frac{E}{\pi} T^\uparrow \rho + \frac{E}{\pi} S T^\uparrow \rho^2 + \frac{E}{\pi} S^2 T^\uparrow \rho^3 + \dots, \quad (4.4.1)$$

where L_0 is the path radiance (scattered light from the atmosphere), E is the total solar irradiance reaching the surface, T^\uparrow is the total upward transmittance and S is the atmospheric spherical albedo, which accounts for the reflections occurred from the atmosphere to the surface. Likewise, E can be understood as the contribution of the solar irradiance diffusely transmitted to the surface (E_{dif}) and the solar irradiance directly transmitted to the surface (E_{dir}), corrected by the solar zenith angle (θ):

$$E = E_{dir} \cos(\theta) + E_{dif} \quad (4.4.2)$$

Equation (4.4.1) is mathematically known as a geometrical series expression, which converges into Equation (4.4.3):

$$L_{sen} = L_0 + \frac{E\rho T^\uparrow}{\pi(1 - S\rho)} \quad (4.4.3)$$

Furthermore, in the particular case of vegetation, the SIF emission (F in the formulation for brevity) can be included in Equation (4.4.3) as an additional source of energy. Since SIF is orders of magnitude lower than the TOA radiance reaching the sensor, it can be physically considered as a small perturbation of Equation (4.4.3):

$$L_{sen} = L_0 + \frac{(\frac{E}{\pi}\rho + F)T^\uparrow}{(1 - S\rho)} = L_0 + \frac{E\rho_{app}T^\uparrow}{\pi(1 - S\rho)} \quad (4.4.4)$$

where ρ_{app} is the so-called apparent reflectance defined as Equation 4.4.5, which accounts for the reflectance and the SIF emission normalized by the solar irradiance at surface level:

$$\rho_{app} = \rho + \frac{\pi F}{E} \quad (4.4.5)$$

As it will be later demonstrated in Chapter 5, the term ρ , which is coupled with the atmospheric spherical albedo S in the denominator of Equation 4.4.4, can also be approximated by ρ_{app} . This approximation only marginally impacts the atmospheric characterization and the surface apparent reflectance retrieval, but it decreases the number of unknown variables in Equation 4.4.4.

Then, to invert ρ_{app} from at-sensor radiance, atmospheric functions at high spectral resolution, i.e., L_0 , S , T , E_{dir} and E_{dif} should be convolved according to the Instrumental Spectral Response Function (ISRF). However, Equation 4.4.4 cannot be directly used to derive surface apparent reflectance since the product of spectral convolutions differs from the spectral convolution of products, i.e., $\langle a * b \rangle \neq \langle a \rangle * \langle b \rangle$, especially important in spectral ranges inside absorption bands. More details about this inequality for the SIF retrievals can be found in Chapter 5. In order to solve this inequality, the inversion is performed over the original series

expansion expression truncated to second order (see Equation 4.4.6):

$$L_{TOA} = \int_{\lambda_i}^{\lambda_f} (L_0 * f) d\lambda + \frac{1}{\pi} \int_{\lambda_i}^{\lambda_f} (TE_{TOC} \rho_{app} * f) d\lambda + \frac{1}{\pi} \int_{\lambda_i}^{\lambda_f} (TE_{TOC} S \rho_{app}^2 * f) d\lambda \quad (4.4.6)$$

where f is the ISRF and ρ_{app} is apparent surface reflectance introduced in Equation 5.3.2. Therefore, approximations assumed to obtain surface apparent reflectance are listed below:

1. Considering a Lambertian and a isotropic surface behaviour.
2. Taking TOA radiance expression as a series expansion until second order (see Chapter 5).
3. Assuming the Lambertian surface reflectance term (ρ) as the surface apparent reflectance (ρ_{app}) coupled with the spherical albedo term (S). This approach simplifies the number of unknown variables with an impact on SIF that can be neglected. (see Chapter 5).

Then, using Equation 4.4.6 and the atmospheric functions at high spectral resolution provided by an atmospheric radiative transfer code, apparent reflectance is obtained by isolating ρ_{app} of Equation 4.4.6:

$$\rho_{app} = \frac{-A + \sqrt{A^2 - 4B\pi(L_0 - L_{TOA})}}{2B} \quad (4.4.7)$$

where $A = \int_{\lambda_i}^{\lambda_f} (TE_{TOC} * f) d\lambda$ and $B = \int_{\lambda_i}^{\lambda_f} (TE_{TOC} S * f) d\lambda$ are the convolutions of the atmospheric function products previously computed at higher spectral resolution, i.e., in this case at 0.1 cm^{-1} .

Finally, once the apparent reflectance term has been retrieved, it is possible to decouple F and ρ terms. Many different techniques, from simple Fraunhofer Linear Discriminator (FLD) [Plascyk, 1975] or the improved version of Fraunhofer Linear Discriminator (FLD) method [Alonso *et al.*, 2008] to more complex methods, e.g., Spectral Fitting Methods (SFM) [Meroni *et al.*, 2010; Cogliati *et al.*, 2015b], can be applied to disentangle these signals according to the required precision.

Aerosol optical property retrieval

Generally, atmospheric correction algorithms based on atmospheric radiative transfer LUT inversion assume that a predefined aerosol model is known, e.g., urban, rural, maritime, etc., and the only invertible variable is the Aerosol Optical Thickness (AOT) [Benas *et al.*, 2013]. This classification into predefined aerosol models, inherently implies to fix a set of predefined optical properties that do not necessarily match with those present in the acquired image [Carr, 2005]. The aerosol retrieval method presented here will instead parametrize the aerosol optical properties through the following variables: (1) the AOT at 550 nm (τ_{550}), (2) the Ångström coefficient

(α), and (3) the asymmetry parameter (g) of the Henyey–Greenstein (HG) scattering phase function. The selection of these three aerosol optical properties results from a compromise between the number of unknown variables to be inverted and the flexibility to reproduce the scattered radiance for a wide range of aerosol scenarios. Firstly, τ_λ represents the aerosol content in the atmosphere. Secondly, the Ångström law through the Ångström coefficient α models the wavelength dependency of the τ_λ . The Ångström coefficient is in fact spectrally dependent (see Section 2.1.1). However, since the relevant FLEX spectral region covers from 680 – 780 nm, where O_2 absorptions are located, a single α coefficient is considered in the inversion process. Conversely, if a larger spectral range would be required, two or more Ångström coefficients would be necessary to describe the spectral behaviour of τ_λ . Finally, the aerosol scattering anisotropy is approximated by the HG phase function through its asymmetry parameter g .

HG phase function is commonly used in radiative transfer calculation due its simplicity [Toublanc, 1996]. Many experimentally measured scattering phase functions, as those included in MODTRAN, e.g., rural, maritime, urban or desert classes [Shettle and Fenn, 1979], offer a more realistic description of light scattered [Carr, 2005]. However, this not always necessarily matches the real conditions under study. Accurate estimations of the scattering phase function would require multi–angular measurements, e.g., the Multi–angle Imaging SpectroRadiometer (MISR), the POLarization and Directionality of the Earth's Reflectances (POLDER) or the Compact High Resolution Imaging Spectrometer (CHRIS) on board Proba satellite. In the case of S3, the use of Sea and Land Surface Temperature Radiometer (SLSTR) with its conical scanning, provides only two viewing angles which results insufficiently to characterize the complete aerosol scattering pattern. Therefore, and given that FLEX is dedicated to SIF monitoring and not to atmospheric studies, the use of the simplistic HG scattering phase function is considered adequate to characterize the atmospheric state.

Figure 4.4.3 shows the impact on TOA radiance when varying the aerosol optical properties defined in the inversion process, i.e., τ_{550} , the Ångström exponent (α) and, the HG asymmetry parameter g . Variations in TOA radiance produced by changes in α and g are more significant for high aerosol loads (higher τ_{550}). In addition, it is worth noting that areas in the plot with the same color indicate that identical variations per wavelength can be attributed to different combinations of τ_{550} , α and g .

The aerosol optical properties retrieval process is based on an iterative optimization process (see Figure 4.4.4) that minimizes the cost function (Equation 4.4.8):

$$\delta_\lambda = \sum_{pix} \left[\sum_{\Omega} \frac{1}{N} \sum_{\lambda} \phi \left(L_{sen}^{SLSTR} - L_i^{SLSTR} \right)^2 + \frac{1}{M} \sum_{\lambda} \omega \left(L_{sen}^{OLCI} - L_i^{OLCI} \right)^2 \right] \quad (4.4.8)$$

where N and M are the number of bands in SLSTR, excluding both thermal bands and O_2 and water vapour absorption bands, and OLCI sensors respectively. Ω refers to the dual viewing angle of SLSTR, and ϕ and ω are weighting functions defined as $\frac{1}{\lambda^2}$ according to each sensor band configuration. These weighting functions are defined to drive the inversion towards

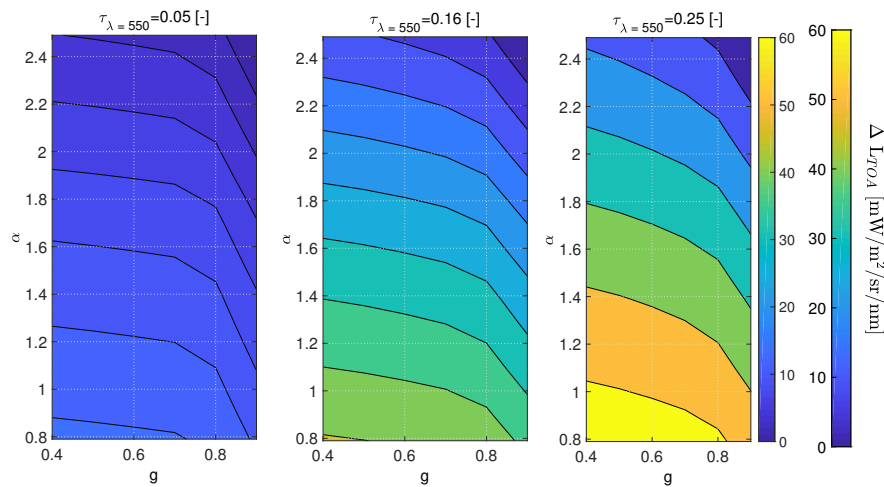


FIGURE 4.4.3: Variations on TOA radiance at 400 nm and different aerosol load $\tau_{550} = 0.05$, $\tau_{550} = 0.16$ and $\tau_{550} = 0.25$ produced by changes in the Ångström exponent and the g aerosol scattering asymmetry. As the aerosol load increases (an incremental step of τ_{550}) variations both in the Ångström and the g parameter results in a stronger variation of TOA radiance. Only positive values of g are considered in the inversion assuming the scattering process dominates in the forward direction.

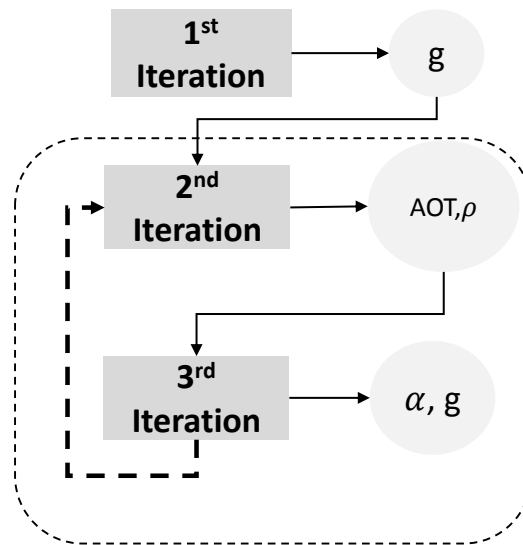


FIGURE 4.4.4: Iterative process followed to estimate the atmospheric aerosol optical properties characterization.

smaller wavelengths, where the effect of aerosol is larger while most of the natural surfaces reflectance is lower [Guanter *et al.*, 2007b]. Finally, L_{sen} are OLCI and SLSTR nadir and oblique viewing angle TOA radiances, and L_i are the corresponding simulated TOA radiances for each sensor.

The aerosol characterization process is based on the following three iterative steps, each one of them with a specific purpose. The entire cycle, i.e., steps 1, 2 and 3, are repeated until retrieval of AOT stabilizes. The first step is exclusively dedicated to estimating the g parameter value, i.e., to characterize the asymmetry of the HG scattering phase function. Once a first estimation for g is obtained, second and third iterative steps will subsequently search for AOT and α values. Finally, the third step also looks for a refinement of the initial estimated g value. In the presented work, no minimum-finding algorithm has been employed to avoid local minimum and to guarantee the convergence of the result by covering and evaluating the full range of the possible aerosol optical parameter combinations.

Moreover, while atmospheric properties remain nearly constant for wide areas, surface properties tend to present a more heterogeneous spatial pattern for high spatial resolution satellite observation. This natural contrast, introduced mathematically as a boundary condition in the cost function (Equation 4.4.8), is the main reason why the aerosol characterization is not applied on a pixel-wise basis, but over medium surface size, i.e., around 30 km, image areas [Guanter *et al.*, 2007b]. Thus, pixels included in the minimization cost function summation of Equation 4.4.8, must be representative of the diversity in surface reflectance while atmospheric conditions remain constant. In the presented work, the pixels selection process has not been performed since the 5 surface reflectance pixels used in the FLEX-DB are assumed to represent the diversity of an arbitrary scenario for FLEX, with a diversity of vegetation and bare soil pixels. However, pixels selection can be easily performed by means of applying a previous classification using from a classical vegetation index such as the Normalized Difference Vegetation Index (NDVI), to more sophisticated classification techniques, i.e., supervised, non-supervised, parametric or non-parametric [Camps-Valls *et al.*, 2011], according to the prior image information available.

Therefore, taking L_i dependency into account, during this part of the process the ρ_{app} and the atmospheric water vapour content are two unknown variables. Then, two approximations are introduced to calculate and minimize the cost function of Equation 4.4.8:

1. An auxiliary reflectance database is used to estimate surface reflectance. This database stores a wide variety of spectra, including bare soil, different vegetation types, man-made materials and water.
2. Water vapour, among other gaseous absorption bands, are easily identified in the radiance spectrum (e.g., centred at 820 nm, 940 nm, 1.4 μm , 1.8 μm , etc.). Outside these absorption bands water vapour absorption features can be ignored. Thus, it is possible to perform the aerosol characterization process out of the water vapour absorption features by assuming a default value of the total water vapour content.

Water vapour retrieval

The Columnar Water Vapour (CWV) is derived based on a differential absorption technique using OLCI data [Schläpfer *et al.*, 1998]. In essence, differential absorption techniques calculate the ratio $R = L_{out}/L_{in}$ between radiances inside (L_{in}) and outside (L_{out}) the water vapor absorption band [Schläpfer *et al.*, 1998]¹. In OLCI this ratio is calculated at the water vapour absorption band centred at 940 nm. While L_{in} is directly the TOA radiance acquired inside the absorption band, L_{out} is obtained at the same wavelength by linear regression from the reference channels, i.e., channels nearby the absorption band yet unaffected by it. In Figure 4.4.5, measurement and reference channels for OLCI instrument are plotted using a TOA radiance spectrum as example.

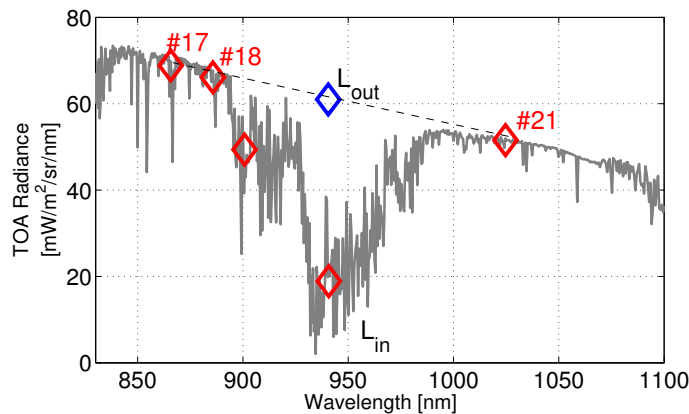


FIGURE 4.4.5: High resolution TOA radiance around the water vapour absorption band centred at 940 nm. OLCI reference bands, i.e., channels 17, 18 and 21 are also indicated. The proposed CWV algorithm computes the ratio between TOA radiance L_{in} deep inside the absorption, band 20, and the radiance at this wavelength obtained from a linear fit of the reference bands, i.e., L_{out} .

The CWV is retrieved by a LUT inversion, using Brent's method [Brent, 1971] that aims to minimize the cost-function between the acquired by the sensor (R_{sen}) and simulated (R_{sim}) ratios $X = R_{sim} - R_{sen}$. The simulated ratio uses the previously derived aerosol properties, (Section 4.4.1), and approximates the surface reflectance in the measurement spectral channel as a linear interpolation between the reference channels (Figure 4.4.5). The CWV is retrieved pixel-wise due to its high spatial variability. A linear behaviour between the reference channels and the measurement channel for most surface reflectance can be assumed.

However, in the particular case of vegetation with a high liquid water content on leaves, surface reflectance moves away from linearity at wavelengths close to water vapour absorption band. The reflectance spectrum of vegetation exhibits weak liquid water absorption features centred as approximately 1000 and 1200 nm [Gao and Goetz, 1990]. As can be observed in Figure 4.4.6, water vapour and liquid water absorption bands are close to each other but not

¹A review of most known differential absorption techniques is provided in Section 2.4.2. Radiances inside and outside the absorption band are generally identified with the terms *measurement* and *reference*, respectively.

completely overlapping, with a separation between centres of around 5 nm. The shifts in wavelengths of the absorption bands are caused by larger intermolecular forces of water molecules in liquid phase than in the gas phase [Bunting and d’Entremont, 1982]. Thus, using this separation between bands, spectral fitting techniques can be applied to disambiguate atmospheric water vapour from liquid water content on leaves in case it was necessary. At the same time, pixel-wise water vapour estimation can be improved by means of a spatial smoothness to avoid possible unexpected water vapour transitions caused by changes in the underlying surface. However, these techniques would be explored only in case retrieved accuracy in water vapour estimations would be insufficient to accomplish the FLEX mission requirements.

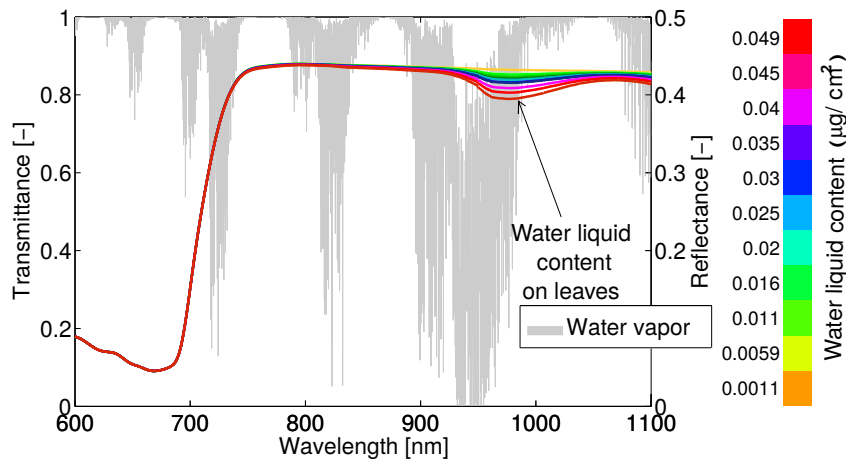


FIGURE 4.4.6: Water vapour and water vapour continue transmittance modelled by MODTRAN for a standard mid-latitude summer atmosphere (Left axis). Set of vegetation surface reflectance spectra with different liquid water content (0-0.5 $\mu\text{g}/\text{cm}^2$) simulated using the leaf radiative transfer model PROSPECT4 [Feret *et al.*, 2008] (Right axis).

4.4.2 Fluorescence estimation

Once the atmospheric state is characterized, i.e., being ρ_{app} and E_{TOC} the products derived from the atmospheric inversion, it is possible to disentangle SIF from solar reflected light at surface level by applying any FLD family technique or any Spectral Fitting Methods (SFM) strategy. On the one hand, the FLD family techniques (e.g., Plascyk, 1975; Plascyk and Gabriel, 1975; Maier *et al.*, 2003; Alonso *et al.*, 2008) were designed to estimate SIF by exploiting the information at the Fraunhofer or the oxygen absorption features. Consequently, SIF is only estimated at these absorption regions. Conversely, with the SFM it is possible to estimate SIF in the oxygen absorption regions Mazzoni *et al.*, 2010; Meroni *et al.*, 2010 or/and in a wider spectral range [Cogliati *et al.*, 2015b]. In this work, fluorescence retrieval was estimated by coupling two SIF retrieval techniques: (1) the Peak Height (PH) method [Alonso *et al.*, 2014], which estimates SIF at the oxygen absorption regions and is used as an initialization step for (2), the SFM developed by Cogliati *et al.*, 2015b, that allows estimating SIF in a wider spectral range.

The Peak Height (PH) method

The Peak Height (PH) method, developed by [Alonso *et al.*, 2014](#), is based on the idea that peaks appreciated on the apparent reflectance are a coupled consequence of the SIF emission and the absorption (solar or telluric) features. Under a mathematical point of view, since in the formulation used to invert TOA radiance, SIF emission is only included through the surface apparent reflectance term ρ_{app} , it results into an artificial in-filling of the absorption region that generates the characteristic peaks in ρ_{app} (See Figure 4.4.7).

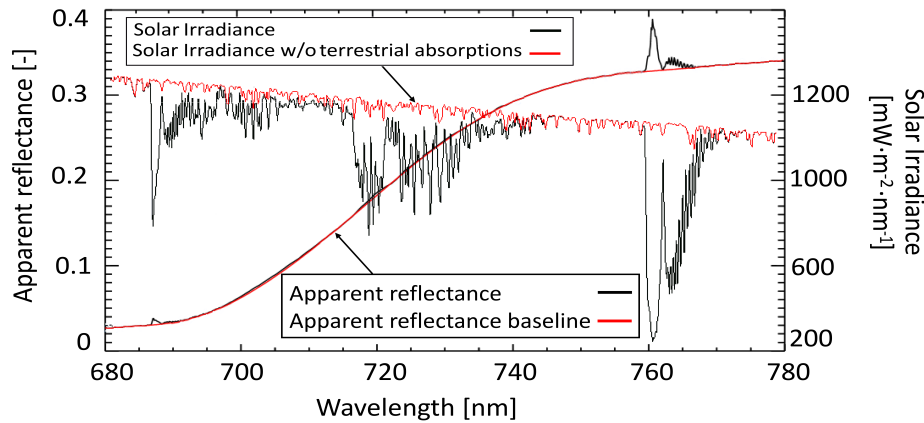


FIGURE 4.4.7: Apparent reflectance, ρ_{app} , and the lower envelop of the apparent reflectance, $\widehat{\rho_{app}}$ (black and red lines, respectively). Solar irradiance at TOC with and without accounting for the water vapour and oxygen molecular absorption features (black and red lines, respectively).

Thus, the main idea of the PH is that peaks appearing in the apparent reflectance are observed due to the SIF emission but especially due to the presence of the absorption features. Note that while SIF is emitted between 650-800 nm, peaks are only observed in the absorption features. Therefore, in an hypothetical atmosphere that was free of oxygen and water vapour molecular gases, the derived surface apparent reflectance $\widehat{\rho_{app}}$ will result into a smooth function that corresponds to the lower envelope of the apparent reflectance. To avoid any future misunderstanding, the difference between the lower envelope of the apparent reflectance, $\widehat{\rho_{app}}$, and the actual surface reflectance, ρ is here detailed and showed in Figure 4.4.8. While both functions are smooth, i.e., no peaks are observed, $\widehat{\rho_{app}}$ is always higher than surface reflectance ρ , due to it accounts for the contribution of the SIF spectrum emitted from 650 nm to 800 nm approximately. In addition, there is an extra advantage about using $\widehat{\rho_{app}}$ instead of ρ , since no assumptions about the actual shape of the reflectance in the absorption features has to be done as is the case of traditional FLD family techniques.

Thus, using the general definition of the surface apparent reflectance (Equation 4.4.5), in

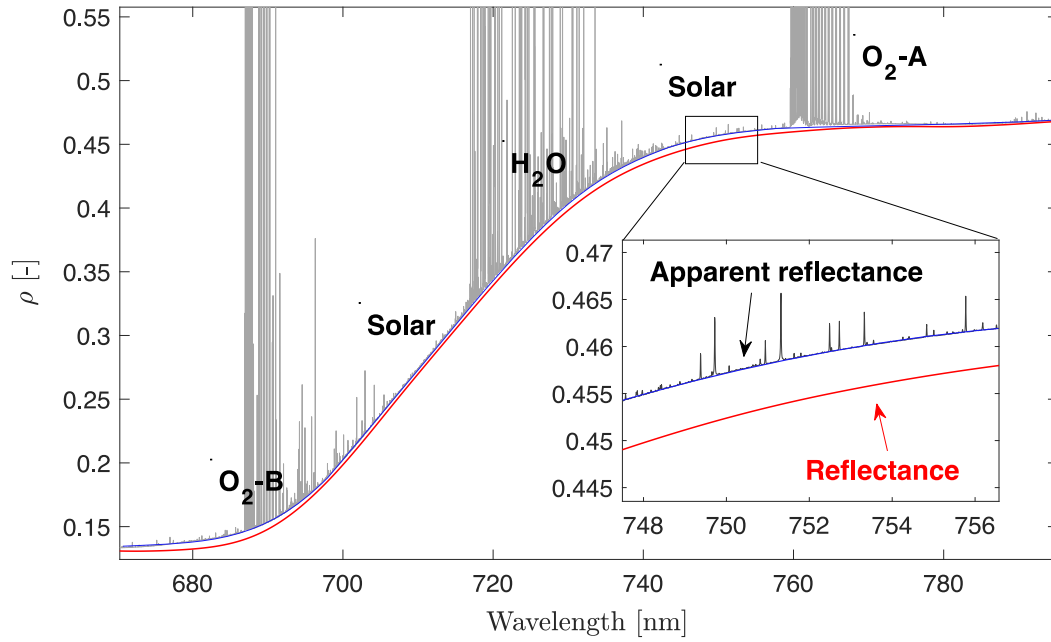


FIGURE 4.4.8: Apparent reflectance ρ_{app} (gray), lower envelope of the apparent reflectance $\widehat{\rho_{app}}$ (blue), and surface reflectance ρ (red) simulated at high spectral resolution.

case of a molecular oxygen and water vapour free atmosphere, $\widehat{\rho_{app}}$ can be described as (Equation 4.4.9):

$$\widehat{\rho_{app}} = \rho + \frac{\pi F}{\widehat{E_{TOC}}} \quad (4.4.9)$$

where $\widehat{E_{TOC}}$ is the solar irradiance at TOC level, in a molecular oxygen and water vapor free atmosphere (See Figure 4.4.7). This way, if the difference between $\widehat{\rho_{app}}$ and ρ is computed, SIF (F in the formulation for brevity) results into an expression (Equation 4.4.10) were all the terms are known:

$$F = (\rho_{app} - \widehat{\rho_{app}}) \frac{E_{TOC} \widehat{E_{TOC}}}{\pi (\widehat{E_{TOC}} - E_{TOC})} \quad (4.4.10)$$

On the one hand, $\widehat{\rho_{app}}$ can be estimated by means of simple interpolation of the apparent reflectance in the absorption spectral regions. On the other hand, solar irradiance in a molecular oxygen and water vapour free atmosphere can be estimated by means of an atmospheric RTM, such as MODTRAN. Details regarding best interpolation strategy can be found in [Alonso *et al.*, 2014](#).

The Spectral Fitting Method

As mentioned before, SFM has been applied to disentangle SIF from reflected solar irradiance for years. Generally its application was limited to the absorption spectral regions [Mazzoni *et al.*, 2010; Meroni *et al.*, 2010], but more recently it has been applied to the full SIF spectral range [Cogliati *et al.*, 2015b]. In this work, SIF was estimated by means of the algorithm developed in Cogliati *et al.*, 2015b. In essence, the enhancement comes from the modelling used for true reflectance and SIF. True reflectance is approximated by a multi-piece cubic spline function while fluorescence is fitted to a combination of two Lorentzians functions, one symmetric and another asymmetric. Thus, SIF and reflectance can be estimated by minimizing the difference between the measured radiance at TOC level, i.e., radiance derived from the atmospheric correction; and radiance simulated by using the parametrization proposed for ρ and F (see Equation 4.4.11):

$$\delta = \sum_{\lambda} \left(L_{TOC}(\lambda) - L_{TOC(sim)}(\lambda) \right)^2 = \sum_{\lambda} \left(L_{TOC}(\lambda) - F(\lambda) - \rho(\lambda) \frac{E_{TOC}(\lambda)}{\pi} \right)^2 \quad (4.4.11)$$

where L_{TOC} and $L_{TOC(sim)}$ are radiance at canopy level derived from the atmospheric correction and simulated using the proposed parametrization for the surface reflectance (ρ) and the emitted SIF (F), and E_{TOC} is the solar irradiance at TOC. Note that from the Atmospheric Correction (AC) algorithm, L_{TOC} can be estimated by simply multiplying $\rho_{app} E_{TOC}$.²

4.5 Database simulation

Details regarding the mathematical procedure followed to model TOA radiance spectra stored in the FLEX-DB to evaluate the performance of the proposed AC algorithm are presented in Section 4.5.1. Afterwards, a general description of the FLEX-DB design together with a justification about the parameters evaluated and the radiative transfer models selected is given in Section 4.5.3.

4.5.1 TOA radiance modelling

Radiance at TOA level was modelled using the formulation detailed in Section 2.3.1, which is based on Verhoef and Bach, 2012; Verhoef *et al.*, 2014. The general expression used to obtain radiance reaching the sensor is also here described in Equation 4.5.1:

²In Chapter 5 the consistency and validity of this formulation is analysed

$$\begin{aligned}
L_{TOA} = L_0 + & \left[\rho_{so} T_{dir}^{\downarrow} \left(\frac{E_s^0 \cos \theta}{\pi} \right) + F_d + \rho_{do} \frac{(T_{dif}^{\downarrow} + T_{dir}^{\downarrow} \bar{\rho}_{sd} S) E_s^0 \cos \theta + \pi \bar{F}_d S}{\pi(1 - \bar{\rho}_{dd} S)} \right] T_{dir}^{\uparrow} \\
& + \left[\frac{(T_{dif}^{\downarrow} \rho_{dd} + T_{dir}^{\downarrow} \bar{\rho}_{sd}) E_s^0 \cos \theta + \pi \bar{F}_d}{\pi(1 - \bar{\rho}_{dd} S)} \right] T_{dif}^{\uparrow}
\end{aligned} \tag{4.5.1}$$

where, as it was pointed in Chapter 2; terms ρ_{so} , ρ_{do} , $\bar{\rho}_{sd}$, $\bar{\rho}_{dd}$ corresponds to the fraction between up-welling and down-welling incident radiance at surface level coming from the transmitted downward-upward direct-direct, diffuse-direct, direct-diffuse, and diffuse-diffuse components; respectively. Transmittance terms are decoupled into the contribution of direct or diffuse (indicated by means of the suffix *dir* or *dif*), and downward or upward sense (indicated by means of the upward and downward arrows). Finally, E_0 is the solar extraterrestrial irradiance, θ corresponds to the solar zenith angle, L_0 is the atmospheric path radiance and S is the atmospheric spherical albedo. The atmospheric components F_d and \bar{F}_d correspond to the emitted SIF in the Line Of Sight (LOS) direction and emitted SIF isotropically. Contributions described in Equation 4.5.1 are also represented in Figure 4.5.1, highlighting in green the emitted fluxes where SIF is involved.

This formulation includes: the BRDF surface reflectance effects, the anisotropic SIF emission, and the inclusion of the adjacency effects. Including all these effects in the forward modelling (Equation 4.5.1) aims to perform a realistic simulation (radiometric noise is included later). However, since the retrieval strategy makes use of several mathematical assumptions, the selection of the reference surface and emitted SIF for validation purposes is not straightforward. For instance, a Lambertian surface reflectance behaviour is assumed in the retrieval strategy, while the forward modelling accounts for the surface BRDF effects. Similarly, the emitted SIF is assumed as isotropic, whereas the modelling was including the disentangled contribution of the isotropic hemispherical SIF emission and the target to sensor LOS emission. Therefore, the modelling exercise also requires to simulate those reference or equivalent surface reflectance and SIF spectra that will be used for the algorithm validation. On the one hand, in case of the surface reflectance spectra, reference spectra will be built by assuming the atmospheric parameters used in the forward modelling also for the inversion procedure. In other words, the validation of the atmospheric correction process will be performed by comparing the estimated ρ_{app} obtained: (1) by using the atmospheric parameters derived from the atmospheric characterization process, and (2) by using the reference atmospheric parameters used for the forward modelling (ideal atmospheric correction process). On the other hand, the construction of a reference isotropic SIF is not as straightforward as the estimation of a reference surface apparent reflectance. Thus, the next subsection is dedicated to describe the formulation and the strategy used to define the reference SIF spectra used.

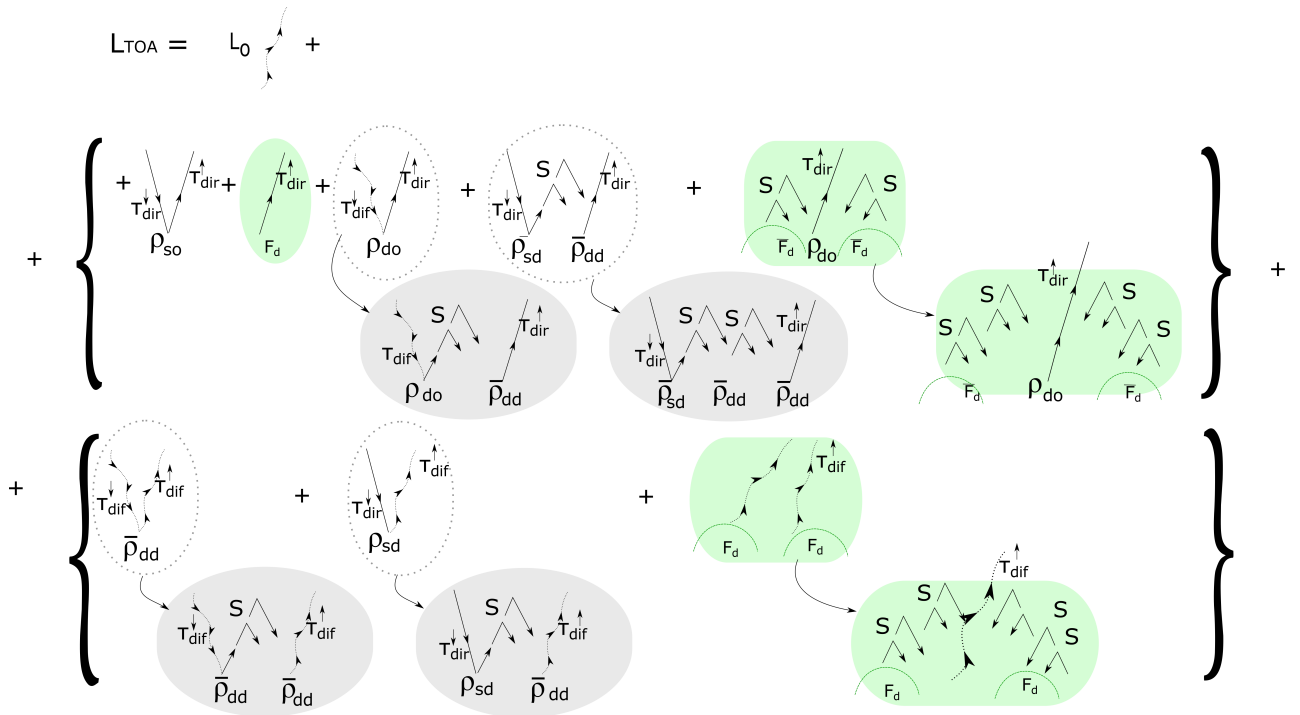


FIGURE 4.5.1: Schematic view of all the contributions included in the forward modelling detailed in Equation 4.5.1. Straight lines corresponds to direct atmospheric components while curve lines describe diffuse atmospheric components. Green areas denote those terms related with the emitted SIF. Terms grouped in the first and second claudators correspond to terms grouped in first and second claudators in Equation 4.5.1, respectively.

4.5.2 Building a reference fluorescence spectra for BRDF scenarios

Since the formulation proposed for the retrieval strategy is unable to disentangle between the different SIF emitted components, directional and hemispherical (Equation 4.5.1); it is necessary to define a kind of equivalent isotropic SIF spectra to be used as a reference to validate the retrieval strategy. To do so, we computed the radiance spectrum emitted at TOC level considering the four surface reflectance components, i.e., $\bar{\rho}_{sd}$, ρ_{so} , $\bar{\rho}_{dd}$ and ρ_{do} and both fluorescence emission terms, i.e., \bar{F}_d and F_d , by following Equation 4.5.2. Note that Equation 4.5.2 equals Equation 4.5.1 without the transmittance and the path radiance terms. Similarly, radiance at TOC assuming no fluorescence emission ($L_{TOC}(SIF = 0)$) is computed in Equation 4.5.3, i.e., setting \bar{F}_d and F_d as zero.

$$L_{TOC} = \left[\rho_{so} T_{dir}^{\downarrow} \left(\frac{E_s^0 \cos\theta}{\pi} \right) + F_d + \rho_{do} \frac{(T_{dif}^{\downarrow} + T_{dir}^{\downarrow} \bar{\rho}_{sd} S) E_s^0 \cos\theta + \pi \bar{F}_d S}{\pi(1 - \bar{\rho}_{dd} S)} \right] \quad (4.5.2)$$

$$+ \left[\frac{(T_{dif}^{\downarrow} \rho_{dd} + T_{dir}^{\downarrow} \bar{\rho}_{sd}) E_s^0 \cos\theta + \pi \bar{F}_d}{\pi(1 - \bar{\rho}_{dd} S)} \right]$$

$$L_{TOC}(F_d = 0, \bar{F}_d = 0) = \left[\rho_{so} T_{dir}^{\downarrow} \left(\frac{E_s^0 \cos\theta}{\pi} \right) + \rho_{do} \frac{(T_{dif}^{\downarrow} + T_{dir}^{\downarrow} \bar{\rho}_{sd} S) E_s^0 \cos\theta}{\pi(1 - \bar{\rho}_{dd} S)} \right] \quad (4.5.3)$$

$$+ \left[\frac{(T_{dif}^{\downarrow} \rho_{dd} + T_{dir}^{\downarrow} \bar{\rho}_{sd}) E_s^0 \cos\theta}{\pi(1 - \bar{\rho}_{dd} S)} \right]$$

Thus, an equivalent SIF emitted at TOC level can be easily computed as a difference between 4.5.2 and 4.5.3:

$$SIF_{ref} = L_{TOC} - L_{TOC}(F_d = 0, \bar{F}_d = 0) \quad (4.5.4)$$

The suffix *ref* has been added to indicate that the final goal of SIF_{ref} is to be used as a reference for the algorithm's validation. However, due to the formulation used to derive SIF_{ref} and the finite spectral resolution used, residuals in the absorption features appear. Figure 4.5.2 shows the estimated reference SIF (SIF_{ref}) together with the emitted SIF in the sensor LOS (F_d). As can be observed, SIF_{ref} is always higher than F_d , since it should include a fraction of the SIF emitted isotropically (\bar{F}_d) that reaches the sensor. In addition, especially in the absorption features such as the oxygen regions presented in Figure 4.5.3, residuals appear in the estimation of a reference SIF signal. To avoid residuals particularly in the oxygen regions, SIF_{ref} is interpolated inside these regions of interest. Therefore, it is possible to obtain an equivalent smoothed SIF emitted spectra that accounts for the directional and the hemispherical contribution simultaneously (black lines in Figures 4.5.3).

4.5.3 FLEX-DB design

TOA radiance spectra from FLEX-DB were simulated by coupling two Radiative Transfer Models (RTMs), one at canopy level and other at atmospheric level following Equation 4.5.1. At the surface level, the selected RTM was the Soil-Canopy Observation of Photosynthesis and Energy (SCOPE)[Tol *et al.*, 2014]. SCOPE is a vertical (1-D) integrated radiative transfer and energy balance model that calculates radiation transfer in a multilayer canopy. Among other outputs, it generates reflectance and fluorescence in the observation direction as a function of the solar zenith angle and leaf properties. The irradiance and the distribution of absorbed radiation within the canopy is calculated with the Scattering of Arbitrarily Inclined Leaves (SAIL)

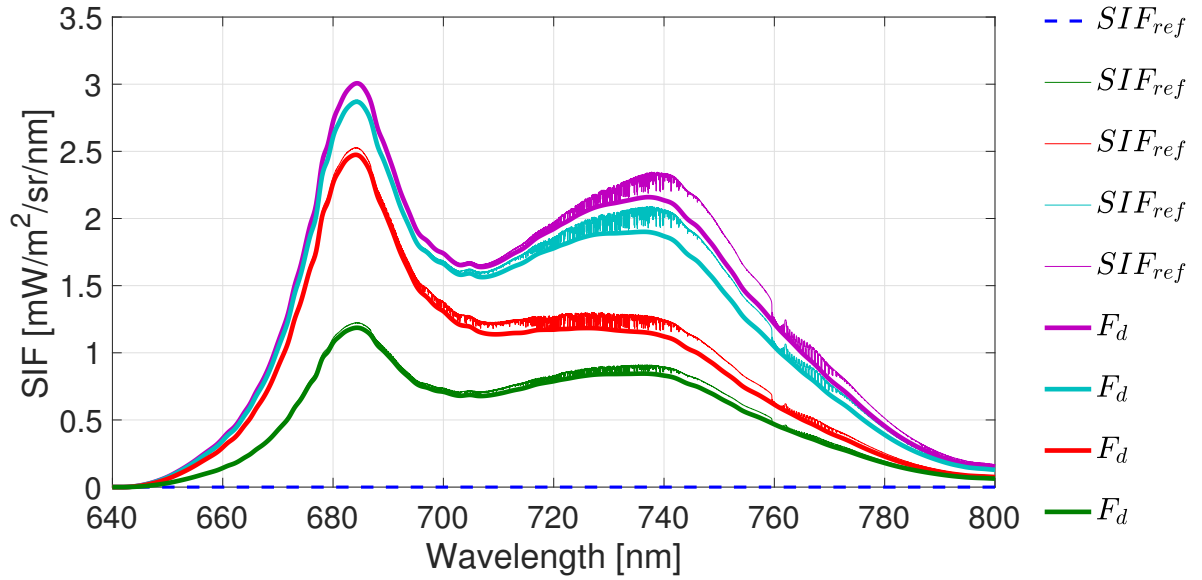


FIGURE 4.5.2: Reference SIF signal (SIF_{ref}) computed for the validation of the proposed algorithm. Reference emitted SIF includes simultaneously the emitted SIF components F_d and \bar{F}_d .

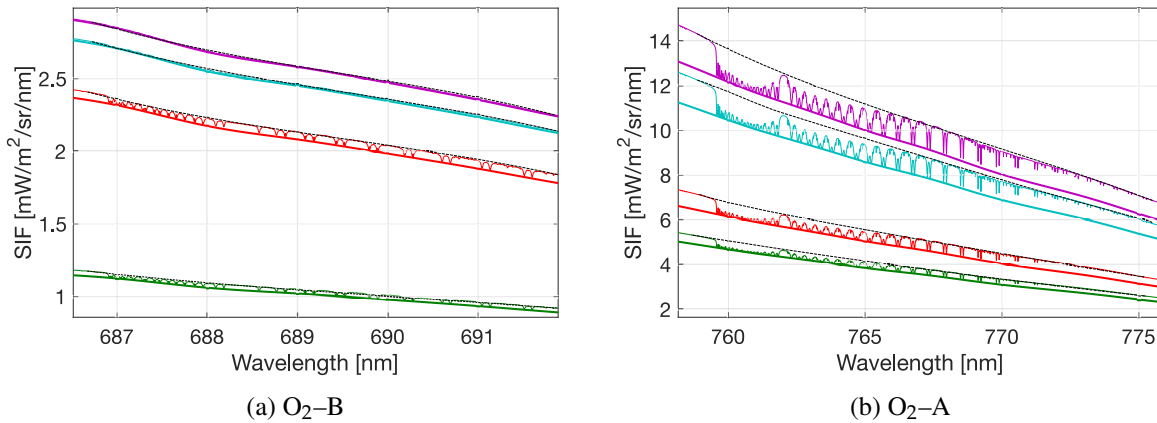


FIGURE 4.5.3: Zoom in the oxygen regions of the reference SIF (SIF_{ref}) computed for validation. Black dashed lines are the interpolated SIF_{ref} signal at the oxygen regions.

model [Verhoef, 1984]. The distribution of absorbed radiation is further used in a micro-meteorological representation of the canopy for the calculation of photosynthesis, fluorescence, latent and sensible heat. The fluorescence and thermal radiation emitted by individual leaves is finally propagated through the canopy, again with the SAIL modelling concept [Tol *et al.*, 2009]. At the atmospheric level, the MODerate resolution atmospheric TRANsmittance and radiance code (MODTRAN5) [Berk *et al.*, 1987] was selected. MODTRAN is a “narrow band model” atmospheric radiative transfer code. The atmosphere is modelled as stratified (horizontally homogeneous), and its constituent profiles, both molecular and particulate, may be defined either using built-in models or by user-specified vertical profiles. The atmospheric extinction

due to molecules and aerosol is considered together for every light path, accounting for absorption between two consecutive scattering events. Among many of its attributes, two main arguments supports the election of MODTRAN as an ideal atmospheric RTM for the FLEX–DB construction :

1. The rigorous treatment of absorption and scattering coupling and multiple scattering.
2. The high spectral resolution provided (0.1 cm^{-1}).

These two considerations were decisive to guarantee an accurate FLORIS TOA radiance simulation, especially on absorption band regions. FLEX–DB is understood as a set of 240 test images (Figure 4.5.4) corresponding to 240 different atmospheric conditions (see Table 4.5.1). Each test image is composed by 5 pixels which covers from bare soil to different vegetation classes. Thus, surface reflectance and fluorescence spectra used for the 5 pixels simulation remain identical for all the FLEX–DB, while the atmospheric conditions assumed to the TOA radiance simulation changes (Figure 4.5.4).

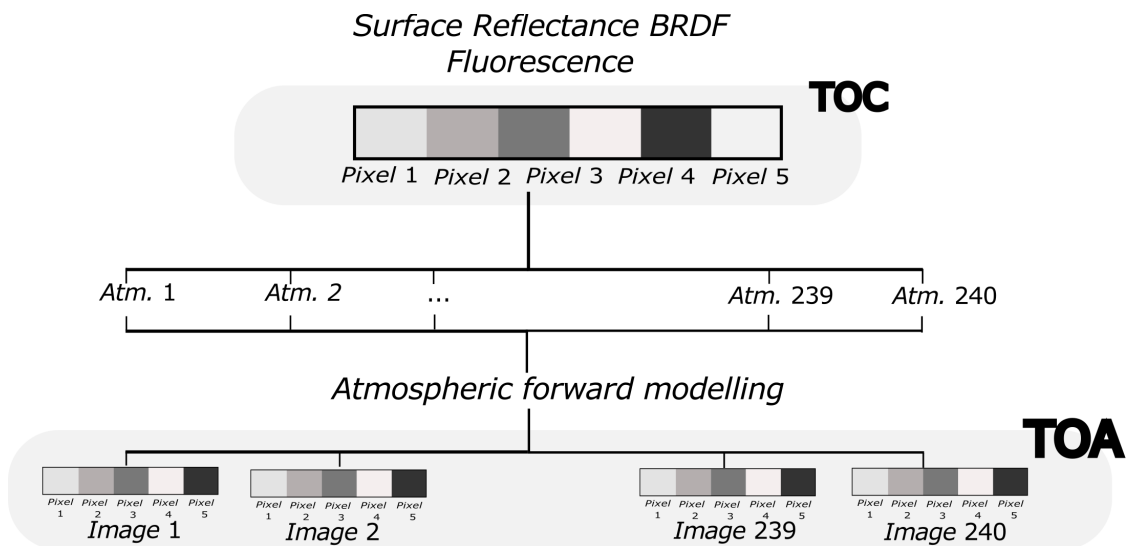


FIGURE 4.5.4: FLEX–DB structure. At TOC level, only 5 pixels are defined by means of the $\bar{\rho}_{sd}$, ρ_{s0} , $\bar{\rho}_{dd}$ and ρ_{d0} , and the F_d and \bar{F}_d terms. Then using the range of atmospheric parameters defined in Table 4.5.1, 240 different atmospheric states are simulated. Consequently, at TOA level, 240 images, with 5 pixels each, are simulated.

The rationale behind doing so is because the goal of this work is focused on the validation of the proposed atmospheric correction method; so, the more atmospheric conditions tested the better for the validation purposes. Input atmospheric parameters covered as part of the atmospheric simulation process are summarized in Table 4.5.1.

For SIF retrieval strategies based on exploiting oxygen absorption band regions, aerosol scattering and surface pressure can be considered as potential sources of error [Guanter *et al.*, 2010]. On the one hand, while surface pressure is major affected by surface elevation, a minor

MODTRAN input values					
τ_{550} [-]	0.05	0.16	0.25		
α [-]	0.79	1.39	1.54	1.74	2.5
g [-]	0.4	0.75	0.8	0.9	
CWV[g/cm ²]	1.2	2.4			
SZA[°]	45				
VZA[°]	0	55			
RAA[°]	0				
Elevation[m]	100	1500			

TABLE 4.5.1: Summary of input parameters used to create the 240 atmospheric conditions using the atmospheric RTM MODTRAN.

variation is introduced by changes in the atmospheric state (by alterations in temperature and humidity). Although changes on surface pressure can impact on SIF estimations, since both surface level pressure and surface elevation data can be derived from external existing meteorological operational products and Digital Elevation Models (DEM), the assessment of the impact on estimated SIF due to disturbances on the surface pressure estimation has been considered out of the scope of this work. On the other hand, as introduced in Section 4.4.1, aerosol scattering is determined by means of three different aerosol optical properties in the FLEX-DB: (1) the Aerosol Optical Thickness AOT, (2) the Ångström exponent (α), and (3) the asymmetry parameter (g) of Hengey–Greenstein scattering phase function. The reasons for selecting these aerosol optical properties, as well as the selection of the remaining set of atmospheric and illumination conditions in the FLEX-DB, are here outlined:

- The proposed atmospheric correction algorithm is based on the retrieval of AOT, α and g . Thus, forward modelling was simulated using the same parametrization for an easier comparison of the estimated and the reference aerosol optical properties.
- The variation of these three parameters allows representing a high variety of aerosol scenarios.
- The impact of changes in the aerosol vertical profile on TOA radiance is assumed as secondary as demonstrated in [Vicent *et al.*, 2017].
- AOT values range from very low to medium–high aerosol load conditions. Extreme events such as a Saharan dust intrusion are out of these ranges. However, this is not considered a priority on this study. For similar reasons, atmospheric Columnar Water Vapour content (CWV) only covers two values, low and medium–high (double). Extremely wet atmospheres, typical from tropics are not studied in this work.
- Visual Zenith Angle (VZA) was simplified to a full nadir viewing in case of FLORIS and OLCI, and SLSTR nadir acquisitions. For the SLSTR oblique acquisition the Visual Zenith Angle (VZA) was set as 45.

- FLEX–DB images are defined as cloud–free images. Cloud screening possibilities offered by the FLEX/S3 tandem mission are expected to guarantee an accurate of cloud free pixels identification. From SLSTR instrument a series of tests, most of them derived from a heritage of the Advanced Along Track Scanning Radiometer (AATSR), can be applied in turn to the brightness temperature data in the 3.7, 11 and 12 μm and to the reflectance data in 1.6 μm and visible channels [European Space Agency, 2015b]. Furthermore, the inclusion of new bands at 2.25 and 1.375 μm , this last band dedicated to the *Cirrus* thin clouds detection, may permit an improved identification of cloudy pixels. Further, simulated images from S3 (OLCI and SLSTR) and FLEX are considered to be previously co–registered and cross–calibrated.
- The spectral dependency on the degree of polarization of the solar irradiance reflected by the atmosphere could lead to in–filling effects of the O₂–A and O₂–B absorption features which might in turn lead to errors in SIF estimations [Guanter *et al.*, 2010]. In order to avoid signal distortions due to polarization of the incoming light, the polarization level should be limited along the whole spectral range covered by the FLORIS instrument. Therefore, FLORIS will guarantee that the response of the instrument to a fully polarized beam shall not differ by more than 1% for the O₂ regions, and 2% for the rest of the spectral range covered; of the response to a depolarized incoming beam of the same total intensity [Drusch, 2016].
- A perfect cross–calibration between FLORIS, OLCI, and SLSTR nadir and oblique viewing angles is assumed.

Regarding SIF emission, 5 different SIF emission levels; from 0 [$\text{mW}/\text{m}^2/\text{sr}/\text{nm}$] (bare soil) to ~ 3 [$\text{mW}/\text{m}^2/\text{sr}/\text{nm}$], associated to the 5 simulated pixels on each test image are presented in Figure 4.5.5. Associated surface reflectance spectra for the 4 components (ρ_{sd} , ρ_{so} , $\bar{\rho}_{dd}$ and ρ_{do}) are shown in Figure 4.5.6. The corresponding values of the Leaf Area Index (LAI) and Chl. content used as part of the TOC simulation process are summarized in Table 4.5.2.

	LAI [-]	Chl [g/cm^2]
<i>Pixel 1</i>	0	0.47
<i>Pixel 2</i>	0.5	40
<i>Pixel 3</i>	1.5	10
<i>Pixel 4</i>	2.5	40
<i>Pixel 5</i>	4	70

TABLE 4.5.2: Summary biophysical parameters, LAI and Chl. content used as input in SCOPE.

In addition, expected levels of radiometric noise for FLEX were also included in the simulation of FLORIS FLEX–DB spectra. Radiometric noise simulated follows Equation 4.5.5

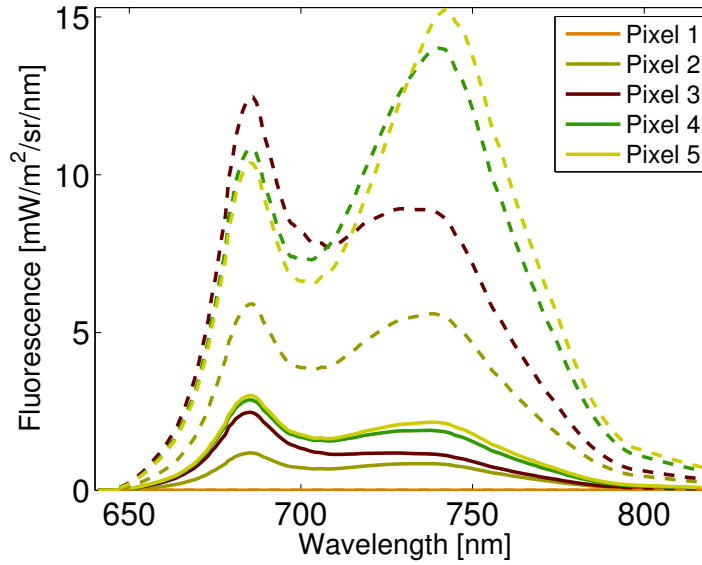


FIGURE 4.5.5: F_d (solid lines) and \bar{F}_d (dashed lines) fluorescence emission fluxes associated to the nadir acquisition geometry. Fluorescence spectra were simulated using SCOPE model and fixing the biophysical parameters of LAI and Chl content according to Table 4.5.2

	NBS		WBS
	O ₂ -B	O ₂ -A	
α	1.560e4	1.850e4	2.2e3
β	2.971e3	7.525e3	3.452e3
γ	1.055e4	1.055e4	1.055e4

TABLE 4.5.3: parameters α , β and γ defined for noise simulation of FLORIS instrument specified at the ESA technical note [Kraft, 2012](#).

provided by the ESA technical note of the FLORIS instrument [[Kraft, 2012](#)]:

$$L_{Noise} = \sqrt{\frac{2SSI_{samp}(\lambda_i)}{SSI}(N_{el} + \beta) + \gamma} \quad (4.5.5)$$

where SSI_{samp} is the width of the spectral channel as provided by the instrument and SSI the natural sampling of the instrument, which is 0.1 nm for the NBS and 0.65 nm for the WBS. The values of the parameters β and γ are detailed in Table 4.5.3. Finally, N_{el} is the number of photons the instrument detects, which depends on the reference radiance L_{ref} , and the parameter α (also detailed in Table 4.5.3).

$$N_{el} = \alpha SSIL_{ref} \quad (4.5.6)$$

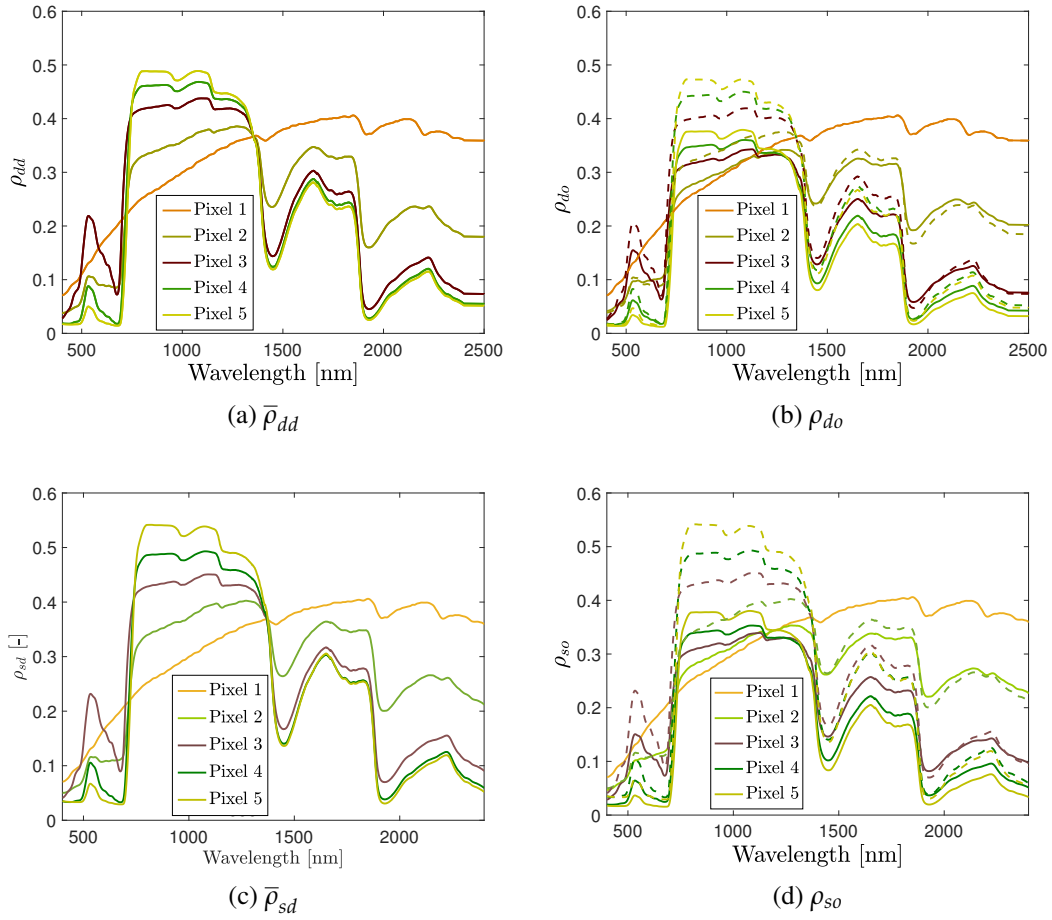


FIGURE 4.5.6: BRDF surface reflectance components simulated with SCOPE model and used for the non-Lambertian TOA radiance modelling of the FLEX-DB spectra (Equation 4.5.1). Dashed lines in Figures (b) and (d) are diffuse component spectra showed in (a) and (c) for a better comparison between them.

4.6 Results

This section is divided in two main parts. First, results related to the atmospheric characterization, i.e., derived CWV and aerosol optical properties, are presented comparing retrieved atmospheric properties and their corresponding reference values used in the FLEX-DB. Then, the second part focusses on comparing retrieved and reference surface apparent reflectance and fluorescence spectra.

4.6.1 Atmospheric retrieved parameters analysis

Water vapour retrieval

Retrieved CWV results are summarized in Figure 4.6.1. This figure presents retrieved values evaluated under the FLEX-DB atmospheric conditions, i.e., 120 images simulated with a low value of 1.2 g/cm^2 and another 120 images corresponding to a medium value of 2.4 g/cm^2 . Results are shown through of a set of box-plots which represent the statistics (mean, the 1st and 3rd quartile and the outliers) of the retrieved CWV values for each pixel.

As it can be observed, a noticeable better accuracy is obtained from pixel 1 (relative error between reference and mean estimated CWV is lower than 0.25%), corresponding to a bare soil spectrum, compared to the rest of pixels (i.e., vegetated spectra), which derive relative errors around 1%. The appearance of higher error in vegetated spectra can be attributed to the assumed approach (see Section 4.4.1) to define reflectance inside water vapour absorption band. Reflectance values inside the absorption band at 940 nm are estimated as a linear function of reference bands (OLCI channels #17, #18 and #21). While bare soil reflectance shows a linear trend in this spectral region, vegetated spectra around 940 nm will move away from a linear behaviour as liquid water content of the leaves increases (see Figure 4.4.6).

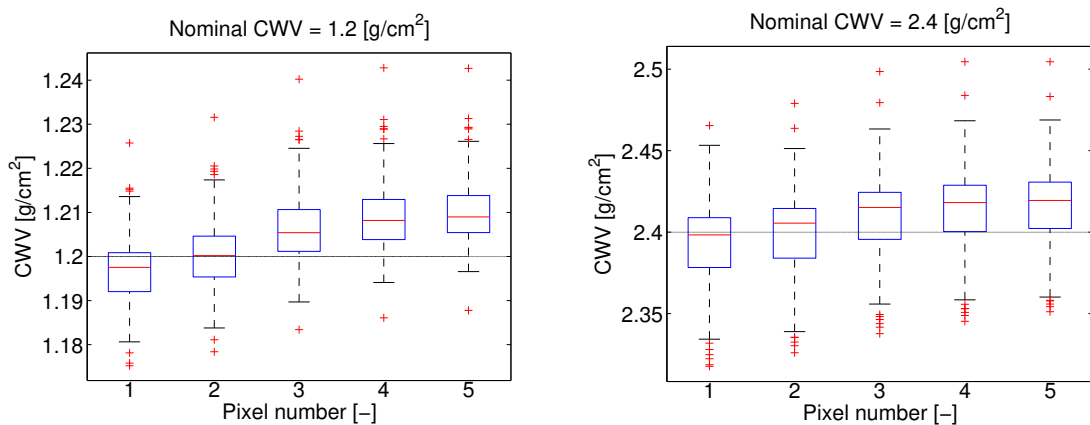


FIGURE 4.6.1: Water vapour content (g/cm^2) for the 240 images with low (120 combinations) and medium-high (120 combinations) CWV values (a) and (b) respectively. Labels in the X-axis indicate the pixel number associated with bare soil or vegetation pixels (see legend in Figure 4.5.6).

Aerosol Optical Properties retrieval

When retrieving surface reflectance spectra from TOA radiance, aerosols are always a significant source of uncertainty. Therefore, aerosol characterization becomes the bottleneck for any atmospheric correction algorithm. In this section, derived aerosol optical properties when applying the proposed AC algorithm to the simulated FLEX-DB are presented. In addition,

since FLEX is dedicated to vegetation and not to atmospheric studies, this section also analyses how errors in the aerosol estimation impact the derived surface apparent reflectance, and consequently SIF estimations. In Figures 4.6.2 and 4.6.3 estimated aerosol optical properties are plotted together with their associated relative error of surface apparent reflectance at the bottom of the O_2 -B and the O_2 -A absorption regions, respectively.

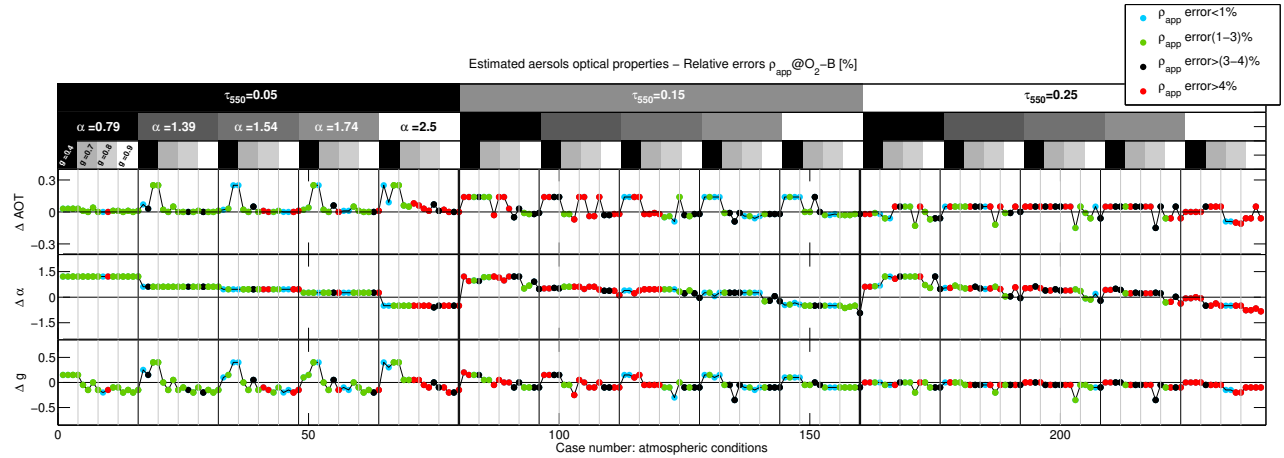


FIGURE 4.6.2: Error on estimated aerosol optical properties (AOT, α , g) together with the relative error [%] on the surface apparent reflectance for the O_2 -B absorption region.

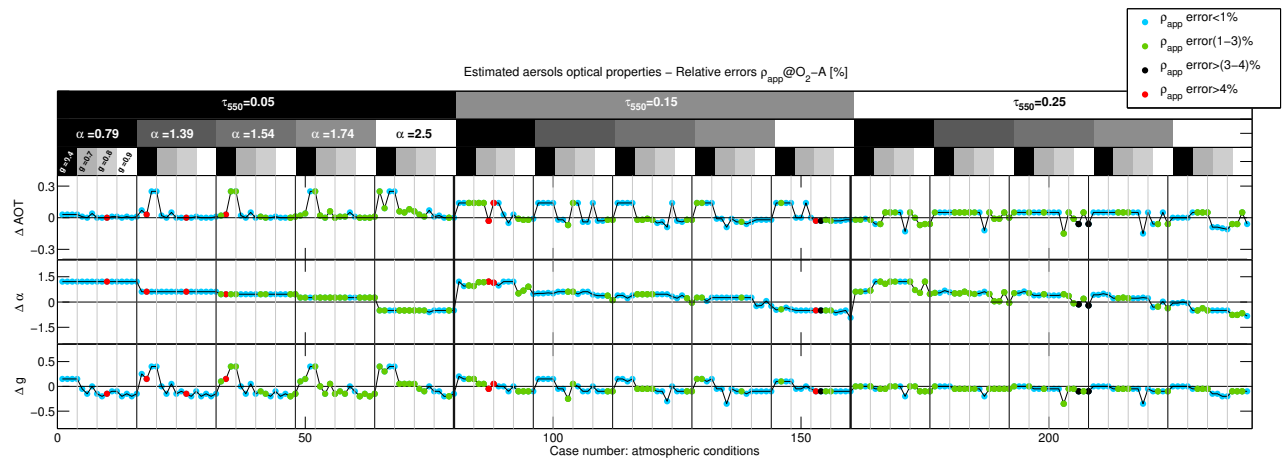


FIGURE 4.6.3: Error on estimated aerosol optical properties (AOT, α , g) together with the relative error [%] on the surface apparent reflectance for the O_2 -A absorption region.

From Figures 4.6.2 (O_2 -B) and 4.6.3 (O_2 -A) the following general observations can be summarized:

- There is a larger number of cases with high surface apparent reflectance relative errors ($\geq 4\%$) (red dots) in Figure 4.6.2 compared to Figure 4.6.3. This suggests that errors

associated to the estimated aerosols optical properties lead to a stronger impact at the O₂-B than at the O₂-A region.

- For high aerosol content, i.e., AOT=0.25; more cases with high surface apparent reflectance relative errors, $\geq 4\%$ at the O₂-B (red dots) and $\geq 1\%$ at the O₂-A (green, black and red dots), are found.
- For medium aerosol content, i.e., AOT=0.15, cases with a high surface apparent relative errors, $\geq 4\%$ at the O₂-B (red dots) and $\geq 1\%$ at the O₂-A (green, black and red dots), seems to be associated to big aerosol sizes, i.e., low α values.
- Lower relative errors in the apparent reflectance (cyan dots) appear in Figures 4.6.2 and 4.6.3, even in those cases where AOT was inaccurately estimated. This suggests that a possible balance between the estimated aerosol optical properties can be produced to minimize the error in surface apparent reflectance even when each individual optical property (AOT, α and g) is not accurately estimated.

To analyse in more detail those cases where certain combinations of inaccurately derived aerosol optical properties (by balancing their radiative effects) leads to an accurate surface apparent reflectance estimation, a 3D scatter plot that relates errors associated to the estimated AOT, α and g values with the derived surface apparent reflectance error at the bottom of the O₂-A region are presented in Figure 4.6.4.

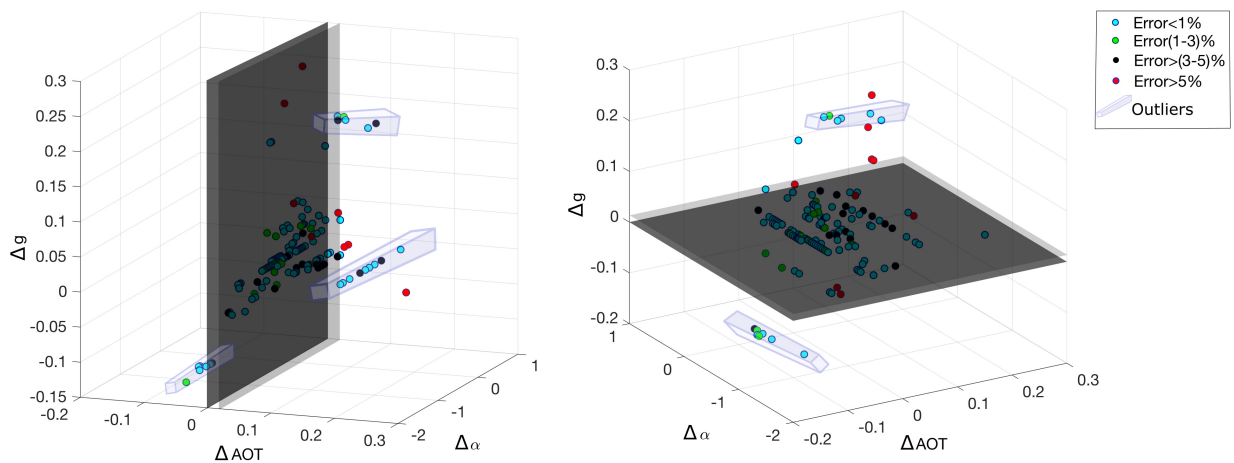


FIGURE 4.6.4: Errors of estimated aerosol optical properties (ΔAOT , $\Delta\alpha$, and Δg) together with its associated surface apparent reflectance relative error at the bottom of the O₂-A absorption region. (Left) gray-shaded plane covering accurate AOT estimations, i.e., $\Delta AOT = \pm 0.025$. (Right) gray-shaded plane covering accurate g estimations, i.e., $\Delta g = \pm 0.03$.

To facilitate the interpretation, Figure 4.6.4 includes two gray-shaded planes which limit the 3-D space to accurate estimates of AOT (left) and g (right). As can be deduced from this

figure, the Ångström exponent seems not to be a driving parameter, since accurate estimations of apparent reflectance are mainly restricted to those points that are included in the gray–shaded planes (accurate AOT and g estimations) regardless the error associated to the α parameter. In addition, some accurate estimations of the surface apparent reflectance can be observed outside the gray–shaded planes (called in the Figure legend as outliers), supporting the idea that a balance between the estimated aerosol optical properties, i.e., their radiative effects, can also deal with an accurate surface apparent reflectance estimation.

Impact of surface reflectance heterogeneity in the aerosol optical properties retrieval

As explained in Section 4.4.1, the proposed aerosol optical properties retrieval algorithm was designed to exploit surface reflectance image heterogeneity. Thus, through the selection of a number of pixels (fixed as 5 in this work) a set of vegetated spectra and a bare soil spectrum was used. However, since the FLEX mission is specifically designed for vegetation monitoring, it is of special interest to quantify the impact in the retrieved surface apparent reflectance when only vegetated pixels take part in the aerosol characterization process. To do so, the bare soil spectrum was replaced by a vegetated spectrum with a LAI and Chl. values of 4 [-] and 50 [$\mu\text{g}/\text{cm}^2$], respectively. Then, surface apparent reflectance was estimated for the 240 atmospheric conditions defined in the simulated FLEX–DB. Figure 4.6.5 compares, for the bottom of the O₂–A and O₂–B absorption regions, the associated surface apparent reflectance relative error averaged for the pixels selected in case of: (a) having the bare soil spectrum included in the selected pixels (**Mixed** case, black solid line), or (b) only vegetated surface reflectance spectra (**Vegetation** case, dashed red line).

Figure 4.6.5 indicates that surface heterogeneity reduction impacts negatively the estimated surface apparent reflectance. For the majority of evaluated cases, errors in the surface apparent reflectance are higher when only vegetated spectra are selected as part of the aerosol optical properties retrieval process.

4.6.2 Surface apparent reflectance and fluorescence estimation

Once having the atmospheric state characterized, i.e., total CWV and aerosol optical properties, surface apparent reflectance is estimated by means of Equation 4.4.7. Figures 4.6.6 and 4.6.7 present statistics of estimated ρ_{app} for the 240 cases of the simulated FLEX–DB, for the O₂–B and the O₂–A, respectively.

The following main observations can be derived from Figures 4.6.6 and 4.6.7:

- As expected, an inaccurate estimation of the aerosol optical properties lead to a significant degree of uncertainty in the estimated surface apparent reflectance.
- Significant spectral distortions are generated in the surface apparent reflectance at the oxygen regions, i.e., downward looking peaks.

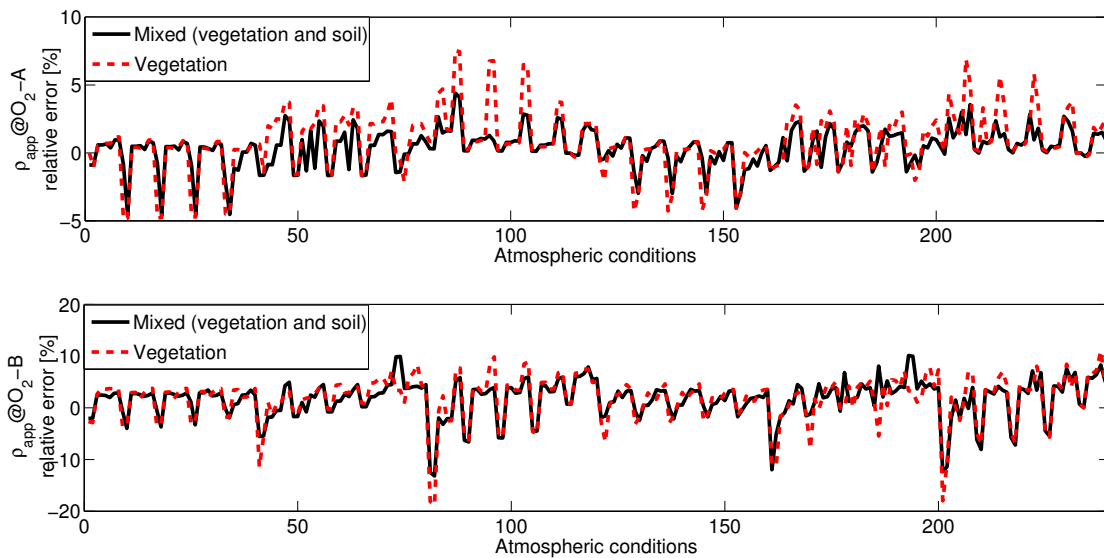


FIGURE 4.6.5: Surface apparent reflectance relative error in percentage [%] for the O₂-A and the O₂-B bottom of the absorption bands. Red dashed lines correspond to relative errors in case only vegetated spectra are used in the aerosol optical properties retrieval algorithm. Black solid line corresponds to the case in which bare soil and vegetated spectra is used.

- As earlier shown in Section 4.6.1, the AOT and the asymmetry parameter of the HG scattering phase function are key to obtain an accurate surface apparent reflectance. This becomes clear, when excluding those cases with errors on g higher than ± 0.05 . Note that excluded points are located outside of the gray planes in Figure 4.6.4.

Estimated SIF is derived after the atmospheric correction process by coupling the PH method together with the SFM. The goal of this section is therefore twofold: (1) to analyse the impact of the atmospheric correction algorithm, and (2) to analyse the impact of the SFM retrieval strategy, both on the resulting SIF signal. To do so, Figure 4.6.8 shows the averaged retrieved SIF signal (black solid line) and the standard deviation (gray shaded areas) for the 240 atmospheric cases. In addition, in order to quantify how large errors in g impact on the resulting SIF signal, those cases with relative errors on g higher than ± 0.05 , have been excluded. Thus, after the filtering, the average SIF signal (red solid line) is now closer to the reference SIF (blue solid line), and the standard deviation have been highly reduced. After filtering, SIF estimation's accuracy and precision were significantly improved for most of the cases, i.e., Pixels #1, #2, #4 and #5. However, even after excluding cases where errors on g are higher than ± 0.05 , the first SIF peak is still insufficiently accurately retrieved in Pixel #3. To analyse better the particularities of Pixel #3, and also to disentangle errors derived because of the atmospheric correction and because of the SIF retrieval strategy, in Figure 4.6.9 estimated SIF assuming a perfect atmospheric correction (using the reference input parameters for the atmospheric inversion) is plotted together with the reference SIF. In Figure 4.6.9, reference and estimated SIF are plotted in blue and black, respectively; while estimated SIF standard deviation is highlighted in gray. It

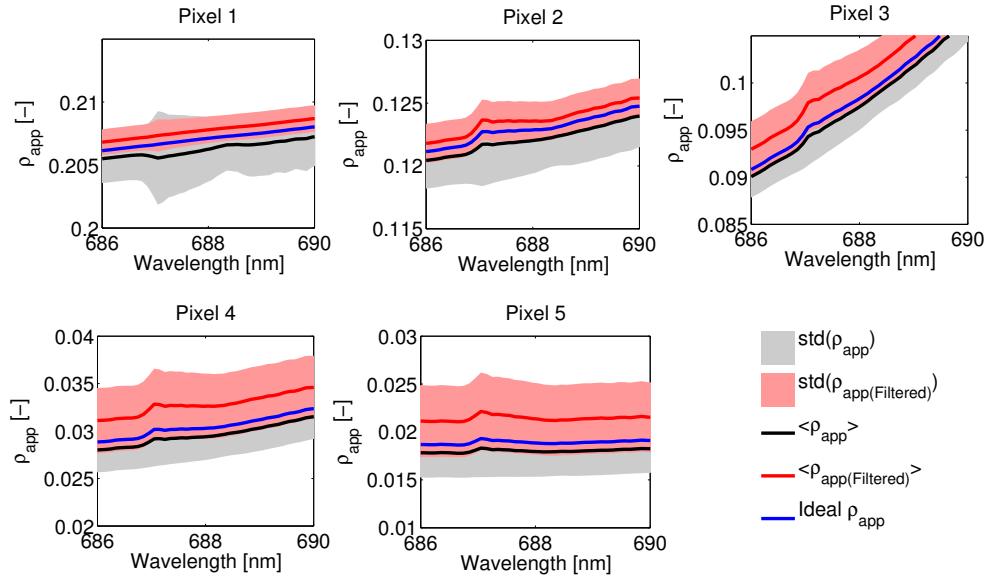


FIGURE 4.6.6: Overview statistics of estimated surface apparent reflectance (ρ_{app}) at the O₂-B region for the 240 cases included in the FLEX-DB. Black solid line and gray area show the averaged $\overline{\rho_{app}}$ and the standard deviation $\pm\sigma(\rho_{app})$ of the 240 cases. Red solid line and reddish areas show the average $\overline{\rho_{app}}$ and the standard deviation $\pm\sigma(\rho_{app})$ when screening out those cases in which the error in the scattering anisotropy estimation was higher than ± 0.05 . Blue solid line is the reference surface apparent reflectance (ρ_{app}) estimated by doing the inversion with the corresponding reference atmospheric parameters (AOT, α , g and CWV) for each case.

can be observed that SIF standard deviation has been drastically reduced, which indicates that the SFM is a precise strategy to retrieve SIF. In addition, the SIF second peak is estimated with higher precision and accuracy than the first peak. This is especially true for Pixel #3, dealing with the conclusion that the current parametrization of the SFM should be slightly improved to be able to reproduce a wider range of SIF spectral shapes. If analysing the values of Chl. content and LAI corresponding to Pixel #3, a low Chl. content was assumed, generating a big asymmetry between the first and the second SIF peaks, both in the SIF_{dir} and the SIF_{hem} .

4.7 Discussion

This section provides a broad perspective of key aspects studied in this work, such as how the accuracy of the atmospheric correction impacts the estimated SIF or the suitability of the formulation assumed for the retrieval strategy. In addition, advantages and disadvantages of using the so-called **two-steps** method are also discussed. Finally, limitations found under this study are listed, providing guidelines to the improvements implemented as part of Chapter 5.

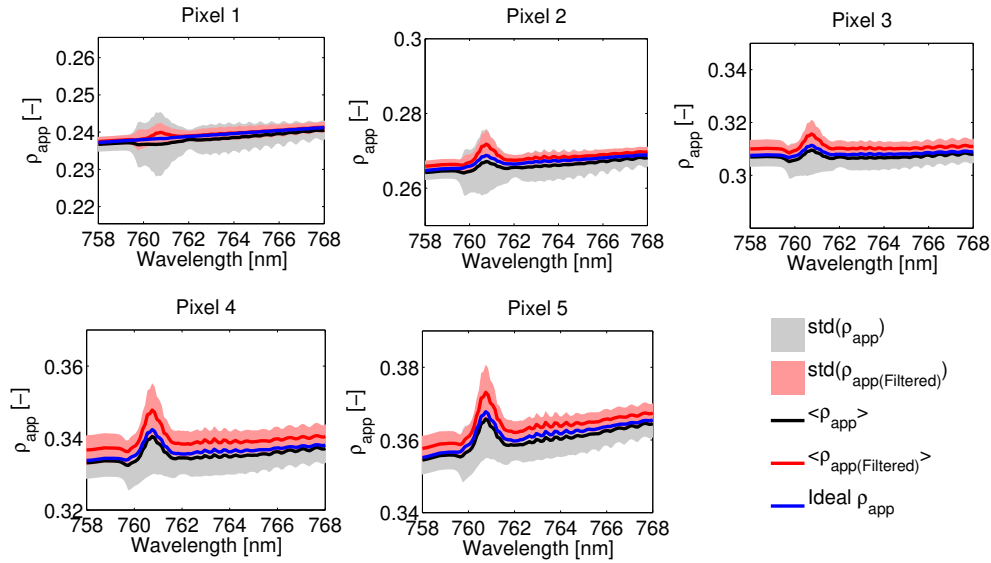


FIGURE 4.6.7: Overview statistics of estimated surface apparent reflectance (ρ_{app}) at the O₂-A region for the 240 FLEX-DB cases. Black solid line and gray area show the averaged $\overline{\rho_{app}}$ and the standard deviation $\pm\sigma(\rho_{app})$ of the 240 cases evaluated. Red solid line and reddish areas show the average $\overline{\rho_{app}}$ and the standard deviation $\pm\sigma(\rho_{app})$ when excluding those cases where the error in the scattering anisotropy estimation was higher than ± 0.05 . Blue solid line is the reference surface apparent reflectance (ρ_{app}) estimated by doing the inversion with the corresponding reference atmospheric parameters (AOT, α , g and CWV) for each case.

4.7.1 Atmospheric correction impact on SIF estimation

As demonstrated in this chapter, errors derived from the atmospheric correction process strongly impact the retrieved surface reflectance, and consequently the estimated SIF. This observation was also reported in the past by [Guanter *et al.*, 2010](#); [Frankenberg *et al.*, 2011a](#), where the impact of atmospheric effects was evaluated on red and/or far-red SIF but not in the full SIF emitted spectrum. Although aerosol retrieval becomes the ‘bottleneck’ due to its strong impact on SIF, accuracy achieved on estimated water vapour also needs to be discussed. Main water vapour absorption bands, centred around 820, 940 and 1300 nm, are not spectrally overlapping with the oxygen features, which are the main regions of interest for SIF estimation under the FLEX framework. Nevertheless, since water vapour continuum affects the red-edge region, it can affect the performance of the SFM, which minimizes spectral differences between 650-800 nm approximately. Consequently, the proposed technique seems adequate since water vapour estimations present relative errors lower than 1%, even in vegetated spectra where assumptions regarding the linear surface reflectance behaviour are not met. Although most of the water vapour techniques are based on measuring the differential absorption generated within the water vapour absorption region (See Section 2.4.2); other techniques that better disentangling the effect of the liquid water content on leaves from the atmospheric water vapour, e.g., curve fitting techniques [[Gao and Goetz, 1990](#); [Ceccato *et al.*, 2001](#); [Cheng *et al.*, 2006](#)] could be tested in

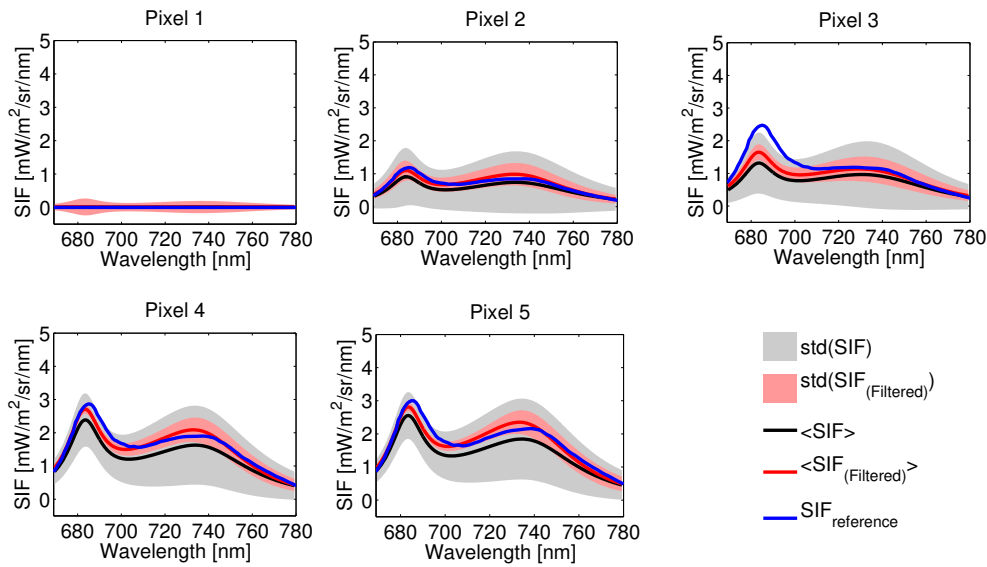


FIGURE 4.6.8: Overview statistics of estimated SIF for the 240 atmospheric conditions simulated in the FLEX-DB. Black solid line and gray area show the averaged \overline{SIF} and the standard deviation $\pm\sigma(SIF)$ of the 240 cases evaluated. Red solid line and reddish areas show the average \overline{SIF} and the standard deviation $\pm\sigma(SIF)$ when excluding those cases where the error in the scattering anisotropy estimation was higher than ± 0.05 . Blue solid line is the reference emitted SIF_{ref} estimated by the process detailed in Section 4.5.2.

the future to quantify their impact or improvement on SIF. Similarly, since water vapour affects SIF estimations because of the spectral range covered, it could also be possible to manage the influence of this spectral region by means of weighting the minimization process of the SFM.

Regarding the influence of the aerosol characterization on the estimated SIF, it has been demonstrated how the aerosol load and the scattering effects significantly impact SIF precision and accuracy. Main aspects related to the followed process to characterize aerosol optical properties are here discussed. For instance, it was assumed that surface reflectance spectra used as part of the modelling process to simulate TOA radiance was selected from a database that stores a variety of surface reflectance spectra ranging from vegetation and bare soils to man-made material, water, etc. In addition, this database is built of both measured and simulated spectra. In case of the simulated spectra, they were generated with different illumination and acquisition geometries, which avoids assuming any approximation to relate nadir and oblique viewing surface spectra, such as in the synergy algorithm developed in [North *et al.*, 2009a]. Also, any approximation to simulate surface reflectance, such as finding the best linear combination of two surface reflectance end-members [Guanter, 2006] was used. Conversely, disadvantages associated to the use of a predefined database are associated to the limited number of spectra stored and how well these spectra fits, in this case, with spectra coming from S3 and FLEX image data.

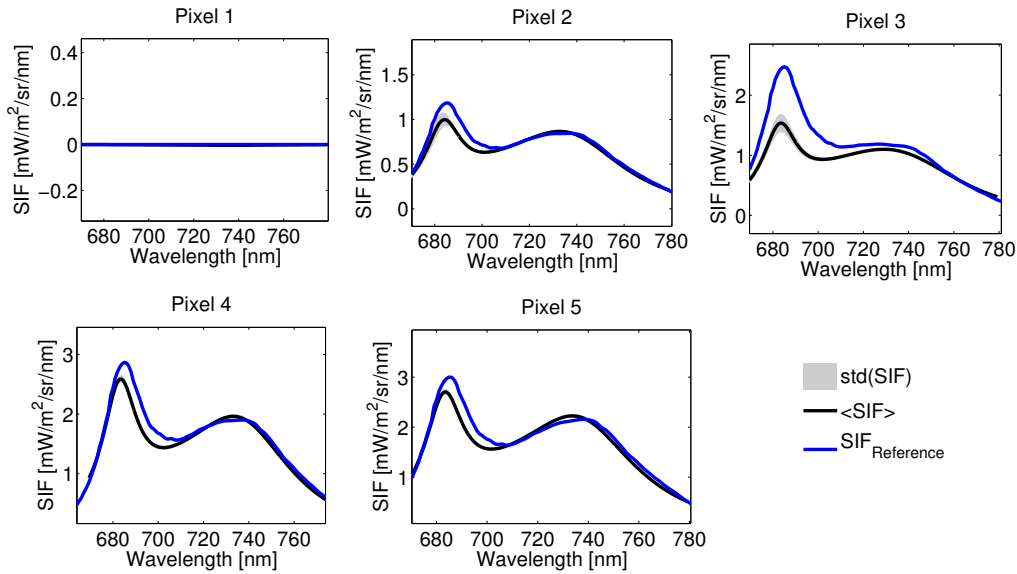


FIGURE 4.6.9: Overview statistics of estimated SIF for the simulated in the FLEX-DB assuming a perfect atmospheric correction. The black solid line and gray area show the averaged \overline{SIF} and the standard deviation $\pm\sigma(SIF)$ of the 240 cases. The blue solid line is the reference emitted SIF_{ref} estimated by the process detailed in Section 4.5.2.

Regarding the aerosol optical parameters to characterize the atmospheric state, two considerations are worth noting. On the one hand, only three aerosol optical properties, i.e., AOT, the Ångström exponent, and the asymmetry parameter of the HG scattering phase function, are considered in this study to characterize the atmospheric state. Although these parameters characterize the aerosol load, shape and scattering pattern, respectively; it may be that the inclusion of other parameters such as the extinction coefficient and the aerosol vertical profile (assumed as fixed in this study) can improve the performance for a wider range of aerosol scenarios. A similar simulation study was recently developed by [Vicent *et al.*, 2017](#). By evaluating the importance of the aerosol optical properties here under discussion it was concluded that the inclusion of the extinction coefficient could help to better represent a wider variety of atmospheric scenarios. However, in any inversion algorithm, when increasing the number free parameters to be inverted, the inversion procedure becomes less stable and therefore more prone to errors. Furthermore, the used inversion algorithm was an iterative process based on: (1) set a first approximation of g , then (2) search the appropriate AOT and ρ spectra, and finally (3) search the α parameter, which was assumed in the previous steps. This process repeated with each time a narrower interval of search and until the AOT value becomes stable. However, the hierarchical search process may affect the estimated results and probably other algorithms that simultaneously search for all the parameters may lead to improved aerosol optical properties estimations.

4.7.2 Impact of the formulation assumed under the proposed two-steps method

The formulation assumed as part of the proposed **two-steps method** to estimate SIF from Level-1b data is here analysed threefold: (1) regarding the atmospheric characterization and inversion process, (2) regarding the assumed fluorescence retrieval strategy, and (3) analysing how these two steps, and consequently the formulation assumed on each, can be consistently coupled. With regards to the formulation considered for the atmospheric correction process some approximations were assumed, such as the series expansion development until second order or the use of a Lambertian surface reflectance. These approximations can affect the accuracy of the estimated surface apparent reflectance and will be evaluated in Chapter 5. In case of the formulation used for the SIF retrieval strategies here applied, they have been reviewed and applied for similar applications [Alonso *et al.*, 2014; Cogliati *et al.*, 2015b]. However, probably the most critical step regarding the assessment of the formulation is not related to the individual performance of these two steps separately, but rather how the formulation developed at each step (for the atmospheric inversion and the fluorescence retrieval) is consistently coupled. This aspect is extensively analysed in Chapter 5, showing the differences especially in the oxygen absorption regions between: (1) radiance measured or simulated at TOC, and (2) radiance derived from the atmospheric correction algorithm (even when assuming a perfect atmospheric characterization). As explained in next chapter, these differences can be quantified either at TOC radiance or at surface apparent reflectance.

4.8 Conclusions

In this chapter main aspects of the FLEX/ Sentinel-3 tandem space mission have been introduced, including a brief analysis of the most sensitive spectral regions of FLORIS instrument to detect SIF. Then, a **two-steps** atmospheric correction algorithm was proposed and evaluated. To do so, a wide range of simulated scenarios (240 atmospheric conditions) were generated in order to evaluate the performance of the algorithm and its suitability for SIF retrieval purposes. Results suggest that the methodology used leads to precise and accurate SIF estimations if aerosol scattering effects and aerosol load are also accurately estimated. Consequently, aiming to improve the general performance of the atmospheric characterization and the full **two-steps method**, formulation assumed through the complete retrieval strategy will be assessed in Chapter 5. The formulation assessment will be particularly focusing on the existing coupling process between the atmospheric correction process and the application of the SIF retrieval strategy. In addition, with the aim of improving the aerosol characterization process to obtain better estimates of SIF, the possible exploitation of the high spectral resolution FLORIS data as part of the atmospheric correction strategy is proposed and evaluated in next chapter.

5

Atmospheric Inversion Effects on Solar–Induced Chlorophyll Fluorescence and apparent reflectance exploitation

Contents

5.1	Abstract	114
5.2	Introduction	115
5.3	The AI process: from TOA radiance to SIF through the apparent reflectance inversion .	116
5.4	Apparent reflectance error analysis and its predictive power	122
5.5	Discussion	130
5.6	Conclusions	133

This chapter is based on :

Neus Sabater, Jorge Vicent, Luis Alonso, Sergio Cogliati , Jochem Verrelst, and José Moreno



Impact of Atmospheric Inversion Effects on Solar–Induced Chlorophyll Fluorescence: Exploitation of the Apparent Reflectance as a Quality Indicator

5.1 Abstract

In the last decade, significant progress has been made in estimating Solar-Induced chlorophyll Fluorescence (SIF) by passive remote sensing techniques that exploit the oxygen absorption spectral regions. As introduced in Chapter 4, although the O₂-B and the deep O₂-A absorption features present a high sensitivity to detect SIF, these regions are also largely influenced by atmospheric effects. Therefore, an accurate Atmospheric Correction (AC) process is required to measure SIF from oxygen bands. In this regard, the suitability of a **two-step** approach, i.e., first an AC and second a Spectral Fitting technique to disentangle SIF from reflected light, is evaluated under this chapter. One of the advantages of the **two-step** approach resides in the derived intermediate products provided prior to SIF estimation, such as surface apparent reflectance. Results suggest that errors introduced in the AC, e.g., related to the characterization of aerosol optical properties, are propagated into systematic residual errors in the apparent reflectance. However, of interest is that these errors can be easily detected in the oxygen bands thanks to the high spectral resolution required to measure SIF. To illustrate this, the predictive power of the apparent reflectance spectra to detect and correct inaccuracies in the aerosols characterization is assessed by using a simulated database with SCOPE and MODTRAN radiative transfer models. In 75% of cases, the aerosol optical thickness, the Ångström coefficient and the scattering asymmetry factor are corrected with a relative error below of 0.5%, 8% and 3%, respectively. These errors in the aerosol optical characterization produce an error in the surface apparent reflectance within the threshold defined varying the emitted SIF a 10% of its value. To conclude with, and in view of future SIF monitoring satellite missions such as FLEX, the analysis of the apparent reflectance can entail a valuable quality indicator to detect and correct errors in the AC prior to the SIF estimation.

5.2 Introduction

As introduced in Section 4.2 of Chapter 4, SIF consists of photons of red and near infra-red light (650–850 nm) that are emitted by chlorophyll foliar pigments in response to absorption of photosynthetically active radiation. At satellite level, the SIF signal is around two orders of magnitude lower than the reflected radiance, which makes its detection by remote sensing instruments challenging. However, SIF emission can still be detected by exploiting the fact that SIF is a proportionally larger fraction of the total radiance within dark lines and bands of the atmospheric spectrum [Joiner *et al.*, 2011]. These dark features include both solar Fraunhofer and telluric absorption regions such as the O₂–B and the O₂–A bands. Taking advantage of this fact, multiple SIF retrieval strategies have been developed in the last decade [Ni *et al.*, 2016]. For instance, some SIF retrieval strategies exploit the Fraunhofer solar lines, which are generally weak and narrow but not as influenced by atmospheric effects as the oxygen bands [Joiner *et al.*, 2011, 2012; Guanter *et al.*, 2012; Khosravi, 2012; Köhler *et al.*, 2015a,b]. Other SIF retrieval strategies use the O₂–A absorption band, which is deeper and wider but is more affected by the atmospheric effects [Guanter *et al.*, 2007a; Damm *et al.*, 2010; Guanter *et al.*, 2010; Mazzoni *et al.*, 2010; Frankenberg *et al.*, 2011a; Raychaudhuri, 2014; Liu *et al.*, 2015; Damm *et al.*, 2014; Cogliati *et al.*, 2015b; Sabater *et al.*, 2015]. Some other strategies exploit both, the O₂–A and some Fraunhofer lines in the retrieval scheme [Guanter *et al.*, 2013; Joiner *et al.*, 2013], and recently, the O₂– γ band has also been used in combination with some solar Fraunhofer lines to anchor the O₂–B band and to provide additional information on red SIF [Joiner *et al.*, 2016a].

At global scale, first SIF maps were retrieved by the exploitation of the Fraunhofer lines from atmospheric chemistry satellite missions (e.g., Joiner *et al.*, 2011, 2012; Guanter *et al.*, 2012; Khosravi, 2012; Köhler *et al.*, 2015a,b; Joiner *et al.*, 2013). However, since these missions were not designed for vegetation monitoring, SIF was detected with a coarse spatial resolution e.g., ~ 10 km for GOSAT–2 and 2.25 km for OCO–2. Conversely, as introduced in Chapter 4, the ESA's Fluorescence Explorer (FLEX) mission [European Space Agency, 2015a] is specifically designed to monitor the health status of terrestrial vegetation and to retrieve the full SIF signal from 650–800 nm at a spatial resolution of 300 m. See Appendix A.2 for more details about the FLuOREscence Imaging Spectrometer (FLORIS) on board FLEX.

Although measurements in the O₂–B and the deep O₂–A absorption bands possess the maximum sensitivity to detect SIF (see Section 4.3), these bands are also highly affected by atmospheric effects, especially by multiple scattering of aerosols and molecules (see Section 4.6). SIF at satellite level is about 1–2 orders of magnitude (depending on the spectral region) lower than the reflected radiance, which implies that any inaccuracy in the Atmospheric Correction (AC) can rapidly make SIF estimation prone to errors [Ni *et al.*, 2016]. Thus, given the importance of the AC as a prior step to the application of any SIF retrieval method, e.g., Spectral Fitting (SF) [Meroni *et al.*, 2010], it is important to analyse how errors and assumptions on AC modify the inverted apparent reflectance. Consequently, this chapter begins with evaluating the mathematical formulation assumed in Chapter 4 for the FLEX/Sentinel–3 data processing scheme [European Space Agency, 2015a], from the Atmospheric Inversion (AI) and to its

coupling with the at–surface level SF method. In the following, the spectral distortions on the apparent reflectance caused by an inaccurate estimation of aerosol optical properties are also evaluated and analysed using simulated data from the Soil Canopy Observation Photochemistry and Energy (SCOPE) [Tol *et al.*, 2009] and the MODerate resolution atmospheric TRANsmission (MODTRAN) [Berk *et al.*, 2005] radiative transfer models. As a result, this chapter proposes the use of the apparent reflectance as quality indicator to refine the AC. Notice that while AC, *atmospheric correction*, includes the atmospheric characterization and the mathematical inversion from Top–Of–Atmosphere (TOA) radiance to surface reflectance, AI, *atmospheric inversion*, refers only to this last step.

This chapter is structured as follows. Section 5.3 introduces and assesses the impact of the mathematical assumptions considered in the FLEX AI and also used in the computations performed in Chapter 4. This part focuses on analysing all the steps required to consistently couple SF fluorescence retrieval with inverted Top–of–Canopy (TOC) apparent reflectance. Section 5.4 evaluates errors derived in the apparent reflectance due to an inaccurate AC process, essentially by an inaccurate aerosol characterization. As an outcome of this analysis, the predictive power of the apparent reflectance to detect and correct the retrieved aerosols optical properties from the AC is tested and evaluated. Section 5.5 discusses the suitability of the mathematical approximations assumed in the AI, highlights the limitations of the presented study and subsequently proposes future in–depth analyses to establish the use of the apparent reflectance as an indicator of inconsistencies in the AC. Finally, Section 5.6 provides the main conclusions.

5.3 The AI process: from TOA radiance to SIF through the apparent reflectance inversion

5.3.1 Assessment of mathematical approximations

As introduced in Chapter 4 (Section 4.4.1); TOA radiance can be expressed by means of Equation 5.3.1 assuming a Lambertian surface reflectance behaviour:

$$L_{sen} = L_0 + \frac{(\frac{E}{\pi}\rho + F)T^\uparrow}{(1 - S\rho)} = L_0 + \frac{E\rho_{app}T^\uparrow}{\pi(1 - S\rho)} \quad (5.3.1)$$

where L_0 is the path radiance (scattered light from the atmosphere), E is the total solar irradiance reaching the surface, T^\uparrow is the total upward transmittance, S is the atmospheric spherical albedo, and ρ_{app} is the so–called apparent reflectance. The term ρ_{app} is defined in turn, as Equation (5.3.2), which accounts for the reflectance and the SIF emission normalized by the solar irradiance at surface level (Figure 5.3.1):

$$\rho_{app} = \rho + \frac{\pi F}{E} \quad (5.3.2)$$

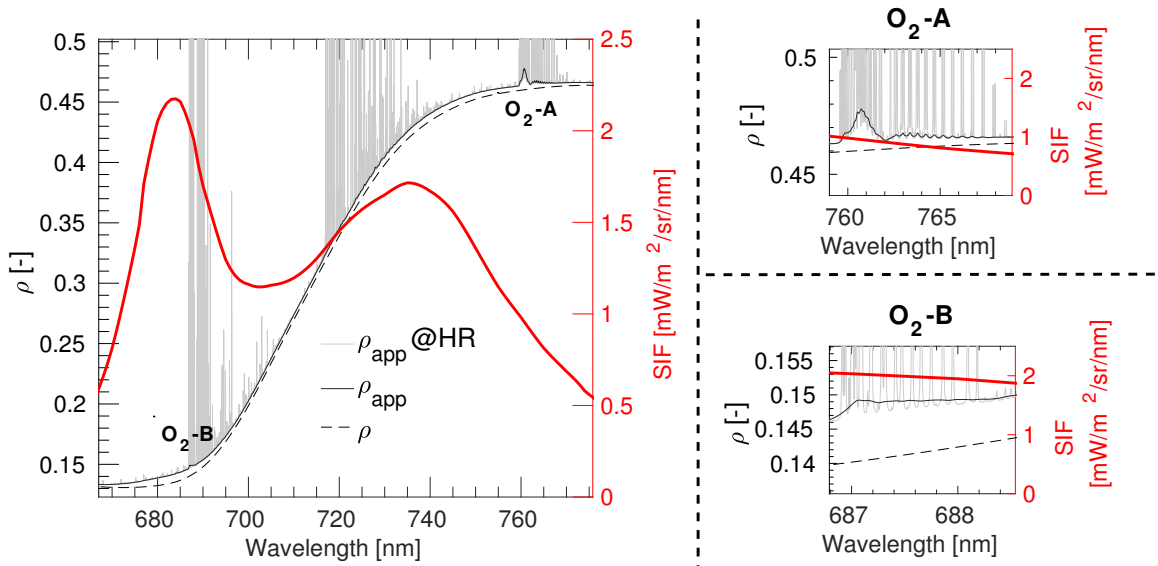


FIGURE 5.3.1: Reference reflectance (ρ), fluorescence (F), and apparent reflectance (ρ_{app}) spectra marked as black dashed line, red solid line and black solid line, respectively. High resolution (HR) ρ_{app} , at 0.1 cm^{-1} , is also shown as a thin grey solid line. The MODTRAN inputs parameters used in the simulation and values used for the spectral convolution are detailed in Table 5.3.1. Reflectance and SIF spectra are mean reference values defined in an internal FLEX technical note [Moreno *et al.*, 2012].

	MODTRAN Input Parameter	Value (Units)
Atmospheric parameter	Model of atmosphere	Mid Latitude Summer
	AOT at 550 nm	0.05(-)
	Angstrom exponent	0.79 (-)
	Henyeý–Greenstein asymmetry (g)	0.8 (-)
	Water vapour	2.4 (g/cm ²)
Geometry parameter	Surface elevation	100 (m)
	Solar Zenith Angle	45 (°)
	Viewing Zenith Angle	0 (°)
	Relative Azimuth Angle between sun and sensor	0 (°)
High Spectral Resolution	Spectral Resolution at O ₂ –B	0.005 (nm)
	Spectral Resolution at O ₂ –A	0.006 (nm)
Instrumental Spectral Response	Spectral function	Double sigmoid *
	Spectral Sampling Interval (SSI)	0.1 (nm)
	Spectral bandwidth (σ)	0.3 (nm)

* The double sigmoid function used as the instrumental spectral response function corresponds to Equation (5.3.3):

$$f_{\lambda}(c, \sigma, s) = \text{sgm}[-s(\lambda - c + \sigma/2)] - \text{sgm}[-s(\lambda - c - \sigma/2)] / \text{sgm}[x] = \frac{1}{1 + e^{-x}}, \quad (5.3.3)$$

where σ is the FWHM, s the slope and c is the barycentre in the wavelength domain.

TABLE 5.3.1: MODTRAN input parameters used to generate Figures 5.3.1–5.3.3. In the particular case of Figure 5.3.2 (a, b) the AOT values range from 0.05 (-) to 0.42 (-), as indicated in the figure legend.

However, note (see Chapter 4) the impossibility of retrieving the reflectance (ρ) and the apparent reflectance (ρ_{app}) terms simultaneously from Equation (5.3.1). To overcome this limitation, the proposed AI for FLORIS data assumes that $S \cdot \rho \approx S \cdot \rho_{app}$, which leads to the following Equation (5.3.4):

$$L_{sen} = L_0 + \frac{E\rho_{app}T^\uparrow}{\pi(1 - S\rho_{app})} \quad (5.3.4)$$

Thus, assuming the atmospheric transfer functions (L_0 , S , E and T^\uparrow) as known, it becomes now possible to invert the apparent reflectance from the radiance acquired by a sensor, L_{sen} . This approximation, however, comes with an associated error, which is illustrated in Figure 5.3.2 (a,b). Here, the relative difference on TOA radiance (%) between using Equations 5.3.1 and 5.3.4 is evaluated for the reference fluorescence and reflectance spectra used in Figure 5.3.1 and various atmospheric conditions (low to high aerosol load). As it is demonstrated, the impact of this approximation on TOA radiance is one order of magnitude lower than the impact caused by an increase of 10% in the SIF emission. The selection of such a threshold for comparison, 10% of the emitted SIF, follows the criteria defined by the FLEX mission [European Space Agency, 2015a].

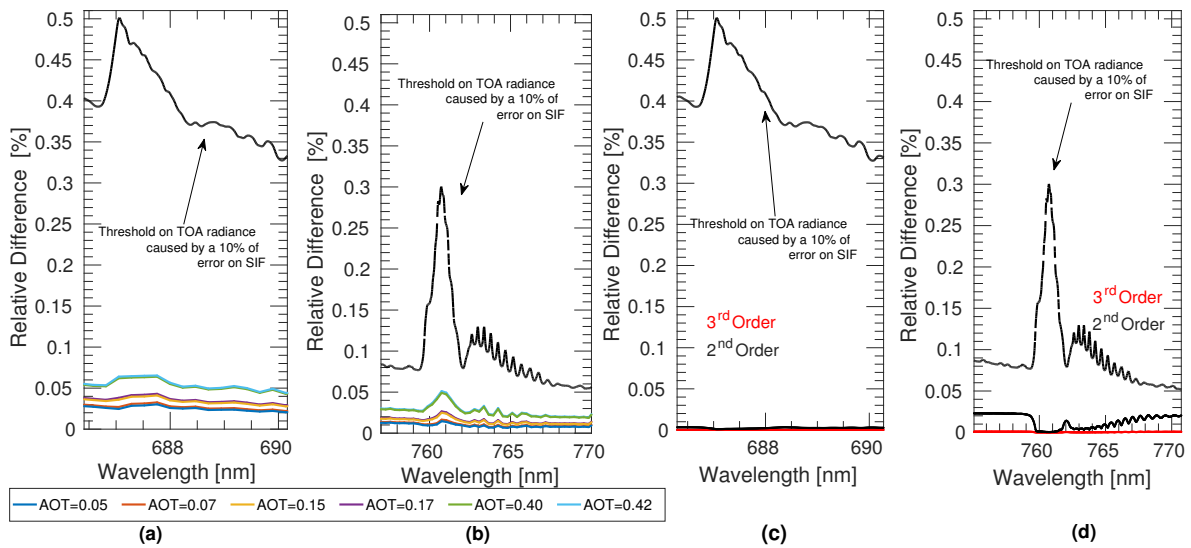


FIGURE 5.3.2: Relative difference on Top-Of-Atmosphere (TOA) radiance (%) between Equations (5.3.1) and (5.3.4) for a range of aerosol loads in the O₂-B (a) and the O₂-A (b) spectral regions. Relative difference on TOA radiance (%) between using the series expansion (2nd or 3rd order) and the TOA radiance expression (Equation 5.3.4) in the O₂-B (c) and the O₂-A (d) spectral regions. MODTRAN inputs parameters used in the simulation and values used for the spectral convolution are detailed in Table 5.3.1.

An additional factor to consider is that the radiance acquired by an instrument, L_{sen} , is spatially and spectrally convolved by its instrumental response function. Consequently, the

isolation of ρ_{app} term from Equation 5.3.4 would imply the convolution of each atmospheric transfer function independently, which would derive a wrong apparent reflectance estimation:

$$\rho_{app} \neq \frac{L_{sen} - \langle L_0 \rangle}{\langle \frac{ET^\dagger}{\pi} \rangle + (L_{sen} - \langle L_0 \rangle) \langle S \rangle} \quad (5.3.5)$$

This inequality exists because the convolution of the product of two given functions is not mathematically equivalent to the product of these functions convolved, i.e., $\langle a \cdot b \rangle \neq \langle a \rangle \cdot \langle b \rangle$. This fact becomes especially relevant when working with non-smooth functions, such as the atmospheric transfer functions within the absorption regions and at high spectral resolution. In order to derive ρ_{app} and thereby avoiding errors associated with the convolution of each individual atmospheric transfer function, it is possible to take the original series expansion in Equation 5.3.6. As such, the high spectral resolution atmospheric transfer functions provided by a radiative transfer model (e.g., MODTRAN [Berk *et al.*, 2005], 6S [Vermore *et al.*, 1997b]) can now be multiplied and then convolved with the corresponding Instrumental Spectral Response Function (ISRF):

$$L_{sen} = \langle L_0 \rangle + \langle \frac{E}{\pi} T^\dagger \rangle \rho_{app} + \langle \frac{E}{\pi} S T^\dagger \rangle \rho_{app}^2 + \langle \frac{E}{\pi} S^2 T^\dagger \rangle \rho_{app}^3 + \dots \quad (5.3.6)$$

Hence, it is necessary to evaluate until which order the series expansion in Equation 5.3.6 must be taken so that the errors in the inverted apparent reflectance are below a required threshold. In this case, the threshold has been defined as the relative difference in ρ_{app} caused by increasing the SIF emission 10% of its value. Figure 5.3.2 (c,d) evaluates the relative difference (%) on TOA radiance between taking the series expansion expression (Equation 5.3.6) until the 2nd and 3rd order and its convergence (Equation 5.3.4) in the O₂-B and the O₂-A regions, respectively. As can be observed, the error derived from the 2nd order approximation is one order of magnitude lower than the impact caused by the defined threshold. Consequently, FLEX AI inverts ρ_{app} by resolving a second order equation:

$$\rho_{app(atm)} = \frac{-\langle ET^\dagger \rangle + \sqrt{\langle ET^\dagger \rangle^2 - 4\langle ET^\dagger S \rangle \pi (\langle L_0 \rangle - L_{sen})}}{2\langle ET^\dagger S \rangle} \quad (5.3.7)$$

Note that the suffix (*atm*) in Equation 5.3.7 distinguishes between the apparent reflectance obtained from an AI process, $\rho_{app(atm)}$, and from the definition presented in Equation 5.3.2, ρ_{app} .

5.3.2 Coupling spectral fitting and apparent reflectance

In order to couple consistently the AI with the SF, it is necessary to understand the difference between ρ_{app} (introduced in Equation 5.3.1) and $\rho_{app(atm)}$ (after the AI from Equation 5.3.6) [Verhoef *et al.*, 2014]. Even in the ideal case of a perfectly characterized atmosphere, the

mathematical approximations presented in Section 5.3.1 introduce discrepancies between these two apparent reflectance expressions (see Figure 5.3.3).

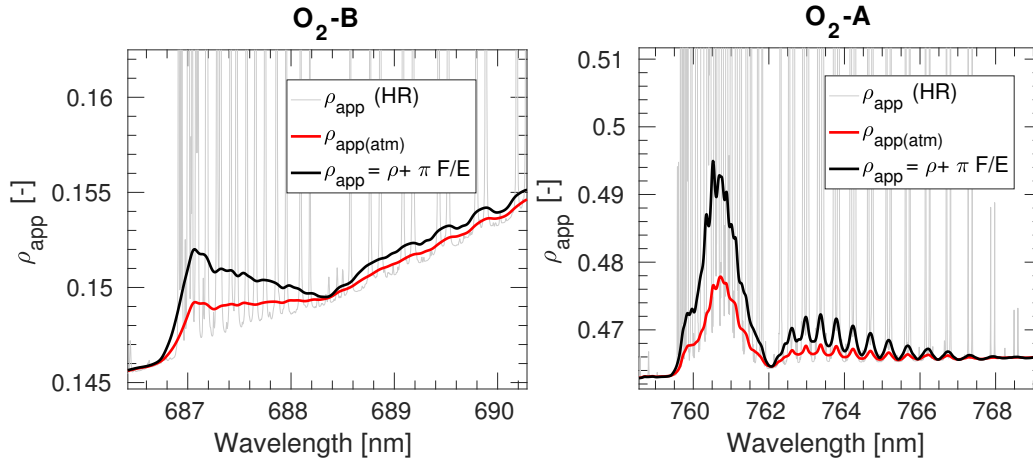


FIGURE 5.3.3: Apparent reflectance ρ_{app} (black) computed as $\rho + \pi F/E$, and apparent reflectance $\rho_{app(atm)}$ (red) from an atmospheric inversion process where all the atmospheric parameters are perfectly known for the O₂-B (a) and O₂-A (b) spectral regions. HR ρ_{app} , at 0.1 cm^{-1} , is also shown as a thin grey solid line. MODTRAN inputs parameters used in the simulation and the values used for the spectral convolution are detailed in Table 5.3.1.

SF methods such as [Cogliati et al., 2015b](#); [Meroni et al., 2010](#) are generally based on the minimization between: (1) the sensor acquired radiance, measured at surface level; and (2) the simulated radiance, built from $L_{toc} = \frac{E\rho}{\pi} + F$ with parametric expressions for ρ and F (see Section 4.4.2 for more details). However, in the case of airborne or satellite scale, radiance at surface level comes from an AI procedure. Thus, in order to couple consistently AI with SF, two alternatives can be considered (Figure 5.3.4):

- *Option 1*: To perform the SF method at TOA level, thereby minimizing the difference between the radiance acquired by the spaceborne instrument and the simulated radiance using Equation 5.3.1.
- *Option 2*: To perform the SF method at TOC level, thereby minimizing the difference between the atmospherically corrected radiance (or apparent reflectance) and the simulated radiance (or apparent reflectance) accounting for the AI procedure.

Note that in Figure 5.3.4 the inconsistent coupling process is also described and labelled as Wrong Option 2. In this case, the discrepancy between the simulated, ρ_{app} , and the inverted, $\rho_{app(atm)}$, shown in Figure 5.3.3 would therefore lead to an inconsistent minimization process, and hence to an erroneous SIF estimation.

Here, the coupling process performed at TOC is analysed. While both options are valid (*Option 1* and *Option 2*), coupling at TOC implies the retrieval of the $\rho_{app(atm)}$ as an intermediate product, which has the additional advantage that it can be used as a quality indicator of the

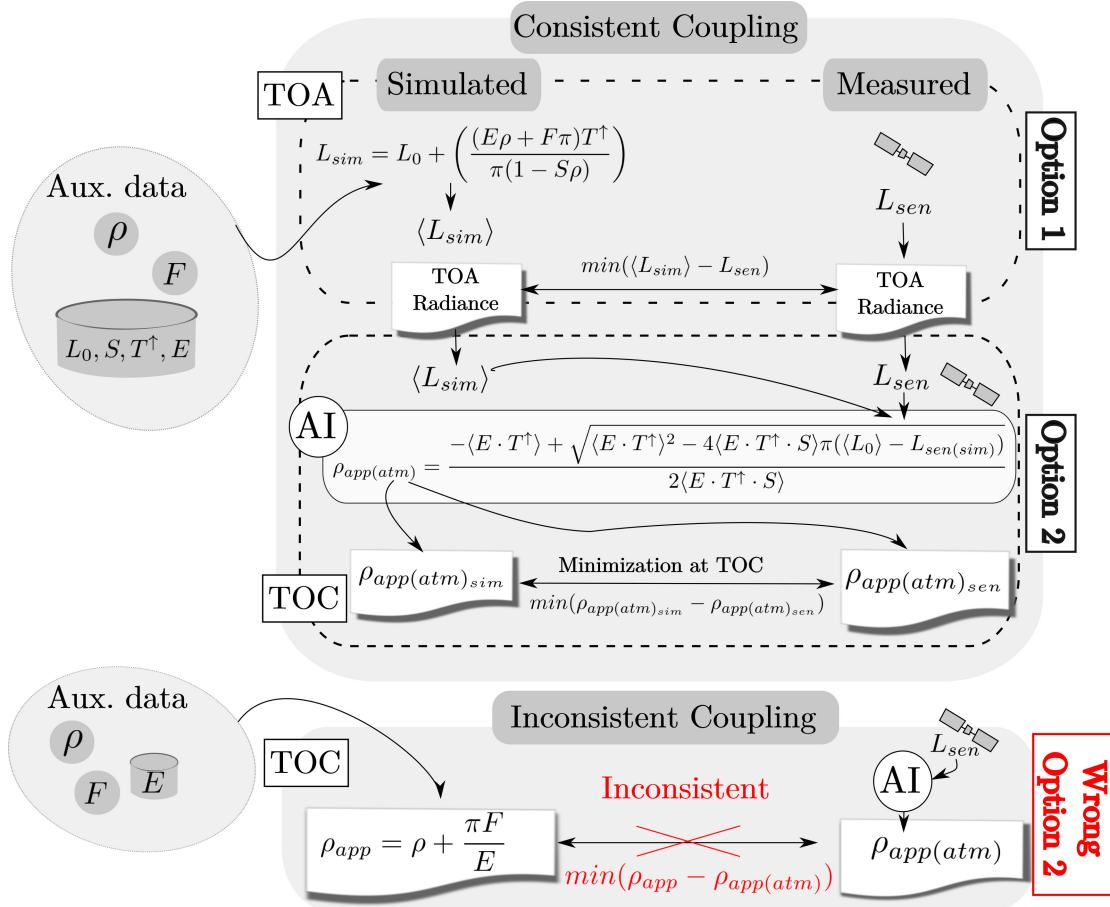


FIGURE 5.3.4: Processing scheme detailing the two possible consistent options described to couple Atmospheric Correction (AC) and Spectral Fitting (SF) methods: (*Option 1*) at TOA, and (*Option 2*) at the TOC level. In *Option 2*, the suffix *sen* and *sim* on $\rho_{app(atm)_{sen}}$ and $\rho_{app(atm)_{sim}}$ indicates if radiance in the AI, $L_{sen(sim)}$, is measured by the sensor or simulated according to Equation (5.3.1). Additionally, the inconsistent coupling process is also described at the TOC level (*Wrong Option 2*).

atmospheric correction process (see Section 5.4.2). Therefore, the impact of coupling consistently (*Option 2*) and inconsistently (*Wrong Option 2*, from Figure 5.3.4) the AI process and the SF method into the retrieved SIF in the O_2 -A absorption region is evaluated. This evaluation was conducted in set of wavelength intervals labelled as R1, R2, R3 and R4 corresponding to (759.3–765) nm, (759.3–767.5) nm, (759.3–770) nm and (759.3–772) nm. In addition, a range of atmospheric aerosol load was simulated to test its influence under both coupling processes. Surface reflectance and SIF spectra, ρ and F , were modelled as quadratic functions. The first guess of the ρ polynomial coefficients was estimated by fitting the ρ_{app} with a quadratic function in the spectral region around the O_2 -A but avoiding the absorption band. The first guess of the F polynomial coefficients was estimated by fitting the reference F spectrum to a quadratic function.

Figure 5.3.5 shows the relative error between the retrieved and the reference SIF spectrum evaluated at the bottom of the O_2 -A absorption band for:

- An inconsistent coupling process, i.e., modelling ρ_{app} at TOC as $\rho_{app} = \rho + \frac{\pi \cdot F}{E}$. The inconsistent coupling causes a large relative error between the retrieved and the reference SIF values for all of the minimization wavelength intervals considered (R1–R4). In addition, a slight dependency on the Aerosol Optical Thickness (AOT) can also be observed.
- A consistent coupling between AI and SF as introduced in Figure 5.3.4 (*Option 2*). In this case, all of the SIF retrieved values (i.e., for the different AOT) are overlapping, meaning that when the atmospheric state is perfectly known, the retrieved SIF is completely independent from the AOT value. Consequently, the accuracy of the SF minimization process only depends on the wavelength interval considered.

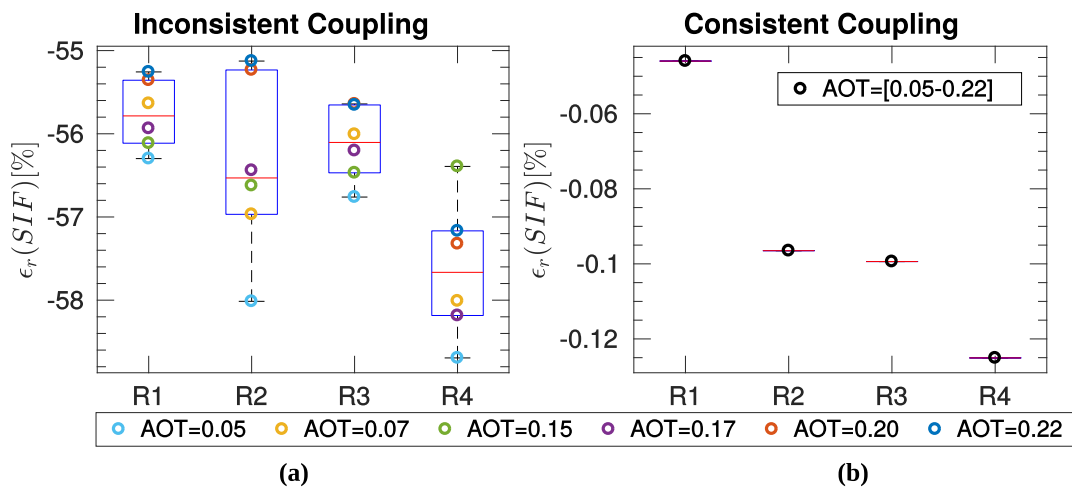


FIGURE 5.3.5: Relative error (ϵ_r) between retrieved and reference SIF values at the bottom of the O_2 –A absorption band, 760.7 nm, covering different values of AOT at 550 nm and wavelength intervals (R1–R4) for an inconsistent coupling process (a) and a consistent coupling process (b). The following error statistics are provided: median (horizontal red line), 25th and 75th percentiles (blue boxes) and extreme min/max values (black dashed lines).

Note that in both cases atmospheric transfer functions were assumed as known. Thus, the larger error derived in the inconsistent coupling case is mainly caused by the different ρ_{app} and $\rho_{app(atm)}$ definitions. Consequently, because of the different definitions used, estimated SIF strongly depends on AOT only in the inconsistent coupling process. Conversely, in both coupling strategies, residual relative errors appear according to the wavelength interval defined.

5.4 Apparent reflectance error analysis and its predictive power

5.4.1 Spectral error analysis on apparent reflectance

This section analyses the spectral distortions in $\rho_{app(atm)}$ caused by an inaccurate AC, fundamentally due to errors in the estimation of aerosol optical properties. We emphasized the

aerosol optical properties since aerosol characterization can be considered as one of the main sources of uncertainty when retrieving SIF from space [Frankenberg *et al.*, 2011a]. However, it must be noted that distortions in $\rho_{app(atm)}$ can also be caused by other factors such as: an inaccurate instrumental spectral characterization [Vicent *et al.*, 2015], instrumental radiometric calibration errors or an inaccurate surface pressure estimation. While the characterization of other key atmospheric parameters such as the Water Vapour (WV) or the ozone (O_3) are also crucial in any AC algorithm [Guanter *et al.*, 2007b; Vermote *et al.*, 2002; Cooley *et al.*, 2002], their radiometric effect can be neglected in the O_2 absorption regions, whereas the aerosol radiometric effect cannot. Thus, the spectral distortions derived from an inaccurate estimation of the following aerosol optical properties are studied ¹:

- The AOT, which is directly related to the total aerosol load in a vertical atmospheric column, becoming the greater aerosol load the higher the AOT value.
- The Ångström exponent (α) [Ångström, 1929], which accounts for the AOT spectral variation and is associated with the aerosol size, becoming the higher (α) exponent the smaller aerosol size.
- The asymmetry parameter (g) of the Henyey–Greenstein (HG) scattering phase function [Henyey and Greenstein, 1941], which indicates the anisotropy of the scattering pattern, being this parameter limited to $[-1, 1]$. The g parameter takes the value -1 and 1 for a full backward and forward scattering respectively, while taking the value 0 for an isotropic scattering pattern.

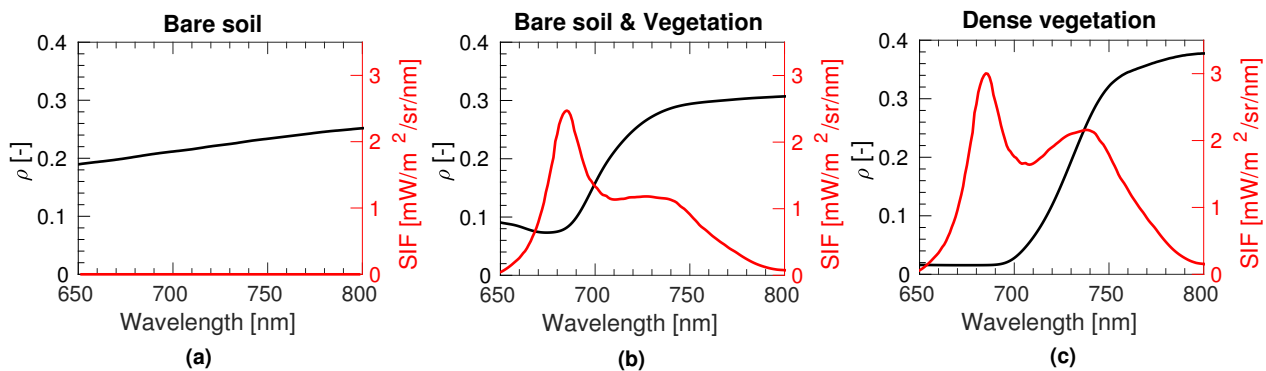


FIGURE 5.4.1: (a) bare soil, (b) mixed bare soil and vegetation, and (c) vegetation surface reflectance and fluorescence spectra simulated with the version 1.53 of SCOPE model. The corresponding biophysical parameters of Leaf Area Index (LAI) and Chlorophyll (Chl) content used in the simulations are detailed in Table 5.4.1.

These three possible causes of distortions are evaluated over three different surfaces types (see Figure 5.4.1): (a) a bare soil, (b) a mixture of vegetation and bare soil and (c) a dense

¹Note that aerosol optical properties studied in Chapter 4 are also here evaluated in Chapter 5

vegetation. We selected this variety of spectra to ascertain if errors derived from the AC produced a systematic error in the surface apparent reflectance, $\rho_{app(atm)}$, regardless of the nature and shape of the underlying surface. LAI and *Chl* content used to model surface reflectance and emitted SIF spectra are detailed in Table 5.4.1.

	LAI(-)	<i>Chl</i> (g/cm ²)
Bare soil (a)	0	0.47
Mixed bare soil and dense vegetation	0.5	40
Mixed bare soil and dense vegetation (b)	1.5	10
Mixed bare soil and dense vegetation	2.5	40
Dense vegetation (c)	4	70

TABLE 5.4.1: Biophysical parameters, LAI and *Chl* content used as input in the SCOPE model (v1.53) to generate the simulated DB. Spectra labelled as (a), (b), and (c) corresponds to the spectra showed in Figure 5.4.1. LAI and *Chl* values are equivalent to those used in Chapter 4 for *Pixels* 1–5.

This section thus performs an assessment of how an erroneous estimation of aerosol optical properties leads to spectral distortion on the $\rho_{app(atm)}$. Particularly, the main objective is to quantify (a) how the spectral distortion pattern depends on the evaluated aerosol optical variable, and more specifically, (b) if these distortions can be totally disentangled from the underlying surface reflectance and SIF emission. To account for that, TOA radiance spectra were simulated following Equation 5.3.1 using the three surface reflectance and SIF emission spectra from Figure 5.4.1, and assuming a reference atmospheric state defined by AOT = 0.16, $\alpha = 1.39$ and $g = 0.75$. Afterwards, by using Equation 5.3.7, the AI was performed by overestimating and underestimating the AOT, the α and the g values used as a reference in the simulation. In Figures 5.4.2 and 5.4.3, the over/underestimation is represented as a percentage of the initial values on the Y-axis, while the differences in $\rho_{app(atm)}$ are shown in a color scale. Main findings for the O₂–B region are summarized as follows:

- The over/underestimation of the AOT causes an under/overestimation of $\rho_{app(atm)}$ in SIF emitting surfaces, i.e., partially–mixed or dense vegetation, while the opposite effect is observed in non–SIF emitting surfaces, i.e., bare soil.
- Errors in the the Ångström parameter (α) hardly lead to errors in $\rho_{app(atm)}$. However, the spectral distortion appears to be driven by the underlying surface reflectance, the spectral distortions being more abrupt for the bare soil and the mixed vegetation and bare soil than in a full vegetation spectrum.
- The asymmetry parameter (g) of the HG scattering phase function is clearly the driving parameter that causes the strongest distortion in the $\rho_{app(atm)}$. Additionally, the spectral distortions mostly follow a similar spectral pattern regardless of the surface reflectance spectra.

The main findings for the O₂–A region are summarized as follows (see Figure 5.4.3):

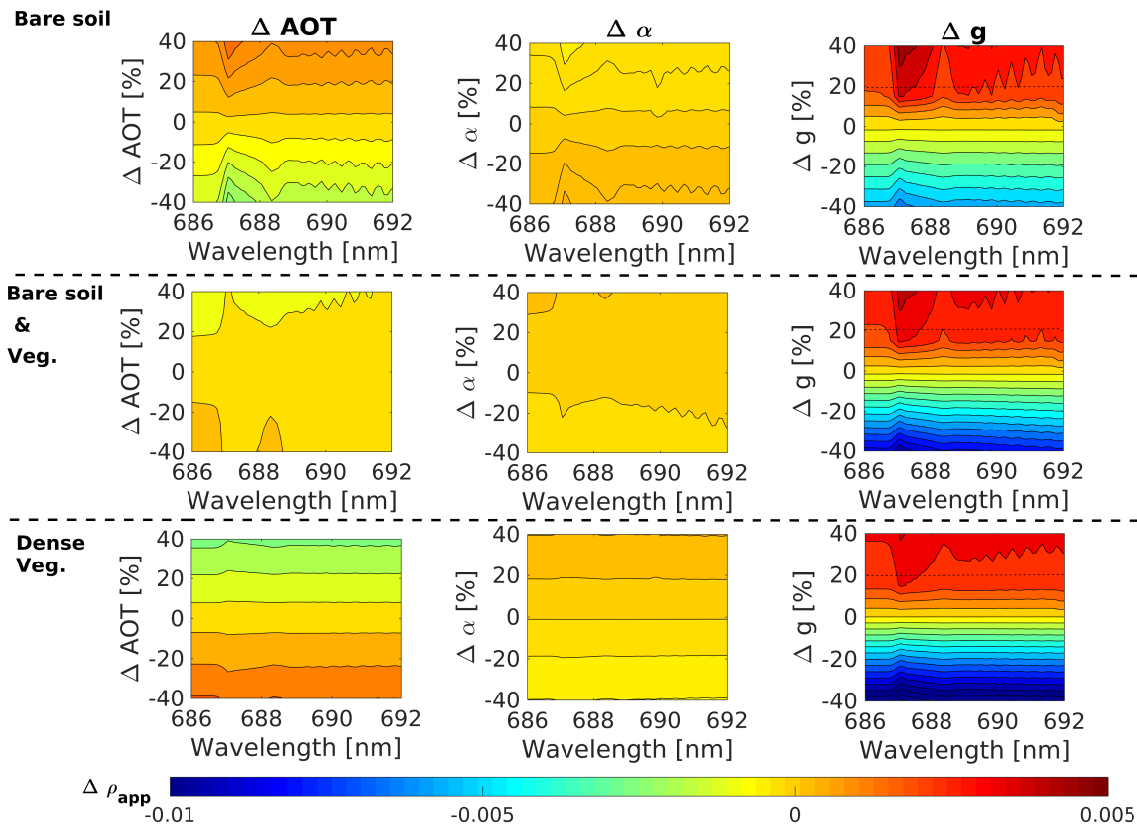


FIGURE 5.4.2: Apparent reflectance spectral distortion caused by an over/underestimation of the AOT, α and g aerosol optical properties for three different surfaces at the O₂-B absorption band at FLORIS spectral resolution. The dashed horizontal black line over the g parameter figures delimits the area where the ρ_{app} spectral distortions have been computed by extrapolating g values higher than 1.

- Spectral distortions in the O₂-A caused by each aerosol optical property follow a similar distortion pattern regardless of the surface reflectance and the fluorescence emission. Due to the deepest absorption in the O₂-A band, this region seems spectrally more sensitive to aerosol over/underestimation.
- Although distortions on $\rho_{app(atm)}$ produced by changes in the AOT and g , which are the driving parameters, are approximately on the same order of magnitude, the spectral distortion pattern is slightly different.
- As in the O₂-B region, the over/underestimation of the α parameter produces a weaker spectral distortion than those produced by the AOT and the g parameters.

Note that the spectral distortion patterns observed in both O₂ regions are the result of: (1) the specific shape of the reflectance and the fluorescence emission spectra, and (2) the distortions in the atmospheric transfer functions.

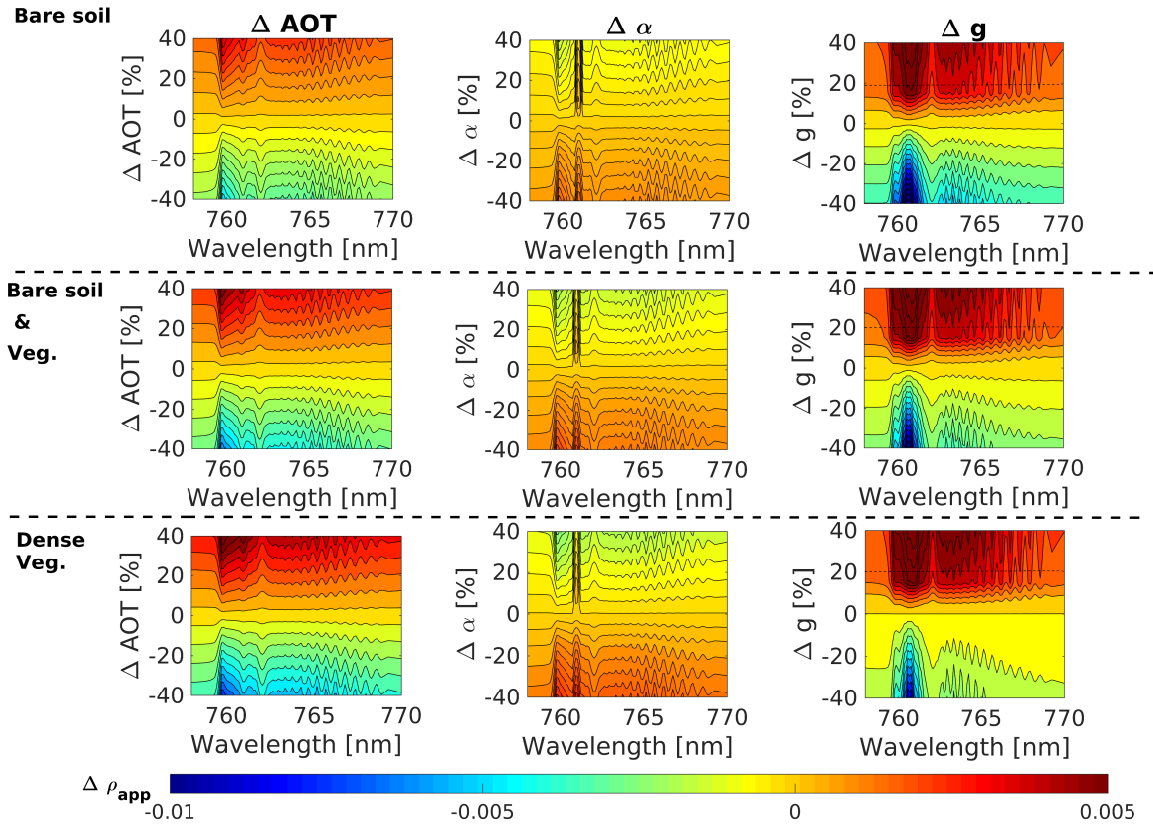


FIGURE 5.4.3: Apparent reflectance spectral distortion caused by an over/underestimation of the Aerosol Optical Thickness (AOT), α and g aerosol optical properties for three different surfaces at the O_2 -A absorption band for the FLORIS spectral resolution. The dashed horizontal black line over the g parameter figures delimits the area, where the ρ_{app} spectral distortions have been computed by extrapolating g values higher than 1.

5.4.2 Spectral distortions in the apparent reflectance as quality indicator of the atmospheric correction

In Section 5.4.1, it was demonstrated that errors in the retrieved aerosol optical properties lead to specific spectral distortions in the $\rho_{app(atm)}$. In this section, the idea of using the retrieved $\rho_{app(atm)}$ spectra to infer errors in the aerosol optical properties, i.e., ΔAOT , $\Delta \alpha$ and Δg is explored. In this way, for a given known instrumental response, $\rho_{app(atm)}$ could be used to refine the characterization of atmospheric parameters. As a proof of concept, a database (DB) containing a set of simulated TOA radiance spectra was created using MODTRAN and SCOPE. At the surface level, five reflectance and SIF spectra were used (three of them shown in Figure 5.4.1 and two additional spectra between the mixed vegetation and bare soil cases (b) and (c)). The corresponding LAI and *Chl* of the five spectra selected are detailed in Table 5.4.1. For the atmospheric transfer functions simulations, all possible combinations of reference values of the atmospheric parameters $AOT = 0.16$, $\alpha = [1.39, 1.54, 1.74]$, $g = [0.75, 0.8]$, $WV = [1.2, 2.4]$ g/cm^2 and surface elevation $h = [100, 1500]$ m, assuming the viewing and illumination

geometric conditions detailed in Table 5.3.1 are covered. The motivation of these reference values is as follows:

- to select a medium AOT value to evaluate the aerosols effect but avoiding extreme cases [Dubovik *et al.*, 2002];
- to range variations around the α and g values of 1.54 and 0.8, respectively, which corresponds to typical values found for continental aerosol types [Hess *et al.*, 1998];
- to simulate the effect of the surface pressure by including two different altitudes;
- to determine if the different WV content impacts the predictive power of the $\rho_{app(atm)}$ on the O₂–B absorption region.

For each TOA radiance spectra, the surface apparent reflectance was atmospherically inverted by over/underestimating the corresponding reference values of AOT, α and g by a factor of 0%, $\pm 5\%$, $\pm 15\%$, $\pm 25\%$ and $\pm 50\%$ (all possible combinations). Accordingly, the DB comprised a collection of more than $\sim 8 \cdot 10^4$ wrongly corrected $\rho'_{app(atm)}$ spectra and its corresponding wrongly estimated values of AOT', α' and g' . As an extra parameter, the Normalized Difference Vegetation Index (NDVI') was also computed from ρ'_{app} and stored in the DB. The NDVI' values were included to add an extra source of information related to the surface reflectance spectral shape out of the oxygen absorption regions. Therefore, following the multivariate linear regression formulation, $Y = MX$, the used input values (X) were: ρ'_{app} , AOT', α' , g' , and the NDVI' index. The output values (Y) were the Δ AOT, $\Delta\alpha$ and Δg , i.e., the over-/under-estimation of each aerosol parameter in percentage [%]. In order to accelerate the regression process, the spectral DB dimensionality was reduced by means of applying a Principal Component Analysis (PCA) technique, taking the first 50 components. Then, 30% of the DB was randomly selected to train, i.e., to obtain the multivariate linear regression coefficient matrix $M = (X^T \cdot X)^{-1} \cdot X^T \cdot Y$. Afterwards, the remaining 70% of the DB was used to *test* the retrieved outputs ($\widehat{\Delta AOT}$, $\widehat{\Delta\alpha}$ and $\widehat{\Delta g}$) versus their reference counterparts (Δ AOT, $\Delta\alpha$ and Δg). For clarification, all steps concerning the DB simulation, regression training and testing are summarized in Figure 5.4.4.

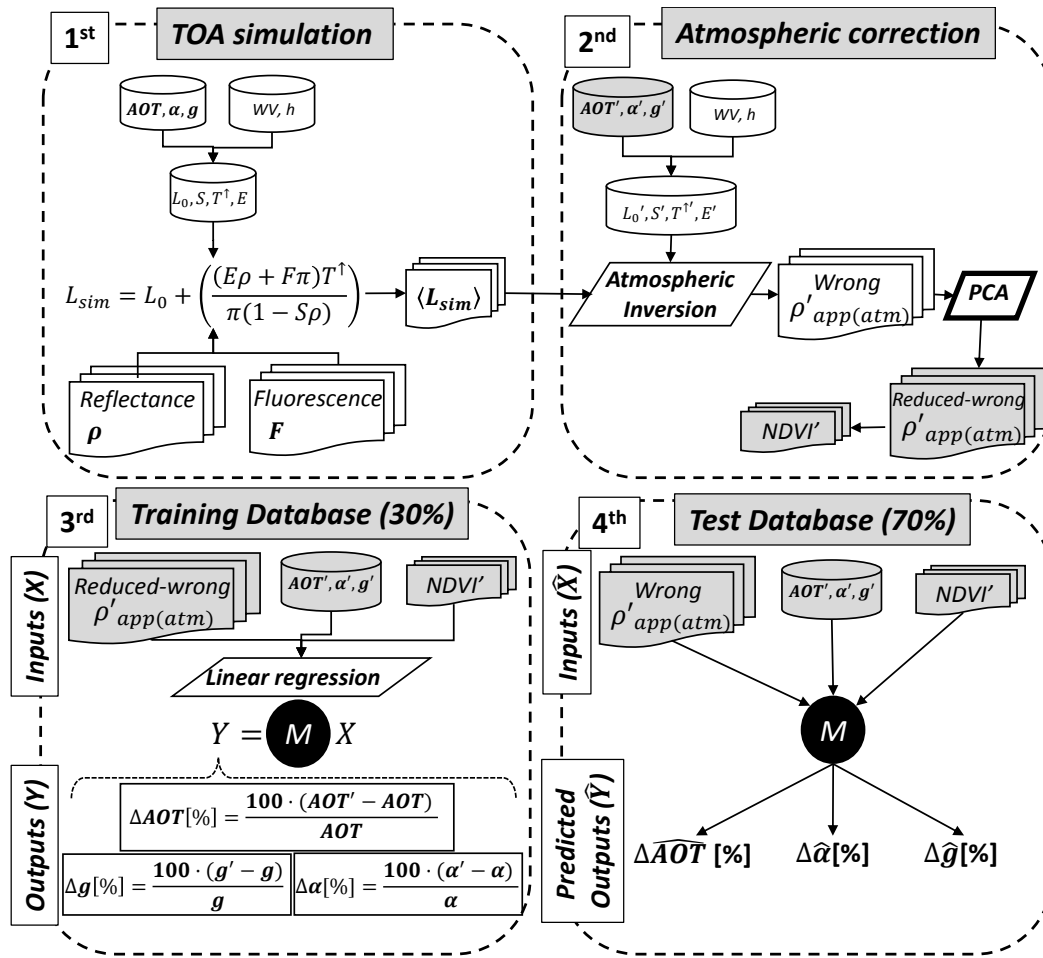


FIGURE 5.4.4: Database (DB) generation process: TOA radiance simulation (1st) and atmospheric correction process (2nd). DB multivariate linear regression training (3rd) and validation (4th) processes. Grey-shaded boxes correspond to the multivariate linear regression inputs.

Regarding the predictive power of the ρ_{app} to correct the estimation of the aerosols optical properties retrieval, Figure 5.4.5 summarizes the results obtained for the O₂-B and the O₂-A absorption bands.

For both oxygen regions, the applied method reduces in 75% of the validation cases the errors below 0.5%, 8% and 3% for aerosol parameters AOT, α and g , respectively. As expected, and in agreement with the results in Section 5.4.1, the predictions of the $\Delta \hat{\alpha}$ coefficient are much less sensitive than predictions of the $\Delta \hat{AOT}$ and the $\Delta \hat{g}$ parameters. In addition, results suggest that the linear regression predicts the over/underestimation of the aerosol optical properties precise enough despite including different input values of WV and surface pressure. However, to quantify this effect, the same statistics as showed in Figure 5.4.5, but only considering one WV and surface pressure value in the DB (not shown) were computed. As expected, obtained results were in 75% of the validation cases slightly better than in the full DB case, deriving relative errors below 0.2%, 6% and 2% for aerosol parameters AOT, α and g , respectively.

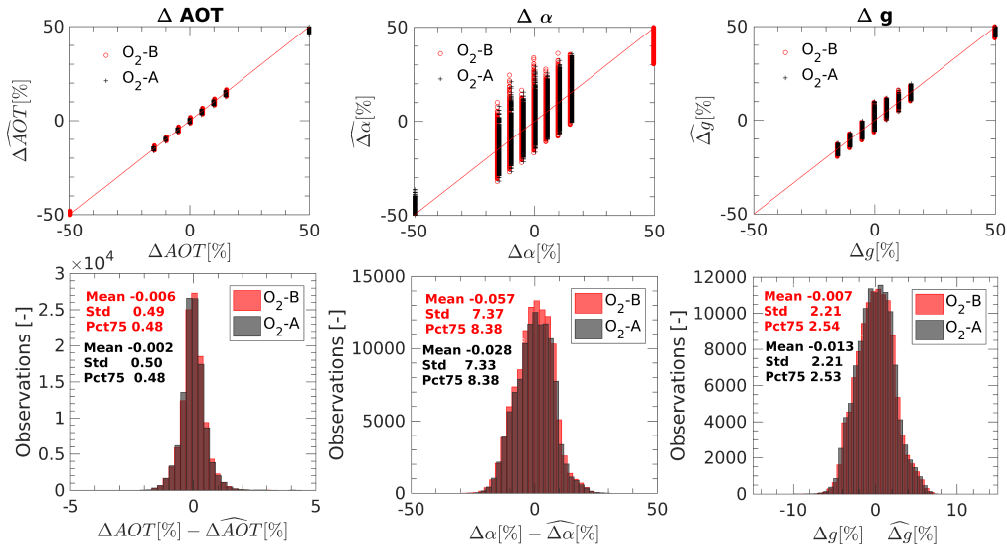


FIGURE 5.4.5: (upper row) Scatter plots for the retrieved ($\widehat{\Delta AOT}$, $\widehat{\Delta \alpha}$, and $\widehat{\Delta g}$) versus the reference (ΔAOT , $\Delta \alpha$ and Δg) parameters. (bottom row) Histograms showing the difference between the retrieved and the reference parameters, i.e., $\widehat{\Delta AOT} - \Delta AOT$, $\widehat{\Delta \alpha} - \Delta \alpha$, and $\widehat{\Delta g} - \Delta g$.

Finally, estimated errors on the aerosol optical properties (AOT, α , and g) have been propagated into $\rho_{app(atm)}$ for the mixed bare soil and vegetated spectrum, and the dense vegetated spectrum (Figure 5.4.1 cases (b) and (c), respectively). Thus, taking errors reported in Figure 5.4.5 for each of the aerosol optical properties; $\rho_{app(atm)}$ spectra was derived by following Equation 5.3.7 and considering the three scenarios detailed in Table 5.4.2.

	Reference scenario	Over-estimated scenario	Under-estimated scenario
AOT	0.16	0.16+0.5%(0.16)	0.16-0.5%(0.16)
α	1.54	1.54+8%(1.54)	1.54-8%(1.54)
g	0.8	0.8+2.5%(0.8)	0.8-2.5%(0.8)

TABLE 5.4.2: Aerosol optical properties assumed in the AI for the three scenarios.

In Figure 5.4.6, estimated $\rho_{app(atm)}$ under the three scenarios detailed in Table 5.4.2, i.e., reference overestimated and underestimated, is plotted. In addition, $\rho_{app(atm)}$ threshold caused by increasing and decreasing SIF a 10% of its value is also shown. As can be observed, for all the cases evaluated in the O₂-B regions, estimated ρ_{app} is under the mission requirement. In case of the O₂-A region, only the case of the mixed bare soil and vegetated spectrum the overestimated scenario is slightly beyond the mentioned threshold.

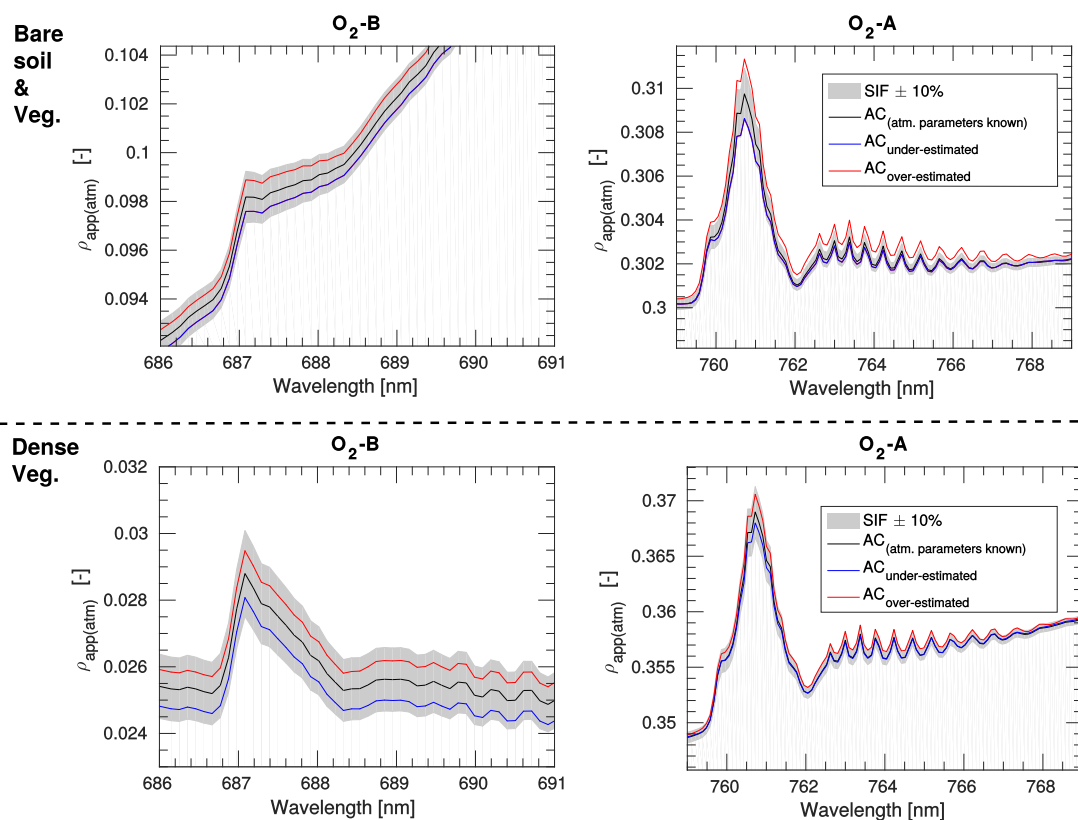


FIGURE 5.4.6: Atmospherically inverted $\rho_{app(atm)}$ for the reference (*black*), overestimated (*red*) and underestimated (*blue*) scenarios. Estimated $\rho_{app(atm)}$ for the mixed bare soil and vegetated spectrum (upper row) and the dense vegetated spectrum (bottom row) in the O₂-B and the O₂-A spectral regions. In all the panels, the threshold in $\rho_{app(atm)}$ corresponding to changes in SIF of 10% is shaded in gray.

5.5 Discussion

This section discusses the most important messages derived from this work in the context of current remote sensing fluorescence retrieval strategies. Limitations identified and proposed improvements for futures studies are also addressed.

5.5.1 Suitability of the mathematical approximations assumed in the FLEX AI

Over the last few years, various SIF retrieval strategies have been developed based on the exploitation of different spectral regions, the solar Fraunhofer lines [Joiner *et al.*, 2011, 2012; Guanter *et al.*, 2012; Khosravi, 2012; Köhler *et al.*, 2015a,b] or the telluric oxygen absorption bands [Guanter *et al.*, 2007a; Damm *et al.*, 2010; Guanter *et al.*, 2010; Mazzone *et al.*, 2010; Frankenberg *et al.*, 2011a; Raychaudhuri, 2014; Liu *et al.*, 2015; Damm *et al.*, 2014; Cogliati

et al., 2015b; Sabater *et al.*, 2015]. Alternatively, remote sensing SIF retrieval strategies can also be categorized according to those which retrieve SIF directly from TOA level, e.g., Joiner *et al.*, 2011, 2012; Guanter *et al.*, 2012, or those which retrieve SIF from TOC after the AC of the signal, e.g., Guanter *et al.*, 2007a; Damm *et al.*, 2010; Cogliati *et al.*, 2015b; Sabater *et al.*, 2015. The latter are the so-called two-step approximations and involve: (1) performing the AC, and (2) coupling an SF method to estimate SIF at surface level. Two-step approaches have been used in the past to estimate SIF from airborne data [Daumard *et al.*, 2015; Vicent *et al.*, 2014], and also a two-step strategy has been proposed in the context of the forthcoming FLEX/Sentinel-3 tandem mission [European Space Agency, 2015a; Cogliati *et al.*, 2015b]. Although there are many advantages about the use of this approximation, e.g., the derivation of the $\rho_{app(atm)}$ as an intermediate product to be analysed (discussed in Section 5.5.2), it requires an accurate AI procedure.

To start with, when it comes to inverting non-smooth high spectral resolution functions, such as the atmospheric transfer functions with their characteristic absorption regions, an important aspect implies dealing with the convolution to the sensor instrumental spectral response function. On the one hand, all the assumptions considered in Chapter 4 for the AI procedure of the FLEX mission were evaluated. Although in general terms it follows the classical full physics atmospheric inversion procedures [Guanter *et al.*, 2007b; Vermote *et al.*, 2002; Cooley *et al.*, 2002], FLEX AI introduces two main approximations: (1) considering $S \cdot \rho \approx S \cdot \rho_{app}$, and (2) using the second order series expansion. Assuming both, the independent convolution of each of the atmospheric transfer functions is avoided, which would otherwise rapidly derive into errors in the estimated SIF. Results suggest that the impact of these two approximations is at least one order of magnitude lower than the impact on TOA radiance caused by varying 10% of the SIF signal. This implies that FLEX AI formulation becomes suitable for fluorescence retrieval.

On the other hand, at the surface level, apparent reflectance (ρ_{app}) must be disentangled from emitted SIF and reflectance. As it was earlier noted by Verhoef *et al.* [Verhoef *et al.*, 2014], $\rho_{app} = \rho + \frac{\pi \cdot F}{E}$ and $\rho_{app(atm)}$ from the AI are substantially different, particularly in the absorption regions. This bears consequences to the SF method. In essence, SF strategies are based on minimizing the difference between simulated and measured spectra to decouple ρ and SIF. In the case of spaceborne or even airborne scale, measured data at the surface level are always derived from an AI procedure. Thus, in order to consistently couple the atmospherically inverted and the simulated signal; the formulation used should be consistent in both processes. Conversely, if a different formulation was used in the simulation and in the AI, then the SF method would minimize the differences between two inconsistently defined spectra. As demonstrated in Section 5.3.2, this would lead to errors depending on the atmospheric transfer functions, thus, depending on the atmospheric state.

To close this section, it should be remarked that reported error values are estimated under the assumption of a Lambertian surface without considering instrument noise. Evaluating the formulation under ideal conditions allows any other source of uncertainty to be discarded. Therefore, the errors identified here must be understood as an error baseline, intrinsic to the AI and to the coupling processes.

5.5.2 Apparent reflectance spectral distortion analysis and exploitation

An initial analysis was designed to evaluate the apparent reflectance spectral distortions produced in the oxygen regions by over/underestimating three different aerosol optical properties. The selected varying aerosol optical properties were the AOT, the Ångström exponent (α) and the asymmetry parameter of the HG scattering phase function (g), related to the aerosol load, aerosol size, and aerosol scattering anisotropy. Among them, the AOT and the g are the driving aerosol optical parameters, as they have a higher impact on the spectral distortions of the surface apparent reflectance ($\rho_{app(atm)}$). These results are in agreement with the aerosol sensitivity analyses performed in [Verrelst *et al.*, 2016a; Vicent *et al.*, 2017].

From this analysis, it was found that the spectral distortions produced by each evaluated aerosol property differ not only in magnitude but also in the spectral shape. This suggests that spectral distortions in the ρ_{app} could be used to refine the estimation of atmospheric parameters in the AC process. Therefore, the possibility of using the apparent reflectance to detect inaccuracies in the AC is investigated. A simple exercise was performed as a proof of concept, creating a DB of erroneously corrected $\rho'_{app(atm)}$. Using a simple multivariate linear regression algorithm, 30% of the DB was used for training and the remaining 70% of the DB was used for validation. Results suggest that the driving aerosol optical properties, i.e., AOT and g , can be predicted with an error below 0.5% (for the AOT) and 3% (for g) for 75% of the cases. Despite the low sensitivity to the Ångström exponent, the proposed method can still reduce its errors below 8% for 75% of the cases. However, some limitations are worth noting. Although these results support the hypothesis that the retrieval of aerosol optical properties from an inaccurate AC could be refined due to the distinct spectral pattern produced, the study should be extended to a more complex DB in a future work. Regarding expected improvements related to atmospheric simulations, they should not be limited to the spectral distortions produced by the AOT, α and g aerosol properties, but should be extended to other aerosol parameters such as the aerosol vertical distribution or the single scattering albedo, as it was also proposed to expand the proposed atmospheric correction strategy evaluated at Chapter 4. In the particular case of the aerosol vertical distribution, its radiometric effect on TOA radiance will strongly depend on the mathematical function assumed to model the vertical distribution, e.g., Gaussian [Frankenberg *et al.*, 2011a] or exponential [Vicent *et al.*, 2017]. Thus, it would be beneficial to conduct a more extensive aerosol sensitivity analysis in order to identify the driving aerosol parameters to be included in a future DB simulation, i.e., those parameters that highly distort the TOA radiance at the oxygen regions under realistic scenarios. With respect to how other atmospheric parameters affecting the DB training statistics, e.g., WV or surface pressure, this will strongly depend on the range of the values covered. While the used DB included two WV and surface pressure (surface height) values, in a new DB design, a wider range and a larger number of grid-points values should be incorporated. Also regarding the surface level, not only simulated but real surface reflectance and SIF spectra should be considered. Cases where each reflectance spectrum is associated to a range of SIF spectra should also be incorporated. At the same time, more efforts are required to study the impact of an inaccurate ISRF characterization on the predictive power of ρ_{app} , as well as other instrumental effects, such as radiometric noises,

residual polarisation effects, or stray-light contamination. In the particular case of the FLEX mission, a polarization scramble will be located in front of the telescope to cover the full pupil. Thus, while the remaining polarisation effects are expected to be within 1% of the threshold limit established by the FLEX mission [European Space Agency, 2015a], other effects such as stray-light contamination can deserve more attention when the observed image presents bright objects. In this respect, to make the apparent reflectance exploitation a solid strategy to improve the accuracy of the atmospheric correction process, future work should also consider the spectral distortions generated by each of these instrumental effects. In addition, this study assumed a Lambertian surface reflectance to create the simulated DB. Future work should therefore consider using a non-Lambertian surface reflectance. A more extensive analysis should also ascertain the most suitable regression algorithm to avoid local minima or divergent solutions. In addition, with respect to the use of a dimensionality reduction technique, it is necessary to determine the most effective method and the optimal number of components that keep the key spectral features intact.

As a final remark, the regression algorithm was trained and validated here for the O₂-A and O₂-B bands separately. In the future, the refinement of the atmospheric correction by using both regions simultaneously to disentangle atmospheric distortions should also be investigated. For instance, while spectral changes in the scattering phase function are typically smooth, others such as the stray-light contamination will probably become stronger in the O₂-A band than in the O₂-B due to its dependency on the radiance spectral contrast.

The use of the apparent reflectance as a quality indicator opens up new possibilities to implement an extra quality check into the Level-1 to Level-2 retrieval strategy of the FLEX/Sentinel-3 tandem mission. In this respect, under the framework of the **two-steps method**, its planned to integrate the exploitation of the FLORIS apparent reflectance as part of the Level-2 Retrieval Module (L2RM) of the FLEX End-To-End Mission simulator [Vicent *et al.*, 2016], not only to improve the aerosol optical properties characterization; but as a standard quality check of the process performed prior to disentangle the emitted SIF from the reflected light. However, prior to the integration of this strategy it is mandatory to evaluate the capabilities of the apparent reflectance exploitation technique to potentially distinguishing errors coming from the atmospheric state or instrument performance characterization.

5.6 Conclusions

Remote sensing retrieval of Solar-Induced chlorophyll Fluorescence (SIF) from Top-Of-Atmosphere (TOA) is challenging due to the tininess of the SIF signal. For this reason, the multiple strategies developed in the last few years to retrieve SIF from satellite data make use of the solar and terrestrial absorption regions where radiance at TOA is considerably reduced. In the particular case of the O₂-B and O₂-A bands, these are conveniently located in the SIF spectrum, i.e., close to each of the typical SIF emission peaks, being wider and deeper than the solar lines and thus more sensitive for SIF detection. However, oxygen bands are highly affected by atmospheric effects, especially by the aerosols scattering and surface pressure. For

this reason, the FLuorescence EXplorer (FLEX)/Sentinel-3 tandem space mission proposes an SIF retrieval strategy based on a **two-step** approach: (1) performing the Atmospheric Correction (AC), and (2) applying a Spectral Fitting (SF) technique to retrieve SIF. Given the tininess of the SIF signal, it is well-known that any inaccuracy in the atmospheric state characterization can lead to errors in the estimated SIF. However, just as important as the atmospheric parameters characterization, is the use of an appropriate formulation to infer surface apparent reflectance from TOA radiance and to apply a consistent coupling process between the AC and SF strategies. Thus, assuming the atmospheric state as known, the mathematical formulation of the FLEX data processing scheme, from the TOA radiance inversion to its coupling with the at-surface level SF method was evaluated. It was shown that the impact on TOA radiance of the approximations assumed by FLEX is around one order of magnitude lower than an expected variation caused by increasing 10% of the value of a typically SIF emission spectrum. It was also demonstrated that an inconsistent AC-SF coupling process derives errors that depend on the atmospheric transfer functions because of the formulation involved in the process. One of the advantages of using a **two-step** approach resides in the intermediate products generated, such as the apparent reflectance (ρ_{app}). Using simulated data with SCOPE and MODTRAN radiative transfer models, the spectral distortions propagated to ρ_{app} due to inaccuracies in the estimation of aerosol optical properties were subsequently analysed. As it was expected, distinct distortion patterns appear in the ρ_{app} due to the over/underestimation of each of the key aerosol optical properties: the AOT, the Ångström exponent (α) and the Henyey-Greenstein (HG) scattering anisotropy parameter (g). This allows proposing to exploit the use of the ρ_{app} as a quality indicator of the AC. As a proof of concept, a simple exercise was performed over $\sim 8 \cdot 10^4$ incorrectly atmospherically corrected ρ_{app} database by using a multivariate linear regression technique to predict the over/underestimation of the aerosol optical properties. First, results showed that the AOT, α and the g parameters can be corrected with a relative error lower than 0.5%, 8% and 3%, respectively, for 75% of the evaluated data. When these statistics are propagated to surface apparent reflectance they result in distortions below the threshold set in ρ_{app} caused by increasing the emitted SIF $\pm 10\%$ of its original value. In the context of the FLEX/Sentinel-3 tandem mission, the exploitation of the apparent reflectance spectral distortions can open up new opportunities to refine the atmospheric parameters obtained from the AC process, and therefore obtain more accurate SIF estimations.

6

Atmospheric compensation on proximal sensing data for satellite validation

Contents

6.1	Abstract	136
6.2	Introduction	137
6.3	SIF retrieval methods for proximal sensing	141
6.4	Impact of oxygen transmittance compensation on SIF	146
6.5	Analysis in Temperature and Pressure Environmental Conditions	157
6.6	Discussion	160
6.7	Conclusions	163

This chapter is based on:

Neus Sabater, Jorge Vicent, Luis Alonso, Jochem Verrelst, Elizabeth M. Middleton, Albert Porcar-Castell and José Moreno



Compensation of Oxygen Transmittance Effects for Proximal Sensing Retrieval of Canopy–Leaving Sun–Induced Chlorophyll Fluorescence [submitted]

6.1 Abstract

Satellite validation campaigns are essential activities to guarantee the success of any space mission. When designing validation campaigns and protocols, in-situ or proximal sensing acquired data must be considered as a reference to validate the specific mission objectives and products. For high spatial resolution missions, large homogeneous areas are typically selected in order to minimize, as far as possible, the influence of adjacency effects. For high spectral resolution missions, validation strategies must account the actual pixel heterogeneity, which can generally involve hundreds of meters. In the particular case of the FLEX mission, to enable validating the canopy emitted Solar Induced Chlorophyll Fluorescence (SIF) in an extended area, measurement systems are generally mounted on towers or elevated platforms. Consequently, an optical path between the measured target and the sensor is present. Whereas correction of atmospheric effects is a standard airborne or satellite data processing step, there is no consensus regarding whether it is required for SIF proximal sensing measurements nor what is the best strategy to be followed. Thus, by using simulated data, this Chapter provides a comprehensive analysis about how atmospheric effects can affect SIF estimations on proximal sensing, regarding: (1) the measurement of the up-welling and down-welling radiance when either are made from a distance above the canopy; (2) the SIF retrieval technique used, e.g., Fraunhofer Line Discriminator (FLD) family or Spectral Fitting Methods (SFM); and, (3) the instrument's spectral resolution. It is demonstrated that although compensating for atmospheric effects by simply introducing an O_2 transmittance function into the FLD or SFM formulations apparently improves the estimated SIF accuracy, this can lead to significant and unintended errors due to appearing disturbances related to the Instrumental Spectral Response Function (ISRF) convolution effects. To mitigate these errors, it is proposed and evaluated a new SIF retrieval strategy based on the SFM, which simultaneously compensates for the O_2 transmittance spectrum and the ISRF, as part of the SFM minimization process. Finally, due to the key role of O_2 absorption playing in many SIF retrieval strategies in proximal sensing situations, its dependency on surface pressure (p) and air temperature (T) was also evaluated by combining simulated spectral data with p and T measurements obtained for a one-year period in the Hyytiälä Forestry Field Station in Finland. Of interest hereby is that seasonal dynamics in terms of (T, p) , if not appropriately considered as part of the retrieval strategy, can result into an erroneous SIF seasonal trend. These erroneous trends mimic those of known dynamics for temperature-dependent physiological responses of vegetation, and amplify the summertime values.

6.2 Introduction

Sun-Induced chlorophyll Fluorescence (SIF) measured from proximal remote sensing platforms, e.g., systems mounted on towers; becomes ideal to continue monitoring small-medium canopy areas. Plants respond actively and continuously to different environmental conditions, therefore continuous and long term observations become crucial in vegetation monitoring to understand terrestrial biosphere processes [Zhang *et al.*, 2016]. With this aim, in recent years many ground-based field spectroscopy systems have been developed and mounted on towers [Mac Arthur *et al.*, 2014]. In addition, with production of global SIF maps from atmospheric satellites, e.g., [Joiner *et al.*, 2012; Guanter *et al.*, 2014], and with the forthcoming new ESA's mission, the FLuorescence EXplorer (FLEX) [Moreno *et al.*, 2016], the use of tower-based SIF continuous measurements will play a key role in supporting validation and calibration activities for satellite and airborne measurements.

Many of the currently existing systems mounted on towers dedicated to detecting SIF typically measure both (1) the up-welling radiance coming from the surface, and (2) the incoming down-welling solar irradiance; at sensor level for practical reasons. The height of towers for measuring SIF mainly depends on the vegetation type to be monitored, ranging from 5-25 m to measure agricultural fields, to 20-50 m to monitor SIF over forests. Examples include: (1) the NASA FUSION tower (<ftp://fusionftp.gsfc.nasa.gov/FUSION>); (2) the Multiplexer Radiometer Irradiometer (MRI) [Bresciani *et al.*, 2013; Cogliati *et al.*, 2015a] and (3) the HyperSpectral Irradiometer (HSI) [Meroni *et al.*, 2011; Rossini *et al.*, 2012, 2014], both developed by Università degli Studi Milano-Bicocca; (4) and the UNEDI system [Drolet *et al.*, 2014] at the FluxNet Hyytiälä site (<http://fluxnet.ornl.gov>).

There are several critical factors to consider when retrieving SIF from spectral measurements within O₂ absorption regions. As the atmospheric path between the vegetated target and the sensor increases, it becomes more critical to correct measurements from atmospheric effects. Because of that, past field campaign experiments dedicated to measure SIF from airborne sensors always counted on atmospheric correction strategies to correct acquired airborne radiances [Damm *et al.*, 2014; Daumard *et al.*, 2015]. However, ignoring atmospheric O₂ absorption even when vegetation is monitored from a lower height above the canopy ($h \sim 10$ m), highly impacts retrieved SIF [Liu *et al.*, 2017]. On top of that, errors in retrieved SIF strongly depend on the technique chosen for disentangling emitted SIF from reflected light at canopy level, whether using the FLD-family of techniques [Plascyk, 1975; Plascyk and Gabriel, 1975; Maier *et al.*, 2003; Alonso *et al.*, 2008] or Spectral Fitting Methods (SFM) [Mazzoni *et al.*, 2010; Meroni *et al.*, 2010; Cogliati *et al.*, 2015b].

The FLD and SFM families of SIF retrievals have been formulated to be applied at Top Of Canopy (TOC) level, assuming that: (a) the atmospheric path between the target and the sensor is short enough to be neglected; and (b) the solar irradiance is acquired directly at the same height as the target. However, these assumptions are not met when the atmospheric path length increases as with a higher mount on towers or larger solar or view zenith angles (SZA, VZA) [Sabater *et al.*, 2017b]. Oxygen absorption is proportional to air pressure [Pierluisi and

Chang Mind, 1986], and at the bottom of the atmosphere where pressure is highest, even a few meters distance between the target and the sensor could impose significant errors in the retrieved SIF at TOC. This fact becomes crucial when aiming for a proper SIF comparison between varying acquisition geometries in multi-angular acquisition systems [Zhang *et al.*, 2016; Sabater *et al.*, 2017b]. It must be mentioned that few past field campaign experiments (tower and ground-based) dedicated to measure SIF incorporated a processing strategy to compensate for atmospheric effects [Davidson *et al.*, 2002; Louis *et al.*, 2005]. In addition, in the recent publication from Liu *et al.*, 2017, transmittance effects on SIF canopy-leaving measurements made with hemispherical sensors were analysed through an effective transmittance correction. However, an in-depth analysis should be conducted to quantify how proximal sensing measurements consisting of solar irradiance and up-welling canopy radiance at sensor level, while not accounting for atmospheric effects between target and sensor, impact the estimated fluorescence. In this Chapter, possible O₂ compensation strategies that function through modifying the FLD family of retrieval methods or SFM formulations are presented and assessed. However, these simplistic approaches ignore the spectral convolution effects of the instrument utilized. For this reason, an alternative strategy to compensate for atmospheric effects while taking into account the particular Instrumental Spectral Response Function (ISRF) is proposed. In addition, since O₂ transmittance depends on air temperature (T) and surface pressure (p), it is aimed to assess to what extent seasonal changes in T and atmospheric p would interfere with the retrieved SIF signals. In other words, an important question raised here is this: Can seasonal changes in T and p generate a significant false SIF signal, if not appropriately compensated, that mimics seasonal patterns related to temperature-dependent physiological responses expressed with vegetation SIF? Thus, by using simulated spectra, work developed in this chapter aims to address all these issues within a theoretical framework.

The remainder of this Chapter is organized as follows. Section 6.2.1 describes the relationship between the measured at-sensor and at-surface solar irradiance and up-welling canopy radiances. Section 6.3 briefly reviews the FLD-family and SFM SIF retrieval approaches and modifies these standard formulations to introduce a first order O₂ transmittance compensation, and analyses their limitations. Then, an alternative strategy to compensate for O₂ effects while also accounting for effects due to the instrument's spectral resolution is proposed. Section 6.4 is dedicated to the results: (1) supporting the need to compensate for O₂ absorption when retrieving SIF at proximal sensing; (2) reporting the expected SIF accuracy when a first O₂ compensation is applied to either the FLD or SFM retrievals for different instrument resolutions and sensor heights; and, (3) reporting the expected SIF accuracy when the full proposed O₂ compensation strategy is applied. Section 6.5 examines the O₂ transmittance dependency on T and p conditions and its potential impact when monitoring long temporal series. Section 6.6 discusses main results found in this chapter in a broader scientific context regarding experimental field campaigns and satellite validation activities. Finally, main conclusions are summarized in Section 6.7.

6.2.1 At–sensor and at–canopy solar irradiance

For practical reasons, solar irradiance is commonly measured at a distance from the vegetated target location. Therefore, the relationship between the solar irradiance (E) measured at sensor level, when assumed to be placed at the same height (e.g., on a tower or Unmanned Aerial Vehicles (UAV)), and the solar irradiance reaching the surface at TOC (\bar{E}) is driven by Equation 6.2.1:

$$\bar{E} \sim Et^\downarrow \quad (6.2.1)$$

where t^\downarrow is the downward total (direct and diffuse) transmittance from the reference panel or sensor to the TOC level, for a given illumination geometry. Note that hereinafter the over–line symbol on \bar{E} (or over L) refers to magnitudes measured at the surface/canopy level. In addition, for the sake of readability, the spectral dependency of each term is omitted in the formulation presented in this section.

Thus, the difference between solar irradiance measured by the tower–mounted calibration panel (or sensor) and the actual solar irradiance reaching the surface at TOC will increase as either the distance between them, or the SZA increase (See Figure 6.2.1).

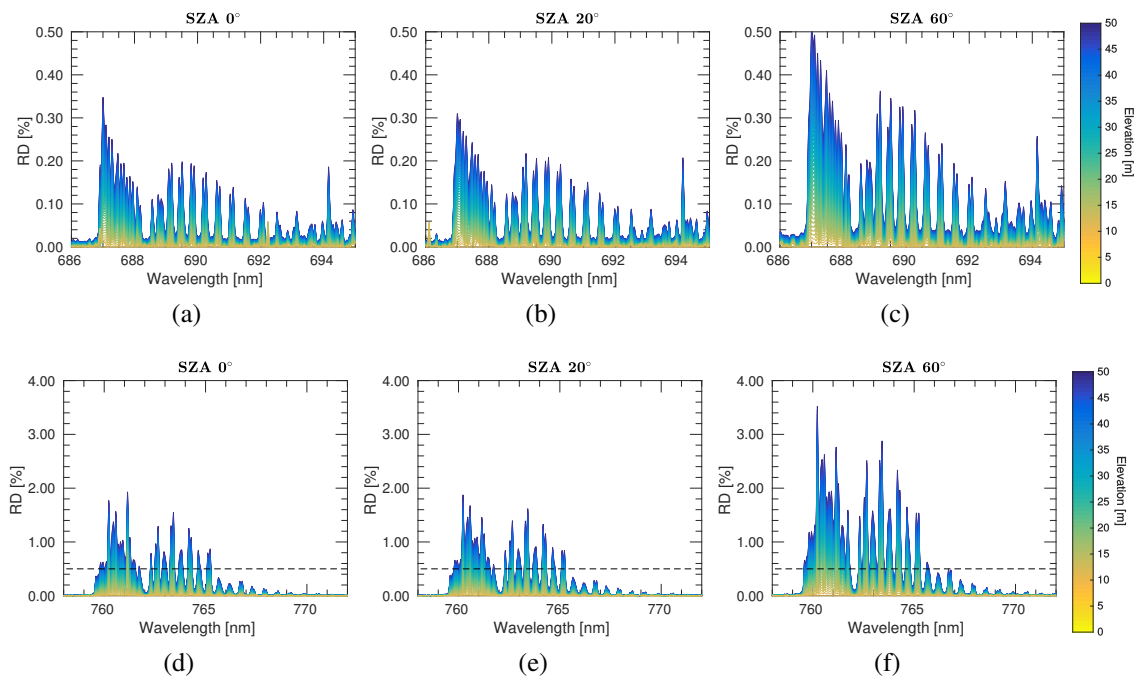


FIGURE 6.2.1: The percent (%) relative difference (RD) between the at–sensor and at–surface measured solar irradiance for different SZAs (0° , 20° , and 60°) and a range of target–sensor distances from 0 to 50 m Figures (a), (b),(c), and (d), (e), (f) show the solar irradiance RD[%] corresponding to the O_2 –B and O_2 –A regions, respectively. The black dashed–line in the Figures (d), (e), and (f) indicate the maximum RD reached in the O_2 –B region to facilitate the comparison.

6.2.2 Upward atmospheric transmittance from surface TOC to sensor level

Assuming a Lambertian surface reflectance, the Top Of Atmosphere (TOA) radiance, L_{TOA} , can be written as Equation 6.2.2 ¹:

$$L_{TOA} = L_0 + \frac{(\bar{E}\rho + \pi F)t^\uparrow}{\pi(1 - S\rho)} \quad (6.2.2)$$

where L_0 is the atmospheric path radiance, S is the spherical albedo, t^\uparrow is the total upward atmospheric transmittance (diffuse and direct contributions) from surface TOC to TOA, \bar{E} is the solar irradiance reaching the surface, F is the emitted SIF (F hereinafter for brevity) and ρ the Lambertian surface reflectance. Adjacency effects are not considered in Equation 6.2.2, and it is assumed that an infinite uniform target, with surface reflectance, ρ .

In case of only a few meters distance between the TOC target and the sensor, it is possible to neglect the contribution of the atmospheric path radiance, L_0 , [Liu *et al.*, 2017], considering that the total upward atmospheric transmittance is dominated by the direct transmittance component (see Figure 6.2.2), and assuming that the contribution of the spherical albedo at TOC and at sensor level is equivalent. On the one hand, Figure 6.2.2a shows the minor contribution of the path radiance, L_0 , in comparison to the expected at-sensor radiance, L (~ 4 orders of magnitude). On the other hand, Figure 6.2.2b presents the negligible contribution of the diffuse upward transmittance, t_{dif}^\uparrow , relative to the direct upward transmittance, t_{dir}^\uparrow (~ 5 orders of magnitude). Therefore, the relationship between the at-sensor radiance, L , and the up-welling canopy radiance from the surface, \bar{L} , can be described as:

$$L \simeq \left(\frac{\bar{E}}{\pi}\rho + F \right) t^\uparrow = \bar{L} t_{dir}^\uparrow \quad (6.2.3)$$

where the t_{dir}^\uparrow is the direct upward transmittance from the surface to the sensor level for a given viewing geometry. For the O_2 -A absorption band, the direct upward transmittance is mostly dominated by O_2 concentration (see Figure 6.2.3). Therefore, for the O_2 -A absorption band and a near target-sensor distance, it is possible to assume that $t_{dir}^\uparrow \sim t_{O_2}^\uparrow$, being $t_{O_2}^\uparrow$ the oxygen transmittance.

In the particular case of multi-angular acquisition systems like the FUSION tower-mounted system [Middleton *et al.*, 2013], O_2 transmittance correction becomes even more critical if the objective is aiming to integrate measurements over the footprint to include contributions from multiple acquisition geometries. Apart from the different field of views (FOV) projections at surface, the varying atmospheric optical path must be also included in the transmittance compensation strategy.

¹Note that this expression has been already introduced in Chapters 4 and 5. However, it is also here mentioned to keep each of the Thematic chapters self-consistent.

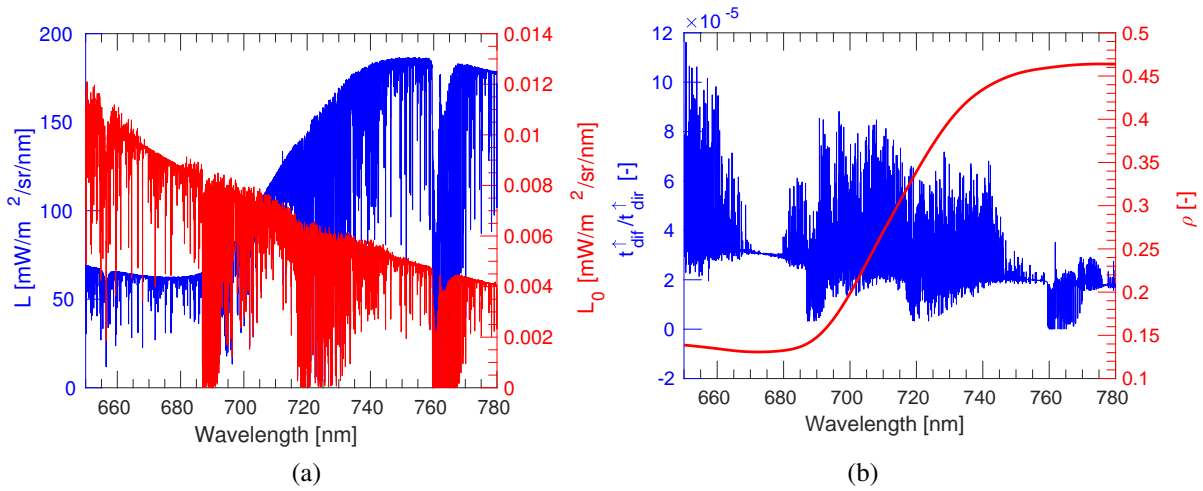


FIGURE 6.2.2: **(a)** Simulated radiance (blue) and path radiance (red) for a tower-mounted sensor level 10 m height above the TOC, acquired with nadir acquisition geometry for a mid-latitude summer atmosphere with a visibility of 23 km. **(b)** Simulated ratio (diffuse/direct) for upward diffuse (t_{diff}^{\uparrow}) and direct (t_{dir}^{\uparrow}) transmittance (blue). Surface reflectance (red) used for the at-sensor radiance simulation with Equation 6.2.2, assuming no fluorescence emission.

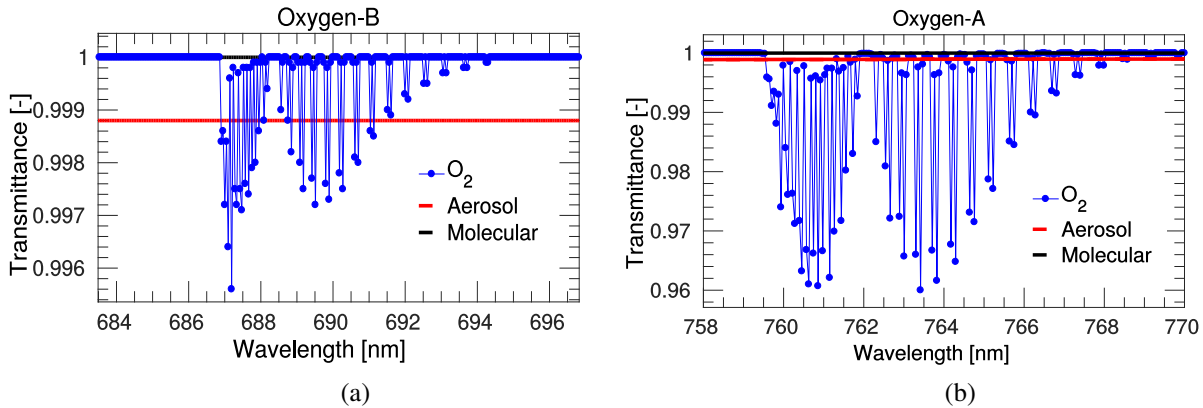


FIGURE 6.2.3: Simulated upward atmospheric transmittance from a 0 m surface elevation to a tower sensor at 10 m height, with nadir viewing geometry and sea-level pressure conditions. Transmittance has been simulated at 0.1 cm^{-1} spectral resolution for the O_2 -B **(a)**, i.e., $\sim 0.005 \text{ nm}$, and the O_2 -A **(b)**, i.e., $\sim 0.006 \text{ nm}$, absorption regions. Note the different Y-axis ranges used to appreciate details in both panels for the O_2 -B and O_2 -A.

6.3 SIF retrieval methods for proximal sensing

This section firstly reviews the commonly used FLD and SFM formulated retrieval approaches to disentangle the emitted SIF signal and the reflected light at TOC. Then, the O_2 transmittance compensation factors are introduced into the standard FLD and SFM retrieval strategies. However, since the instrument spectral resolution also plays a role, a new strategy that deals with the oxygen compensation and the instrument spectral resolution convolution effects simultaneously

is proposed.

6.3.1 FLD and SFM methods

The family of FLD-methods, typically applied to the O₂-A band or Fraunhofer lines to retrieve SIF, are based on the exploitation of two or more channels inside and outside the selected absorption band to retrieve SIF. Assuming a Lambertian behaviour of surface reflectance, radiance measured from a vegetated target at surface level \bar{L} can be expressed as two complementing contributions: (1) the reflected solar irradiance, and (2) the SIF emission. Mathematically, this can be expressed at a given wavelength (λ) as Equation 6.3.1:

$$\bar{L}(\lambda) = \rho(\lambda) \frac{\bar{E}(\lambda)}{\pi} + F(\lambda) \quad (6.3.1)$$

where \bar{E} is the total solar direct and diffuse irradiance reaching the surface, ρ is the Lambertian surface reflectance, and F is the fluorescence emission. Commonly to all FLD family of retrieval techniques, the radiances inside (\bar{L}_{in}) and outside (\bar{L}_{out}) of the absorption band are related by assuming a simplified behaviour of the ρ and F . For the FLD, a constant wavelength response is assumed [Plascyk, 1975], whereas a spectral dependency is introduced for the iFLD method [Alonso *et al.*, 2008]. In view of these assumptions, the FLD and 3FLD methods can be considered as a particular cases of the iFLD formulation [Alonso *et al.*, 2008]:

$$F = \frac{\alpha_R \bar{E}_{out} \bar{L}_{in} - \bar{E}_{in} \bar{L}_{out}}{\alpha_R \bar{E}_{out} - \alpha_F \bar{E}_{in}} \quad (6.3.2)$$

where $\alpha_R = \frac{\rho_{out}}{\rho_{in}}$ and $\alpha_F = \frac{F_{out}}{F_{in}}$ are the coefficients that introduce the spectral variation of ρ and F in the absorption band region. Note that the FLD method is the particular case where $\alpha_R = 1$ and $\alpha_F = 1$ [Alonso *et al.*, 2008], and the 3FLD formulation is equivalent to the original FLD formulation when \bar{L}_{out} and \bar{E}_{out} are obtained by linear interpolation of two bands at each side of the absorption [Maier *et al.*, 2003].

Unlike the simpler FLD methods, the SFM approach exploits all the spectral information around the selected absorption band [Mazzoni *et al.*, 2010; Meroni *et al.*, 2010], or even the complete spectral SIF range from 650 nm to 800 nm [Cogliati *et al.*, 2015b]. According to the selected spectral interval, reflectance and fluorescence spectra can be described by appropriate mathematical functions. Therefore, there exist an spectral difference, $\epsilon(\lambda)$, between the modelled and observed radiance at TOC:

$$\epsilon_{sen}(\lambda) = \bar{L}(\lambda) - \bar{L}_{MOD}(\lambda) = \bar{L}(\lambda) - \left(\rho_{MOD}(\lambda) \frac{\bar{E}(\lambda)}{\pi} + F_{MOD}(\lambda) \right) \quad (6.3.3)$$

where $\bar{L}(\lambda)$ is the observed radiance at TOC from Equation 6.3.1, and ρ_{MOD} and F_{MOD} are the parametric functions used to describe the two key variables. For narrow spectral intervals covering the O₂-A region, the SFM typically models ρ_{MOD} and F_{MOD} by polynomial

(quadratic or cubic) functions [Meroni *et al.*, 2009]. Thus, the inversion process disentangles F_{MOD} from ρ_{MOD} by finding the coefficients of the parametric functions for ρ_{MOD} and F_{MOD} that minimizes $\epsilon(\lambda)$ [Meroni *et al.*, 2010].

6.3.2 O₂ transmittance compensation on FLD and SFM methods

Following the initial FLD assumptions, i.e., $F(\lambda_{out}) \sim F(\lambda_{in})$ and $\rho(\lambda_{out}) \sim \rho(\lambda_{in})$; and introducing Equations 6.2.1 and 6.2.3 into Equation 6.3.2, SIF can be formulated as:

$$F = \frac{\frac{L_{in}}{t_{in}^{\uparrow}} E_{out} t_{out}^{\downarrow} - \frac{L_{out}}{t_{out}^{\uparrow}} E_{in} t_{in}^{\downarrow}}{E_{out} t_{out}^{\downarrow} - E_{in} t_{in}^{\downarrow}} \quad (6.3.4)$$

Thus, Equation 6.3.4 represents the improved formulation for the O₂-corrected FLD and 3FLD methods. For iFLD-O₂ formulations, the O₂ compensation is introduced together with the spectral fluorescence and reflectance correction factors, such that:

$$F = \frac{\frac{L_{in}}{t_{in}^{\uparrow}} \alpha_R E_{out} t_{out}^{\downarrow} - \frac{L_{out}}{t_{out}^{\uparrow}} E_{in} t_{in}^{\downarrow}}{E_{out} \alpha_R t_{out}^{\downarrow} - E_{in} \alpha_F t_{in}^{\downarrow}} \quad (6.3.5)$$

Outside the O₂-A absorption band, downward and upward transmittances (i.e., t^{\uparrow} and t^{\downarrow}) can be set to unity, which simplifies Equations 6.3.4 and 6.3.5. In the case where solar irradiance is measured at TOC level, then $E t^{\downarrow}$ is replaced by \bar{E} ; and thus no O₂ correction needs to be applied to the solar irradiance term. Inside the O₂-A absorption band, upward and downward oxygen transmittance can be simulated using an atmospheric radiative transfer code, such as the MODerate resolution atmospheric TRANsmission (MODTRAN, Berk *et al.*, 2005) or the HIGH-resolution TRANsmission molecular absorption database (HITRAN, Rothman *et al.*, 2009). Alternatively, empirical O₂ transmittance approximations [Pierluisi and Chang Mind, 1986] as shown in Equations 6.3.6 and 6.3.7 can also be used for moderate spectral resolution (~ 0.22 nm) measurements:

$$t(\lambda) = \exp\left[-(10^{C'(\lambda)} \left(\frac{p}{p_0}\right)^n \left(\frac{T_0}{T}\right)^m U)^a\right] \quad (6.3.6)$$

$$U = 0.773210^{-4} M \rho_a Z \quad (6.3.7)$$

where p (atm), T (K), M (ppmv) and ρ_a (gm⁻³) are the pressure, temperature, absorber concentration, air density conditions, respectively, for a particular optical path; and U (atm cm) is the total absorber amount in the path length, Z (km). Finally the subscript T_0 , p_0 indicates the standard conditions, i.e., 273.16 K and 1 atm, and the values of the parameters a , m and n are set to 0.5641, 0.9353 and 0.1936, respectively. Refer to Pierluisi and Chang Mind, 1986 for more details and default values typically assumed for the C' spectral coefficients.

When using the SFM for proximal sensing retrievals, then the observed radiance at sensor level (L from Equation 6.3.3), is affected by atmospheric transmittance between the TOC target and the sensor. Therefore, assuming that the solar irradiance (E) and the up-welling radiance (L), are both measured away from the surface and using the relationship from Equation 6.2.3, the modified formulation of the SFM for a first order O_2 compensation would be:

$$\epsilon_{sur}(\lambda) = \frac{L}{t_{vza}^{\uparrow}} - \underbrace{\left(\frac{Et_{sza}^{\downarrow}}{\pi} \rho_{MOD} + F_{MOD} \right)}_{Surface} \iff \epsilon_{sen}(\lambda) = L - \underbrace{\left(\frac{Et_{sza}^{\downarrow}}{\pi} \rho_{MOD} + F_{MOD} \right)}_{Sensor} t_{vza}^{\uparrow} \quad (6.3.8)$$

where the t_{sza}^{\downarrow} and t_{vza}^{\uparrow} are the (wavelength-dependent) downward and upward atmospheric transmittances. Suffixes *sza* and *vza* indicate the main dependence on the solar illumination and the sensor acquisition geometry, respectively. In Equation 6.3.8, the spectral dependency of each of the functions involved is omitted for brevity. Note from Equation 6.3.8 that it is mathematically equivalent to minimizing the spectral difference between the modelled and measured radiance at TOC or at sensor level, given that the O_2 transmittance correction was included in the formulation.

The first order O_2 compensation techniques detailed here are addressed for measurements acquired at a few meters distance from TOC. These techniques, when applied to the FLD-family and SFM (Equations 6.3.5 and 6.3.8), ignore (i.e., do not address) the instrumental spectral convolution effects in their modified formulations (more details in Section 6.3.3). In addition, these techniques cannot be extrapolated to airborne or satellite level, where the atmospheric path radiance (L_0) and spherical albedo (S) must be included in the atmospheric correction scheme. Furthermore, whereas O_2 absorption affecting proximal sensing is still dominated by O_2 gas concentration (Figure 6.2.3), as the atmospheric path increases, aerosols and molecular scattering also play an important role in this spectral region and thus must be carefully compensated.

6.3.3 A proposed strategy to compensate for both atmospheric and instrument spectral convolution effects on the SFM

In subsection 6.3.2, the standard FLD and SFM formulations were modified to include a first order compensation of the O_2 absorption effects acting on the atmospheric path between the target and the sensor. Some mathematical aspects were assumed in those modifications and are worth noting. Regardless of the technique used, FLD or SFM, the signal acquired by the sensor is convolved according to its ISRF, i.e., $\langle L \rangle$ and $\langle E \rangle$. Taking this fact into account, in order to compute Equations 6.3.4 and 6.3.8, it is required that the O_2 transmittance terms must be also convolved according to the corresponding ISRF, i.e., $\langle t^{\uparrow} \rangle$ $\langle t^{\downarrow} \rangle$. However, the product of two given generic functions spectrally convolved $\langle a \rangle \langle b \rangle$ is not mathematically equivalent to the spectral convolution of the two functions product $\langle ab \rangle$. As it was mentioned in a previous

work [Sabater *et al.*, 2017a], this becomes especially relevant when working with non-smooth functions, such as the atmospheric transfer functions, and particularly when working with high spectral resolution data in the O₂ absorption regions. Therefore, as it will be quantified in Sections 6.4.2 and 6.4.3, the O₂ transmittance compensation in the FLD and SFM formulations will lead to higher errors on the retrieved SIF as the sensor resolution decreases, in other words, with wider spectral bands. Although errors derived due to the spectral convolution effects can become significant, they are still lower than simply ignoring O₂ absorption effects. In order to compensate for the ISFR convolution effects, it is necessary to use the atmospheric functions at a finer spectral resolution than the instrument's spectral resolution. Since this is not usually the case in practice, here a strategy is proposed to deal with: (1) the O₂ absorption effects, and (2) the particular instrument ISRF, when measuring both solar irradiance and the up-welling canopy radiance for proximal sensing (Figure 6.3.1).

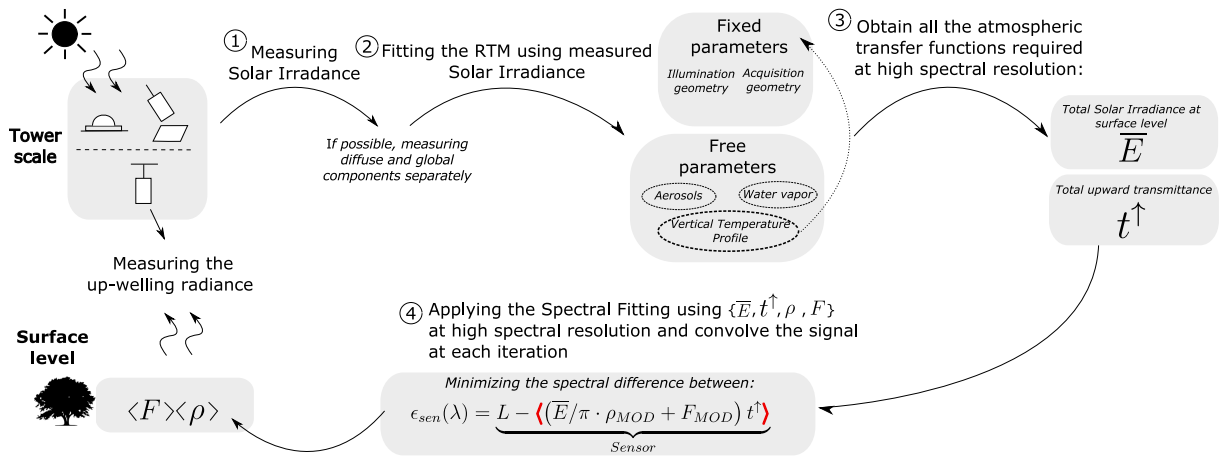


FIGURE 6.3.1: Proposed scheme to compensate for atmospheric effects when applying the SFM SIF retrieval approach for proximal sensing data. Red bold angle brackets in step 4 indicate the signal to be convolved according to the ISRF.

In essence, the idea is based on using the solar irradiance signal acquired at the same tower-mounted height (e.g., top of the tower), either using a reference panel or with an upward looking cosine corrected sensor, to fit an atmospheric Radiative Transfer Model (RTM). This way, the atmospheric state is fully characterized and the RTM can provide all the atmospheric functions required to apply the SFM with the O₂ compensation, according to Equation 6.3.9 at high resolution. Note that the use of a finer spectral resolution sensor for acquiring the solar irradiance will not entirely solve the problem since the upward O₂ transmittance it is still required.

Accordingly, when applying the SFM approach to the O₂ region, the signal will be convolved according to the ISRF (red bold angle brackets in Figure 6.3.1) on each iteration of the

minimization process. The SF minimization process is then performed at sensor level, according to Equation 6.3.9:

$$\epsilon_{sen}(\lambda) = L - \underbrace{\langle (\bar{E} / \pi \rho_{MOD} + F_{MOD}) t_{vza}^\uparrow \rangle}_{Sensor} \quad (6.3.9)$$

6.4 Impact of oxygen transmittance compensation on different SIF retrieval strategies.

In order to quantify the expected improvement achieved by each of the proposed compensation techniques in Section 6.3, now a collection of tests developed using a set of simulated radiance spectra at sensor level (from 3 m to 20 m above TOC) following Equation 6.2.3 is presented. In the simulation process, total atmospheric upward transmittance (including aerosols) and at-surface solar irradiance from Equation 6.2.3 were simulated using the atmospheric RTM MODTRAN. In total, four different tests were performed to disentangle errors derived for SIF due to the O₂ effects and from those due to the retrieval technique: (1) a high spectral resolution test assuming the knowledge of surface reflectance (Section 6.4.1); (2) a test using the 3FLD O₂ compensated formulation (Section 6.4.2); (3) a test using the O₂ compensation SFM formulation (Section 6.4.3); and, (4) a final test coupling the O₂ transmittance with the compensation of the ISRF convolution on the SFM (Section 6.4.4).

6.4.1 High spectral resolution

An initial simulated experiment was conducted to estimate the impact of ignoring oxygen effects on the retrieved SIF at a high spectral resolution of 0.06 nm, regardless of the retrieval technique implemented. To do so, four scenarios were evaluated: (1) L corrected for target-sensor O₂ absorption and \bar{E} measured at TOC (Figure 6.4.1a), (2) L not corrected for target-sensor O₂ absorption and \bar{E} measured at TOC (Figure 6.4.1b), (3) L corrected for target-sensor O₂ absorption and E measured at sensor level on a tower (Figure 6.4.1c), and (4) L not corrected for target-sensor O₂ absorption and E measured at sensor level on a tower (Figure 6.4.1d).

In all cases, SIF was estimated by isolating F from Equation 6.2.3, assuming the surface reflectance spectrum was known. Thus, the resulting expression used to estimate SIF in each scenario was:

- Scenario (1); $F = L / t_{O_2}^\uparrow - (\bar{E}\rho) / \pi$
- Scenario (2); $F = L - (\bar{E}\rho) / \pi$
- Scenario (3); $F = L / t_{O_2}^\uparrow - (E\rho) / \pi$

- Scenario (4); $F = L - (E\rho)/\pi$

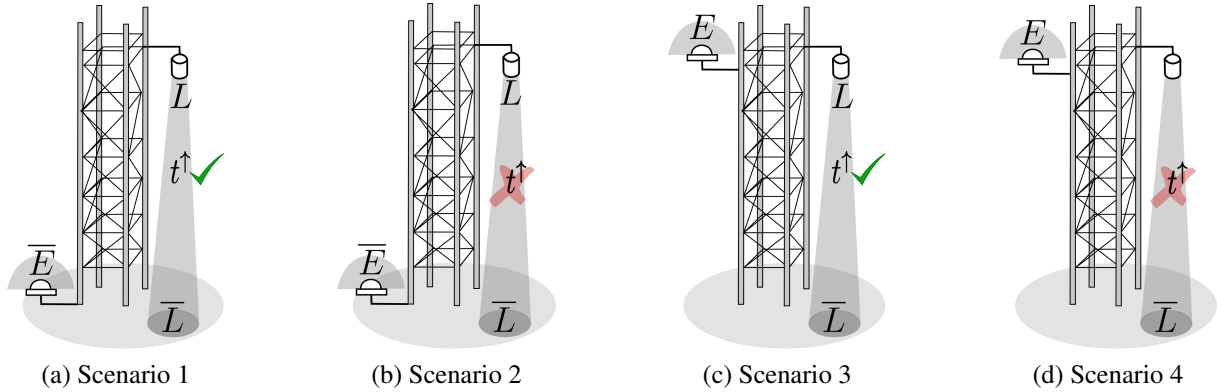


FIGURE 6.4.1: Diagrams in **(a)**, **(b)**, **(c)**, and **(d)** corresponding to the scenarios (1), (2), (3) and (4), respectively, described in Section 6.4.1. Figure **(d)** represents the general configuration of instrument devices mounted to measure SIF at tower-scale. In some cases, downward looking sensors mounted at the top allows multi-angular data collections. When acquiring down-welling solar irradiance with hemispherical or a conical systems, this last typically measuring a reference panel. Here t^\uparrow is the upward atmospheric transmittance.

Retrieved O_2 -A band SIF from all scenarios (1 – 4) was obtained for a nadir observation geometry and covering sensor mounted-heights from 3 m to 20 m on a tower (Figure 6.4.2). Analogously, Figure 6.4.3 shows retrieved SIF at O_2 -B band for scenarios (1 – 4). When the sensor height increases above the TOC, the impact of aerosol and molecular oxygen on retrieved SIF becomes more critical. However, results suggest that this effect is already noticeable from a few meters distance, i.e., 3 m.

Inside the O_2 -A absorption band, estimated (coloured lines) and reference (black solid line) SIF values are reasonably close, especially for bands deep inside the absorption dip, and particularly in cases where the O_2 correction was applied, i.e., scenarios (1) and (3). However, when no O_2 absorption correction on the target-to-sensor optical path is applied, i.e., scenarios (2) and (4), then retrieved SIF is highly underestimated. According to Figure 6.4.2, retrieved SIF outside the O_2 -A absorption region is biased compared with the reference SIF (black solid line) for all the scenarios, and this effect increases with the sensor height increases. This is attributed to limiting the correction of the atmospheric transmittance (t^\uparrow) to only the O_2 transmittance ($t_{O_2}^\uparrow$). This effect is demonstrated in Figure 6.4.4a where SIF was estimated by correcting the at-sensor radiance only for the aerosol transmittance (t_{aer}^\uparrow). As it can be observed, the earlier existing bias in the spectral region outside of the O_2 absorption band has disappeared. In addition, in Figure 6.4.4b, the impact of using the solar irradiance at sensor level instead of at TOC is evaluated. To do so, SIF was estimated by correcting the at-sensor radiance using the total atmospheric transmittance (t^\uparrow). This case is quite similar to the scenario 3, but residuals in the estimated SIF are now exclusively caused by the at-sensor measured solar irradiance. In both cases of Figure 6.4.4, because the at-sensor radiance has been corrected by the total or aerosol

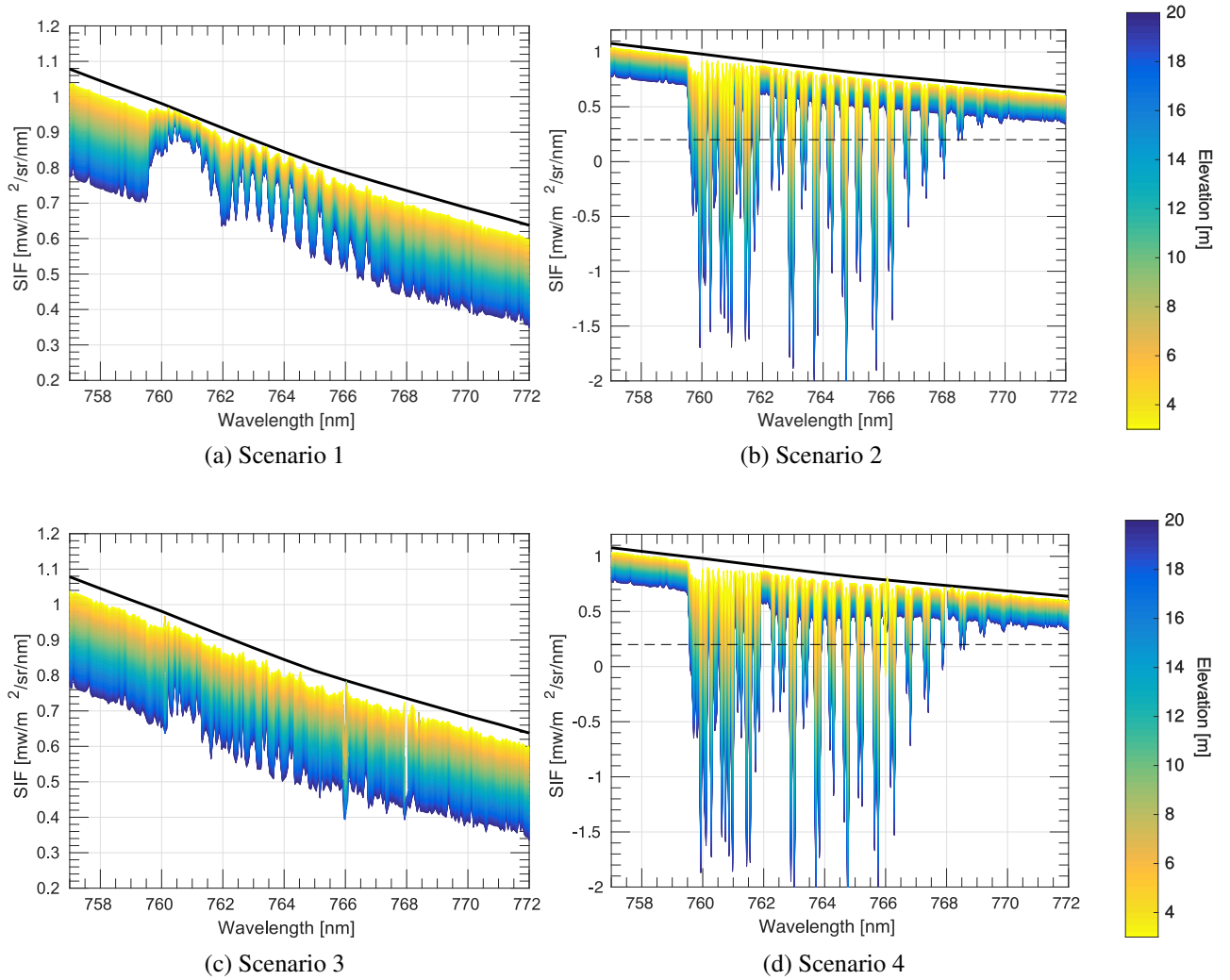


FIGURE 6.4.2: Retrieved SIF under conditions configured for scenarios (1 – 4). Figure (a) Upward oxygen transmittance corrected ($t_{O_2}^\uparrow$) and solar irradiance measured at surface level (\bar{E}); (b) No upward O_2 transmittance corrected and solar irradiance measured at surface level (\bar{E}); (c) Upward oxygen transmittance corrected ($t_{O_2}^\uparrow$) and solar irradiance measured at sensor level (E); (d) No upward O_2 transmittance corrected and solar irradiance measured at sensor level (E). The black dashed line in (b), and (d) shows the lower y-axis limit set in (a), and (c).

transmittance, there are no residuals caused by aerosols outside the absorption band (i.e., no bias is observed).

Information regarding the most relevant input parameters used in the MODTRAN RTM as part of the simulation, as well as the surface reflectance and fluorescence spectra used in the simulation are detailed in Table 6.4.1 and Figure 6.4.5, respectively.

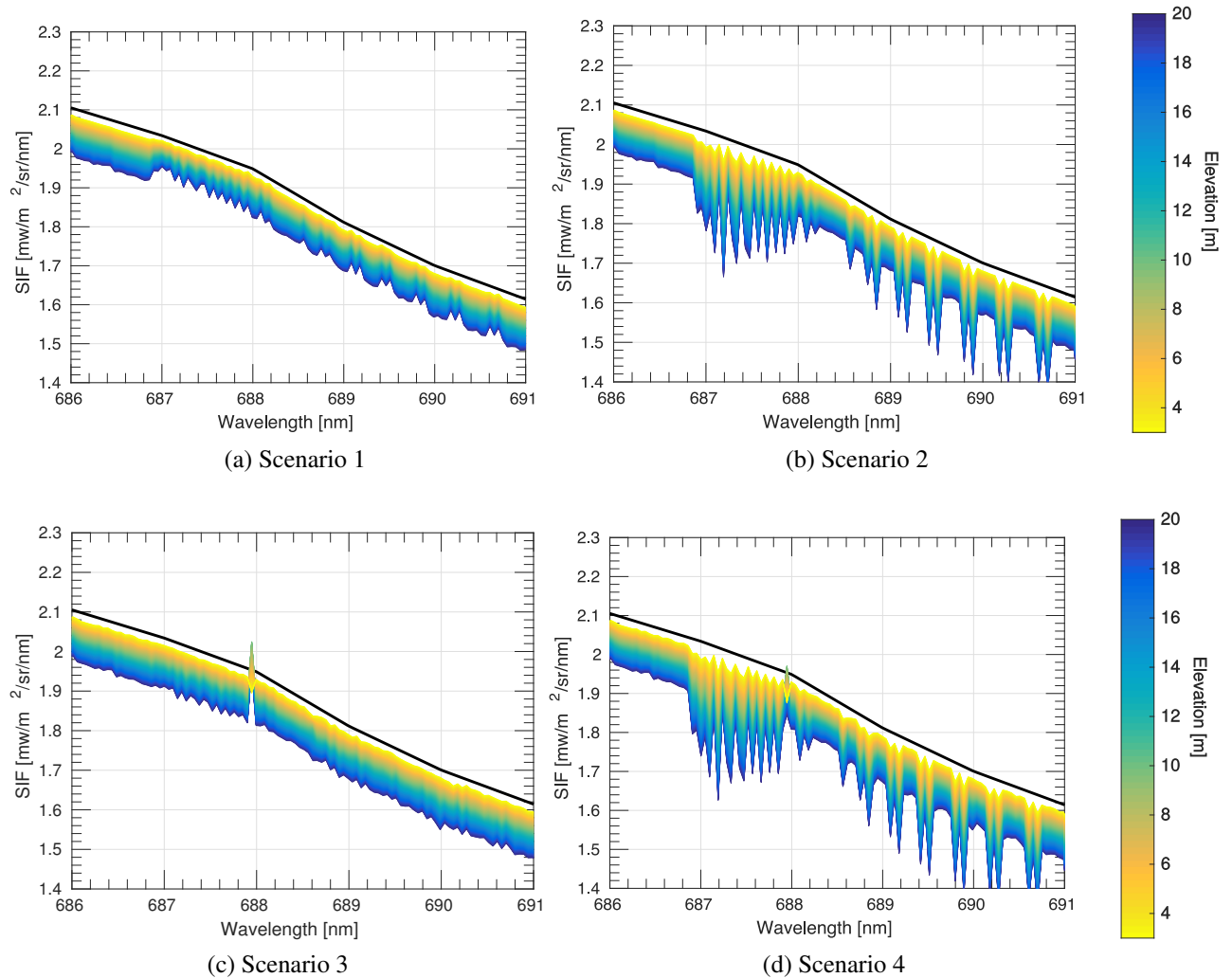


FIGURE 6.4.3: Retrieved SIF under conditions configured for scenarios (1 – 4) for the O_2 -B spectral range. Figure (a) Upward oxygen transmittance corrected ($t_{O_2}^\uparrow$) and solar irradiance measured at surface level (\bar{E}). (b) No upward O_2 transmittance corrected and solar irradiance measured at surface level (\bar{E}). (c) Upward oxygen transmittance corrected ($t_{O_2}^\uparrow$) and solar irradiance measured at sensor level (E). (d) No upward O_2 transmittance corrected and solar irradiance measured at sensor level (E). Black dashed line in (b), and (d) shows the lower y-axis limit set in (a), and (c).

6.4.2 Oxygen compensated 3FLD

A second simulation experiment was performed by varying the sensor height above TOC (from 3 m to 20 m), and the instrument spectral configuration for the 4 scenarios as described in Section 6.4.1. In this section, the 3FLD method with the approximation for compensating the O_2 -A transmittance effect as given in Equation 6.3.4 is applied. The selected sensor specifications covered, i.e., Spectral Resolution (SR) and the Spectral Sampling Interval (SSI); are listed in the legend of Figure 6.4.6 based on configurations evaluated by [Damm *et al.*, 2011].

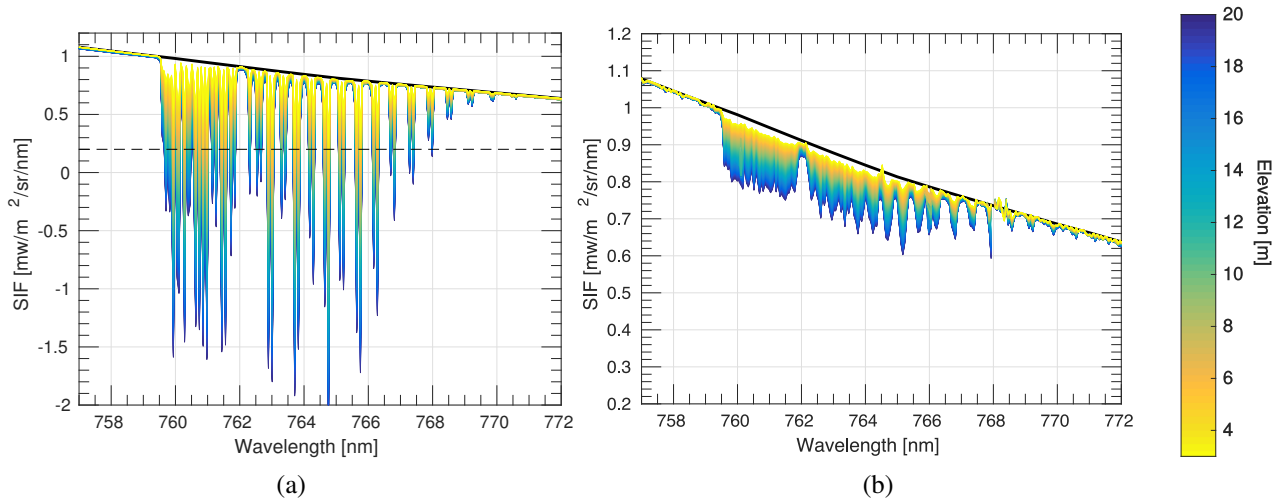


FIGURE 6.4.4: SIF was estimated by :**(a)** correcting the at-sensor radiance for the aerosol transmittance (t_{aer}^{\uparrow}) and measuring the solar irradiance at TOC; **(b)** correcting the at-sensor radiance for the total transmittance (t^{\uparrow}) and measuring the solar irradiance at sensor level. Black dashed line in **(a)** shows the lower y-axis limit established in **(b)**.

	MODTRAN Input Parameter	Value (Units)
Atmospheric parameter	Model of atmosphere	Mid Latitude Summer
	AOT at 550 nm	0.15 (-)
	Aerosol Type	Rural (-)
	Water vapour	2.5 (g/cm ²)
Geometry parameter	Surface elevation	0 (m)
	Solar Zenith Angle	40 (°)
	Viewing Zenith Angle	0 (°)
	Relative Azimuth Angle between sun and sensor	90 (°)
	Sensor height	3–20 (m)
High Spectral Resolution	Spectral Resolution at O ₂ -B	1 (cm ⁻¹) ~ 0.04 (nm)
	Spectral Resolution at O ₂ -A	1 (cm ⁻¹) ~ 0.05 (nm)

TABLE 6.4.1: MODTRAN input parameters used to generate data from Section 6.4. MODTRAN transmittance mode was used to compute the upward atmospheric transmittance (allowing for the transmittance decomposition between the different molecular species, trace gases and aerosols). MODTRAN radiance with scattering mode was used to compute the solar irradiance at different tower height levels.

Figure 6.4.6 shows the performance of the 3FLD method under scenarios 1-4 for different sensor configurations. Since the 3FLD method depends strongly on the wavelength locations, especially on the wavelength at bottom of the O₂-A absorption region, the central wavelength of the band located at the bottom of the O₂-A absorption region has been kept constant at 760.6 nm in all the sensor configurations evaluated. Consistent with results shown in Figure 6.4.2, as the sensor height above TOC increases, scenarios 2 and 4 underestimate the retrieved SIF. For scenarios 1 and 3, where O₂ transmittance between the target and the sensor is corrected,

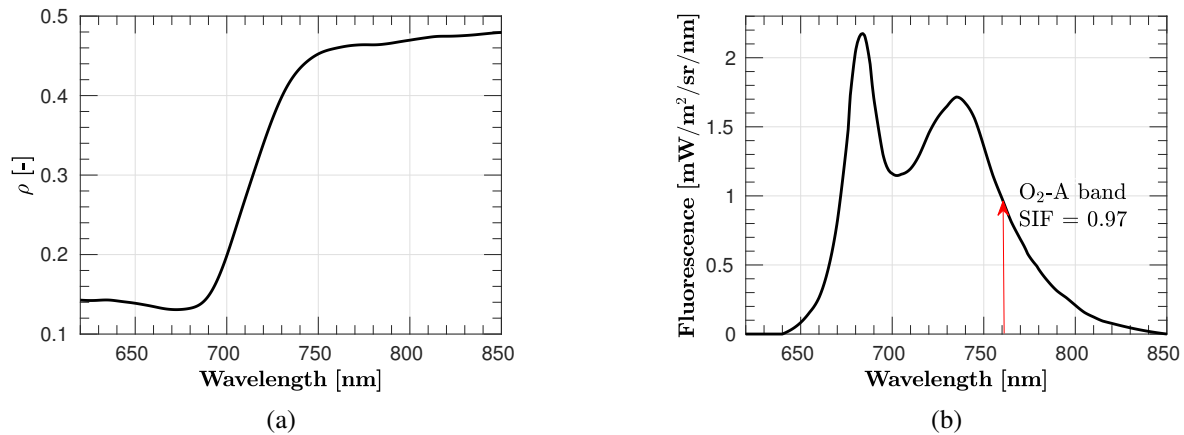


FIGURE 6.4.5: Surface reflectance **(a)** and fluorescence spectra **(b)** used in Section 6.4. These spectra were originally derived from the Fluorescence EXplorer (FLEX) mission requirement document [Drusch \[2016\]](#), where they are used as a reference dataset. The red upward arrow indicates the SIF value at the bottom of the O₂-A absorption band.

SIF was overestimated as the sensor height increases, and as the sensor resolution decreases. In addition, according to Figure 6.4.2, it could be expected that SIF estimations from scenario 1 were more accurate (provide lower relative errors [%]) than from scenario 3. However, this is not the case. The main reason for that is because a compensation exists between the overestimation produced by the 3FLD technique and the stronger SIF underestimation produced in scenario 3 by measuring the solar irradiance at sensor level. Note that for all the scenarios SIF was retrieved at TOC level using the 3FLD method to identify the relative error baseline for each of the sensor configuration evaluated (black symbols and lines in Figure 6.4.6).

SIF relative errors in Figure 6.4.6 have been limited to a range of $\pm 50\%$. For scenario 4, where no O₂ compensation is applied, the application of the 3FLD method results into high underestimation of the SIF value, even for sensors located as close to the surface as 3 m, regardless of the instrument configuration used. For scenarios 1 and 3, only in the particular cases where the instrument acquires the signal at high spectral resolution (i.e., $SSI < 0.2$ nm and $SR < 0.4$ nm), does the compensation for the O₂ effects leads to SIF relative errors less than 30%, for all sensor heights.

6.4.3 Oxygen compensated SFM

This section assesses the performance of the O₂ compensated SFM for a range of sensor heights above TOC level (from 3 m to 20 m) on the O₂-A absorption region and for the same instrument configurations evaluated in subsection 6.4.2. For a specific sensor, the SIF retrieval performance relies on optimal SR, SSI, and SFM which depend strongly on: (1) the considered wavelength interval, (2) the use of weighting functions, and (3) the mathematical functions used to model fluorescence, F , and reflectance, ρ , spectra [[Meroni et al., 2010](#)].

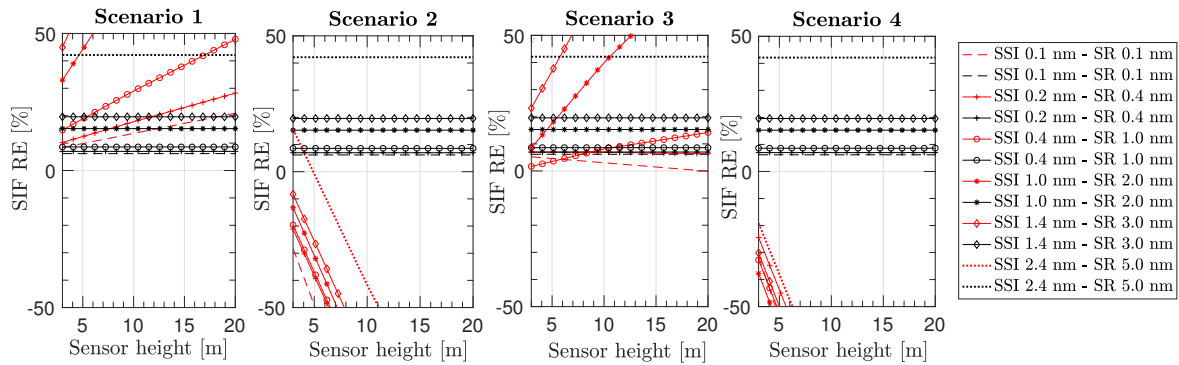


FIGURE 6.4.6: Relative error (%) on retrieved SIF when applying the 3FLD method according to Equation 6.3.4 are shown for a range of spectral resolutions, applied to scenarios 1-4 (red symbols and lines). The SIF relative error obtained when applying the 3FLD at TOC is indicated with black symbols and lines.

According to the results obtained in [Meroni *et al.*, 2010] for noise-free data, the best SFM performance was obtained by modelling SIF (F) as a quadratic function and reflectance (ρ) as a cubic function for a narrow spectral interval ranging between 759.3–762.0 nm, without any weighting function. Due to multiple spectral configurations considered here, in order to ensure that enough wavelengths are selected (specially for the lower resolutions evaluated), the selected spectral interval has been expanded to 759.3–767.5 nm (which corresponds to the third range interval described in [Meroni *et al.*, 2010]). For the SFM calculation, on the one side, the first guess of the F polynomial coefficients was estimated by fitting the reference SIF spectrum to a quadratic function and distorting the derived coefficients by 10% of their value. Conversely, the first guess of the ρ polynomial coefficients was estimated by fitting the apparent reflectance spectrum ρ_{app} to a cubic function, in the spectral region around the O₂-A, but avoiding the absorption band. The apparent reflectance spectrum, ρ_{app} , was obtained as the ratio between the upward radiance and the incoming solar irradiance measured at sensor level. In Figure 6.4.7, ρ_{app} at the highest and lowest spectral resolution evaluated are presented at-TOC, at 3 m and at 20 m height. It can be observed that with increasing sensor height peaks in the apparent reflectance become lower. In the particular case of the 20 m sensor height peaks in the ρ_{app} have been transformed into depressions.

Prior to showing the impact of the O₂ effects on the modified SFM formulation, to establish a reference point (Figure 6.4.8), the level of accuracy of the retrieved SIF when the SFM is applied at TOC for the given surface reflectance and SIF spectra, with the polynomial functions used to model these signals, and the selected spectral interval is presented. As can be seen in Figure 6.4.8, for high resolution spectrometers relative error are lower than 10%, however this error increases with decreasing spectral resolution (i.e., for sensor with wider bands).

Therefore, following the same configuration (i.e., same spectral interval and polynomial functions to model ρ and F), the performance of the SFM is presented for the case when O₂ transmittance effects are compensated using Equation 6.3.8 (Figure 6.4.9).

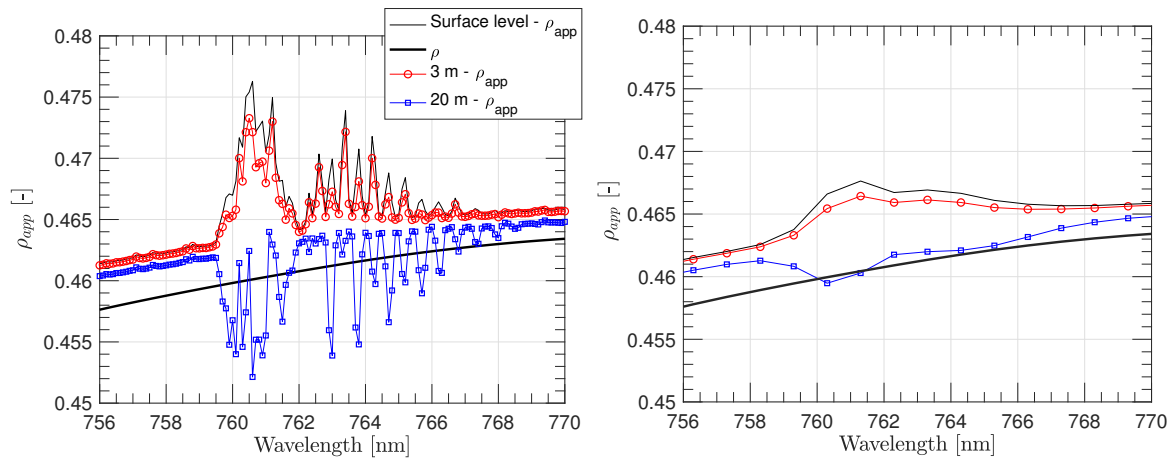


FIGURE 6.4.7: Apparent reflectance (ρ_{app}) derived at high (SSI 0.1 nm - SR 0.1 nm) and low (SSI 1 nm - SR 2 nm) instrument resolutions for 3 m and 20 m sensor heights above the TOC level (red with circles and blue with squares lines respectively). The solid thin black lines correspond to the ρ_{app} derived at surface level. The solid thick black line corresponds to the surface reflectance used here as a reference.

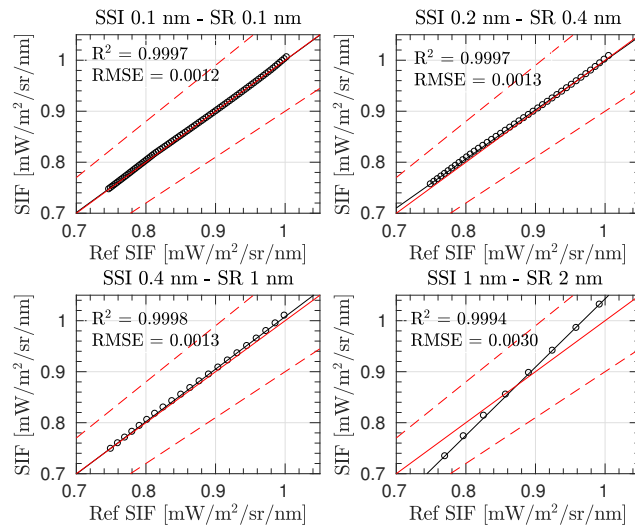


FIGURE 6.4.8: Scatter plots of the reference spectra and estimated SIF spectra values (black circles) in the interval between 759.0–767.5 nm, for different instrumental spectral resolutions (SR) and sampling interval (SSI). Estimated SIF was derived by applying the SFM at TOC. Red solid line represents the 1:1 line, and red dashed lines define the region for a SIF relative error lower than 10%.

Figure 6.4.9 shows the estimated SIF for each of the above-evaluated scenarios 1–4. Errors on retrieved SIF are derived due to: (1) modelling the F and ρ signals as a cubic and a quadratic function, respectively, (2) introducing the O_2 transmittance compensation but ignoring the effects of the ISRF convolution mentioned in Section 6.3.3, and (3) not restricting the modelled

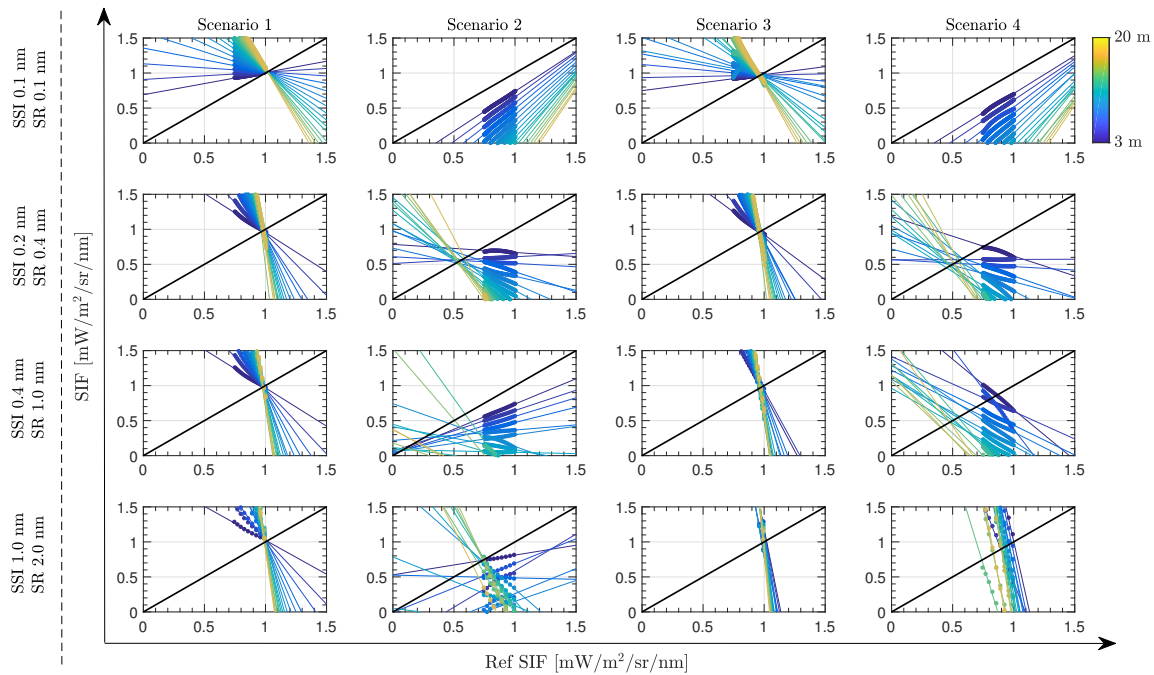


FIGURE 6.4.9: Scatter plots of reference SIF versus estimated SIF spectra in the interval between 759.0–767.5 nm using the SFM retrieval approach and O_2 compensation while ignoring instrument spectral convolution effects for scenarios 1–4. Simulations are shown for different instrument resolutions (rows 1–4) and sensor heights between 3 m to 20 m (colour scale). Solid lines are regression lines. Actual estimations are presented as circles.

functions to realistic values. In scenarios 1 and 3, where the upward O_2 transmittance from target to sensor is corrected ($t_{O_2}^\uparrow$) the estimations of values close to 0.97 [$mW/m^2/sr/nm$] (which corresponds to the SIF reference value at the bottom of the O_2 –A band, see Figure 6.4.5) are accurately retrieved. However, estimated SIF values far away from the deepest region of the oxygen band are not successfully derived (not following the 1:1 line) due to not considering the convolution by the ISRF in the formulation. In case of scenarios 2 and 4, neither the values at the bottom of the O_2 –A band nor those vicinities have been successfully retrieved.

6.4.4 Coupling oxygen transmittance and ISRF compensation with the SFM

As has been demonstrated during this section, O_2 transmittance effects must be compensated when retrieving SIF from proximal remote sensing data. However, significant errors in estimating SIF can occur, even applying an O_2 transmittance compensation factor (or spectrum) in the formulations of the 3FLD (or SFM) approach(es). Thus, here errors derived in the estimated SIF under scenario 1 when following the strategy detailed in Figure 6.3.1, which also includes the ISRF convolution as part of the SFM minimization process, are assessed.

Figure 6.4.10 shows the estimated SIF at multiple sensor heights above the TOC level when

applying the proposed strategy and considering the same conditions presented in Section 6.4.3, i.e., the same spectral interval and the same polynomial functions used to model F and ρ . Although higher relative errors are derived at lower spectral resolution, errors have significantly improved in comparison to the situation described by scenario 1 from Section 6.4.3, where the SFM approach was used while ignoring the convolution effects in the O_2 compensation. Therefore, a successful SIF estimation was achieved, including those values that were not close to the bottom of the O_2 $-A$, i.e., SIF from (0.7–1 $mW/m^2/sr/nm$) for high spectral resolution cases.

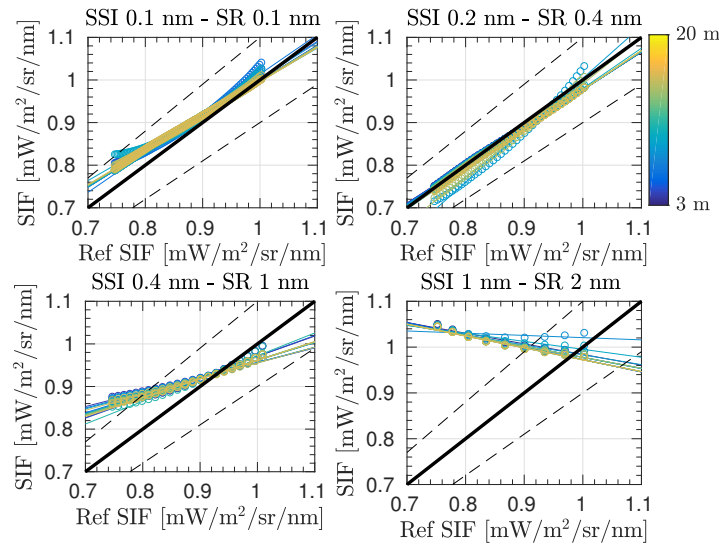


FIGURE 6.4.10: Scatter plots showing reference SIF versus estimated SIF in the interval between 759.0–767.5 nm, using the proposed SFM retrieval approach to compensate for oxygen effects while also accounting for the instrument spectral convolution effects, for different instrument spectral resolutions and above TOC level sensor heights from 3 m to 20 m (colour scale). Coloured solid lines are regression lines for the range of sensor heights evaluated while actual estimations are marked as circles. Black solid line represents the 1:1 line and dashed lines define the area with a SIF relative error lower than 10%.

Finally, in order to evaluate the impact of excluding the aerosol compensation on the upward transmittance from the TOC target to the sensor, the impact of replacing the O_2 transmittance with the total atmospheric transmittance function, i.e., replacing $t_{O_2}^\uparrow$ by t^\uparrow , is quantified. Due to the improvement achieved in accuracy on estimated SIF is not significant, to better showing the slight gain, Figure 6.4.13 presents a scatter plot between estimated SIF (labelled as SIF_{O_2}), with compensation only for O_2 transmittance, versus compensation for the total atmospheric transmittance (labelled as SIF_{tot}).

In addition, since the SFM provides as outputs the emitted SIF as well as the reflected surface spectrum, scatter plots comparing reference surface reflectance with estimated reflectance when compensating for either oxygen transmittance only, or for total atmospheric transmittance, are also here included (Figures 6.4.11 and 6.4.12). Thus, according to this analysis, for a few meters target–sensor distance, using the SFM approach and only compensating for O_2 absorption and ISRF convolution effects, without corrections for other factors, would be sufficient to accurately estimate SIF on sensors with a $SR < 1$ nm.

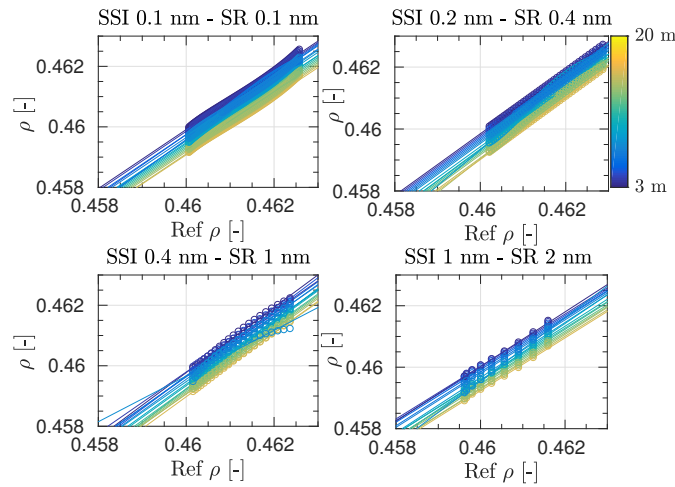


FIGURE 6.4.11: Scatter plots showing reference surface reflectance ($\text{Ref } \rho$) versus estimated surface reflectance (ρ) in the interval between 759.0-767.5 nm, using the proposed SFM to compensate for oxygen absorption effects while also accounting for the instrument spectral convolution effects for different instrument resolution and above TOC sensor heights from 3 m. to 20 m. (color scale). Coloured solid lines are regression lines for the range of sensor heights evaluated while actual estimations are marked as circles.

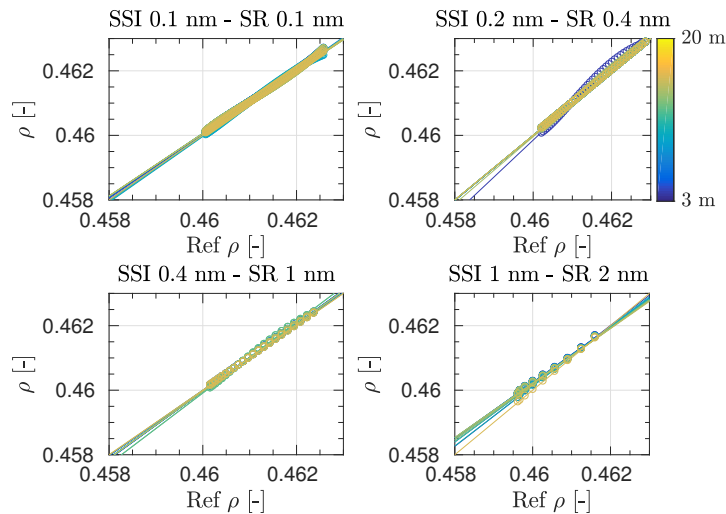


FIGURE 6.4.12: Scatter plots showing reference surface reflectance ($\text{Ref } \rho$) versus estimated surface reflectance (ρ) in the interval between 759.0-767.5 nm, using the proposed SFM to compensate for total atmospheric effects while also accounting for the instrument spectral convolution effects for different instrument resolution and above TOC sensor heights from 3 m. to 20 m. (color scale). Coloured solid lines are regression lines for the range of sensor heights evaluated while actual estimations are marked as circles.

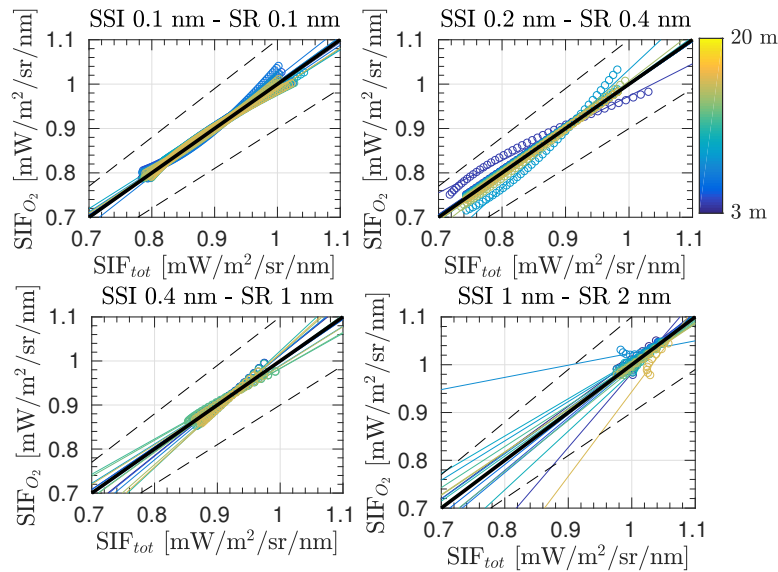


FIGURE 6.4.13: Scatter plots of estimated SIF using the proposed SFM retrieval approach to compensate (1) for oxygen effects and (2) for total atmospheric transmittance, accounting in both cases for the instrument spectral convolution effects at different instrument resolutions and sensor heights from 3 m to 20 m (colour scale). Coloured solid lines are regression lines for the range of sensor heights evaluated while actual estimations are marked as circles. Black solid line represents the 1:1 line and dashed lines define the area having a SIF relative error lower than 10%.

6.5 Temporal analysis in temperature and pressure environmental conditions

In real scenarios, the accuracy of the retrieved SIF will also depend on the accuracy achieved in modelling the atmospheric conditions. As concluded in Section 6.4, oxygen transmittance compensation becomes essential to accurately estimate SIF for proximal sensing. In the particular case of conducting a long temporal data series analysis of measured SIF from a tower, oxygen transmittance variations caused by seasonal p and T changes within the year must also be properly taken into account. As an illustrative example, the expected variation, first for the oxygen transmittance and then for the acquired at-sensor radiance, caused by changes in T and p conditions is analysed (see Figure 6.5.1 for T and p values used). In this example, radiance variations that would be observed at a measurement tower mounted on the Hyytiälä Forestry Field Station due only to changes in the meteorological conditions while keeping invariant the surface properties, i.e., reflectance and emitted SIF, were reproduced. Thus, for the at-surface level the reference surface reflectance and SIF spectra shown in Figure 6.4.5 were taken. For the atmospheric simulation the exercise was performed in three steps: (1) taking the T and p registered in Hyytiälä, transmittance following the empirical approximations presented in Equations 6.3.6 and 6.3.7 was computed, (2) the resulting transmittance spectra were scaled to a high resolution MODTRAN spectra (0.1 cm^{-1}). Finally, in (3) MODTRAN was used to compute, according to the oxygen transmittance spectra, the sensor radiance over a full one year period

sensor radiance using Equation 6.2.3.

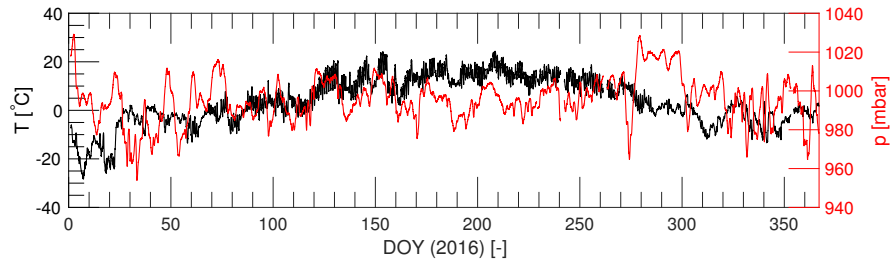


FIGURE 6.5.1: Annual temperature (black) and air pressure (red) registered in the Hyytiälä Forest Field Station during the year 2016.

Regarding the simulation protocol, while T was directly measured at the top of the tower (~ 30 m), air pressure was measured at surface level. Therefore, surface pressure at the top of the tower was computed following Equation 6.5.1, developed by combining the hydrostatic equation together with the ideal gas law, assuming the measured total pressure as dry air pressure.

$$p_{sen} = p \cdot \exp\left(\frac{gM_0Z}{R_0T}\right) \quad (6.5.1)$$

In Equation 6.5.1, p_{sen} is the pressure at sensor level, p and T are the pressure and Temperature measured at TOC level, M_0 is the molar mass of the dry air, R_0 is the ideal gas constant, and g is the standard gravity constant. In this simulation exercise, it was evaluated how variations in the meteorological conditions impact the O_2 transmittance locally, and how this influence on O_2 transmittance could be translated into perceived changes in the retrieved SIF signal if not appropriately compensated. For this exercise, an example having an invariant surface up-welling signal throughout the year at the Hyytiälä tower research site in Finland was chosen. Since the selected Hyytiälä tower height is around 30 m tall, about 15 above the evergreen forest canopy that it monitors, and assuming nadir acquisition geometry, the optical path was fixed as 15 m, i.e., the Z term in Equation 6.3.7.

Figure 6.5.2 shows oxygen molecular transmittance in the O_2 -A and O_2 -B absorption bands caused by T and p changes throughout a full year (2016) for the tower geometrical configuration in the Hyytiälä Forestry Field Station. As observed, the band depth in both, the O_2 -A and O_2 -B regions tracks the expected thermal dynamics related to seasonality, i.e., as T increases from winter minima (DOY 0, ~ 350) to reach maximum values in the summer season (e.g., DOY, ~ 180), the O_2 absorption band depth becomes shorter. For the O_2 -A band, the seasonal change in transmittance is 0.01 [–] (Figure 6.5.2a), whereas for the O_2 -B case, the seasonal transmittance change is only 0.002 [–] (minimum and maximum values of 0.990 and 0.992), although still evident (Figure 6.5.2b).

Now that a temperature-driven seasonal change in O_2 transmittance at the Hyytiälä tower site during 2016 has been shown, the expected at-sensor radiance variations for the for the

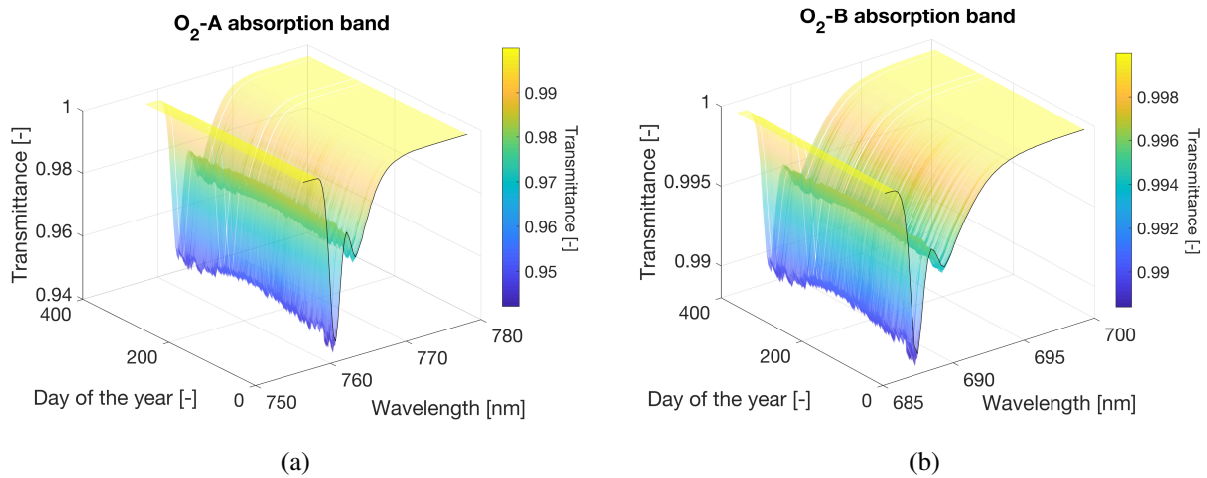


FIGURE 6.5.2: Spectral oxygen transmittance variation for the O₂-A (a) and O₂-B (b) absorption bands for the T and p conditions registered at 30 m tall tower at the Hyytälä Forest Field Station.

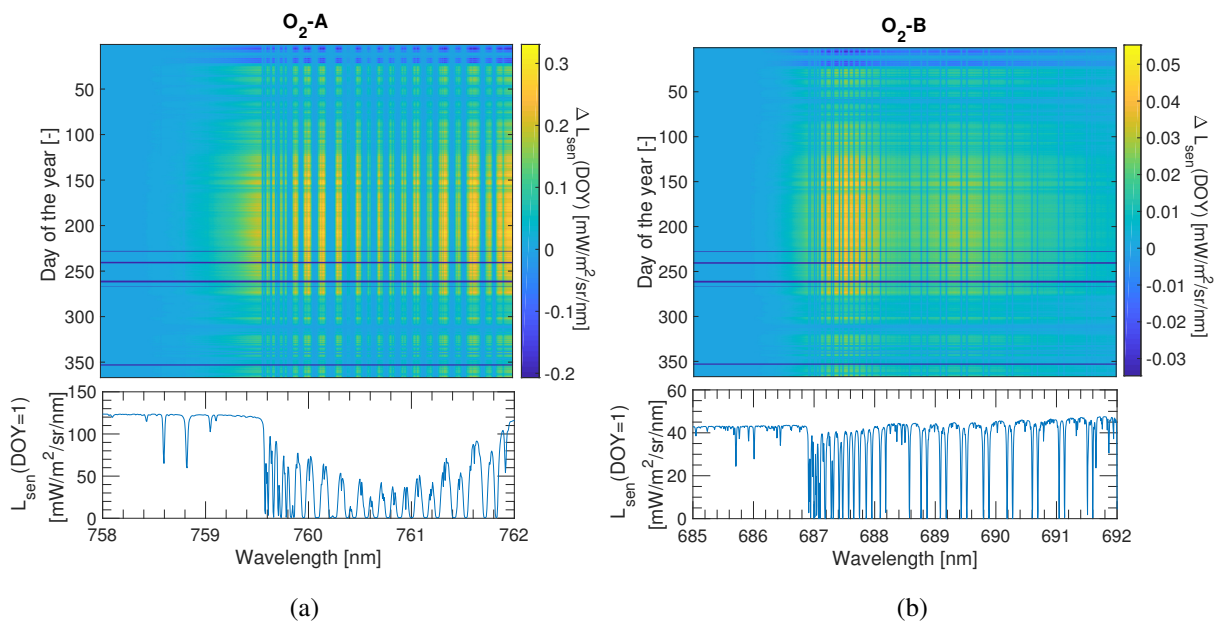


FIGURE 6.5.3: Variation in radiance units computed as $L_{sen}(\text{DOY}) - L_{sen}(\text{DOY}=1)$ for the O₂-A (a) and the O₂-B (b) absorption regions. The acronym DOY refers to the Day Of Year from 1–365.

O₂-A and O₂-B absorption regions (Figure 6.5.3) using MODTRAN simulations at the highest spectral resolution (~ 0.006 nm of SSI in the O₂-A region) was next computed. As observed, for the O₂-A absorption band, seasonal changes in radiance units reached maximum values of 0.25 [mW/m²/sr/nm], which represents around 30% of the SIF signal at the O₂-A band used as a reference in this example. Conversely, radiance barely reached 0.04 [mW/m²/sr/nm] for the O₂-B region, representing less than 2% of the SIF signal at the O₂-B band. This exercise

indicates that SIF retrievals must account with T and p measurements as part of the O_2 compensation strategy to avoid overestimating in summer or underestimating in winter the retrieved SIF signal due to environmental effects.

6.6 Discussion

Accurately measuring SIF variations due to changes in the environmental conditions, can facilitate better interpretation and constrain SIF and Gross Primary Productivity (GPP) relationships. Studies have recently reported the existing correlation between SIF and GPP, by combining GPP data acquired either from Eddy–Covariance (E–C) flux towers or satellites, with satellite–derived SIF from the Greenhouse Gases Observing Satellite (GOSAT) [Frankenberg *et al.*, 2011b; Guanter *et al.*, 2012], the Global Ozone Monitoring Mission–2 (GOME–2) [Joiner *et al.*, 2014; Guanter *et al.*, 2014; Zhang, Y. *et al.*, 2014; Zhang, Yao. *et al.*, 2016] and recently with the Orbiting Carbon Observatory–2 (OCO–2) [Sun *et al.*, 2017]. However, some concerns regarding the ecophysiological basis between SIF and GPP relationship under varying environmental conditions are still present in the scientific community [Verma *et al.*, 2017; Verrelst *et al.*, 2016b], and particularly in the gap in the mechanism understanding between SIF–GPP temporal short–term and spatial small–scale mechanisms [Zhang, Y. *et al.*, 2016]. In this respect, systematic SIF tower based measurements can play a key role: (1) to validate SIF maps derived at a global scale from satellite, (2) to analyse the impact of vegetation structure on emitted SIF, and (3) to better understand the existing relationship between SIF and other energy fluxes such as the GPP, the ecosystem respiration, latent and sensible heat fluxes, etc., which are typically indirectly products derived from E–C flux towers.

At proximal sensing scale, the idea of linking ground–based remote sensing measurements to ecosystem CO_2 flux data has been addressed in the past by many international initiatives, such as the SPECNET [Gamon *et al.*, 2010], and the European cost actions EUROSPEC ES0930 [Porcar-Castell *et al.*, 2015] and the OPTIMISE–ES1309 (<http://optimise.dcs.aber.ac.uk/>) networks. These projects have explored, under a different perspective, the use of proximal passive optical remote sensing data of ecosystems whereby carbon and water vapour fluxes are estimated at research–tower sites by E–C techniques. In particular, these network initiatives have focused on analysing, comparing and standardizing measurement protocols; while also promoting the design, testing, and development of new optical instrumentation. However, when SIF is one of the biophysical parameters under study, additional critical attention must be drawn to processing strategies as well as to instrument and measurement protocols. For instance, while instrument specifications needed to determine some biophysical remote sensing indexes such as the Normalized Difference Vegetation Index (NDVI) [Tucker, 1979] or the Enhanced Vegetation Index (EVI) [Huete *et al.*, 2002], can be easily reached; measuring SIF from passive remote sensing techniques is still quite challenging. In terms of the instrument specifications, high spectral resolution spectrometers with high signal to noise ratio are generally required, but these instruments are more expensive and more difficult to maintain [Damm *et al.*, 2011]. In terms of data processing, as demonstrated in this chapter, atmospheric absorption and

scattering effects cannot be ignored even when measuring data at a few meters distance from the TOC target. Here, it was demonstrated the need for compensating O₂ molecular absorption when measuring SIF using proximal remote sensing techniques inside the O₂-A absorption band. Since oxygen absorption is proportional to surface pressure, even a few meters distance between the TOC target and the sensor strongly impacts the retrieval of the weak fluorescence signal. Thus, it would be of great interest not only to seek a standardizing measuring protocol in future experimental projects, but also to standardize common data processing strategies that deal with the compensation of O₂ transmittance, the ISRF convolution effects, and the changing environmental conditions related to thermal and surface pressure dynamics, T and p .

This demonstration began with three cases, analysing a set of simulated noise-free scenarios in order to distinguish between errors derived from the SIF retrieval technique and errors caused by O₂ absorption effects: (1) using high-spectral resolution data and assuming the knowledge of surface reflectance, i.e., an ideally perfect retrieval; (2) compensating O₂ effects using the 3FLD technique; and, (3) compensating O₂ effects using the SFM strategy. Results suggest that by applying a simple oxygen compensation strategy (either by modifying the FLD or SFM approaches) while ignoring the convolution effects associated with sensor spectral resolution, does improve SIF estimations. However, significant errors can occur as the instrumental resolution becomes lower (spectral resolution ≥ 0.4 nm). To mitigate that, the performance of a strategy that (1) compensates for atmospheric effects, and (2) properly accounts for the ISRF in each iteration of the SFM is proposed and evaluated. Results demonstrate that following this strategy, SIF can be estimated, for all the sensor heights differences (TOC to sensor) evaluated (3–20 m), with a relative error lower than 10% across the O₂-A absorption region when using a high spectral resolutions sensor (≤ 0.4 nm). For lower spectral resolution sensors, only SIF estimated at those wavelengths close to the bottom of the O₂-A absorption band are within 10% of accuracy. The main steps of this strategy, as well as some recommendations to its application, are summarized here:

1. It is recommended to use the downward acquired solar irradiance at sensor level, E , to model the atmospheric state. This can be easily achieved by minimizing the spectral error between the measured versus a modelled solar irradiance spectrum. In most atmospheric RTMs, parameters related to the illumination and acquisition geometry as well as those depending on the atmospheric state, such as the Aerosol Optical Thickness (AOT) or the temperature profile, can be modified. The number of free parameters to be fitted within the RTM will depend on the auxiliary information available or measured and the flexibility to vary the inputs in the selected RTM. In this respect, the separate measurement of solar irradiance terms for the global, E , and diffuse, E_{dif} , which better accounts for aerosol scattering, can improve the atmospheric characterization process.
2. Once having the atmospheric state characterized, the selected atmospheric RTM can be used to model all the atmospheric transfer functions required to perform the proposed compensation strategy to account for O₂ and instrument convolution effects. Note that using an atmospheric RTM enables the modelling not only of those functions that account

for the entire atmospheric column, but also for those that account for the atmospheric path length between the target and the sensor.

3. To avoid inter-calibration issues between different instruments acquiring down-welling and up-welling radiances, the use of a single spectrometer is advisable. To do so, in the recent years dual field of view instruments have been developed, which guarantees quasi-simultaneous measurements of down-welling and up-welling radiation, e.g., [Mac Arthur et al. \[2014\]](#).
4. Finally, a SFM technique should be applied to disentangle emitted SIF from the reflected solar irradiance to minimize the spectral difference shown in Equation 6.3.8.

Regarding up-scaling issues: BRDF effects, footprint variability, and scale mismatch are still factors that are difficult to characterize in linking and up-scaling remotely sensed SIF and E-C data. In this respect, notable advances in UAV technology provides a current opportunity to face these challenges [[Porcar-Castell et al., 2015](#)]. While optical systems mounted on towers can monitor the vegetation canopy of interest from a fixed height (5~ 50 m), UAVs can attain heights of hundred of meters, and are flexible to acquire the same target from different heights. However, most of the atmospheric approximations assumed for tower-basis cannot be met for UAVs. For instance, while in this work it was demonstrated that only compensating for oxygen absorption effects was enough to properly estimate SIF from a few meters distance; conversely, aerosols effects should also be compensated when processing data from UAVs. Certainly, the impact of aerosols on the estimated SIF from UAVs will definitively depend on the atmospheric conditions and the sample-sensor distance. Overall, the application of a full atmospheric correction strategy, like those applied for airborne sensors, will avoid errors in the estimated SIF caused by ignoring atmospheric effects. Given the continuing progress in the development of more advanced UAVs platforms and the increasing number of data and campaigns [[Aasen, 2017](#)], there is room to exploit new possible atmospheric compensation strategies that, while being more simplistic than full-physics inversion algorithms, could still derive accurate SIF estimations.

Finally, this chapter intends to draw attention to some aspects that are typically ignored or considered as secondary, such as the O₂ transmittance dependency on the environmental conditions, e.g., T and p . This dependency, analysed in this work within a theoretical framework and following the approximation of [Pierluisi and Chang Mind \[1986\]](#), may imply the detection of trends in the retrieved SIF that are not actually related to the emitted signal but are caused by a failure to apply a proper oxygen transmittance compensation. The impact of seasonal changes in $T - p$ was more significant for the O₂-A than for the O₂-B spectral region. Therefore, for proximal sensing scenarios attention should be paid on the O₂-A absorption lines. Results indicate that summer-winter transitions (i.e., in this case with T and p variations of ~ 40°C and 30 mbar) can produce changes in radiance units reaching maximum values of 0.25 mW/m²/sr/nm, which can become a significant fraction of the SIF signal.

6.7 Conclusions

When estimating the weak Sun-Induced chlorophyll Fluorescence (SIF) signal by resolving the strong O₂-A absorption region and using passive remote sensing techniques, atmospheric effects must always be compensated, even at proximal sensing scenarios. In this chapter it was demonstrated that utilizing simple atmospheric compensation strategies, based on modifying the existing Fraunhofer Line Discriminator (FLD) family or the Spectral Fitting Method (SFM) formulations, alone are not enough to accurately estimate SIF due to appearing disturbances related to the Instrumental Spectral Response Function (ISRF) convolution effects. Due to that finding, a new strategy that simultaneously deals with both the oxygen compensation and the ISRF convolution, as part of the SFM minimization process was proposed. The assessment is that the proposed strategy results into a SIF relative error lower than 10% in the O₂-A absorption region when using fine spectral resolutions sensors (≤ 0.4 nm) for the range of target-sensor distances evaluated (3–20 m). When using lower spectral resolution sensors (> 0.4 nm), only SIF estimated at those wavelengths close to the bottom of the O₂-A absorption band are within 10% of accuracy. In addition, this work addresses the need to consistently compensate oxygen transmittance according to air temperature (T) and pressure (p) conditions. This fact is of particular relevance for those experiments measuring long temporal SIF data series, especially at latitudes subject to strong T and p seasonality effects.

7

Summary and conclusions

Contents

7.1 Summary. Main results	165
7.2 General conclusions	169

7.1 Summary. Main results

In satellite Earth Observation, when aiming to study Earth surface, i.e., land cover classification, vegetation monitoring, water bodies or ocean color; atmospheric effects must always be accounted for. As light passes through the atmosphere, photons reaching the sensor are affected by molecular and aerosol scattering; as well as for gaseous absorption. According to the instruments' characteristics, when working with optical remote sensing data, these effects can be noticeable in the spatial and in the spectral domain. Spatial and spectral atmospheric effects at different scales, global and local, have been analysed in this Thesis, taking respectively the future space missions Ingenio/SEOsat and FLEX/Sentinel-3 as a reference.

On the one hand, the impact of atmospheric effects in the spectral and spatial domain was analysed according to the Ingenio/SEOsat mission specifications. Regarding the atmospheric spatial effects, they were evaluated based on the theoretical foundations of previous studies that model the atmospheric spatial effects by defining an atmospheric Modulation Transfer Function (MTF) [Kaufman, 1989]. Based on this theoretical framework, an atmospheric aerosol strategy was developed as part of the atmospheric correction process. This strategy was based

on an image deconvolution process using a set of atmospheric MTFs, corresponding to ranging Aerosol Optical Thickness (AOT) values, and analysing the flatness of pixels in vicinities of those classified as borders or transitions pixels between homogeneous areas. This strategy worked perfectly under simulated 1-D and 2-D images, even when noise was added to the signal. However, this strategy requires an accurate knowledge of the instrument MTF and does not represent a full atmospheric correction scheme per se. Consequently, for the Ingenio/SEOSat mission an alternative atmospheric correction strategy was formulated. This alternative was based on a per-pixel radiative transfer model inversion technique by using a set of auxiliary data to characterize the atmospheric state. Additionally, a second step was applied to correct for the spatial atmospheric effects, whereby the image is deconvolved using the atmospheric MTF according to the aerosol content. Results from this strategy have been successfully validated using for this purpose Sentinel-2 data that were atmospherically corrected by the ESA's Sen2Cor toolbox.

On the other hand, high spectral resolution effects were evaluated under the context of the FLEX/Sentinel-3 mission activities. This was performed under CHAPTERS 4 and 5. First, an atmospheric correction strategy was evaluated using data merely from the Sentinel-3 mission, particularly from the Ocean and Land Colour Imager (OLCI) and the Sea Land Surface Temperature Radiometer (SLSTR) instruments. Although results can be satisfactory for many applications, the proposed strategy did not meet the accuracy requirements needed to estimate SIF in certain scenarios, which were analysed in this CHAPTER 4. Consequently, all the formulations used in the atmospheric inversion model, as well as the formulations used to couple the atmospheric inversion and the SIF retrieval process, were evaluated under the FLEX mission requirements. In addition, the exploitation of the high spectral resolution FLORIS surface apparent reflectance in the oxygen regions was hypothesized and tested using simulated data to improve the characterization of the aerosol optical properties. It was demonstrated that the exploitation of the apparent reflectance can improve the aerosol characterization, and therefore the SIF estimations.

Finally, in the thematic CHAPTER 6, also under the FLEX mission context, atmospheric effects were analysed for proximal sensing scenarios; particularly, for high spectral resolution systems mounted on towers. Even for a few meters distance, atmospheric absorption must be compensated in order not to derive errors in estimated SIF. This analysis also evaluated the impact on SIF that is caused by ignoring oxygen absorption effects using the most known SIF retrieval strategies, i.e., the Fraunhofer Line Discriminator (FLD) or the Spectral Fitting Methods (SFM). This work showed that when aiming to compensate for oxygen absorption effects by simply correcting the FLD or SFM formulation by means of introducing the oxygen transmittance function, errors related to the instrument ISRF convolution appear if they are not simultaneously accounted for in the formulation. To remedy this, a novel strategy that simultaneously deals with the oxygen compensation and the instrument ISRF convolution was proposed and successfully evaluated. Finally, due to the key role oxygen transmittance is playing, its dependency on air pressure and temperature conditions was also evaluated. Of interest is that temperature and pressure environmental conditions, if not appropriately accounted for as part of the oxygen compensation strategy, can lead to erroneous winter-summer SIF temporal

trends.

In the following, research questions posed in the **Introduction** 1.3, are again formulated and answered with respect to this Thesis' achievements:

- ***What are the particularities to be considered when developing an atmospheric correction strategy for high spatial resolution satellite images?*** Regardless of the atmospheric effects in the spectral domain, which strongly depends on the band's location; in high spatial resolution images, atmospheric spatial effects such as the blurring produced by the aerosol presence or the adjacency effects between neighbouring pixels are critical and have to be mitigated. In the specific case of the Ingenio/SEOSat space mission, atmospheric spectral and spatial effects were analysed in CHAPTER 3. Regarding the spectral domain, it was shown that although not having bands located at any atmospheric absorption feature, atmospheric effects on bands in the RGB and NIR region are significantly affected by aerosols, and in the case of the NIR band also by water vapour. Regarding the spatial domain, atmospheric spatial effects were analysed following the empirical formulation developed in the 80's that relates the blurring effects produced by aerosol and molecular scattering with the aerosol and molecular content and their vertical distribution. Based on this formulation, a method that exploits transition pixels (edges) between radiometric contrasting areas to detect aerosol content was developed using synthetic images with different geometrical patterns in 1-D and 2-D. This method was based on the construction of a range of MTFs, which are in turn parametrized by the AOT. By deconvolving the images according to the defined MTFs and evaluating the resulting flatness in pixels close to edges, it was possible to derive a successful AOT estimation. This technique was also evaluated on noisy images, and results were also satisfactory. However, this technique does not represent a complete atmospheric correction method per se and its application requires an accurate knowledge of the instrument MTF, since both the instrument and the atmospheric MTF are coupled. Thus, an atmospheric correction strategy called Hybrid was proposed to correct future Ingenio/SEOSat images for those cases where the instrument MTF is not precisely known, and especially, if auxiliary data to characterize the atmospheric state is available. This strategy combines: (1) a per-pixel radiative transfer model inversion technique using auxiliary data, with (2) a spatial image deconvolution modulated by the aerosol load to correct for adjacency effects. The validation was performed using Sentinel-2 images by comparing resulting surface reflectance spectra from the Hybrid method and the ESA's Sen2Cor atmospheric correction Toolbox.
- ***What are the particularities to be considered when developing an atmospheric correction strategy for high spectral resolution satellite images? What are the specific considerations in the particular case of the FLEX/Sentinel-3 tandem space mission?*** The higher spectral resolution, the more information available to characterize the atmospheric state in the spectral domain. However, when working with high spectral resolution spectrometers, assumptions considered in the formulation to perform the atmospheric inversion process, i.e., to transform TOA radiance into surface reflectance, must be inspected. This topic is addressed in CHAPTERS 4 and 5. Results suggest that formulation assumed

to invert TOA radiance is suitable to accomplish the FLEX mission requirements. Special attention is given not only on the spectral convolution of the terms involved in the formulation, but also on how formulation dedicated to the atmospheric inversion and to the SIF estimation is coupled. All these aspects are fully described and assessed in CHAPTER 5.

- ***What kind of considerations have to be taken into account when a classical atmospheric correction strategy (by means of a radiative transfer model inversion) is applied to the FLEX/Sentinel-3 tandem space mission?*** FLEX is designed as a tandem mission with the Copernicus Sentinel-3 space mission. The main reason for doing so is to expand FLEX capabilities for its atmospheric correction. In CHAPTER 4 an atmospheric correction strategy was proposed and assessed under a wide range of simulated atmospheric conditions. Whereas this strategy only makes use Sentinel-3 data to characterize the atmospheric state, i.e., aerosol presence and water vapour content, the successful criteria was set into the derived surface reflectance and estimated SIF from FLORIS instrument. Results underline the importance of accurately estimating not only the AOT, but also the aerosol scattering (by means of the anisotropy parameter). It was observed that filtering out those scenarios where errors in the aerosol scattering asymmetry parameter g were higher than ± 0.05 , significantly reduced the dispersion of the estimated SIF and surface reflectance. This observation reinforces the need to accurately estimate aerosol scattering prior to SIF estimation.
- ***Is the current mathematical formulation used for the atmospheric inversion process suitable for working with high spectral resolution data?*** When working with very high spectral resolution data, certain particularities regarding the formulation assumed to perform atmospheric correction must be evaluated. With this aim, in CHAPTER 5 all the mathematical assumptions done as part of the atmospheric inversion to convert radiance at top of atmosphere to surface reflectance are reviewed. Results conclude that the set of assumptions considered are in agreement with the FLEX mission requirements. Likewise, and given the FLEX mission context, consistency between formulation used as part of the atmospheric correction process and formulation used in the fluorescence estimation strategy was also evaluated. Particularly, the bottleneck resides on the distinct definition of the surface apparent reflectance term typically used in both processes. Consequently, in order to avoid inconsistencies in this respect, CHAPTER 5 presented a formulation able to consistently couple the atmospheric correction strategy with the SIF retrieval process.
- ***In the particular case of the FLEX mission: How can the exploitation of the very high spectral resolution help in the characterization of the aerosol optical properties?*** This question was addressed in CHAPTER 5. While in CHAPTER 4 the need of an accurate atmospheric characterization was shown, in CHAPTER 5 the possible predictive power of the FLORIS high resolution data was tested. In particular, the spectral distortions on FLORIS surface apparent reflectance caused by changes in the aerosol optical properties, AOT, α and g were analysed. The systematic spectral pattern produced due to changes of each aerosol optical property

was used in a multivariate linear regression strategy to improve the initial inaccurate aerosol characterization. Results suggest that the exploitation of FLORIS surface apparent reflectance at the oxygen regions can improve the aerosol estimation and consequently the SIF estimation. Results obtained using a simulated database shows that for the 75% of the observations, relative errors in the estimation of the AOT, the Ångström exponent and the asymmetry coefficient of the scattering pattern were below 0.2%, 6% and 2%; respectively. The successful criteria were applied into the derived FLORIS surface apparent reflectance, taking the FLEX mission requirement regarding SIF estimation within a 10% of accuracy as a threshold. To do so, an error of 10% in SIF was propagated into the FLORIS surface apparent reflectance. Results show that estimated errors in the surface apparent reflectance after applying the multivariate linear regression strategy successfully accomplish the FLEX mission requirements to estimate SIF.

- ***At proximal sensing scale: Is it necessary to compensate for atmospheric effects?*** When acquiring remote sensing data at proximal sensing scenarios, the short atmospheric path covered between the target and the sensor is generally neglected. However, in the context of the FLEX mission activities, even when measurements are taken at proximal scale, oxygen absorption has to be taken into account. In CHAPTER 6 this scenario was evaluated when the goal is to estimate SIF using passive remote sensing techniques. Following this aim, the impact of the atmospheric oxygen absorption was quantified when applying different SIF strategies: the Fraunhofer Line Discriminator (FLD), and the Spectral Fitting Method (SFM). Results suggest that not only oxygen absorption needs to be corrected but also, as part of the correction strategy, instrumental spectral convolution effects must be corrected. In addition, as part of the results derived in this CHAPTER 6, the dependency of the oxygen absorption into the environmental conditions, pressure and temperature, were evaluated for long temporal series (1-year period). It was found that if the atmospheric oxygen compensation is applied without accounting for changes regarding these two environmental parameters, in case abrupt temperature or pressure gradients will be expected, e.g., summer–winter transitions; a false SIF trend can be derived, due to SIF overestimations in the summer or SIF underestimations in the winter.

7.2 General conclusions

In this Thesis, novel strategies have been developed to atmospherically correct satellite image data acquired in the visible and near-infrared spectral domain, both at very high spectral resolution and at high spatial resolution. While for multi-spectral and medium spatial resolution missions atmospheric correction is a well-known process, this process needs to be reformulated for more extreme spectral and spatial resolution data. This work was conducted in the framework of two missions during their phase of development: (1) the Spanish Ingenio/SEOSat mission, and (2) the ESA's tandem FLEX/Sentinel-3 mission.

In the context of the Ingenio/SEOsat mission, the capability to exploit the spatial information for atmospheric correction purposes was analysed. Ingenio/SEOsat is equipped with 4 channels, 3 in the visible (RGB) and 1 in the near-infrared (NIR), and then also a panchromatic (PAN) band that overlaps the green and the red channels. The interval sampling interval is 10 m and 2.5 m for the multispectral and the PAN bands. According to these specifications a first analysis led to the following conclusions:

- The provided spectral information is insufficient to characterize the atmospheric state (mainly aerosol presence and water vapour content). This fact implies that for the atmospheric characterization auxiliary information is required to atmospherically correct Ingenio/SEOsat images.
- Bands located in the RGB and NIR are significantly affected by aerosol content, cloud presence and water vapour content. This fact reinforces the need to atmospherically correct the Ingenio/SEOsat images.
- Given the high spatial resolution of Ingenio/SEOsat, it is possible to characterize the aerosol load by exploiting atmospheric spatial effects.

Regarding the exploitation of the atmospheric spatial effects to characterize aerosol presence, a new technique to estimate the image AOT was proposed and evaluated. This technique was based on the idea that atmospheric spatial effects generate a kind of blurring distortion over the image that is especially observable in transitions between areas with a high radiometric contrast, i.e., edges. Therefore, atmospheric effects tend to reduce the image contrast. In a transition area, if no atmospheric effects would take place, radiometric spatial profiles should follow the shape of a step function. However, atmospheric effects smoothen this transition instead making radiometric profiles to follow a sigmoid function. This fact was already earlier observed where some works were dedicated to describe atmospheric light attenuation effects as optical instruments do, i.e., by means of a MTF. The atmospheric MTF can be formulated as an empirical expression parametrized by means of four parameters: (1) AOT, (2) molecular optical thickness, and height in the atmosphere at which the maximum density of (3) aerosol, and (4) molecules are found. Since AOT drives the MTF shape, this was the parameter to be estimated while default values were assumed for the rest. In essence, the strategy is based on deconvolving the image using multiple MTFs for a given range of AOT values. Therefore, analysing the profiles of the deconvolved images in transition areas, the estimated AOT corresponds to the MTF that best reproduces a step function shape around edges. By applying this technique on simulated images, the following conclusions were derived:

- The defined criterion for the AOT estimation based on analysing the shape of the deconvolved image profiles around edges seems adequate to successfully retrieve AOT.
- The larger number of homogeneous pixels around the edge, the more sensitivity to detect AOT. However, sensitivity to AOT detection saturates around 10 pixels.

- The performance over noisy data (to simulate imperfect homogeneous pixels around the edge), still successfully retrieved the AOT value only using 2 pixels around the edge.

However, also some limitations regarding the application of this technique must be also highlighted:

- This study merely focused on the atmospheric MTF, thereby disentangling the effect of the instrumental MTF. This was done thanks to the use of simulated data. However, on real data both atmospheric and instrumental MTFs are coupled. In order to enable reproducing results reported in this Chapter using real data, then a precise knowledge of the instrument MTF is required.
- In this study, default values were assumed for molecular optical thickness, and the vertical distribution of aerosol and molecules. Although AOT is the driving parameter for the MTF shape, for low AOT conditions, the role of the other parameters become more important. Thus, in that particular case, the assumption of default values for these 3 parameters can result into an inaccurate AOT estimation.

Finally, although being a valuable technique for the aerosol presence characterization, it is not a fully atmospheric correction strategy per se. Consequently, and also because of the need of using auxiliary information for a full atmospheric characterization, an atmospheric correction method called ‘Hybrid’ was presented. The Hybrid method combines: (1) a per-pixel atmospheric radiative transfer model inversion technique, followed by (2) an image deconvolution technique using the atmospheric MTF expression to correct for atmospheric spatial effects. The Hybrid method was applied to Sentinel-2 data, particularly over bands acquired at 10 m resolution due to its similarities with the Ingenio/SEOsat mission. The Hybrid method was tested in an urban area with contrasting dark and bright surfaces. Results from the Hybrid method were validated against results provided by the Sen2Cor ESA’s atmospheric correction toolbox. Regarding the spatial domain, the Hybrid method corrects for adjacency effects by respectively reducing and increasing reflectance values in dark and bright pixels. When validating it with the Sen2Cor strategy, it was observed that: (a) a similar spatial pattern was obtained, (b) the correction reached by the Hybrid method was stronger, especially on narrow streets, (c) there is less dependency on the kernel size used to correct for adjacency effects. Regarding the spectral domain, when comparing reflectance spectra from both strategies, results show a Root Mean Square Error (RMSE) of 0.0048 and 0.1100 for the blue and NIR bands. These discrepancies were expected and due to the different atmospheric correction process followed. In case of the Sen2Cor, all the Sentinel-2 bands are used through the Dark Dense Vegetation method to characterize the atmospheric state and perform the correction. In the Hybrid strategy, auxiliary data from the Aeronet network was used to characterize the atmospheric state. In addition, the different processes implemented in Sen2Cor and in the Hybrid method to correct for adjacency effects also impact reflectance spectra, both in the blue and NIR bands (especially on water pixels). Given this analysis, the Hybrid strategy is proposed to atmospherically correct future Ingenio/SEOsat images.

Following, under the ESA's tandem FLEX/Sentinel-3 mission, an atmospheric correction based on the exploitation of the spectral information was proposed and evaluated. In CHAPTER 4, an atmospheric correction strategy based on characterizing the atmospheric state by means of using information provided by OLCI and SLSTR on board Sentinel-3 is presented. This strategy was based on a per-pixel inversion of a radiative transfer model, similarly to some earlier developed methods in the past for the ENVISAT mission, but with some novelties. These include: (1) the aerosol characterization by means of their optical properties, and (2) the use an external database to model surface reflectance as part of the aerosol characterization process. Regarding the optical properties used to describe the aerosol presence, these are: AOT, the Ångström coefficient (α), and the HG scattering asymmetry coefficient (g). By using this parametrization to describe the aerosol presence, choosing between multiple aerosol models or predefined aerosol mixtures is avoided (as is frequently done in atmospheric correction algorithms). Regarding the usage of an auxiliary surface reflectance database, this avoids assuming any approximated relationship between nadir and oblique surface reflectance observations. In addition, any approximation regarding modelling surface reflectance spectra as a combination of end-members (frequently done) is also avoided.

Based on simulated data considering 240 different atmospheric conditions, the proposed strategy was evaluated in view of: (a) the atmospheric characterization, (b) the estimated error in surface apparent reflectance, which must guarantee a proper SIF estimation within 10% of relative error (equivalent to $0.2 \text{ mW/m}^2/\text{sr/nm}$ in the $\text{O}_2\text{-B}$ and $0.1 \text{ mW/m}^2/\text{sr/nm}$ in the $\text{O}_2\text{-A}$).

Respecting the atmospheric characterization and its impact of surface apparent reflectance, it was observed that:

- Derived errors in surface apparent reflectance in the $\text{O}_2\text{-B}$ are greater than in the $\text{O}_2\text{-A}$ region.
- Derived errors for high AOT values result into the highest impact on surface apparent reflectance.
- In a few cases the relative errors in surface apparent reflectance were lower than 1% even when the derived errors in AOT exceeded ± 0.1 . This suggests that aerosol optical properties can be combined in a way that their radiometric effects are balanced.
- Among the selected aerosol parameters, the AOT and the asymmetry of the scattering function are the key parameters driving surface apparent reflectance. The Ångström coefficient seems not to play such an important role.
- Derived precision, quantified by the standard deviation of the 240 atmospheric conditions evaluated for each pixel (5 different surface types) did not accomplish the FLEX mission requirements. The precision of the estimated SIF was higher than the 10% of relative error required. However, when excluding those cases where the error in the asymmetry parameter of the aerosol scattering exceeds ± 0.05 (generally it involves high errors also in AOT estimation), precision and accuracy of the estimated SIF improved significantly.

Accordingly, two aspects deserve to be remarked: (1) the important role of the aerosol scattering effects to appropriately determine surface apparent reflectance and therefore, SIF estimations; and (2) the need to review and improve the proposed methodology to accomplish the FLEX mission requirements.

The FLEX mission requires rigorous specifications in terms of accuracy of the surface apparent reflectance estimations in the oxygen absorption regions. It is worth noting that a relative error of 10% on SIF generally implies a relative error of 1-2% in surface apparent reflectance. Given that, it was mandatory to review all the aspects assumed as part of the atmospheric characterization process, as well as the formulation used to perform the inversion. With this aim, CHAPTER 5 focused on the formulation assessment, concluding that:

- The use of the top-of-atmosphere radiance expression as a series expansion until second order to invert surface apparent reflectance accomplishes the FLEX mission requirements.
- Assuming that all the surface reflectance terms appearing in the top-of-atmosphere radiance expression are surface apparent reflectance accomplishes the FLEX mission requirements.
- The coupling between formulations used as part of the atmospheric correction process, and as part of the fluorescence estimation strategy must be consistent. However, an inconsistency typically occurs between these two processes due to a different definition of the surface apparent reflectance. Consequently, a strategy that estimates SIF while using a consistent formulation in both processes was proposed and successfully assessed.

CHAPTER 5 also focused on the possible exploitation of the high spectral resolution data provided by the FLORIS instrument, particularly in the oxygen absorption spectral region for a better aerosol characterization. Following this goal, the distinct spectral distortion pattern generated by errors in the estimation of each of the aerosol optical properties regardless the considered surface reflectance spectra was analysed. Given that the spectral distortion pattern generated by each aerosol optical property was different, this fact was used to improve aerosol estimations. A simulated database was built including more than 8×10^4 combinations of inaccurate atmospherically corrected spectra. By means of a multivariate linear regression algorithm (trained using 30 % of the database), the relative error in each aerosol optical property was predicted, i.e., the relative error in AOT, in Ångström exponent and in asymmetry parameter. To do so, input data used were erroneous estimated aerosol optical properties and its associated erroneous surface apparent reflectance estimation (at the O₂-A and O₂-B regions), together with the corresponding Normalized Difference Vegetation Index (NDVI). As a proof of concept, when the trained multivariate linear regression was applied to the remaining cases of the database (70%), a respectively relative error of 0.5%, 8% and 3 % for the AOT, the Ångström coefficient, and the asymmetry parameter was obtained for the percentile 75, both in the O₂-A and O₂-B regions. By using derived error statistics in the aerosol characterization, estimated surface apparent reflectance spectra accomplished the FLEX mission requirements. Consequently,

the proposed strategy exploits the high spectral resolution provided by FLORIS to improve the aerosol characterization and therefore SIF estimations. It must be noted that a more exhaustive analysis is required when aiming to use this method operationally as part of the retrieval process, especially regarding how errors in the instrumental performance characterization distorts surface apparent reflectance spectra at the oxygen regions. Since both instrumental and aerosol characterization errors impact the resulting surface apparent reflectance spectra, the exploitation of the high spectral resolution data should be able to disentangle both effects in order to guarantee a proper SIF estimation.

Finally, this Thesis focused on the FLEX mission validation strategy. To validate SIF as obtained from satellite observations it requires to be measured at a local scale. Generally, elevated platforms are required for monitoring extended canopy areas such as field crops or forests. In this framework, CHAPTER 6 reviewed the need to correct for atmospheric effects when the target and the sensor are separated by a few meters only. For most remote sensing applications, atmospheric disturbances produced at this scale are typically ignored. However, if the final objective is to measure SIF through the exploitation of the oxygen absorption bands, atmospheric effects – and particularly oxygen absorption – must be corrected even at proximal sensing scale. In this Chapter, it was evaluated how ignoring oxygen absorption correction impacts SIF estimations: (a) independently from the technique used, (b) using a Fraunhofer Line Discriminator (FLD) family retrieval technique, and (c) using a spectral fitting method (SFM). It was observed that, even when the sample and the sensor are only separated around 3 m, at least for the O₂–A region oxygen absorption must be corrected. Absorption at the O₂–B region is weaker and its correction can be ignored at least for the first few meters. To further explore the best and most convenient strategy to compensate for atmospheric effects, the possibility to correct the FLD and SFM by simply introducing an oxygen transmittance correction factor already convolved according to the Instrumental Spectral Response Function (ISRF) was assessed. Although this simplistic strategy slightly improved estimated SIF, especially at the deepest regions of the oxygen bands, it turns out to be insufficient to achieve accurate SIF estimations. Main reason why these simplistic correction strategies are insufficient is related to the used of an already convolved oxygen transmittance function. In line with CHAPTER 5, it is especially critical to multiply or divide high spectral resolution functions when they are already convolved to the ISRF, especially at the absorption regions. Therefore, an alternative strategy able to simultaneously correct for: (1) oxygen absorption effects, and (2) the instrument ISRF, was proposed. The strategy was based on the SFM, but using in each iteration the solar irradiance and the oxygen transmittance atmospheric functions at very high spectral resolution. This way all required products are first produced at high spectral resolution and then convolved according to the ISRF. The study reported that for high spectral resolution sensors, i.e., considering 0.4 nm of spectral sampling interval and a bandwidth of 1 nm, SIF estimations achieve the FLEX mission requirements even for target–sensor distances of 20 m. In fact, similar SIF estimations were derived for target–sensor distances between 3 and 20 m. This observation suggests that the proposed strategy effectively corrects the optical path between the target and the sensor. Although oxygen absorption correction is sufficient for a few meters target–sensor distance, it must be noted that the proposed strategy may be insufficient for other kind of applications such as the use of

Unmanned Aerial Vehicles (UAVs), which can easily reach a height of hundreds of meters. In that case, the proposed technique can still be applicable, but compensation may be required for both oxygen and aerosol transmittance.

This work identified difficulties associated to atmospheric correction when applying to high spatial and especially to very high spectral resolution data. To resolve these, under this Thesis an adequate formulation has been developed, and successful methodologies have been designed for the particular cases of SEOSat (high spatial resolution) and FLEX (high spectral resolution); two future remote sensing space missions that will be launched in the forthcoming years.

8

Relevance



Contents

8.1	Achievements and relevance	177
8.2	Acknowledgments	184
8.3	Research collaboration in other centres	184
8.4	Future and on-going research projects	185

8.1 Achievements and relevance


The results generated during this thesis have been presented on several conferences and published as research papers on different international journals. The following list summarizes the published journal and conference papers directly related to this Thesis:


INTERNATIONAL JOURNAL PAPERS:

- **March 2018 | Compensation of Oxygen Transmittance Effects for Proximal Sensing Retrieval of Canopy-Leaving Sun-Induced Chlorophyll Fluorescence** . Remote Sensing. *Neus Sabater, Jorge Vicent, Luis Alonso, Jochem Verrelst, Elizabeth M. Middleton, Albert Porcar-Castell and José Moreno*  [Submitted]
- **January 2018 | Emulation as an accurate alternative of interpolation to sample RTM look-up table parameter space**. ISPRS Journal of Photogrammetry and Remote Sensing. *Jorge Vicent, Jochem Verrelst, Juan Pablo Rivera, Neus Sabater, Jordi Muñoz-Marí, Gustau Camps-Valls, and José Moreno*  [Submitted]


- **December 2017 | Design of a generic 3D Scene Generator for passive optical missions and its implementation for ESA's FLEX/Sentinel-3 tandem mission** IEEE Transactions on geoscience and remote sensing. *Carolina Tenjo, Juan Pablo Rivera, Neus Sabater, Jorge Vicent, Luis Alonso, Jochem Verrelst and José Moreno* 
- **June 2017 | Impact of Atmospheric Inversion Effects on Solar-Induced Chlorophyll Fluorescence: Exploitation of the Apparent Reflectance as a Quality Indicator.** Remote Sensing. *Neus Sabater, Jorge Vicent, Luis Alonso, Sergio Cogliati, Jochem Verrelst and José Moreno* 
- **June 2017 | Assessment of Approximations in Aerosol Optical Properties and Vertical Distribution into FLEX Atmospherically-Corrected Surface Reflectance and Retrieved Sun-Induced Fluorescence.** Remote Sensing. *Jorge Vicent, Neus Sabater, Jochem Verrelst, Luis Alonso and José Moreno* 
- **June 2016 | Emulation of Leaf, Canopy and Atmosphere Radiative Transfer Models for Fast and Accurate Global Sensitivity Analysis.** Remote Sensing. *Jochem Verrelst, Neus Sabater, Juan Pablo Rivera, Jordi Muñoz-Marí, Jorge Vicent, Gustau Camps-Valls, and José Moreno* 
- **November 2015 | FLEX End-to-End Mission Performance Simulator.** IEEE Transactions on geoscience and remote sensing. *Jorge Vicent, Neus Sabater, Carolina Tenjo, Juan Ramon Azcarreta, Juan Pablo Rivera, Pedro Jurado, Raffaella Franco, Luis Alonso, Jochem Verrelst and José Moreno* 
- **July 2015 | Evaluating the predictive power of sun-induced chlorophyll fluorescence to estimate net photosynthesis of vegetation canopies: a SCOPE modelling study.** Remote Sensing of Environment. *Jochem Verrelst, Christian Van der Tol, Federico Magnani, Neus Sabater, Juan Pablo Rivera and José Moreno* 
- **March 2015 | Retrieval of sun-induced fluorescence by advanced spectral fitting methods.** Remote Sensing of Environment. *Sergio Cogliati, Wouter Verhoef, Stefan Kraft, Neus Sabater, Luis Alonso, Jorge Vicent, Jose Moreno, Matthias Drusch and Roberto Colombo* 


NATIONAL JOURNAL PAPERS:


- **2016 | Development of advanced products for the SEOSAT/Ingenio mission.** Revista Española de Teledetección. *Neus Sabater, Antonio Ruiz-Verdú, Jesús Delegido, Rubén Fernández-Beltrán, Pedro Latorre-Carmona, Filiberto Pla, María González Audicana, Jesús Álvarez-Mozos, Ignacio Sola, Guillermo Villa, Juan Antonio Tejeiro, Eduardo de Miguel, Mario Jimenez, Sergio Molina and José Moreno* 
- **2014 | MISIÓN FLEX (FLuorescence EXplorer: Observación de la fluorescencia por teledetección como nueva técnica de estudio del estado de la vegetación terrestre**


a escala global.) Revista Española de Teledetección. *José Moreno, Luis Alonso, Jesús Delegido, Juan Pablo Rivera, Antonio Ruiz-Verdú, Neus Sabater, Carolina Tenjo, Jochem Verrelst and Jorge Vicent* 


INTERNATIONAL CONFERENCE CONTRIBUTION:

- **July 2017 | Oxygen transmittance correction for Solar-Induced Chlorophyll Fluorescence measured on proximal sensing: Application to the NASA-Goddard FUSION tower** International Geoscience and Remote Sensing Symposium (IGARSS). Texas (USA). *Neus Sabater, Elizabeth M. Middleton, Zbynek Malenovsky, Luis Alonso, Jochem Verrelst, Karl F. Huemmrich, Petya K. Entcheva-Campbell, W.P. Kustas, Jorge Vicent, Shari Van Wittenberghe and José Moreno*  [Oral]

- **April 2017 | Multi-angular and diurnal modelling of solar-induced chlorophyll fluorescence in structurally explicit three-dimensional plant canopies using DART** 10th EARSeL SIG Imaging Spectroscopy Workshop. Zurich (Switzerland). *Zbynek Malenovsky ; Jean-Philippe Gastellu-Etchegorry; Nicolas Lauret ; Tiangang Yin; Jordan Guilleux, ; Eric Chavanon; Verhoef Wout; Christiaan van der Tol; Neus Sabater; Elizabeth M. Middleton; Petya K. Entcheva-Campbell; Karl F. Huemmrich; Bruce D. Cook; Douglas C. Morton*  [Oral]

- **April 2017 | Emulation of Radiative Transfer Models: New Opportunities for Spectroscopy Data Processing.** 10th EARSeL SIG Imaging Spectroscopy Workshop. Zurich (Switzerland). *Verrelst, Jochem; Neus Sabater; Juan Pablo Rivera; Jordi Muñoz-Marí; Jorge Vicent; Gustau Camps-Valls; Jose Moreno*  [Oral]

- **January 2017 | Atmospheric Effects on Fluorescence Retrieval at Different Scales: Proximal Sensing, Airborne and Satellite** Remote sensing of fluorescence. photosynthesis and vegetation status. Rome (Italy). *Neus Sabater; Jorge Vicent; Sergio Cogliati; Luis Alonso; Jochem Verrelst and Jose Moreno*  [Oral]

- **January 2017 | Impact of Aerosol Optical Properties and Aerosol Vertical Distribution into FLEX Top-of-Atmosphere Radiances and their Compensation with Parametric Approximations.** Remote sensing of fluorescence. photosynthesis and vegetation status. Rome (Italy). *Jorge Vicent, Neus Sabater, Luis Alonso, Jochem Verrelst and Jose Moreno*  [Oral]

- **January 2017 | Impact of Instrument Characterization in the Retrieval of SIF: Hy-Plant Case Study** Remote sensing of fluorescence. photosynthesis and vegetation status.

Rome (Italy). *Luis Alonso, Jorge Vicent, Neus Sabater, Sergio Cogliati, Francisco Pinto, Patrick Rademske, Uwe Rascher, Stefan Kraft and Jose Moreno* 🌐 [Oral]

- **January 2017 | Updates on Fluorescence Retrieval Algorithm Based on Spectral Fitting Approach and Results on High-Resolution Radiance Observations** Remote sensing of fluorescence. photosynthesis and vegetation status. Rome (Italy). *Sergio Cogliati, Wouter Verhoef, Neus Sabater, Luis Alonso, Jose Moreno, Uwe Rascher, Elizabeth M. Middleton, Gina Mohammed, Matthias Drusch, et al.* 🌐 [Oral]

- **January 2017 | Bidirectional Transfer of Leaf Fluorescence: Influence of Species and Leaf Stacking.** Remote sensing of fluorescence. photosynthesis and vegetation status. Rome (Italy). *Shari Van Wittenberghe, Luis Alonso, Jochem Verrelst, Neus Sabater, Jolien Verhelst and Jose Moreno* 🌐 [Poster]

- **January 2017 | Oxygen Transmittance Correction for Canopy Solar-Induced Chlorophyll Fluorescence Measured on Proximal Sensing** Remote sensing of fluorescence. photosynthesis and vegetation status. Rome (Italy). *Neus Sabater, Elizabeth Middleton, Luis Alonso, Zbynek Malenovsky, Fred Huemmrich, Jochem Verrelst, Shari Van Wittenberghe, Petya Campbell and José Moreno.* 🌐 [Poster]

- **June 2016 | The FLuorescence EXplorer (FLEX) Space mission.** 6th Annual HypsIRI Data Product Symposium and Aquatic Forum. NASA Goddard Space Flight Center. Greenbelt (USA). *Neus Sabater, José Moreno and Elizabeth M. Middleton on behalf of the FLEX team.* 🌐 [Oral]

- **May 2016 | FLEX End-to-End Mission Performance Simulator** ESA's Living Planet Symposium. Prague (Czech Republic). *Jorge Vicent, Neus Sabater, Carolina Tenjo, Juan Ramón Acarreta, María Manzano, Juan Pablo Rivera, Pedro Jurado, Raffaella Franco, Luis Alonso, and José Moreno)* 🌐 [Poster]

- **May 2016 | Capabilities of the future Earth Explorer 8 FLEX mission for the retrieval of fluorescence and biophysical products in marine and inland waters** ESA's Living Planet Symposium. Prague (Czech Republic). *Antonio Ruiz-Verdu, Carolina Tenjo Gil, Jesús Delegido, Luis Alonso, Neus Sabater, Jochem Verrelst, Jorge Vicent, Juan Pablo Rivera, Ramón Peña, Juan Soria, Eduardo Vicente and José Moreno* 🌐 [Poster]

- **May 2016 | The Earth Explorer 8 FLEX mission for the retrieval of the full fluorescence signal to estimate photosynthetic activity of terrestrial vegetation** ESA's

Living Planet Symposium. Prague (Czech Republic). *Jochem Verrelst, Christiaan van der Tol, Federico Magnani, Neus Sabater, Juan Pablo Rivera, Gina Mohammed and José Moreno* 🌐 [Poster]

- **May 2016 | Spectrum Fitting – a potential fluorescence retrieval for the FLEX mission** ESA's Living Planet Symposium. Prague (Czech Republic). *Sergio Cogliati, Wouter Verhoef, Stefan Kraft, Neus Sabater, Luis Alonso, José Moreno, Uwe Rascher, Matthias Drusch and Roberto Colombo* 🌐 [Oral]
- **May 2016 | A novel dual–field–of–view hyperspectral field spectrometer and a dual–field–of–view hyperspectral sunphotometer for simultaneously measuring of direct and diffuse solar irradiance, both systems covering the 400 nm to 2.500 nm region and the O₂–A and O₂–B absorption regions at very high resolutions** ESA's Living Planet Symposium. Prague (Czech Republic). *Alasdair Mac Arthur, Iain Robinson, Luis Alonso, Neus Sabater and José Moreno* 🌐 [Poster]
- **August 2015 | Propagation of spectral characterization errors of imaging spectrometers at Level–1 and its correction within a Level–2 recalibration scheme.** SPIE Optics and Photonics (SPIE). San Diego (USA). *Jorge Vicent, Luis Alonso, Neus Sabater, Christophe Miesch, Stefan Kraft and José Moreno* 🌐 [Oral]
- **August 2015 | Design of a satellite end–to–end mission performance simulator for imaging spectrometers and its application to ESA's FLEX/Sentinel–3 tandem mission.** SPIE Optics and Photonics (SPIE). San Diego (USA). *Jorge Vicent, Neus Sabater, Carolina Tenjo, Juan Ramón, Maria Manzano, Juan Pablo Rivera, Pedro Jurado, Rafaela Franco, Luis Alonso and José Moreno.* 🌐 [Oral]
- **July 2015 | HICO L1 and L2 data processing: radiometric recalibration, atmospheric correction and retrieval of water quality parameters.** International Geoscience and Remote Sensing Symposium (IGARSS). Milan (Italy). *Jorge Vicent, Neus Sabater, Carolina Tenjo, Antonio Ruiz-Verdu, Jesus Delegido, Ramon Peña and José Moreno* 🌐 [Oral]
- **July 2015 | A sun–induced vegetation fluorescence retrieval method from top of atmosphere radiance for the FLEX/Sentinel–3 tandem mission.** International Geoscience and Remote Sensing Symposium (IGARSS). Milan (Italy). *Neus Sabater, Luis Alonso, Sergio Cogliati, Jorge Vicent, Carolina Tenjo, Jochem Verrelst and José Moreno* 🌐 [Oral]

- **June 2015 | Synergies between Sentinel–3 and FLEX for Fluorescence and Water Quality Retrieval in Inland and Coastal Waters** ESA's Sentinel–3 workshop. Lido, Venice (Italy). *Antonio Ruiz-Verdú, Carolina Tenjo, Jesús Delegido, Luis Alonso, Neus Sabater, Jochem Verrelst, Jorge Vicent, Juan Pablo Rivera, Ramón Peña and José Moreno* 🌐 [Poster]

- **June 2015 | Design of FLEX/Sentinel–3 Mission Simulator and its Reusability to Future Convoy and Tandem Mission Concepts** ESA's Sentinel–3 workshop. Lido, Venice (Italy). *Carolina Tenjo, Jorge Vicent, Neus Sabater, Juan Pablo Rivera, Luis Alonso, Jochem Verrelst and José Moreno* 🌐 [Poster]

- **April 2015 | Hyperspectral synthetic scene simulator for the assessment of fluorescence retrieval with ESAs FLEX/Sentinel–3 tandem mission (EARSeL).** Luxembourg (Luxembourg). *Carolina Tenjo, Jorge Vicent, Neus Sabater, Juan Pablo Rivera, Luis Alonso, Jochem Verrelst and José Moreno* 🌐 [Oral]

- **June 2014 | A fluorescence retrieval method for the FLEX/Sentinel–3 tandem mission** Workshop on Hyperspectral Image and Signal Processing (WHISPERS). Lausanne (Switzerland). *Neus Sabater, Sergio Cogliati, Luis Alonso, Jorge Vicent and José Moreno* 🌐 [Oral]

- **June 2014 | Synthetic scene simulator for hyperspectral spaceborne passive optical sensors. Application to ESA's FLEX/Sentinel–3 tandem mission** Workshop on Hyperspectral Image and Signal Processing (WHISPERS). Lausanne (Switzerland). *Juan Pablo Rivera, Neus Sabater, Carolina Tenjo, Jorge Vicent, Luis Alonso and José Moreno* 🌐 [Oral]

- **June 2014 | HICO Level–2 data processing toolbox for the atmospheric correction and the retrieval of water quality parameters** Workshop on Hyperspectral Image and Signal Processing (WHISPERS). Lausanne (Switzerland). *Jorge Vicent, Neus Sabater, Carolina Tenjo, Antonio Ruiz-Verdú, Jesus Delegido, Ramon Peña and José Moreno* 🌐 [Oral]

- **April 2014 | Retrieval of sun induced fluorescence using advanced spectral fitting methods from Radiative Transfer simulations and HyPlant imagery** 5th ESA Fluorescence workshop. Paris (France). *S. Cogliati, M. Rossini, T. Julietta, C. Panigada, A. Schickling, F. Pinto, L. Alonso, J. Vicent, N. Sabater and R. Colombo* 🌐 [Oral]

- **April 2014 | An atmospheric correction algorithm for FLEX/Sentinel-3 tandem mission** 5th ESA Fluorescence workshop. Paris (France). *Neus Sabater, Jorge Vicent, Luis Alonso, Jochem Verrelst and José Moreno* 🌐 [Oral]

- **April 2014 | ESA's FLEX End-to-End Mission Performance Simulator. Architecture design, current status and preliminary results** 5th ESA Fluorescence workshop. Paris (France). *Jorge Vicent, Juan Ramon Acarreta, Luis Alonso, Raffaella Franco, Maria Manzano, Juan Pablo Rivera, Neus Sabater, Carolina Tenjo, Jochem Verrelst and José Moreno* 🌐 [Oral]

- **April 2014 | The scientific modules of FLEX End-To-End simulator: The scene generator and the level-2 retrieval modules** 5th ESA Fluorescence workshop. Paris (France). *Neus Sabater, Juan Pablo Rivera, Carolina Tenjo, Jorge Vicent, Luis Alonso, Jochem Verrelst and José Moreno* 🌐 [Oral]

- **September 2013 | FLEX End-To-End mission performance simulator architecture design using a generic reference architecture for EO missions.** ESA-Living Planet Symposium. Edinburgh (United Kingdom). *Jorge Vicent, Umberto del Bello, Mathias Drusch, Raffaella Franco, Stefan Kraft, Juan Ramón Acarreta, Luis Alonso, María Manzano, José Moreno, Juan Pablo Rivera, Neus Sabater, Carolina Tenjo and Jochem Verrelst.* 🌐 [Oral]

International and national projects related to this Thesis:

Additionally, the outcomes of this work are relevant for the research carried out by the author and her colleagues at the University of València in the context of different research projects in which they are involved. A list of the related projects in which the author of this Thesis has participated is provided:

- FLEX – Performance Analysis and Requirements Consolidation Study (PARCS), ESA–ESTEC Contract No. 4000105078/11/NL/AF [2012-2014].
- Technical Assistance for the Deployment of an Advanced Hyperspectral Imaging Sensor during HYFLEX, ESA–ESTEC Contract No. 400107143/12/NL/FF/If –CNN1–[2102-2014]
- FLEX End-To-End Mission Performance Simulator, ESA–ESTEC Contract No. 4000108364/13/NL/BJ [2013-2015].
- FLEX Bridge Study Project, ESA–ESTEC Contract No. RFP IPL-PEO/FF/If/14.687 [2014-2015]

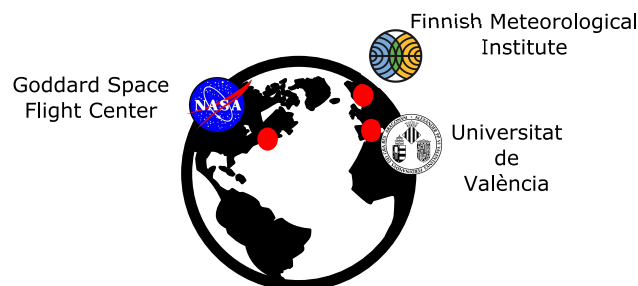
- Generación de productos de nivel 2 para la misión Ingenio/SEOsat
Contract No. ESP2013-48458-C4-1-P [2014-2016]
- AVANFLEX: productos avanzados para la misión FLEX. Spanish Ministry of Economy and Competitiveness through the National Program for the Promotion of Scientific and Technical Research of Excellence. Contract No. ESP2016-79503-C2-1-P [**On-going**]
- HyPlant Processing Experiment (HYPER)
Contract No. IPL-PSO/FF/vb/14.267 [**On-going**]
- FLEX L1B to L2 Algorithm Development Study, ESA–ESTEC
Contract No. AO/1-8897/17/NL/MP [**On-going**]
- FLEX L2 End–To–End Simulator Development and Mission Performance Assessment, ESA–ESTEC Contract No.3-14610/16/NL/MP [**On-going**]

8.2 Acknowledgments

- This work was supported by the Spanish Ministry of Economy and Competitiveness pre-doctoral grant BES-C-2014-0087

8.3 Research collaboration in other centres

This thesis was carried out with the collaboration of international researchers. During the PhD period, the author had the chance to collaborate in two research centres:



- Three months in the NASA Goddard Space Flight Center (Science and Exploration Directory code – 600) headed by Dr. Elizabeth M. Middleton. Activities carried out during the stay in NASA were related to the analysis and processing of measurements acquired by the FUSION tower system, which daily monitors a corn field during its growing season in 2014. Thanks to this research collaboration three main out–comes have been developed:

- CHAPTER 6 from this Thesis is based on a peer-review scientific publication developed as part of the work performed in NASA [**submitted**]
- A new MODTRAN Interrogation Technique developed especially for proximal remote sensing applications. [**In preparation**]
- A local scale study linking diurnal SIF measurements with energy fluxes acquired by the FUSION system and an Eddy-Covariance tower respectively. [**In preparation**]
- Four months in the Aerosol and Remote Sensing group of the Finnish Meteorological Institute headed by Prof. Gerrit de Leeuw. Activities carried out during the stay were related to use the statistics derived to the validation of the aerosol retrieval strategy applied to the AATSR against the global AERONET network. Long temporal series statistics were used as a basis to continue developing the proposed atmospheric aerosol characterization process proposed in CHAPTER 5. This work is still on-going.
 - Apparent reflectance as a quality indicator – Disentangling instrumental from atmospheric errors – [**In preparation**]

8.4 Future and on-going research projects

Next paragraphs describe the on-going and future research works that are a direct consequence of the research and methodology developed in this Thesis.

Linking diurnal cycles of Solar-Induced chlorophyll Fluorescence to water, heat and CO₂ fluxes for a corn field during the growing season.

In the last decade, with the out-coming existing maps at a global scale of Solar-induced chlorophyll Fluorescence (SIF); the possibility to use SIF as a proxy to quantify the photosynthetic activity at a global scale is becoming a priority for the scientific community. In this respect, linking diurnal cycles of SIF to water, heat and CO₂ fluxes at a local scale could help to better understand, model and interpret the role of SIF and a proxy to quantify Gross Primary Productivity (GPP) and the up-taken of CO₂ at a global scale. In this work, using the strategy developed at Chapter 6, data from the NASA FUSION tower has been processed to monitor daily SIF and energy fluxes for a corn field during its growing season.

Apparent reflectance as a quality indicator – Disentangling instrumental from aerosol characterization errors –

Within the FLEX/Sentinel-3 tandem mission concept, the OLCI and SLSTR instruments on board Sentinel-3 will be especially used to derive the atmospheric parameters needed to characterize the atmospheric state to correct FLORIS data. In Chapter 4 the importance of an accurate atmospheric characterization was highlighted while in Chapter 5 the exploitation of the apparent reflectance as a quality indicator of the atmospheric correction process was used for the first time. In this work, expected atmospheric correction accuracy for the FLEX/Sentinel-3 mission will be analysed by using statistics derived from the validation of the aerosol optical properties retrieval obtained for a long temporal series (~ 10 years) of AATSR instrument against the global aerosol network AERONET for two different stations situated in the Amazon and the North Italian mountainous region. Then using the exploitation of the apparent reflectance spectral distortion in the oxygen features this work will assess: (1) the improvement achieved in the aerosol optical properties characterization, and (2) in resolving and disentangling spectral distortions caused by an inaccurate aerosol optical properties estimation or by an inaccurate instrument characterization.

9

Summary in Spanish

Contents

9.1	Introducción	187
9.2	Motivación y objetivos	189
9.3	Metodología y estructura	190
9.4	Resultados	191
9.5	Conclusiones	195

9.1 Introducción

Desde hace años el ser humano sabe que el mejor lugar para la observación y el estudio de nuestro planeta Tierra no se encuentra aquí abajo, sino un poco más arriba, en el espacio [[European Space Agency, 2017a](#)]. Esta motivación ha empujado a miles de científicos a trabajar en el campo de la observación de la Tierra desde satélite, pudiendo así contemplar por primera vez fenómenos a escala global tales como la circulación general de la atmósfera, la oscilación de *el Niño* y *la Niña* o incluso el temido *agujero* de la capa de ozono.

Es gracias a la atmósfera que existen condiciones habitables para el ser humano en el planeta Tierra, no sólo por la presencia de oxígeno permitiendo la respiración; sino por toda esa mezcla de gases como el ozono que absorbiendo parte de la irradiancia solar en el espectro ultra-violeta (UV) permite el desarrollo de la vida. Sin embargo, no siempre en la observación de la Tierra la atmósfera es el foco de estudio. Muchas veces la observación de la Tierra desde satélite se centra en estudiar la cubierta terrestre; analizando la composición de masas de agua, cambios en

la superficie terrestre o incluso observando la dinámica de la vegetación. En todos estos casos y especialmente cuando se trabaja con sensores pasivos (cuya fuente de energía es el sol), la atmósfera deja de ser el foco de estudio para convertirse en ese medio que interfiere en nuestro objetivo, perturbando la señal que llega al satélite.

A lo largo de los últimos 30 años se han desarrollado a este respecto diversos **algoritmos de corrección atmosférica**. Dichos algoritmos tienen como fin último corregir la señal de radiancia recibida por el satélite y producir la señal de radiancia o reflectividad en la superficie terrestre, corrigiendo así las interferencias (principalmente absorciones por gases y dispersión por aerosoles) causadas en el paso de la luz a través de la atmósfera en su recorrido desde la superficie hasta el sensor. Las estrategias de corrección atmosférica varían desde métodos sencillos, desarrollados a finales de los años 80 [Chavez, 1988], hasta métodos basados en la inversión de modelos físicos que resuelven la ecuación de transferencia radiativa de la atmósfera [Verote *et al.*, 1997a]. La evolución de estas estrategias ha ido de la mano con la evolución de los sensores a lo largo de los últimos años. Por ejemplo, los primeros sensores a bordo de satélites dedicados a la observación de la Tierra presentaban un número muy limitado de bandas situadas generalmente en las ventanas atmosféricas; es decir, en aquellas regiones espectrales donde no hay absorciones y el efecto de la perturbación atmosférica se puede ignorar a primer orden. Por el contrario, a medida que la tecnología ha ido avanzando y los sensores han ido aumentando su resolución espectral, radiométrica y espacial; esto ha dado pie a diseñar sensores con bandas colocadas de forma estratégica para una mejor caracterización de la atmósfera, como por ejemplo, bandas colocadas en las absorciones del vapor de agua, bandas en el azul que sean más sensibles a la presencia de aerosoles, bandas en el oxígeno sensibles a la presión, etc.

Ligado al avance tecnológico de los sensores ópticos nace en parte la motivación de esta Tesis. Si bien es verdad que cada vez los sensores cuentan con una mejor resolución en el dominio espacial, radiométrico y espectral; también es cierto que estas características no se dan de forma simultánea. En otras palabras, cuando un sensor tiene una muy alta resolución espacial (del orden de cm y/o m), suele contar con una baja o media resolución espectral (5-12 bandas). Este es el caso de sensores a bordo de satélites como RapidEye, WorldView 1-4, QuickBird, IKONOS o incluso SEOSAT. De la misma forma, sensores hiperespectrales, como el caso de FLORIS a bordo de FLEX, cuentan con un gran número de bandas (~500), pero una resolución espacial media (300 m). Así pues, en el campo del desarrollo de algoritmos de corrección atmosférica nos movemos hacia extremos, muy alta resolución espacial o espectral, que impulsan la necesidad de revisar y desarrollar nuevas técnicas de corrección atmosférica. Desde este punto de vista, resulta obvio que en aquellos sensores donde la resolución espacial es dominante sobre la espectral; sea pues estratégico el intentar explotar los efectos de la atmósfera en el dominio espacial. Por contra, en sensores hiperespectrales es necesario hacer un estudio para determinar si esa mayor resolución espectral puede aportar mejoras a los métodos actuales de corrección atmosférica.

9.2 Motivación y objetivos

El uso cada vez más frecuente de sensores con una mayor resolución espacial o espectral a bordo de una nueva generación de satélites de observación de la Tierra, abre nuevas oportunidades en el uso de datos y su explotación dentro del mundo de la teledetección. Sin embargo, la explotación de los datos adquiridos por este tipo de sensores implica, sin lugar a dudas, la necesidad de desarrollar nuevos algoritmos capaces de lidiar con este tipo de sistemas. En el caso de los algoritmos de corrección atmosférica, éstos deben ser adaptados o re-formulados, prestando especial atención a cómo los efectos atmosféricos distorsionan la señal tanto en el dominio espacial como en el espectral.

Siguiendo esta motivación, el objetivo de la Tesis se divide en tres pilares fundamentales: (1) analizar los efectos atmosféricos en sensores con una alta resolución espacial y baja resolución espectral, utilizando para ello el contexto de la misión Ingenio/SEOSat; (2) definir una nueva estrategia de corrección atmosférica orientada a la explotación de datos de alta resolución espectral, utilizando para ello el contexto de la misión tándem FLEX/Sentinel-3; y por último (3) analizar los efectos atmosféricos en sensores de alta resolución espacial y espectral montados en torres en el contexto de validación de la misión FLEX.

La Tesis en resumen

¿Cómo se aborda la temática de esta Tesis?

La temática de esta Tesis se aborda principalmente desde un marco teórico. La Tesis empieza con una introducción que resume desde los fundamentos físicos esenciales que describen la interacción de la luz solar en la atmósfera, hasta las principales técnicas o algoritmos de corrección atmosférica. Seguidamente, se presentan las estrategias de corrección atmosférica desarrolladas en el marco de esta Tesis y orientadas: (a) a la corrección de imágenes de alta resolución espacial (en el contexto de la misión Ingenio/SEOSat), y (b) a la corrección de imágenes adquiridas en alta resolución espectral (en el contexto de la misión FLEX). Dichas estrategias son presentadas y evaluadas utilizando para ello datos simulados en las fases de preparación de sendas misiones.

¿Cuáles son los principales objetivos?

Por una parte, analizar y diseñar nuevas estrategias de corrección atmosférica para su aplicación en (1) la misión espacial Ingenio/SEOSat, explotando los datos de alta resolución espacial; y (2) la misión tándem FLEX/Sentinel-3, explotando los datos de alta resolución espectral. Por otro lado, analizar los efectos atmosféricos en sensores de alta resolución espectral a escala local en el contexto de la misión FLEX.

¿Por qué esta temática resulta de interés?

Debido al desarrollo tecnológico de los últimos años, los sensores a bordo de satélites para la observación de la Tierra proporcionan cada vez mayor cantidad de información en el dominio espacial y espectral. En este sentido, los algoritmos de corrección atmosférica aplicados a estos sensores deben ser revisados y/o re-formulados para una óptima explotación de sus datos.

9.3 Metodología y estructura

Esta Tesis está desarrollada en un marco puramente teórico. Dos motivos justifican esta decisión:

1. Al trabajar en el desarrollo de algoritmos y estrategias para el procesado de los datos, el uso de datos simulados es idóneo porque permite controlar el proceso en todo momento, siendo más fácil evaluar las causas de error así como identificar los posibles puntos de mejora.
2. La alternativa de utilizar datos reales adquiridos por otros sensores con características similares no resulta adecuada; pues pequeñas diferencias en las especificaciones de los instrumentos pueden afectar la ejecución del algoritmo.

Esta Tesis se compone de nueve capítulos, empezando por una introducción que explica la motivación y los objetivos científicos marcados, así como un resumen de los conceptos fundamentales de física de la atmósfera. Seguidamente se presentan cuatro bloques temáticos que abordan independientemente cada uno de los desarrollos realizados para datos de alta resolución espacial y espectral tanto a escala global como local. Finalmente se suceden una serie de capítulos en los que se presentan y discuten los resultados y se subraya la relevancia de esta Tesis en un contexto científico más amplio. La estructura de la Tesis se organiza como sigue:

- **CAPÍTULO 2:** Presenta un resumen de los conceptos fundamentales de la física de la atmósfera; desde sus mayores constituyentes hasta sus efectos desde el punto de vista radiativo. Asimismo, en este capítulo se introduce la formulación utilizada en esta Tesis y se presenta el concepto de corrección atmosférica haciendo una breve revisión del estado del arte de los algoritmos más conocidos. Se concluye con unas consideraciones relativas a cómo enfocar el problema para los escenarios planteados en esta Tesis.
- **CAPÍTULO 3:** Se centra en analizar, dadas las características de la misión Ingenio/SEO-sat, los posibles efectos atmosféricos en el dominio espacio/espectral. En este capítulo se plantea una nueva metodología basada en la explotación de los datos de alta resolución espacial para inferir información sobre la caracterización de la atmósfera. Finalmente, se

presenta una nueva estrategia de corrección atmosférica diseñada para la corrección de los futuros datos adquiridos por la misión SEOSat y validada con imágenes del satélite Sentinel-2.

- **CAPÍTULO 4:** Propone un método de corrección atmosférica diseñado para la misión tándem FLEX/Sentinel-3, basado en la explotación de los datos de Sentinel-3 para la caracterización de la atmósfera. Esta estrategia se evalúa teniendo en cuenta los objetivos científicos de la misión FLEX, por medio de los requisitos impuestos para la medida de la fluorescencia de la vegetación. Este capítulo analiza los escenarios en los que el método cumple y no cumple con los requisitos de misión. Se esbozan las primeras líneas de investigación hacia la explotación del uso de los datos de alta resolución espectral dados por FLEX para una mejora de la caracterización de la atmósfera (temática abordada en el siguiente capítulo).
- **CAPÍTULO 5:** Analiza toda las aproximaciones consideradas como parte de la estrategia de inversión de los datos tomados por FLEX; haciendo hincapié en el acoplamiento de los diferentes métodos desarrollados, tanto para la corrección atmosférica como para la obtención de fluorescencia a nivel de superficie. Una vez evaluada la formulación, siguiendo las ideas esbozadas en el CAPÍTULO 4, estudia la posibilidad de utilizar los datos de alta resolución espectral tomados por FLEX para la mejora de la caracterización de las propiedades ópticas de los aerosoles.
- **CAPÍTULO 6:** Evalúa los efectos atmosféricos en datos de alta resolución espectral tomados desde torres de medida en el marco de la misión FLEX para la obtención de la señal de fluorescencia. Se centra en el estudio de las bandas de absorción del oxígeno y las posibles estrategias de corrección de las mismas. Asimismo, también evalúa los posibles efectos derivados de ignorar los cambios de presión y temperatura ambientales y cómo este hecho podría llevar a sobrestimar y/o subestimar la señal de fluorescencia en largas series temporales.
- **CAPÍTULO 7:** Presenta los principales resultados alcanzados en esta Tesis y los discute en un contexto más amplio.
- **CAPÍTULO 8:** Señala los objetivos alcanzados en esta Tesis. Se presentan todas las publicaciones internacionales y nacionales relacionadas con las actividades llevadas a cabo bajo el marco de esta Tesis, así como las colaboraciones internacionales y estancias de investigación en centros extranjeros.

9.4 Resultados

Al inicio de esta Tesis (Sección 1.3), se plantearon las cuestiones científicas a responder durante el transcurso y desarrollo de este trabajo. En las siguientes líneas dichas cuestiones se vuelven a plantear, esta vez dando una respuesta gracias a los resultados alcanzados:

- ***¿Cuáles son las particularidades a considerar en el desarrollo de una estrategia de corrección atmosférica dirigida a sensores a bordo de satélites con alta resolución espacial?*** Los efectos atmosféricos en el dominio espacial suelen generar un efecto de difuminado en las imágenes debido a la presencia de aerosoles y moléculas que dispersan la luz. Generalmente, los sensores con alta resolución espacial se ven altamente afectados por los efectos de adyacencia entre píxeles vecinos (provocados por la dispersión de la luz). En el caso particular de la misión Ingenio/SEOsat el impacto de los efectos atmosféricos dadas las características espacio/espectrales del sensor fue analizado en el CAPÍTULO 3. Por una parte, en el dominio espectral, aun no teniendo ninguna de sus bandas localizadas en una región de absorción, los efectos atmosféricos son notables. En el caso de las bandas situadas en el RGB, éstas están básicamente afectadas por la presencia de aerosoles, en particular la banda del azul. En el caso de la banda situada en el NIR, fue demostrado que la presencia de vapor de agua afecta parcialmente a esta banda, incrementando la motivación de la necesidad de una corrección atmosférica. Por otro lado, en relación con los efectos espaciales, éstos fueron analizados siguiendo una formulación empírica desarrollada y validada en los años 80. Dicha formulación parametriza los efectos de difuminado producidos por la dispersión de aerosoles y moléculas con su espesor óptico y su distribución vertical en la atmósfera. Utilizando esta formulación como partida, se desarrolló una metodología que hace uso de los píxeles situados alrededor de aquellos clasificados previamente como bordes, es decir píxeles de entre dos zonas con alto contraste radiométrico. En esencia, este método se basa en la construcción de una serie de Funciones de Transferencia Modulada MTFs, las cuales a su vez vienen parametrizadas por un valor específico de AOT. Así pues, la imagen a corregir se deconvoluciona por cada una de las MTFs definidas para cada valor de AOT y se analizan los píxeles alrededor de los bordes. Si no hay efectos de emborronamiento entre píxeles la transición debe responder a una función cuadrada y cumplir la condición de mínima pendiente en esa región. Esta metodología fue evaluada con imágenes sintéticas, incluso añadiendo ruido a la imagen y los resultados fueron satisfactorios. Sin embargo, esta técnica no es por sí misma una estrategia completa de corrección atmosférica. Además, dado que la MTF tanto de la atmósfera como del instrumento están acopladas, la aplicación de esta técnica en datos reales requiere de un conocimiento exacto de la MTF del instrumento. En consecuencia, y dada la limitada información en el dominio espectral, se desarrolló un método de corrección atmosférica para la misión Ingenio/SEOsat. Este método, llamado Híbrido, combina una inversión pixel a pixel mediante un modelo de transferencia radiativa y datos auxiliares que ayuden a la caracterización de la atmósfera, junto con la corrección de los efectos espaciales mediante la deconvolución de la imagen dada la MTF correspondiente al valor del AOT previamente utilizado. La estrategia de corrección atmosférica fue aplicada a datos Sentinel-2 y validada frente a los resultados obtenidos con la herramienta de corrección atmosférica Sen2Cor proporcionada por la ESA para imágenes Sentinel-2.
- ***¿Cuáles son las particularidades a tener en cuenta en el desarrollo de una estrategia de corrección atmosférica en el caso de sensores con una alta resolución espectral a nivel de satélite? ¿Qué consideraciones particulares habría que tener en cuenta en el***

caso de la misión *tándem FLEX/Sentinel-3*? Ciertamente es que a mayor resolución espectral, mayor es la información disponible para caracterizar el estado atmosférico. Sin embargo, cuando se trabaja con sensores de muy alta resolución espectral, algunas consideraciones matemáticas que se asumen al hacer la inversión de la radiancia en TOA deben ser revisadas. Esta temática es abordada en el CAPÍTULO 4 y 5 de esta Tesis. En vista de los resultados, se puede afirmar que la formulación utilizada en esta Tesis para la inversión de la radiancia en el techo de la atmósfera es correcta y cumple con los requisitos de la misión FLEX. A este respecto, la revisión de la formulación se centra en: (1) evitar la convolución por serparado de las funciones de transferencia atmosféricas, y (2) acoplar consistentemente formulaciones que han sido diseñadas para la corrección atmosférica y para la obtención de la fluorescencia en la superficie. Todo esto se encuentra descrito en el CAPÍTULO 5.

- ***¿Qué consideraciones hay que tener en cuenta cuando una estrategia de corrección atmosférica clásica (inversión de un modelo físico) es aplicada a la misión *tándem FLEX/Sentinel-3*?*** FLEX es una misión diseñada en *tándem* con el satélite Sentinel-3. La motivación principal del concepto *tándem* es que incrementa las capacidades de FLEX para la caracterización y corrección de los efectos atmosféricos. En el CAPÍTULO 4 se propone y evalúa una estrategia de corrección atmosférica utilizando para ello datos simulados de Sentinel-3 y FLEX. La estrategia propuesta tan sólo utiliza los datos de Sentinel-3 para la caracterización de la atmósfera; sin embargo, la validación de la misma se efectúa sobre los datos de FLEX aplicando los criterios de exactitud en la obtención de la fluorescencia definidos por la misión. Dado los ajustados requisitos impuestos por la misión FLEX, se estudian aquellos casos en los que la calidad de la corrección atmosférica no ha sido suficiente para la obtención de fluorescencia dentro de los requisitos establecidos. De este estudio se deduce que no sólo la obtención del espesor óptico de los aerosoles es clave, sino también la correcta parametrización de la dispersión de los aerosoles. Cuando fueron filtrados aquellos escenarios en los que el error en la estimación del parámetro de asimetría de dispersión era mayor que ± 0.05 , el error en la obtención de la fluorescencia y de la reflectividad en superficie fue reducido significativamente.
- ***El uso de la formulación utilizada para la inversión de las radiancias a nivel de satélite como parte del proceso de corrección atmosférica, ¿sigue siendo correcto en el caso de trabajar con sensores de muy alta resolución espectral?*** Al trabajar con datos de muy alta resolución espectral, ciertas particularidades en cuanto a la formulación deben ser evaluadas. A este fin, en el CAPÍTULO 5 se revisan todas las aproximaciones matemáticas asumidas para realizar la inversión de las radiancias en el techo de la atmósfera mediante un modelo de transferencia radiativa. Se concluye que la serie de aproximaciones realizadas son válidas incluso dentro de los requisitos exigidos por la misión FLEX. Asimismo, y dado el contexto de la misión, también se revisa la consistencia entre la formulación utilizada en el proceso de corrección atmosférica con la formulación utilizada típicamente para la estimación de la señal fluorescencia. En particular, el foco se pone en la definición de reflectividad aparente

en superficie tanto en el proceso de corrección atmosférica como en el proceso de estimación de fluorescencia. En el CAPÍTULO 5 se presenta una formulación capaz de acoplar ambos procesos de forma consistente con la definición de reflectividad aparente en superficie.

- ***En el caso particular de la misión FLEX, el análisis y explotación de los datos de alta resolución espectral adquiridos por FLORIS, ¿podría ayudar en la caracterización de las propiedades ópticas de los aerosoles?*** Esta cuestión se estudia dentro del CAPÍTULO 5. Mientras en el CAPÍTULO 4 se demuestra la importancia del proceso de corrección atmosférica para una buena estimación de la fluorescencia; en el CAPÍTULO 5 se plantea el uso de la alta resolución espectral de los datos de FLORIS para mejorar la caracterización de la atmósfera. En concreto, se analizaron las diferentes distorsiones espectrales producidas en la reflectividad aparente en superficie debido a cambios en el espesor óptico de los aerosoles AOT, el coeficiente de Ångström, y la asimetría de la dispersión. Estas distorsiones en la reflectividad aparente fueron utilizadas para predecir el error cometido en la caracterización de los aerosoles. Utilizando parte de una base de datos simulada para el entrenamiento (30 %) y otra para la validación (70 %); los resultados sugieren que la reflectividad aparente en la región de los oxígenos podría emplearse para una mejora en la caracterización de los aerosoles; y consecuentemente una mejor obtención de la fluorescencia. De acuerdo con los resultados obtenidos en el CAPÍTULO 5, la estimación de los parámetros ópticos de los aerosoles alcanzaron, en el 75 % de los casos, errores por debajo del 0.2 %, 6 % y 2 % para el AOT, el coeficiente de Ångström, y el parámetro g , respectivamente. El criterio de validación se definió teniendo en cuenta el objetivo de la misión FLEX de medir la fluorescencia con una exactitud de un 10 %. Para ello, un error de un 10 % de fluorescencia fue propagado en reflectividad aparente. Los resultados muestran que la exactitud de la caracterización de los aerosoles obtenida es suficiente para derivar una reflectividad aparente que cumpliría los requisitos de la misión FLEX para la estimación de la fluorescencia.

- ***En aplicaciones de teledetección donde el sensor se sitúa a escasos metros de la muestra, ¿es necesaria la aplicación de un proceso de corrección atmosférica?*** En general, cuando las técnicas de teledetección son aplicadas a escasos metros del suelo, la contribución de la atmósfera se suele despreciar. Sin embargo, en el contexto de la misión FLEX, incluso en aquellos casos en los que la medida de la fluorescencia se realiza a escasos metros de la cubierta vegetal, la contribución atmosférica, especialmente la absorción del oxígeno, debe ser tenida en cuenta. En el CAPÍTULO 6 este escenario se evaluó teniendo como objetivo final la estimación de la señal de fluorescencia con técnicas de teledetección pasiva y con menos de un 10 % de error. Debido a que el impacto de ignorar los efectos atmosféricos afectará de forma diferente según la técnica utilizada para la estimación de la fluorescencia, ésto se cuantificó de la siguiente forma. Se evaluaron por separado diversos escenarios: (1) de forma independiente a la estrategia de obtención de la fluorescencia, (2) utilizando el método llamado Fraunhofer Line Discriminator (FLD), y (3) utilizando la estrategia llamada Spectral Fitting Method (SFM). Los resultados obtenidos

indican que no sólo la absorción del oxígeno debe ser compensada, sino que como parte de la estrategia de corrección, la convolución de las funciones de transferencia atmosféricas utilizando la ISRF del instrumento debe ser también tenida en cuenta. Es por ello que se propone y se evalúa una estrategia que utiliza el método de SFM como base y realiza la compensación de la absorción del oxígeno y de la ISRF de forma simultánea. Además, como parte del análisis llevado a cabo en este capítulo, la dependencia de la absorción del oxígeno con las condiciones ambientales de presión y de temperatura fue evaluada en el caso de una serie temporal de 1 año. Se observó que si la compensación de la transmisividad del oxígeno no tiene en cuenta las condiciones de presión y de temperatura, en casos como transiciones de invierno a verano en latitudes elevadas, podría llevar a derivar una falsa señal de fluorescencia; observando una estimación de la señal por exceso en verano y por defecto en invierno.

9.5 Conclusiones

En esta Tesis se han desarrollado distintas estrategias de corrección atmosférica para dos casos extremos que corresponden a misiones espaciales con observaciones en el intervalo espectral visible-infrarrojo próximo, en un caso a muy alta resolución espectral y en el otro caso a muy alta resolución espacial. Mientras que la corrección atmosférica es algo bien estudiado para casos menos extremos, la aplicación de la corrección atmosférica a tales casos extremos representa un desafío en cuanto a las metodologías específicas a desarrollar. Este trabajo se ha realizado en el contexto de dos misiones en fase de desarrollo: (1) la misión española Ingenio/SEOsat, y (2) la misión tándem Fluorescence Explorer (FLEX)/Sentinel-3 de la Agencia Espacial Europea (ESA).

La corrección atmosférica basada en la capacidad de explotar la información en el dominio espacial ha sido analizada bajo el contexto de la misión Ingenio/SEOsat. Ingenio/SEOsat está equipado con 4 canales, 3 en el visible (RGB, siglas en inglés de rojo verde y azul) y 1 en el infrarrojo cercano (NIR en inglés). Además, cuenta con una banda pancromática (PAN) que solapa los canales del verde y del rojo. El intervalo de muestreo espacial es de 10 m (RGB y NIR) y de 2.5 m (PAN). De acuerdo con estas especificaciones y tras un primer análisis se derivó que:

- la información espectral disponible no es suficiente, por sí misma, para caracterizar el estado atmosférico (principalmente la presencia de aerosoles y el contenido de vapor de agua). Esto implica que el uso de información auxiliar es necesario para la caracterización de la atmósfera y su posterior corrección atmosférica.
- las bandas situadas en el RGB y NIR se ven altamente afectadas por la presencia de aerosoles, presencia de nubes y el contenido de vapor de agua (ésta última sobre todo en el NIR). Este hecho refuerza la necesidad de aplicar una corrección atmosférica sobre las imágenes de Ingenio/SEOsat.

- dada la alta resolución espacial de Ingenio/SEOSat, se puede explotar el comportamiento de los efectos atmosféricos en el dominio espacial para caracterizar la presencia de aerosoles.

En cuanto a este último punto, se propuso y evaluó una técnica para derivar el espesor óptico de los aerosoles (AOT) tan sólo explotando la información espacial de la imagen. Esta técnica utiliza la idea de que la atmósfera, y concretamente los aerosoles, generan un efecto de difuminado en la imagen que es especialmente visible alrededor de los píxeles de transición (o bordes) entre zonas con un alto contraste radiométrico. La atmósfera, así pues, actúa de forma que suaviza dichas transiciones. Al analizar el comportamiento de los perfiles de radiancia (para cada banda individualmente) se aprecia que estas transiciones no obedecen a una función escalón, sino que más bien responden a una función sigmoide debido al efecto de difuminado antes mencionado. Este hecho ya fue observado en el pasado, donde se formuló una expresión empírica que modeliza el efecto de atenuación y dispersión de la luz en su paso por la atmósfera como si de un instrumento óptico se tratase. La expresión empírica, la llamaremos MTF atmosférica debido a las siglas en inglés de Modulated Transfer Function, utiliza 4 parámetros para su caracterización. Estos 4 parámetros corresponden al espesor óptico total y la altura efectiva a la que se encuentra la máxima concentración tanto de aerosoles como de moléculas. La técnica propuesta asume, a priori, valores por defecto para todos los parámetros excepto para el AOT. En esencia, la estrategia se basa en deconvolucionar la imagen dada la expresión de la MTF atmosférica para un rango de valores de AOT. Al analizar los perfiles resultantes de cada banda en los píxeles alrededor de los bordes, el valor de AOT buscado es aquel que su deconvolución presente un comportamiento similar a una función escalón. Tras la evaluación de esta técnica con imágenes simuladas se llegó a las siguientes conclusiones:

- el criterio aplicado para la detección del AOT basado en la búsqueda del valor que recupera la forma de la función escalón, es satisfactorio.
- cuantos más píxeles homogéneos alrededor de la zona de transición la sensibilidad a detectar el AOT es mayor. Sin embargo, llega un momento que ésta satura (alrededor de los 10 píxeles).
- al añadir ruido a la señal de radiancia (simulando que los píxeles no son del todo homogéneos), la técnica propuesta estima el valor de AOT requerido utilizando sólo 2 píxeles.

Sin embargo, ciertas limitaciones respecto a la aplicación de esta técnica también deben ser remarcadas:

- este estudio se centró en la MTF atmosférica, desacoplando en todo momento el efecto de la MTF del instrumento. Esto se pudo hacer gracias al uso de datos simulados. Sin embargo, si los resultados reportados en este capítulo quieren ser reproducidos con datos reales, se requiere de un conocimiento con gran exactitud de la MTF del instrumento.

- en este estudio se asumieron por defecto los valores del espesor óptico molecular y la altura de máxima concentración de moléculas y de aerosoles. Aunque el AOT es el parámetro que más afecta a la forma de la MTF, para valores de AOT bajos, el resto de parámetros cobran más importancia y el asumirlos puede derivar estimaciones menos exactas del AOT.

Por último, aunque ésta resulta una técnica interesante para la caracterización del contenido de aerosoles, no supone en sí mismo una estrategia de corrección atmosférica completa. Debido a ello, y a la necesidad de la utilización de datos auxiliares para la caracterización completa de la atmósfera, se presentó una estrategia completa de corrección atmosférica para la misión Ingenio/SEOSat llamada Híbrida. El método Híbrido aúna por una parte (1) la inversión de un modelo de transferencia radiativa pixel a pixel, junto con (2) una técnica de deconvolución de la MTF de la atmósfera para corregir los efectos espaciales. Dicha técnica fue aplicada sobre datos reales del satélite Sentinel-2, concretamente a las bandas de 10 m de resolución espacial debido a sus similitudes con Ingenio/SEOSat. En particular se evaluaron los efectos del método Híbrido en una zona urbana con marcados contrastes entre zonas brillantes y oscuras. Éstos fueron validados con los resultados obtenidos por la corrección atmosférica proporcionada por el software de la ESA, Sen2Cor. En el dominio espacial, se pudo observar como la aplicación del proceso de deconvolución del método Híbrido corrige los efectos de adyacencia; reduciendo el nivel de reflectividad en los píxeles más oscuros y aumentándolo en los más brillantes. Al compararlo con la corrección de Sen2Cor, se observó (a) un igual patrón espacial en la corrección, (b) una mayor corrección por parte del método Híbrido, especialmente en estructuras como calles estrechas, (c) una menor dependencia con el tamaño de la ventana aplicada para la corrección de adyacencia. En el dominio espectral, los resultados muestran un RMSE (Raíz del Error Cuadrático Medio en inglés) de 0.0048 y 0.1100 para las bandas del azul y el NIR al comparar las reflectividades de ambos métodos. Estas discrepancias son razonables y esperadas debido al diferente proceso de caracterización de la atmósfera seguido por ambos métodos. En el caso de Sen2Cor, se utilizaron todas las bandas de Sentinel-2 y el método 'Dark Dense Vegetation'. En el caso del método Híbrido, se utilizó como fuente de datos auxiliares la red Aeronet. Asimismo, el diferente tratamiento de los efectos de adyacencia provoca discrepancias, tanto en la banda del azul como el en NIR (especialmente en píxeles de agua). Tras este análisis, se presenta al método Híbrido como propuesta para la corrección atmosférica de imágenes de la misión Ingenio/SEOSat.

Seguidamente, en el contexto de la misión ESA tándem FLEX/Sentinel-3, se propuso y evaluó el desarrollo de una estrategia de corrección atmosférica centrada en la explotación de la información con muy alta resolución espectral. En particular, en el CAPÍTULO 4, se muestra una estrategia de caracterización de la atmósfera basada tan sólo en la información adquirida por los instrumentos Ocean and Land Colour Imager (OLCI) y Sea Land Surface Temperature Radiometer (SLSTR) a bordo de Sentinel-3. La estrategia, similar a otros métodos desarrollados en el pasado para el satélite ENVISAT, se basa en la inversión de un modelo de transferencia radiativa píxel a píxel. Como principales novedades introduce: (1) la parametrización de la presencia de aerosoles por medio de tres parámetros ópticos, y (2) la utilización de una base de

datos para modelizar la reflectividad como parte del proceso de la estimación de aerosoles. Respecto a los parámetros ópticos seleccionados, éstos son el AOT, el coeficiente de Ångström (α) y el coeficiente de asimetría de dispersión (g). Al utilizar esta parametrización de los aerosoles se evita el tener que seleccionar entre diferentes clasificaciones o mezclas predefinidas de aerosoles (práctica muy popular entre estos algoritmos). Por otro lado, al utilizar una base de datos de reflectividades, se evita el tener que asumir una relación entre las observaciones en geometría nadir y oblicua para el sensor SLSTR. Además, de esta forma también se evita el modelizar la reflectividad como una combinación lineal de varios espectros base (práctica bastante común).

Utilizando datos simulados (sobre 240 condiciones atmosféricas), la estrategia propuesta fue evaluada en cuanto: (a) a la calidad de la caracterización de la atmósfera, y (b) al error obtenido en reflectividad aparente, el cual debe garantizar una estimación de la fluorescencia con un error menor al 10 % (suele equivaler a unos 0.2 [mW/m²/sr/nm] en el O₂-B y 0.1 [mW/m²/sr/nm] en el O₂-A). En cuanto a la caracterización de la atmósfera y su impacto en reflectividad aparente se pudo observar que:

- el error en reflectividad aparente en el O₂-B es mayor que en el O₂-A para la mayoría de casos.
- a mayor AOT, cualquier error en la caracterización tiene un gran impacto.
- en algunos casos, la estimación de la reflectividad aparente presentaba un error medio relativo menor de un 1 % incluso habiéndose equivocado significativamente en la estimación del valor del AOT (± 0.1). Éste fue un primer indicativo de la posible compensación radiativa entre las propiedades ópticas seleccionadas para la caracterización de los aerosoles.
- en general los parámetros que tienen más impacto en la estimación de la reflectividad aparente son el AOT y la asimetría de la dispersión de los aerosoles. El coeficiente de Ångström parece no afectar de forma tan drástica.
- la dispersión obtenida, cuantificada como la desviación estándar de los 240 casos evaluados en reflectividad aparente (para cada uno de los 5 tipos de superficies estudiados) no cumplía en su totalidad con los requisitos de la misión FLEX. La dispersión de la fluorescencia estimada para los 240 casos estudiados es significativamente mayor que el requisito de 10 % exigido. Sin embargo, al filtrar sólo aquellos casos en los que el error en la asimetría de la dispersión fue mayor que un ± 0.05 (generalmente estos casos coinciden con un error grande en AOT también) la exactitud y la precisión de la fluorescencia estimada mejoró significativamente. Esto concluyó: (1) la importancia de los efectos de dispersión de los aerosoles en las bandas del oxígeno, y consecuentemente en la estimación de la fluorescencia; y (2) la necesidad de revisar y mejorar el método de corrección atmosférica propuesto.

La misión FLEX requiere de una exactitud en reflectividad aparente muy exigente en la región espectral de absorción del oxígeno, pues un 10 % de error relativo en fluorescencia se

puede traducir en un 1-2 % de error relativo en reflectividad. De esto se desprende la necesidad de revisar todos aquellos aspectos que pudiesen influir tanto en la caracterización de la atmósfera como en la formulación para la inversión y estimación de la fluorescencia. A este fin, el CAPÍTULO 5 se centró en la evaluación de la formulación utilizada derivando lo siguiente:

- la utilización de la expresión de la radiancia en el techo de la atmósfera como expansión en serie hasta segundo orden para la inversión de la reflectividad, cumple con los requisitos de la misión FLEX.
- la aproximación de considerar que la reflectividad acoplada con el albedo esférico es reflectividad aparente cumple con los requisitos de misión.
- el acoplamiento entre las formulaciones utilizadas en el proceso de corrección atmosférica y el de estimación de la fluorescencia (como parte del algoritmo basado en un método de ajuste espectral) debe ser consistente. Sin embargo, en general, existe una inconsistencia debida a que la inversión de la reflectividad aparente como parte del proceso de corrección atmosférica y la definición de reflectividad aparente sobre la vegetación en superficie, son diferentes. En consecuencia, se propuso y evaluó satisfactoriamente una estrategia que utiliza la misma definición de reflectividad aparente tanto para la corrección atmosférica como para la estimación de fluorescencia.

Asimismo, el CAPÍTULO 5 se centró en el posible uso o explotación de la alta resolución espectral proporcionada por FLORIS, especialmente en la región espectral de absorción del oxígeno, para la mejora de la caracterización de los aerosoles. Para ello, se estudió la distinta distorsión espectral (independientemente de la reflectividad en superficie) que se genera al cometer un error en la estimación de los diferentes parámetros ópticos utilizados en la caracterización de los aerosoles. Debido a que la distorsión espectral generada era diferente para cada parámetro óptico e independiente de la superficie subyacente; esto fue un indicativo para explotar dicho comportamiento. Para este estudio se construyó una base de datos que contaba con más de 8×10^4 combinaciones. Así pues, mediante una regresión lineal multivariada (construida con el 30 % de una base de datos) se predice el error relativo de cada parámetro óptico: AOT, coeficiente de Ångström y parámetro de asimetría; dada una primera estimación errónea de la reflectividad aparente en el O₂-A y en el O₂-B y el índice NDVI (Índice de Vegetación de Diferencia Normalizada). A modo de prueba de concepto, al aplicar esta regresión con el 70 % restante de la base de datos, ésta proporcionó una estadística de error menor del 0.5 %, 8 % y 3 % para el AOT, el coeficiente de Ångström y el parámetro de asimetría para el percentil 75 tanto en el O₂-A como en el O₂-B. En esta ocasión, al cuantificar el error sobre reflectividades aparentes, éste cumplía con los requisitos de misión de FLEX. De esta forma, el método propuesto logra explotar la alta resolución espectral para la mejora de la caracterización de los aerosoles y consecuentemente para la estimación de la fluorescencia. Cabe observar, tal y como se mencionó en dicho capítulo, que la utilización de este método de forma operativa implicaría un test más exhaustivo acerca del impacto de los posibles efectos instrumentales sobre las bandas del oxígeno. Tanto los efectos atmosféricos como instrumentales pueden distorsionar la

forma de las bandas de absorción. El garantizar el desacople entre ellos es necesario para una buen procesado de los datos.

Finalmente, la tesis culmina poniendo el foco en la estrategia de validación para la misión FLEX. La validación de la señal de fluorescencia a escala de satélite implica la medida de ésta a escala local. Generalmente, para el seguimiento de cubiertas vegetales tales como cultivos o bosques, se suelen emplear sistemas elevados como torres de medida o grúas. En este contexto, el CAPÍTULO 6 revisa la necesidad corregir los efectos atmosféricos cuando la muestra y el sensor están separados tan sólo unos pocos metros de distancia. Para la mayoría de aplicaciones los efectos atmosféricos a esta escala son típicamente ignorados. Sin embargo, en el contexto de la misión FLEX, y cuando el objetivo último es detectar la señal de fluorescencia mediante las bandas de absorción del oxígeno, la corrección o compensación de los efectos atmosféricos debe ser tomada en cuenta como parte del procesado de los datos incluso a escala local. En particular, se evaluó el impacto de no corregir la absorción del oxígeno en la estimación de la fluorescencia tanto de forma independiente a la técnica empleada, como al aplicar un método de absorción diferencial como el Fraunhofer Line Discriminator (FLD en inglés), y un método de ajuste espectral (SFM en inglés). Se observó que independientemente de la técnica utilizada es necesaria la compensación de la absorción del oxígeno producida en el camino óptico entre la muestra y el detector (>3 m), al menos en la región del O_2 -A. La absorción en el O_2 -B es mucho más débil y a escasos metros puede ser ignorada a primer orden. Con este fin, se evaluó la posibilidad de compensar los efectos atmosféricos de forma sencilla, añadiendo en las formulaciones del FLD y del SFM la componente de la transmisividad del oxígeno previamente calculada y convolucionada a la respuesta espectral del instrumento (ISRF en inglés). Aunque esta alternativa sencilla mejoraba la estimación de la fluorescencia en algunos casos (especialmente en las longitudes de onda de la zona más profunda de la absorción del O_2 -A), no llegaba a ser suficiente. Al igual que se reportó en el CAPÍTULO 5, al trabajar con funciones de transferencia atmosférica en alta resolución espectral y especialmente en bandas de absorción, hace que sea especialmente delicado el hecho de multiplicarlas o dividir las cuando ya están convolucionadas a la respuesta espectral del instrumento. Así pues, se propuso una nueva estrategia capaz de compensar de forma simultánea los efectos (1) de la absorción del oxígeno, y (2) de la respuesta del instrumento. En esencia, esta estrategia está basada en la técnica de SFM, pero simulando en cada iteración, a través de un modelo de transferencia radiativa, la irradiancia solar y la transmisividad de la atmósfera a alta resolución espectral. De esta forma se evita el derivar errores debidos a la multiplicación de términos convolucionados previamente. Los análisis realizados reportaron para una alta resolución espectral (dícese de un mínimo de intervalo espectral de muestreo de 0.4 nm y una resolución de ancho de banda de 1 nm), una estimación de la fluorescencia dentro de los requisitos de la misión FLEX incluso cuando las distancias de la muestra al sensor alcanzan 20 m. De hecho, los resultados obtenidos en fluorescencia en un rango de 3 a 20 m son comparables; lo que indica que la estrategia compensa de forma efectiva el camino óptico de la muestra al sensor. Sin embargo, aunque en este trabajo se demostró que con una primera compensación de la absorción del oxígeno es suficiente cuando se trabaja a escasos metros de distancia de la muestra; para otras aplicaciones como pudiera ser la observación de la vegetación mediante vehículos no tripulados (los cuales pueden fácilmente alcanzar el

centenar de metros); la misma técnica podría ser utilizada pero compensando, en este caso, por la transmisividad tanto de los aerosoles como la del oxígeno molecular. En este trabajo se han puesto de manifiesto las dificultades que representa la corrección atmosférica en casos extremos tales como la muy alta resolución espacial o la muy alta resolución espectral de los datos. Sin embargo, mediante las aproximaciones adecuadas se ha desarrollado la correspondiente metodología que permite abordar tales correcciones y se han desarrollado métodos específicos para el caso de SEOSat (alta resolución espacial) y FLEX (alta resolución espectral), dos misiones futuras de teledetección que serán lanzadas al espacio en los próximos años.



Appendix: Instruments

Contents

A.1	Ingenio/SEOsat	204
A.2	FLORIS	206
A.3	OLCI	209
A.4	SLSTR	212

This appendix is dedicated to describe main instruments involved in the Scientific Earth Observation Satellite (SEOsat) and the FLEX/Sentinel-3 space missions. This appendix is focused on the different instrument's radiometric, spatial and spectral specifications.

A.1 Ingenio/SEOsat

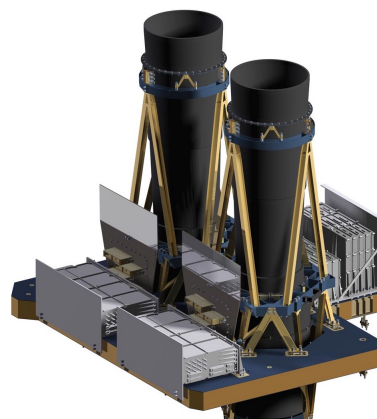
The overall mission objective is to provide information for applications in cartography, land use, urban management, water management, environmental monitoring, risk management and security. The requirements call for panchromatic imagery of 2.5 m and multispectral imagery of 10 m resolution.

Ingenio is also known as SEOsat/Ingenio (Satélite Español de Observación de la Tierra - Spanish System for Earth Observation Satellite). The basic mission requirements are defined according to these main criteria:

- Provision of data services to comply with the Spanish institutional user needs. The global land mission primary objectives call for a *Carpet mapping of Spain plus image acquisition over main areas of interest (Europe, South America and North of Africa)*.
- The SEOsat/Ingenio mission is also regarded to provide complementary services to the GMES program, in particular to the objectives of the Sentinel-2 mission.

More details about the SEOsat mission specifications can be found in the ESA's Earth Observation portal <https://directory.eoportal.org>. In Table A.1.1 and A.1.2 main instrument and satellite specifications are summarized.

FIGURE A.1.1: Ingenio/SEOsat instrument model. Original image source from SENER aerospace www.aeroespacial.sener



Primary Payload	
Spectral bands	<ul style="list-style-type: none"> ■ Panchromatic band–PAN ■ G, R and NIR–4 MS (Multispectral) bands
Performance	<ul style="list-style-type: none"> ■ Swath of 55 km ■ GSD (Ground Sample Distance) of 10 m for MS and 2.5 m for PAN ■ Equivalent FOV= $5.13^\circ \leq 2.5 \text{ m (Pan)}, \leq 10 \text{ m (MS)} \sim 0.1 \text{ MS pixel } (2\sigma) \text{ for RGB MS bands } (0.3 \text{ pixel for NIR})$

TABLE A.1.1: SEOsat/Ingenio primary payload main instrument's specifications.

Mission and system requirements	
Geographical coverage	<p>World coverage, with latitudes from 83°N to 56°S. Systematic coverage of zones of special interest:</p> <ul style="list-style-type: none"> ■ The Spanish Territory ■ Europe ■ Ibero–America ■ North of Africa down to 10° N ■ Main world islands
Performance	<ul style="list-style-type: none"> ■ Pointing accuracy better than 200 m ■ Pointing accuracy better than 1000 m ■ Geo–location accuracy <50 m without GCP, 20 m with GCP. ■ Roll tilt capability of spacecraft = $\pm 35^\circ$
Sun-synchronous orbit	<ul style="list-style-type: none"> ■ Altitude of ~ 670 km ■ LTDN (Local Time of Descending Node) at 10:30 hours 4–day – repeat cycle ■ 3 days accessibility
Mission performance	<ul style="list-style-type: none"> ■ Lifetime = 7years. ■ Design and consumables sized for additional 3 years. ■ Product availability > 95%

TABLE A.1.2: SEOSat/Ingenio mission and system requirements.

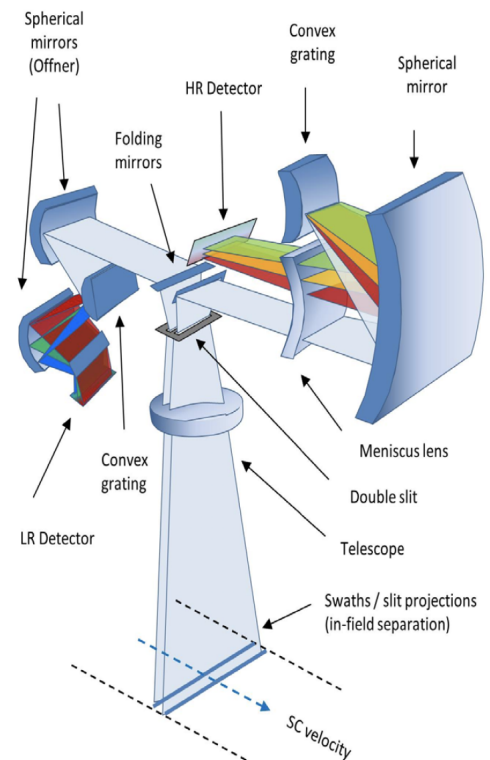
A.2 FLORIS

The main scientific payload on board FLEX is called FLORIS, which is a push–broom hyperspectral imager. FLORIS will measure the Solar–Induced vegetation Fluorescence (SIF) in the spectral range between 500 nm and 780 nm at medium spatial resolution (300 m) and over a swath of 150 km. FLORIS accommodates an imaging spectrometer with a very high spectral resolution (0.3 nm of bandwidth), to measure the SIF spectrum especially exploiting the information within the two oxygen absorption features (O_2 –A and O_2 –B), and a second spectrometer with lower spectral resolution to derive additional atmospheric and vegetation parameters.

During the current FLEX Phase B/C, the selected FLORIS design was the concept developed by Thales Aliena Space (See Figure A.2.1) and described in detail in the FLEX Mission Selection Report [European Space Agency, 2015a] and in Coppo *et al.*, 2017. Due to the FLEX mission requirements set to measure SIF, some aspects such as the light degree of polarization could be critical. Due to that, FLORIS is also provided with a polarization scramble at the entrance of the telescope. One single telescope is used and it images the ground scene onto a double slit assembly. Then radiation is spectrally dispersed onto the focal planes of the grating spectrometers by using mirrors and lens. The absolute radiometric calibration is achieved by observing a dedicated Sun illuminated Lambertian diffuser, while the spectral calibration in flight is performed by means of vicarious techniques.

In Table A.2.1 most important instrument specifications are detailed. Particularly, this Table summarizes, on the one hand, the requirement impose to accomplish the mission goals; and, on the other hand, the performance achieved by the FLORIS instrumentation. Similarly, Table A.2.2 summarizes the spectral requirements and performance achieved by FLORIS in terms of the Spectral Sampling Interval (SSI) and Spectral Resolution (SR). Most information of these Tables has been obtained from Coppo *et al.*, 2017.

FIGURE A.2.1: FLORIS instrument concept from Thales Aliena Space. Original image from the FLEX Mission Selection Report [European Space Agency, 2015a]



Requirement	Specification	Performance
Mission lifetime	3.5/5 years	5 years
Coverage	$-56^\circ < \text{latitude} < 75^\circ$	$-56^\circ < \text{latitude} < 75^\circ$
Satellite height	805–830km	805–830 km
Swath width	>150 km	>151 km
SSD	<300 m (nadir)	<288 m (along-track) <300 m (across-track)
Image Quality	<1.2 SSD	1.1 SSD
Spatial co-registration (HR or LR)	<0.15 SSD	<0.15 SSD
HR vs LR spatial co-registration knowledge	<0.1 SSD	0.08 SSD
Geo-location accuracy	<0.4 SSD	0.24 SSD
Spectral co-registration	<2 SSI	1.2 SSI
Spectral stability	$< \pm 0.1$ SSI (orbit) $< \pm 1$ SSI (lifetime)	$< \pm 0.1$ SSI $< \pm 1$ SSI
ISRF knowledge	$<2\%$	1.6%
HR Straylight ($\text{mW}/\text{m}^2/\text{sr}/\text{nm}$)	0.2 (L_0) 0.04 (L_{1b})	<0.8 (L_0) 0.04 (L_{1b})
ARA/RSRA/RXRA	5%/1%/0.5%	5%/1%/0.5%
Polarisation Sensitivity	$<2\%$ (LR) $<1\%$ (HR)	$<2.0\%$ (LR) $<0.9\%$ (HR)
Inter-channel registration	temporal co- <2.5 s	2.4 s

TABLE A.2.1: FLORIS instrument mission requirements and performance. Following the list of the acronyms used in the Table are detailed: SSD = Spatial Sampling Distance, ARA = Absolute Radiometric Accuracy, RSRA = Relative Spectral Radiometric Accuracy, RXRA = Relative Spatial Radiometric Accuracy, ISRF = Instrument Spectral Response Function, FWHM = Full Width Half Maximum.

Band Name	PRI	Chl.	O₂-B	O₂-B	R-E	O₂-A	O₂-A	O₂-A	O₂-A
Spectrometer	LR	LR	HR	HR	LR	HR	HR	HR	HR
Band (nm)	500-600	600-677	677-686	686-697	697-740	740-755	755-759	759-769	769-780
SSI req. (nm)	2	2	0.5	0.1	1	0.5	0.5	0.1	0.5
SSI per. (nm)	1.8	1.8	0.467	0.093	0.6	0.467	0.467	0.093	0.467
SR req. (nm)	3	3	0.7	0.3	2	0.7	0.7	0.3	0.7
SR per. (nm)	2	2	0.474	0.28	1.8	0.474	0.474	0.28	0.474
SNR req. (nm)	245	245	340	175	425	510- 1015*	1015	115- 455*	1015

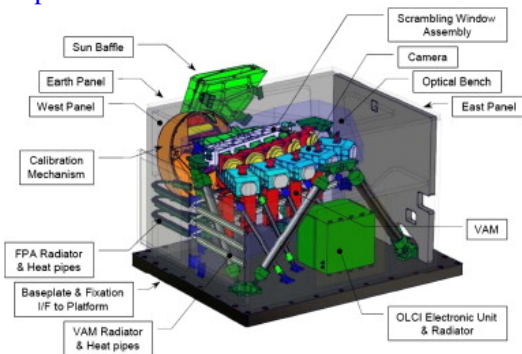
TABLE A.2.2: FLORIS spectral requirements and performance achieved.

A.3 OLCI

The OLCI instrument baseline is an heritage from its predecessor the ENVISAT MERIS, but with additional spectral channels, different camera arrangements and simplified on board processing. OLCI is a push-broom instrument with five camera modules sharing the field of view. Each camera has an individual field of view of 14.2° and a 0.6° overlap with its neighbours. The whole field of view is shifted across track by 12.6° away from the sun to minimise the impact of sun glint. For the FLEX mission purposes, only camera 4 will be used, since FLEX swath is completely overlapped with this central OLCI camera providing the closest viewing to nadir. The OLCI acquisition resolution of approximately 300 m, which is in turn the one used to compute the product grid of Full Resolution (FR) product. A Reduced Resolution (RR) processing mode provides Level-1B data decreasing the spatial resolution to approximately 1.2 km. OLCI is also equipped with on-board calibration hardware based on sun diffusers. There are three sun diffusers: two "white" diffusers dedicated to radiometric calibration and one dedicated to spectral calibration, with spectral reflectance features. As a response to the Sentinel-3 mission requirements [Drinkwater and Rebhan, 2007], main OLCI instrument's specifications are presented in Table A.3.1. Similarly, OLCI spectral bands specifications are detailed in Table A.3.2. In addition, in the following lines some aspects regarding the Sentinel-3 orbit are also summarized:

- The orbit is similar to the ENVISAT's orbit, allowing the continuation of the ERS- family and ENVISAT time series.
- Sentinel-3 orbit's uses a high inclination of 98.65° for optimal coverage of ice and snow parameter in high latitudes. The orbit inclination is the angular distance of the orbital plane from the equator.
- The orbit is a **sun-synchronous** orbit with a descending node equatorial crossing at 10:00 h Mean Local Solar Time. In a sun-synchronous orbit, the surface is always illuminated at the same sun angle.
- The orbital cycle is 27 days ($14+7/27$ orbits per day, 385 orbits per cycle). The orbit cycle is the time taken for the satellite to pass over the same geographical point on the ground.
- The two in-orbit SENTINEL-3 satellites enable a short revisit time of less than two days for OLCI and less than one day for SLSTR at the equator

FIGURE A.3.1: Overview of the Sentinel-3 Ocean and Land Colour Imager (OLCI) Instrument. Image Credit: Thales Aliena Space – France. Original image source <https://sentinel.esa.int/>



- The orbit reference altitude is 814.5 km.
- Sentinel-3B's orbit is identical to the Sentinel-3A's orbit but flies $\pm 140^\circ$ out of phase with Sentinel-3A.

Specification	Requirement
Swath	1440 km
SSD at SSP	300
Calibration	MERIS type calibration arrangement with spectral calibration using: (1) a doped Erbium diffuser plate, (2) PTFE diffuser plate and (3) dark current plate viewed approximately every 2 weeks at the South Pole ecliptic. (4) Spare diffuser plate viewed periodically for calibration degradation monitoring
Detectors	ENVISAT MERIS heritage back-illuminated CCD55-20 frame-transfer imaging device (780 columns by 576 row array of $22.5 \mu\text{m}$ square active elements).
Optical Scanning Design	Push-broom sensor.
Spectral Resolution	1.25 nm (MERIS heritage), 21 bands.
Radiometric Accuracy	<ul style="list-style-type: none"> ■ $< 2\%$ with reference to the sun for the 400-900 nm ■ $< 5\%$ with reference to the sun for > 900 nm ■ 0.1% stability for radiometric accuracy over each orbit ■ 0.5% relative accuracy for the calibration diffuser BRDF
Radiometric Resolution	$< 0.03 [\text{Wm}^{-2}\text{sr}^{-1}\text{mm}^{-1}]$ (MERIS baseline)
Design Lifetime	7.5 years

TABLE A.3.1: OLCI instrument specifications.

Band	λ_0 (nm)	Width (nm)	L_{ref}	SNR at L_{ref}
Oa1	400	15	62.95	2188
Oa2	412.5	10	74.1	2061
Oa3	442.5	10	65.61	1811
Oa4	490	10	51.21	1541
Oa5	510	10	44.39	1488
Oa6	560	10	31.49	1280
Oa7	620	10	21.14	997
Oa8	665	10	16.38	883
Oa9	673.75	7.5	15.70	707
Oa10	681.25	7.5	15.11	745
Oa11	708.75	10	12.73	785
Oa12	753.75	7.5	10.33	605
Oa13	761.25	2.5	6.09	232
Oa14	764.375	3.75	7.13	305
Oa15	767.5	2.5	7.58	330
Oa16	778.75	15	9.18	812
Oa17	865	20	6.17	666
Oa18	885	10	6.00	395
Oa19	900	10	4.73	308
Oa20	940	20	2.39	203
Oa21	1020	40	3.86	152

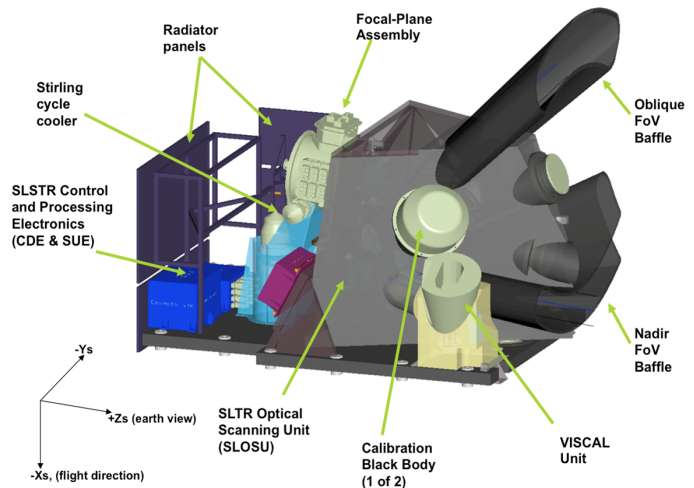
TABLE A.3.2: OLCI instrument specifications. Central band wavelength (λ_0), width of the band in nm, reference radiance for each band (L_{ref}), and the Signal To Noise Ration computed for L_{ref} for each band. Bands highlighted in bold are MERIS heritage.

A.4 SLSTR

The primary mission objective of the SLSTR instrument is to extend the long-term consistent set of global Sea Surface Temperature (SST) measurements. SST has been measured from 1991 from the ATSR-family instruments on board ERS-1 and ERS-2, and finally with the AATSR instrument on board Envisat. Thus, the SLSTR design incorporates the basic functionality of AATSR, but with the addition of some more advanced features. Among the novelties, it includes a wider swath coverage, which completely overlaps the OLCI swath, more spectral bands, and a spatial resolution of 0.5 km for visible and SWIR bands. The SLSTR instrument is a conical scanning imaging radiometer employing the along track scanning dual view technique to provide robust atmospheric correction over a dual-view swath. The instrument includes channels in the visible (VIS), thermal (TIR) and short wave (SWIR) infra-red spectrum. The SLSTR has been developed to retrieve global coverage sea surface skin temperatures with zero bias and an uncertainty of ± 0.3 K for a 5° by 5° latitude-longitude area, having a temporal stability of 0.1 K/decade.

In Tables A.4.1 and A.4.2 most important SLSTR specification regarding the spatial coverage and the spectral resolution covered are summarized. Information contained in this Tables, as well as more details regarding the instrument performance and calibration can be found at the official ESA portal <https://sentinel.esa.int/web/sentinel/user-guides/sentinel-3-slstr>.

FIGURE A.4.1: Overview of the Sentinel-3 Sea Land Surface Temperature Radiometer (SLSTR) Instrument. Original image source <https://sentinel.esa.int/>



Specifications	Parameters	SLSTR Performance
Swath	Nadir view	1400 km
	Dual view	740 km
Global Coverage	1 sat (dual view)	1.9 days
Revisit Times	2 sat. (dual view)	0.9 days
	1 sat. (nadir)	1 day
	2 sat. (nadir)	0.5 days
SSI and SSP		0.5km (VIS-SWIR) 1km (IR-fire)
Radiometric res.	VIS (a=0.5%)	SNR > 20
	SWIR (a=0.5%)	SNR > 20
	MWIR (T=270K)	Ne Δ T < 80 mK
	TIR (T=270K)	Ne Δ T < 50 mK
	Fire-1 (<500 K)	Ne Δ T < 1K
	Fire-2 (<400 K)	Ne Δ T < 0.5 K
Radiometric accuracy	VIS-SWIR(a=2-100%)	< 2% (BOL)
		< 5% (EOL)
	MWIR-TIR(265-310K)	< 0.1 K (goal)
	Fire (<500K)	< 3 K
Life time (in orbit)		7.5 years

TABLE A.4.1: SLSTR instrument specifications. Some clarifications regarding acronyms and abbreviations used in this Table: SSI is the spatial sampling interval at sub-satellite point (SSP), λ_0 is central wavelength, "a" is referred to the top of atmosphere albedo, "T" is referred to the top of atmosphere brightness temperature, SNR is signal-to-noise ratio, "BOL" refers to Beginning of Life, "EOL" refers to End of Life, and NE Δ T is noise equivalent difference temperature.

Band	Wavelength λ_0 [μm]	Width [μm]	Function	Res. [m]
S1	0.555	0.02	Cloud screening vegetation, aerosol	500
S2	0.659	0.02	NDVI, Vegetation aerosol	500
S3	0.865	0.02	NDVI, cloud flagging pixel-corregistration	500
S4	1.375	0.015	Cirrus detection over land	500
S5	1.61	0.06	Cloud clearing, ice snow, vegetation monitor- ing	500
S6	2.25	0.05	Vegetation state and cloud clearing	500
S7	3.74	0.38	SST, LST Active fire	1000
S8	10.85	0.9	SST, LST Active fire	1000
S9	12	1	SST, LST	1000
F-1	3.74	0.38	Active fire	1000
F-2	10.85	0.9	Active fire	1000

TABLE A.4.2: Radiometric bands of SLSTR, central wavelength (λ_0), band width, function and corresponding spatial resolution. Note that F-1 and F-2 fire bands are based on the same detectors as S7 and S8 but with an increased dynamic range to prevent saturation over fires. Some of the acronyms used in the Table are: SST: Sea Surface Temperature, LST: Land Surface Temperature, NDVI: Normalized Differential Vegetation Index.

Bibliography

- Aasen, H. (2017). State-of-the-art in UAV remote sensing survey—first insights into applications of UAV sensing systems. *International Archives of the Photogrammetry, Remote Sensing and Spatial Information Sciences- ISPRS Archives*, **42**(2W6), 1–4.
- Ackerman, S. A., Strabala, K. I., Menzel, W. P., Frey, R. A., Moeller, C. C., and Gumley, L. E. (1998). Discriminating clear sky from clouds with MODIS. *Journal of Geophysical Research: Atmospheres*, **103**(D24), 32141–32157.
- Adler-Golden, S. M., Matthew, M. W., Bernstein, L. S., Levine, R. Y., Berk, A., Richtsmeier, S. C., Acharya, P. K., Anderson, G. P., Felde, J. W., Gardner, J., *et al.* (1999). Atmospheric correction for shortwave spectral imagery based on MODTRAN4. In *SPIE's International Symposium on Optical Science, Engineering, and Instrumentation*, pages 61–69, San Diego (USA). International Society for Optics and Photonics.
- Alonso, L., Gómez-Chova, L., Vila-Francés, J., Amorós-Lopez, J., Guanter, L., Calpe, J., *et al.* (2008). Improved fraunhofer line discrimination method for vegetation fluorescence quantification. *IEEE Geoscience and Remote Sensing Letters*, **5**(4), 620–624.
- Alonso, L., Sabater, N., Vicent, J., Cogliati, S., Rossini, M., and Moreno, J. (2014). Novel algorithm for the retrieval of solar-induced fluorescence from hyperspectral data based on peak height of apparent reflectance at absorption features. In *5th International workshop on Remote Sensing of Vegetation Fluorescence*, Paris (France). European Space Agency.
- Ångström, A. (1929). On the atmospheric transmission of sun radiation and on dust in the air. *Geografiska Annaler*, **11**, 156–166.
- Asrar, G. *et al.* (1989). Theory and applications of optical remote sensing. chapter 9. John Wiley & Sons.
- Barnsley, M. J., Settle, J. J., Cutter, M. A., Lobb, D. R., and Teston, F. (2004). The PROBA/CHRIS mission: A low-cost smallsat for hyperspectral multiangle observations of the earth surface and atmosphere. *IEEE Transactions on Geoscience and Remote Sensing*, **42**(7), 1512–1520.
- Benas, N., Chrysoulakis, N., and Giannakopoulou, G. (2013). Validation of MERIS/AATSR synergy algorithm for aerosol retrieval against globally distributed aeronet observations and comparison with MODIS aerosol product. *Atmospheric Research*, **132**, 102–113.
- Berk, A., Bernstein, L. S., and Robertson, D. C. (1987). MODTRAN: A moderate resolution model for LOW-TRAN. Technical report, DTIC Document.
- Berk, A., Anderson, G. P., Acharya, P. K., Bernstein, L. S., Muratov, L., Lee, J., Fox, M., Adler-Golden, S. M., Chetwynd, J. H., Hoke, M. L., Lockwood, R. B., Gardner, J. A., Cooley, T. W., Borel, C. C., and Lewis, P. E. (2005). MODTRAN 5: a reformulated atmospheric band model with auxiliary species and practical multiple scattering options: update. volume 5806, pages 662–667.
- Bernstein, L. S., Adler-Golden, S. M., Sundberg, R. L., Levine, R. Y., Perkins, T. C., Berk, A., Ratkowski, A. J., Felde, G., and Hoke, M. L. (2005). Validation of the QUick Atmospheric Correction (QUAC) algorithm for VNIR–SWIR multi- and hyperspectral imagery. In *Defense and Security*, pages 668–678. International Society for Optics and Photonics.
- Boardman, J. W. (1998). Post-ATREM polishing of AVIRIS apparent reflectance data using EFFORT: a lesson in accuracy versus precision. In *Summaries of the seventh JPL airborne Earth science workshop*, volume 1, page 53, California (USA). Jet Propulsion Laboratory.
- Brent, R. P. (1971). An algorithm with guaranteed convergence for finding a zero of a function. *The Computer Journal*, **14**(4), 422–425.

- Bresciani, M., Rossini, M., Morabito, G., Matta, E., Pinardi, M., Cogliati, S., Julitta, T., Colombo, R., Braga, F., and Giardino, C. (2013). Analysis of within-and between-day chlorophyll-a dynamics in Mantua Superior Lake, with a continuous spectroradiometric measurement. *Marine and Freshwater Research*, **64**(4), 303–316.
- Bruegge, C. J., Conel, J. E., Margolis, J. S., Green, R. O., Toon, G. C., Carrere, V., Holm, R. G., and Hoover, G. (1990). In-situ atmospheric water-vapor retrieval in support of AVIRIS validation. In *Imaging spectroscopy of the terrestrial environment*, pages 150–163. International Society for Optics and Photonics.
- Bunting, J. T. and d'Entremont, R. P. (1982). Improved cloud detection utilizing defense meteorological satellite program near infrared measurements. Technical report, DTIC Document.
- Camps-Valls, G., Tuia, D., Gómez-Chova, L., Jiménez, S., and Malo, J. (2011). Remote sensing image processing. *Synthesis Lectures on Image, Video, and Multimedia Processing*, **5**(1), 1–192.
- Carr, S. (2005). The aerosol models in MODTRAN: Incorporating selected measurements from northern australia. Technical report, Australian Government Department of Defence-Science and Technology Organisation.
- Ceccato, P., Flasse, S., Tarantola, S., Jacquemoud, S., and Grégoire, J.-M. (2001). Detecting vegetation leaf water content using reflectance in the optical domain. *Remote Sensing of Environment*, **77**(1), 22 – 33.
- Chavez, P. S. (1988). An improved dark-object subtraction technique for atmospheric scattering correction of multispectral data. *Remote Sensing of Environment*, **24**(3), 459–479.
- Cheng, Y.-B., Zarco-Tejada, P. J., Riaño, D., Rueda, C. A., and Ustin, S. L. (2006). Estimating vegetation water content with hyperspectral data for different canopy scenarios: Relationships between AVIRIS and MODIS indexes. *Remote Sensing of Environment*, **105**(4), 354 – 366.
- Chervet, P., Lavigne, C., Roblin, A., and Brusaglioni, P. (2002). Effects of aerosol scattering phase function formulation on point-spread-function calculations. *Applied Optics*, **41**(30), 6489–6498.
- Cogliati, S., Rossini, M., Julitta, T., Meroni, M., Schickling, A., Burkart, A., Pinto, F., Rascher, U., and Colombo, R. (2015a). Continuous and long-term measurements of reflectance and sun-induced chlorophyll fluorescence by using novel automated field spectroscopy systems. *Remote Sensing of Environment*, **164**, 270–281.
- Cogliati, S., Verhoef, W., Kraft, S., Sabater, N., Alonso, L., Vicent, J., Moreno, J., Drusch, M., and Colombo, R. (2015b). Retrieval of sun-induced fluorescence using advanced spectral fitting methods. *Remote Sensing of Environment*, **169**, 344–357.
- Cooley, T., Anderson, G., Felde, G., Hoke, M., Ratkowski, A., Chetwynd, J., Gardner, J., Adler-Golden, S., Matthew, M., Berk, A., *et al.* (2002). FLAASH, a MODTRAN4-based atmospheric correction algorithm, its application and validation. In *Geoscience and Remote Sensing Symposium, 2002. IGARSS'02*, volume 3, pages 1414–1418. IEEE.
- Coppo, P., Taiti, A., Pettinato, L., Francois, M., Taccola, M., and Drusch, M. (2017). Fluorescence imaging spectrometer (FLORIS) for ESA FLEX mission. *Remote Sensing*, **9**(7), 649.
- Corp, L. A., McMurtrey, J. E., Middleton, E. M., Mulchi, C. L., Chappelle, E. W., and Daughtry, C. S. (2003). Fluorescence sensing systems: In vivo detection of biophysical variations in field corn due to nitrogen supply. *Remote Sensing of Environment*, **86**(4), 470–479.
- Damm, A., Schickling, A., Schläpfer, D., Schaepman, M., and Rascher, U. (2010). Deriving sun-induced chlorophyll fluorescence from airborne based spectrometer data. In *Proceedings Hyperspectral 2010 Workshop (SP-683)*, pages 7–7, Frascati (Italy).
- Damm, A., Erler, A., Hillen, W., Meroni, M., Schaepman, M. E., Verhoef, W., and Rascher, U. (2011). Modeling the impact of spectral sensor configurations on the FLD retrieval accuracy of sun-induced chlorophyll fluorescence. *Remote Sensing of Environment*, **115**(8), 1882–1892.
- Damm, A., Guanter, L., Laurent, V. C. E., Schaepman, M. E., Schickling, A., and Rascher, U. (2014). FLD-based retrieval of sun-induced chlorophyll fluorescence from medium spectral resolution airborne spectroscopy data. *Remote Sensing of Environment*, **147**, 256–266.
- Daumard, F., Goulas, Y., Ounis, A., Pedrós, R., and Moya, I. (2015). Measurement and correction of atmospheric effects at different altitudes for remote sensing of sun-induced fluorescence in oxygen absorption bands. *IEEE Transactions on Geoscience and Remote Sensing*, **53**(9), 5180–5196.
- Davidson, M., Moya, I., Ounis, A., Louis, J., Ducret, J.-M., Moreno, J., Casselles, V., Sobrino, J., Alonso, L., Pedros, R., Jimenez, J. C., Gomez, J.-L., Soria, G., Niclos, R., El-Kharraz, J., Martinez-Lozano, J. A., Utrillas,

- M. P., Miller, J., Laurila, T., and Thum, T. (2002). Solar induced fluorescence experiment (SIFLEX–2002): an overview. In *Remote Sensing of Solar-Induced Vegetation*, ESA Special Publication.
- de Leeuw, G., Holzer-Popp, T., Bevan, S., Davies, W. H., Descloitres, J., Grainger, R. G., Griesfeller, J., Heckel, A., Kinne, S., Klüser, L., *et al.* (2015). Evaluation of seven European aerosol optical depth retrieval algorithms for climate analysis. *Remote Sensing of Environment*, **162**, 295–315.
- Deschamps, P. Y., Herman, M., Lenoble, J., Tanre, D., and Viollier, M. (1980). Atmospheric effects in remote sensing of ground and ocean reflectances. In *Remote Sensing of Atmospheres and Oceans*, pages 115–147.
- Diner, D. J., Beckert, J. C., Reilly, T. H., Bruegge, C. J., Conel, J. E., Kahn, R. A., Martonchik, J. V., Ackerman, T. P., Davies, R., Gerstl, S. A., *et al.* (1998). Multi-angle imaging spectroradiometer (MISR) instrument description and experiment overview. *IEEE Transactions on Geoscience and Remote Sensing*, **36**(4), 1072–1087.
- Drinkwater, M. R. and Rebhan, H. (2007). Sentinel 3 : Mission Requirements Document (EOP-SMO/1151/MD-md). Technical report, ESA.
- Drolet, G., Wade, T., Nichol, C. J., MacLellan, C., Levula, J., Porcar-Castell, A., Nikinmaa, E., and Vesala, T. (2014). A temperature-controlled spectrometer system for continuous and unattended measurements of canopy spectral radiance and reflectance. *International Journal of Remote Sensing*, **35**(5), 1769–1785.
- Drusch, M. (2016). FLEX Earth Explorer 8 Mission Requirements Document. Technical report, European Space Agency (ESA)-EOP-SM/2221/MDr-md.
- Drusch, M., Moreno, J., Del Bello, U., Franco, R., Goulas, Y., Huth, A., Kraft, S., Middleton, E. M., Miglietta, F., Mohammed, G., *et al.* (2017). The FLuorescence EXplorer mission concept–ESA's Earth Explorer 8. *IEEE Transactions on Geoscience and Remote Sensing*, **55**(3), 1273–1284.
- D'Almeida, G. A., Koepke, P., and Shettle, E. P. (1991). *Atmospheric aerosols: global climatology and radiative characteristics*. A Deepak Pub.
- Dubovik, O., Holben, B., Eck, T. F., Smirnov, A., Kaufman, Y. J., King, M. D., Tanré, D., and Slutsker, I. (2002). Variability of absorption and optical properties of key aerosol types observed in worldwide locations. *Journal of the Atmospheric Sciences*, **59**(3), 590–608.
- Emde, C., Buras-Schnell, R., Kylling, A., Mayer, B., Gasteiger, J., Hamann, U., Kylling, J., Richter, B., Pause, C., Dowling, T., *et al.* (2016). The libRadtran software package for radiative transfer calculations (version 2.0. 1). *Geoscientific Model Development*, **9**(5), 1647–1672.
- European Space Agency (2015a). FLEX mission selection report: An Earth Explorer to observe vegetation fluorescence ESA- SP-1330/2. Technical report, ESA, Noordwijk, The Netherlands.
- European Space Agency (2015b). Sentinel online Cloud identification. <https://earth.esa.int/web/sentinel/technical-guides/sentinel-3-slstr/level-1/cloud-identification>. [Online; accessed 27-October-2015].
- European Space Agency (2017a). How does earth observation work? http://www.esa.int/Our_Activities/Observing_the_Earth/How_does_Earth_observation_work. [Online; accessed 18-April-2017].
- European Space Agency (2017b). Sentinel online. <https://sentinel.esa.int/web/sentinel/technical-guides/sentinel-3-olci/level-2/alternative-atmospheric-correction>. [Online; accessed 11-August-2017].
- Feret, J.-B., François, C., Asner, G. P., Gitelson, A. A., Martin, R. E., Bidet, L. P., Ustin, S. L., Le Maire, G., and Jacquemoud, S. (2008). PROSPECT-4 and 5: Advances in the leaf optical properties model separating photosynthetic pigments. *Remote Sensing of Environment*, **112**(6), 3030–3043.
- Frankenberg, C., Butz, A., and Toon, G. (2011a). Disentangling chlorophyll fluorescence from atmospheric scattering effects in O₂ A-band spectra of reflected sun-light. *Geophysical Research Letters*, **38**(3).
- Frankenberg, C., Fisher, J. B., Worden, J., Badgley, G., Saatchi, S. S., Lee, J.-E., Toon, G. C., Butz, A., Jung, M., Kuze, A., *et al.* (2011b). New global observations of the terrestrial carbon cycle from GOSAT: Patterns of plant fluorescence with gross primary productivity. *Geophysical Research Letters*, **38**(17).
- Frankenberg, C., O'Dell, C., Guanter, L., and McDuffie, J. (2012). Remote sensing of near-infrared chlorophyll fluorescence from space in scattering atmospheres: implications for its retrieval and interferences with atmospheric CO₂ retrievals. *Atmospheric Measurement Techniques*, **5**(8), 2081–2094.

- Frankenberg, C., O'Dell, C., Berry, J., Guanter, L., Joiner, J., Köhler, P., Pollock, R., and Taylor, T. E. (2014). Prospects for chlorophyll fluorescence remote sensing from the Orbiting Carbon Observatory-2. *Remote Sensing of Environment*, **147**, 1–12.
- Frey, R. A., Ackerman, S. A., Liu, Y., Strabala, K. I., Zhang, H., Key, J. R., and Wang, X. (2008). Cloud detection with MODIS. Part I: Improvements in the MODIS cloud mask for collection 5. *Journal of Atmospheric and Oceanic Technology*, **25**(7), 1057–1072.
- Frouin, R. and Middleton, E. M. (1990). A differential absorption technique to estimate atmospheric total water vapor amounts. In *Symposium on FIFE- First ISLSCP Field Experiment*, pages 135–139, Anaheim, CA (USA).
- Gamon, J., Coburn, C., Flanagan, L., Huemmrich, K., Kiddle, C., Sanchez-Azofeifa, G., Thayer, D., Vescovo, L., Gianelle, D., Sims, D., *et al.* (2010). SpecNet revisited: bridging flux and remote sensing communities. *Canadian Journal of Remote Sensing*, **36**(S2), S376–S390.
- Gao, B.-C. and Davis, C. O. (1997). Development of a line-by-line-based atmosphere removal algorithm for airborne and spaceborne imaging spectrometers. In *Optical Science, Engineering and Instrumentation'97*, pages 132–141. International Society for Optics and Photonics.
- Gao, B.-C. and Goetz, A. F. H. (1990). Column atmospheric water vapor and vegetation liquid water retrievals from Airborne Imaging Spectrometer data. *Journal of Geophysical Research*, **95**(D4), 3549.
- Gao, B.-C., Heidebrecht, K. B., and Goetz, A. F. (1993). Derivation of scaled surface reflectances from AVIRIS data. *Remote sensing of Environment*, **44**(2-3), 165–178.
- Gao, B.-C., Montes, M. J., Davis, C. O., and Goetz, A. F. (2009). Atmospheric correction algorithms for hyperspectral remote sensing data of land and ocean. *Remote Sensing of Environment*, **113**, S17–S24.
- Goetz, A. F., Boardman, J. W., Kindel, B. C., and Heidebrecht, K. B. (1997). Atmospheric corrections: on deriving surface reflectance from hyperspectral imagers. In *Optical Science, Engineering and Instrumentation'97*, pages 14–22. International Society for Optics and Photonics.
- Gómez-Chova, L., Camps-Valls, G., Calpe-Maravilla, J., Guanter, L., and Moreno, J. (2007). Cloud-screening algorithm for ENVISAT/MERIS multispectral images. *IEEE Transactions on Geoscience and Remote Sensing*, **45**(12), 4105–4118.
- Gómez-Chova, L., Camps-Valls, G., Calpe, J., Muñoz, J., and Moreno, J. (2009). MERIS/AATSR Synergy Algorithms for Cloud Screening, Aerosol Retrieval and Atmospheric Correction: Cloud Screening ATBD. Technical report, University of Valencia, Spain.
- Gómez-Chova, L., Amorós-López, J., Muñoz-Mari, J., and Camps-Valls, G. (2014). Cloud masking of multitemporal remote sensing images. In *Proc. SPIE*, volume 9244, page 924411.
- Grey, W. M., North, P. R., and Los, S. O. (2006). Computationally efficient method for retrieving aerosol optical depth from ATSR-2 and AATSR data. *Applied Optics*, **45**(12), 2786–2795.
- Guanter, L. (2006). New algorithms for atmospheric correction and retrieval of biophysical parameters in Earth Observation. Application to ENVISAT/MERIS data. *Valencia-Estudi General*, pages 86–94.
- Guanter, L., Alonso, L., Gómez-Chova, L., Amorós-López, J., Vila, J., and Moreno, J. (2007a). Estimation of solar-induced vegetation fluorescence from space measurements. *Geophysical Research Letters*, **34**(8).
- Guanter, L., Del Carmen González-Sanpedro, M., and Moreno, J. (2007b). A method for the atmospheric correction of envisat/meris data over land targets. *International Journal of Remote Sensing*, **28**(3-4), 709–728.
- Guanter, L., Richter, R., and Kaufmann, H. (2009). On the application of the MODTRAN4 atmospheric radiative transfer code to optical remote sensing. *International Journal of Remote Sensing*, **30**(6), 1407–1424.
- Guanter, L., Alonso, L., Gómez-Chova, L., Meroni, M., Preusker, R., Fischer, J., and Moreno, J. (2010). Developments for vegetation fluorescence retrieval from spaceborne high-resolution spectrometry in the O₂-A and O₂-B absorption bands. *Journal of Geophysical Research: Atmospheres*, **115**(D19).
- Guanter, L., Frankenberg, C., Dudhia, A., Lewis, P. E., Gómez-Dans, J., Kuze, A., Suto, H., and Grainger, R. G. (2012). Retrieval and global assessment of terrestrial chlorophyll fluorescence from GOSAT space measurements. *Remote Sensing of Environment*, **121**, 236–251.
- Guanter, L., Rossini, M., Colombo, R., Meroni, M., Frankenberg, C., Lee, J.-E., and Joiner, J. (2013). Using field spectroscopy to assess the potential of statistical approaches for the retrieval of sun-induced chlorophyll fluorescence from ground and space. *Remote Sensing of Environment*, **133**, 52–61.

- Guanter, L., Zhang, Y., Jung, M., Joiner, J., Voigt, M., Berry, J. A., Frankenberg, C., Huete, A. R., Zarco-Tejada, P., Lee, J.-E., *et al.* (2014). Global and time-resolved monitoring of crop photosynthesis with chlorophyll fluorescence. *Proceedings of the National Academy of Sciences*, **111**(14), E1327–E1333.
- Hadjimitsis, D. G. (2009). Aerosol optical thickness (AOT) retrieval over land using satellite image-based algorithm. *Air Quality, Atmosphere & Health*, **2**(2), 89–97.
- Hagolle, O., Huc, M., Pascual, D. V., and Dedieu, G. (2010). A multi-temporal method for cloud detection, applied to FORMOSAT-2, VENUS, LANDSAT and SENTINEL-2 images. *Remote Sensing of Environment*, **114**(8), 1747–1755.
- Heney, L. G. and Greenstein, J. L. (1941). Diffuse radiation in the galaxy. *The Astrophysical Journal*, **93**, 70–83.
- Hess, M., Koepke, P., and Schult, I. (1998). Optical properties of aerosols and clouds: The software package OPAC. *Bulletin of the American Meteorological Society*, **79**(5), 831–844.
- Holben, B. N., Eck, T., Slutsker, I., Tanre, D., Buis, J., Setzer, A., Vermote, E., Reagan, J., Kaufman, Y., Nakajima, T., *et al.* (1998). Aeronet—a federated instrument network and data archive for aerosol characterization. *Remote Sensing of Environment*, **66**(1), 1–16.
- Huete, A., Didan, K., Miura, T., Rodriguez, E. P., Gao, X., and Ferreira, L. G. (2002). Overview of the radiometric and biophysical performance of the MODIS vegetation indices. *Remote Sensing of Environment*, **83**(1), 195–213.
- Joiner, J., Yoshida, Y., Vasilkov, A., Middleton, E., *et al.* (2011). First observations of global and seasonal terrestrial chlorophyll fluorescence from space. *Biogeosciences*, **8**(3), 637–651.
- Joiner, J., Yoshida, Y., Vasilkov, A., Middleton, E., Campbell, P., Kuze, A., *et al.* (2012). Filling-in of near-infrared solar lines by terrestrial fluorescence and other geophysical effects: simulations and space-based observations from SCIAMACHY and GOSAT. *Atmospheric Measurement Techniques*, **5**(4), 809.
- Joiner, J., Guanter, L., Lindstrot, R., Voigt, M., Vasilkov, A., Middleton, E., Huemmrich, K., Yoshida, Y., and Frankenberg, C. (2013). Global monitoring of terrestrial chlorophyll fluorescence from moderate spectral resolution near-infrared satellite measurements: Methodology, simulations, and application to GOME-2. *Atmospheric Measurement Techniques*, **6**(2), 2803–2823.
- Joiner, J., Yoshida, Y., Vasilkov, A., Schaefer, K., Jung, M., Guanter, L., Zhang, Y., Garrity, S., Middleton, E., Huemmrich, K., Gu, L., and Marchesini, L. B. (2014). The seasonal cycle of satellite chlorophyll fluorescence observations and its relationship to vegetation phenology and ecosystem atmosphere carbon exchange. *Remote Sensing of Environment*, **152**, 375 – 391.
- Joiner, J., Yoshida, Y., Guanter, L., and Middleton, E. M. (2016a). New methods for retrieval of chlorophyll red fluorescence from hyper-spectral satellite instruments: simulations and application to GOME-2 and SCIAMACHY. *Atmospheric Measurement Techniques Discussions*, **9**(January), 1–41.
- Joiner, J., Yoshida, Y., Guanter, L., and Middleton, E. M. (2016b). New methods for the retrieval of chlorophyll red fluorescence from hyperspectral satellite instruments: simulations and application to GOME-2 and SCIAMACHY. *Atmospheric Measurement Techniques*, **9**(8), 3939.
- Junge, C. (1955). The size distribution and aging of natural aerosols as determined from electrical and optical data on the atmosphere. *Journal of Meteorology*, **12**(1), 13–25.
- Kattawar, G. W. (1975). A three-parameter analytic phase function for multiple scattering calculations. *Journal of Quantitative Spectroscopy and Radiative Transfer*, **15**(9), 839–849.
- Kaufman, Y. J. (1982). Solution of the equation of radiative transfer for remote sensing over nonuniform surface reflectivity. *Journal of Geophysical Research: Oceans*, **87**(C6), 4137–4147.
- Kaufman, Y. J. (1984). Atmospheric effect of spatial resolution of surface imagery. *Applied Optics*, **23**(22), 4164.
- Kaufman, Y. J. (1989). *The atmospheric effect on remote sensing and its correction: Theory and applications of optical Remote Sensing* (ed.) Ghassem Asrar. New York: John Wiley & Sons.
- Kaufman, Y. J. and Gao, B.-C. (1992). Remote sensing of water vapor in the near ir from EOS/MODIS. *IEEE Transactions on Geoscience and Remote Sensing*, **30**(5), 871–884.
- Khosravi, N. (2012). *Terrestrial plant fluorescence as seen from satellite data*. Master's thesis, University of Bremen. Bremen (Germany).
- Köhler, P., Guanter, L., and Joiner, J. (2015a). A linear method for the retrieval of sun-induced chlorophyll fluorescence from GOME-2 and SCIAMACHY data. *Atmospheric Measurement Techniques*, **8**(6), 2589–2608.

- Köhler, P., Guanter, L., and Frankenberg, C. (2015b). Simplified physically based retrieval of sun-induced chlorophyll fluorescence from GOSAT data. *IEEE Geoscience and Remote Sensing Letters*, **12**(7), 1446–1450.
- Kokhanovsky, A., Curier, R., De Leeuw, G., Grey, W., Lee, K. H., Bennouna, Y., Schoemaker, R., and North, P. (2009). The inter-comparison of AATSR dual-view aerosol optical thickness retrievals with results from various algorithms and instruments. *International Journal of Remote Sensing*, **30**(17), 4525–4537.
- Kolmonen, P., Sogacheva, L., Virtanen, T. H., de Leeuw, G., and Kulmala, M. (2016). The ADV/ASV AATSR aerosol retrieval algorithm: current status and presentation of a full-mission AOD dataset. *International Journal of Digital Earth*, **9**(6), 545–561.
- Kraft, S. (2012). Update of FLORIS SNR estimation model. Technical report, European Space Agency (esa)-IPD-TN-ESA-313.
- Kraft, S., Del Bello, U., Harnisch, B., Bouvet, M., Drusch, M., and Bézy, J. L. (2012). Fluorescence imaging spectrometer concepts for the earth explorer mission candidate FLEX. In *Proceedings of International Conference on Space Optics, Ajaccio, Corse*, pages 9–12.
- Kramer, H. J. (2002). *Observation of the Earth and its Environment: Survey of Missions and Sensors*. Springer Science & Business Media.
- Kramer, H. J. (2017a). ESA eoPortal directory – FORMOSAT-2. <https://directory.eoportal.org/web/eoportal/satellite-missions/f/formosat-2>. [Online; accessed 11-August-2017].
- Kramer, H. J. (2017b). ESA eoPortal directory – FORMOSAT-5. <https://directory.eoportal.org/web/eoportal/satellite-missions/f/formosat-5>. [Online; accessed 11-August-2017].
- Kramer, H. J. (2017c). ESA eoPortal directory – SEOSat/Ingenio. <https://directory.eoportal.org/web/eoportal/satellite-missions/s/seosat>. [Online; accessed 11-August-2017].
- Kramer, H. J. (2017d). ESA eoPortal directory – SPOT-5. <https://directory.eoportal.org/web/eoportal/satellite-missions/s/spot-5>. [Online; accessed 11-August-2017].
- Kramer, H. J. (2017e). ESA eoPortal directory – SPOT-6-7. <https://directory.eoportal.org/web/eoportal/satellite-missions/s/spot-6-7>. [Online; accessed 11-August-2017].
- Kramer, H. J. (2017f). ESA eoPortal directory – WorldView-1. <https://directory.eoportal.org/web/eoportal/satellite-missions/v-w-x-y-z/worldview-1>. [Online; accessed 11-August-2017].
- Kramer, H. J. (2017g). ESA eoPortal directory – WorldView-2. <https://directory.eoportal.org/web/eoportal/satellite-missions/v-w-x-y-z/worldview-2>. [Online; accessed 11-August-2017].
- Kramer, H. J. (2017h). ESA eoPortal directory – WorldView-3. <https://directory.eoportal.org/web/eoportal/satellite-missions/v-w-x-y-z/worldview-3>. [Online; accessed 11-August-2017].
- Kramer, H. J. (2017i). ESA eoPortal directory – WorldView-4. <https://directory.eoportal.org/web/eoportal/satellite-missions/v-w-x-y-z/worldview-4>. [Online; accessed 11-August-2017].
- Lenoble, J., Remer, J., Remer, L., and Tanre, D. (2011). *Aerosol Remote Sensing*. Springer Praxis Books. Springer.
- Lenoble, J., Remer, L., and Tanre, D. (2013). Aerosol remote sensing. chapter 3, page 53. Springer Science & Business Media.
- Liew, S. (1997). Effects of atmospheric aerosol models on the single scattering point spread function in optical remote sensing. *Geoscience and Remote Sensing, 1997. IGARSS'97. Remote Sensing-A Scientific Vision for Sustainable Development., 1997 IEEE International*, **4**, 1914–1916.
- Liu, X., Liu, L., Zhang, S., and Zhou, X. (2015). New spectral fitting method for full-spectrum solar-induced chlorophyll fluorescence retrieval based on principal components analysis. *Remote Sensing*, **7**(8), 10626–10645.
- Liu, X., Liu, L., Hu, J., and Du, S. (2017). Modeling the footprint and equivalent radiance transfer path length for tower-based hemispherical observations of chlorophyll fluorescence. *Sensors*, **17**(5), 1131.
- Louis, J., Ounis, A., Ducruet, J.-M., Evain, S., Laurila, T., Thum, T., Aurela, M., Wingsle, G., Alonso, L., Pedros, R., *et al.* (2005). Remote sensing of sunlight-induced chlorophyll fluorescence and reflectance of scots pine in the boreal forest during spring recovery. *Remote Sensing of Environment*, **96**(1), 37–48.

- Mac Arthur, A., Robinson, I., Rossini, M., Davis, N., and MacDonald, K. (2014). A dual-field-of-view spectrometer system for reflectance and fluorescence measurements (piccolo doppio) and correction of etaloning. In *Proceedings of the Fifth International Workshop on Remote Sensing of Vegetation Fluorescence*, pages 22–24.
- Maier, S. W., Günther, K. P., and Stellmes, M. (2003). Sun-induced fluorescence: A new tool for precision farming. *Digital imaging and spectral techniques: Applications to precision agriculture and crop physiology*, pages 209–222.
- Mayer, B. and Kylling, A. (2005). The libRadtran software package for radiative transfer calculations—description and examples of use. *Atmospheric Chemistry and Physics*, **5**(7), 1855–1877.
- Mazzoni, M., Falorni, P., and Verhoef, W. (2010). High-resolution methods for fluorescence retrieval from space. *Optics Express*, **18**(15), 15649–15663.
- Mekler, Y. and Kaufman, Y. J. (1982). Contrast reduction by the atmosphere and retrieval of nonuniform surface reflectance. *Applied Optics*, **21**(2), 310–316.
- Meroni, M., Rossini, M., Guanter, L., Alonso, L., Rascher, U., Colombo, R., and Moreno, J. (2009). Remote sensing of solar-induced chlorophyll fluorescence: Review of methods and applications. *Remote Sensing of Environment*, **113**(10), 2037–2051.
- Meroni, M., Busetto, L., Colombo, R., Guanter, L., Moreno, J., and Verhoef, W. (2010). Performance of spectral fitting methods for vegetation fluorescence quantification. *Remote Sensing of Environment*, **114**(2), 363–374.
- Meroni, M., Barducci, A., Cogliati, S., Castagnoli, F., Rossini, M., Busetto, L., Migliavacca, M., Cremonese, E., Galvagno, M., Colombo, R., *et al.* (2011). The hyperspectral irradiometer, a new instrument for long-term and unattended field spectroscopy measurements. *Review of Scientific Instruments*, **82**(4), 043106.
- Middleton, E., Corp, L. A., and Cook, B. D. (2013). FUSION canopy tower system for remote sensing observations of terrestrial ecosystems. <ftp://fusionftp.gsfc.nasa.gov/FUSION/NASA%20FUSION%20White%20Paper%20V1.pdf>. Accessed: 2016-05-25.
- Mie, G. (1908). Beiträge zur optik trüber medien, speziell kolloidaler metallösungen. *Annalen der physik*, **330**(3), 377–445.
- Minomura, M., KUzE, H., and Takeuchi, N. (2001). Adjacency effect in the atmospheric correction of satellite remote sensing data: evaluation of the influence of aerosol extinction profiles. *Optical Review*, **8**(2), 133–141.
- Moreno, J., Alonso, L., and Vicent, J. (2012). Technical Note on FLORIS Reference TOA radiance. Technical report, Image Processing Laboratory (IPL), University of Valencia.
- Moreno, J., Alonso, L., Delegido, J., Rivera, J., Ruiz-Verdú, A., Sabater, N., Tenjo, C., Verrelst, J., and Vicent, J. (2014). Misión FLEX (FLuorescence EXplorer): Observación de la fluorescencia por teledetección como nueva técnica de estudio del estado de la vegetación terrestre a escala global. *Revista Teledetección*, (41), 111–119.
- Moreno, J. F., Goulas, Y., Huth, A., Middleton, E., Miglietta, F., Mohammed, G., Nedbal, L., Rascher, U., Verhoef, W., and Drusch, M. (2016). Very high spectral resolution imaging spectroscopy: The FLuorescence EXplorer (FLEX) mission. In *Geoscience and Remote Sensing Symposium (IGARSS), 2016 IEEE International*, pages 264–267. IEEE.
- Ni, Z., Liu, Z., Li, Z.-L., Nerry, F., Huo, H., Sun, R., Yang, P., and Zhang, W. (2016). Investigation of atmospheric effects on retrieval of sun-induced fluorescence using hyperspectral imagery. *Sensors*, **16**(4), 480.
- North, P., Grey, W., Heckel, A., and Fischer, J. (2009a). MERIS/AATSR Synergy Algorithms for Cloud Screening, Aerosol Retrieval, and Atmospheric Correction. ATBD Contract No 21090, ESRIN.
- North, P., Grey, W., Heckel, A., Fischer, J., Preusker, R., and Brockmann, C. (2009b). MERIS/AATSR Synergy Algorithms for Cloud Screening, Aerosol Retrieval, and Atmospheric Correction. Algorithm Theoretical Basis Document Land Aerosol and Surface Reflectance ATBD. no, **21090**, 1–44.
- Pacifici, F. (2016). Validation of the DigitalGlobe surface reflectance product. In *Geoscience and Remote Sensing Symposium (IGARSS), 2016 IEEE International*, pages 1973–1975. IEEE.
- Pearce, W. (1977). A study of the effects of the atmosphere on thematic mapper observations. *Report 004-77 Washington Analytical Service Center, Riverdale, Md.(USA)*.
- Pierluisi, J. H. and Chang Mind, T. (1986). Molecular transmittance band model for oxygen in the visible. *Applied Optics*, **25**, 2458–2460.
- Plascyk, J. A. (1975). The MK II Fraunhofer line discriminator (FLD-II) for airborne and orbital remote sensing of solar-stimulated luminescence. *Optical Engineering*, **14**(4), 339–0.

- Plascyk, J. A. and Gabriel, F. C. (1975). The Fraunhofer line discriminator MKII—an airborne instrument for precise and standardized ecological luminescence measurement. *IEEE Transactions on Instrumentation and Measurement*, **24**(4), 306–313.
- Porcar-Castell, A., Tyystjarvi, E., Atherton, J., van der Tol, C., Flexas, J., Pfundel, E. E., Moreno, J., Frankenberg, C., and Berry, J. a. (2014). Linking chlorophyll a fluorescence to photosynthesis for remote sensing applications: mechanisms and challenges. *Journal of Experimental Botany*, pages 1–31.
- Porcar-Castell, A., Mac Arthur, A., Rossini, M., Eklundh, L., Pacheco-Labrador, J., Anderson, K., Balzarolo, M., Martín, M., Jin, H., Tomelleri, E., *et al.* (2015). EUROSPEC. *Biogeosciences*.
- Rascher, U., Agati, G., Alonso, L., Cecchi, G., Champagne, S., Colombo, R., Damm, A., Daumard, F., De Miguel, E., Fernández, G., *et al.* (2009). CEFLES2: the remote sensing component to quantify photosynthetic efficiency from the leaf to the region by measuring sun-induced fluorescence in the oxygen absorption bands. *Biogeosciences*, **6**(7), 1181–1198.
- Rast, M., Bezy, J., and Bruzzi, S. (1999). The ESA Medium Resolution Imaging Spectrometer MERIS a review of the instrument and its mission. *International Journal of Remote Sensing*, **20**(9), 1681–1702.
- Raychaudhuri, B. (2014). Solar-induced fluorescence of terrestrial chlorophyll derived from the O₂-A band of Hyperion hyperspectral images. *Remote sensing letters*, **5**(11), 941–950.
- Rayleigh, J. W. S. B. (1871). *On the scattering of light by small particles*.
- Reinersman, P. N. and Carder, K. L. (1995). Monte Carlo simulation of the atmospheric point-spread function with an application to correction for the adjacency effect. *Applied Optics*, **34**(21), 4453–4471.
- Richter, R. (1996). A spatially adaptive fast atmospheric correction algorithm. *International Journal of Remote Sensing*, **17**(6), 1201–1214.
- Richter, R. and Schläpfer, D. (2007a). ATCOR-2/3 user guide. *DLR-German Aerospace Centre, Remote Sensing Data Centre, Oberpfaffenhofen, Germany*.
- Richter, R. and Schläpfer, D. (2007b). Atmospheric/Topographic Correction for Airborne Imagery, ATCOR-4 User Guide, Version 4.2. *DLR, Wessling, Germany, 125p*.
- Rossini, M., Cogliati, S., Meroni, M., Migliavacca, M., Galvagno, M., Busetto, L., Cremonese, E., Julitta, T., Siniscalco, C., Morra di Cella, U., *et al.* (2012). Remote sensing-based estimation of gross primary production in a subalpine grassland. *Biogeosciences*, **9**(7), 2565–2584.
- Rossini, M., Migliavacca, M., Galvagno, M., Meroni, M., Cogliati, S., Cremonese, E., Fava, F., Gitelson, A., Julitta, T., di Cella, U. M., *et al.* (2014). Remote estimation of grassland gross primary production during extreme meteorological seasons. *International Journal of Applied Earth Observation and Geoinformation*, **29**, 1–10.
- Rothman, L. S., Gordon, I. E., Barbe, A., Benner, D. C., Bernath, P. F., Birk, M., Boudon, V., Brown, L. R., Campargue, A., Champion, J.-P., *et al.* (2009). The HITRAN 2008 molecular spectroscopic database. *Journal of Quantitative Spectroscopy and Radiative Transfer*, **110**(9), 533–572.
- Roy, D. P., Wulder, M., Loveland, T., Woodcock, C., Allen, R., Anderson, M., Helder, D., Irons, J., Johnson, D., Kennedy, R., *et al.* (2014). Landsat-8: Science and product vision for terrestrial global change research. *Remote Sensing of Environment*, **145**, 154–172.
- Sabater, N., Alonso, L., Cogliati, S., Vicent, J., Tenjo, C., Verrelst, J., and Moreno, J. (2015). A sun-induced vegetation fluorescence retrieval method from top of atmosphere radiance for the FLEX/Sentinel-3 tandem mission. In *Geoscience and Remote Sensing Symposium (IGARSS), 2015 IEEE International*, pages 2669–2672. IEEE.
- Sabater, N., Vicent, J., Alonso, L., Cogliati, S., Verrelst, J., and Moreno, J. (2017a). Impact of atmospheric inversion effects on solar-induced chlorophyll fluorescence: Exploitation of the apparent reflectance as a quality indicator. *Remote Sensing*, **9**(6), 622.
- Sabater, N., Middleton, E., Malenovsky, Z., Alonso, L., Verrelst, J., Huemmrich, K., Campbell, P., Kustas, W., Vicent, J., Van Wittenberghe, S., and Moreno, J. (2017b). Oxygen transmittance correction for solar-induced chlorophyll fluorescence measured on proximal sensing: application to the NASA-GSFC FUSION tower. In *IEEE International Geoscience and Remote Sensing Symposium, IGARSS, Fort Worth, TX, USA*.
- Santer, R., Carrere, V., Dubuisson, P., and Roger, J. (1999). Atmospheric correction over land for MERIS. *International Journal of Remote Sensing*, **20**(9), 1819–1840.

- Schläpfer, D. (1998). Differential absorption methodology for imaging spectroscopy of atmospheric water vapor. *Remote Sensing Laboratories, Dept. of Geography, University of Zurich*.
- Schläpfer, D. and Richter, R. (2017). Atmospheric correction of imaging spectroscopy data using shadow-based quantification of aerosol scattering effects. *EARS&L eProceedings*, **16**(1), 21.
- Schläpfer, D., Keller, J., and Itten, K. (1996). Imaging spectrometry of tropospheric ozone and water vapor. *AA Balkema, Rotterdam*, pages 439–446.
- Schläpfer, D., Borel, C. C., Keller, J., and Itten, K. I. (1998). Atmospheric precorrected differential absorption technique to retrieve columnar water vapor. *Remote Sensing of Environment*, **65**(3), 353–366.
- SCI NASA (2016). How greenhouse effect works. <http://www.ces.fau.edu/nasa/module-2/how-greenhouse-effect-works.php>. [Online; updated 11-August-2016].
- Shettle, E. P. (1990). Models of aerosols, clouds, and precipitation for atmospheric propagation studies. In *In AGARD, Atmospheric Propagation in the UV, Visible, IR, and MM-WaveRegion and Related Systems Aspects 14 p (SEE N90-21907 15-32)*.
- Shettle, E. P. and Fenn, R. W. (1979). Models for the aerosols of the lower atmosphere and the effects of humidity variations on their optical properties. Technical report, DTIC Document.
- Smith, G. M. and Milton, E. J. (1999). The use of the empirical line method to calibrate remotely sensed data to reflectance. *International Journal of Remote Sensing*, **20**(13), 2653–2662.
- Sobel, I., F. G. (1968). A 3x3 isotropic gradient operator for image processing. In *Stanford Artificial Intelligence Project (SAIL)*.
- Sogacheva, L., Kolmonen, P., Virtanen, T., Rodriguez, E., Sundström, A., and de Leeuw, G. (2015). Determination of land surface reflectance using the AATSR dual-view capability. *Atmospheric Measurement Techniques*, **8**(2), 891.
- Stephens, G. L. (1994). *Remote sensing of the lower atmosphere*, volume 1994. Oxford University Press New York.
- Sterckx, S., Knaeps, E., and Ruddick, K. (2011). Detection and correction of adjacency effects in hyperspectral airborne data of coastal and inland waters: the use of the near infrared similarity spectrum. *International Journal of Remote Sensing*, **32**(21), 6479–6505.
- Strutt, J. W. (1871). XV On the light from the sky, its polarization and colour. *The London, Edinburgh, and Dublin Philosophical Magazine and Journal of Science*, **41**(271), 107–120.
- Sun, Y., Frankenberg, C., Wood, J. D., Schimel, D. S., Jung, M., Guanter, L., Drewry, D. T., Verma, M., Porcar-Castell, A., Griffis, T. J., Gu, L., Magney, T. S., Köhler, P., Evans, B., and Yuen, K. (2017). OCO-2 advances photosynthesis observation from space via solar-induced chlorophyll fluorescence. *Science*, **358**(6360).
- Taiz, L. and Zeiger, E. (2002). *Plant Physiology*. Sinauer Associates.
- Tanre, D., Herman, M., and Deschamps, P. Y. (1981). Influence of the background contribution upon space measurements of ground reflectance. *Applied Optics*, **20**(20), 3676–3684.
- Tanre, D., Herman, M., and Deschamps, P. Y. (1983). Influence of the atmosphere on space measurements of directional properties. *Applied Optics*, **22**(5), 733–741.
- Thomas, C., Briottet, X., and Santer, R. (2011). OSIS: remote sensing code for estimating aerosol optical properties in urban areas from very high spatial resolution images. *Applied Optics*, **50**(28), 5408–5421.
- Tol, C., Verhoef, W., Timmermans, J., Verhoef, A., and Su, Z. (2009). An integrated model of soil-canopy spectral radiances, photosynthesis, fluorescence, temperature and energy balance. *Biogeosciences*, **6**(12), 3109–3129.
- Tol, C., Berry, J., Campbell, P., and Rascher, U. (2014). Models of fluorescence and photosynthesis for interpreting measurements of solar-induced chlorophyll fluorescence. *Journal of Geophysical Research: Biogeosciences*.
- Toublanc, D. (1996). Henyey-greenstein and mie phase functions in monte carlo radiative transfer computations. *Applied Optics*, **35**(18), 3270–3274.
- Tucker, C. J. (1979). Red and photographic infrared linear combinations for monitoring vegetation. *Remote sensing of Environment*, **8**(2), 127–150.
- Van der Meer, F. and De Jong, S. (2000). Improving the results of spectral unmixing of Landsat Thematic Mapper imagery by enhancing the orthogonality of end-members. *International Journal of Remote Sensing*, **21**(15), 2781–2797.

- Van Wittenberghe, S. (2014). Hyperspectral solar-induced chlorophyll fluorescence of urban tree leaves: analyses and applications. *University of Antwerp*.
- Veeffkind, J. P. and de Leeuw, G. (1998). A new algorithm to determine the spectral aerosol optical depth from satellite radiometer measurements. *Journal of Aerosol Science*, **29**(10), 1237–1248.
- Verhoef, W. (1984). Light scattering by leaf layers with application to canopy reflectance modeling: the sail model. *Remote Sensing of Environment*, **16**(2), 125–141.
- Verhoef, W. and Bach, H. (2012). Simulation of Sentinel-3 images by four-stream surface-atmosphere radiative transfer modeling in the optical and thermal domains. *Remote Sensing of Environment*, **120**, 197–207.
- Verhoef, W., Van der Tol, C., and Middleton, E. M. (2014). Vegetation canopy fluorescence and reflectance retrieval by model inversion using optimization. In *Proceedings of the 5th International Workshop on Remote Sensing of Vegetation Fluorescence, Paris, France*, pages 22–24.
- Verma, M., Schimel, D., Evans, B., Frankenberg, C., Beringer, J., Drewry, D. T., Magney, T., Marang, I., Hutley, L., Moore, C., *et al.* (2017). Effect of environmental conditions on the relationship between solar-induced fluorescence and gross primary productivity at an OzFlux grassland site. *Journal of Geophysical Research: Biogeosciences*, **122**(3), 716–733.
- Vermote, E., El Saleous, N., Justice, C., Kaufman, Y., Privette, J., Remer, L., Roger, J., and Tanre, D. (1997a). Atmospheric correction of visible to middle-infrared eos-modis data over land surfaces: Background, operational algorithm and validation. *Journal of Geophysical Research: Atmospheres*, **102**(D14), 17131–17141.
- Vermote, E., Tanré, D., Deuze, J. L., Herman, M., and Morcette, J.-J. (1997b). Second simulation of the satellite signal in the solar spectrum, 6S: An overview. *IEEE transactions on geoscience and remote sensing*, **35**(3), 675–686.
- Vermote, E., El Saleous, N. Z., and Justice, C. O. (2002). Atmospheric correction of modis data in the visible to middle infrared: first results. *Remote Sensing of Environment*, **83**(1), 97–111.
- Vermote, E., Tanré, D., Deuzé, J., Herman, J., and Kotchenova, S. (2006). Second Simulation of a Satellite Signal in the Solar Spectrum - Vector (6SV), User Guide Version 3. Technical report, Department of Geography-University of Maryland, Laboratoire d'Optique Atmosphérique - Université des Sciences et Technologies de Lille and European Centre for Medium Range Weather Forecast (ECWMF).
- Verrelst, J., Sabater, N., Rivera, J. P., Muñoz-Marí, J., Vicent, J., Camps-Valls, G., and Moreno, J. (2016a). Emulation of leaf, canopy and atmosphere radiative transfer models for fast global sensitivity analysis. *Remote Sensing*, **8**(8), 673.
- Verrelst, J., van der Tol, C., Magnani, F., Sabater, N., Rivera, J. P., Mohammed, G., and Moreno, J. (2016b). Evaluating the predictive power of sun-induced chlorophyll fluorescence to estimate net photosynthesis of vegetation canopies: A SCOPE modeling study. *Remote Sensing of Environment*, **176**, 139–151.
- Vicent, J., Alonso, L., Cogliati, S., Damm, Alexander, P. F., Sabater, N., Rasher, U., Verrelst, J., and Moreno, J. (2014). Hyplant airborne data processing in the context of the HYFLEX 2012/13 field campaign for the retrieval of sun-induced fluorescence emission. In *Proceedings of the 5th international workshop on remote sensing of vegetation fluorescence, Paris (France)*. ESA.
- Vicent, J., Alonso, L., Sabater, N., Miesch, C., Kraft, S., and Moreno, J. (2015). Propagation of spectral characterization errors of imaging spectrometers at level-1 and its correction within a level-2 recalibration scheme. In *SPIE Optical Engineering+ Applications*, pages 96110T–96110T. International Society for Optics and Photonics.
- Vicent, J., Sabater, N., Tenjo, C., Acarreta, J. R., Manzano, M., Rivera, J. P., Jurado, P., Franco, R., Alonso, L., Verrelst, J., *et al.* (2016). FLEX end-to-end mission performance simulator. *IEEE Transactions on Geoscience and Remote Sensing*, **54**(7), 4215–4223.
- Vicent, J., Sabater, N., Verrelst, J., Alonso, L., and Moreno, J. (2017). Assessment of approximations in aerosol optical properties and vertical distribution into FLEX atmospherically-corrected surface reflectance and retrieved Sun-Induced Fluorescence. *Remote Sensing*, **9**(7), 675.
- Von Hoyningen-Huene, W., Freitag, M., and Burrows, J. (2003). Retrieval of aerosol optical thickness over land surfaces from top-of-atmosphere radiance. *Journal of Geophysical Research: Atmospheres*, **108**(D9).
- Wetterdienst, D. (2016). Particle-size distribution. <http://www.dwd.de/EN/research/>

- [observing_atmosphere/composition_atmosphere/aerosol/cont_nav/particle_size_distribution_node.html](#). [Online; accessed 08-May-2017].
- Wolanin, A., Rozanov, V., Dinter, T., Noël, S., Vountas, M., Burrows, J., and Bracher, A. (2015). Global retrieval of marine and terrestrial chlorophyll fluorescence at its red peak using hyperspectral top of atmosphere radiance measurements: Feasibility study and first results. *Remote Sensing of Environment*, **166**, 243–261.
- Zhang, Q., Fan, Y., Zhang, Y., Chou, S., Ju, W., and Chen, J. M. (2016). A conjunct near-surface spectroscopy system for fix-angle and multi-angle continuous measurements of canopy reflectance and sun-induced chlorophyll fluorescence. In *SPIE Optical Engineering+ Applications*, pages 99770C–99770C. International Society for Optics and Photonics.
- Zhang, Yao., Xiao, X., Jin, C., Dong, J., Zhou, S., Wagle, P., Joiner, J., Guanter, L., Zhang, Y., Zhang, G., Qin, Y., Wang, J., and Moore, B. (2016). Consistency between sun-induced chlorophyll fluorescence and gross primary production of vegetation in north america. *Remote Sensing of Environment*, **183**, 154 – 169.
- Zhang, Y., Guanter, L., Berry, J. A., Joiner, J., Tol, C., Huete, A., Gitelson, A., Voigt, M., and Köhler, P. (2014). Estimation of vegetation photosynthetic capacity from space-based measurements of chlorophyll fluorescence for terrestrial biosphere models. *Global Change Biology*, **20**(12), 3727–3742.
- Zhang, Y., Guanter, L., Berry, J. A., van der Tol, C., Yang, X., Tang, J., and Zhang, F. (2016). Model-based analysis of the relationship between sun-induced chlorophyll fluorescence and gross primary production for remote sensing applications. *Remote Sensing of Environment*, **187**, 145 – 155.